UNIVERSITY OF NAPLES FEDERICO II

DOCTORAL THESIS

Vibroacoustic Optimal Design and Structural Scalability of Composite Wing for the Next Generation Civil Tiltrotor

---

Author:
Aniello Daniele MARANO

Supervisor:
Prof. Eng. Francesco MARULO

A thesis submitted in fulfillment of the requirements for the degree of Doctor of Philosophy

in

Aerospace Engineering
Department of Industrial Engineering

March 10, 2022

Declaration of Authorship

I, Aniello Daniele MARANO, declare that this thesis titled, "Vibroacoustic Optimal Design and Structural Scalability of Composite Wing for the Next Generation Civil Tiltrotor" and the work presented in it are my own. I confirm that:

- This work was done wholly or mainly while in candidature for a research degree at this University.
- Where any part of this thesis has previously been submitted for a degree or any other qualification at this University or any other institution, this has been clearly stated.
- Where I have consulted the published work of others, this is always clearly attributed.
- Where I have quoted from the work of others, the source is always given. With the exception of such quotations, this thesis is entirely my own work.
- I have acknowledged all main sources of help.
- Where the thesis is based on work done by myself jointly with others, I have made clear exactly what was done by others and what I have contributed myself.

Signed: Aniello Daniele Marano

Date: 10/03/22, Napoli

"Le vent se leve... Il faut tenter de vivre!"

"S'alza il vento... Bisogna osar di vivere!"

Paul Valéry

UNIVERSITY OF NAPLES FEDERICO II

Abstract

Department of Industrial Engineering

Doctor of Philosophy

Vibroacoustic Optimal Design and Structural Scalability of Composite Wing for the Next Generation Civil Tiltrotor

by Aniello Daniele MARANO

This dissertation presents the up-scaled process of an innovative composite wing for the Next Generation Civil Tiltrotor. Inspired from the Technological Demonstrator wing, the purpose is to investigate the up-scaling process of its structural architecture to realize a new high lift, low drag wing optimized to improve downwash impingement in helicopter mode and increase the total fuel capacity.
About the wing primary structure, for the wingbox, a curvilinear rear spar is used instead of the straight spars associated with the conventional transport wings. Additionally, the composite structure is considered for the wing design because it has larger ratios in the strength-to-weight and the stiffness-to-weight than those for the metallic structure, which can further reduce the total tiltrotor structural weight and fuel consumption.
High speed and maneuverability, and at the same time, low vibration and noise are the most important features of the new generation rotorcrafts and tiltrotors. Tiltrotors manufacturers are trying to bring tiltrotor technology to the civil aviation market by reducing the interior vibration and noise level so to make the competitiveness of tilt-rotor aircraft greatly improved for this purpose. For tilt-rotor aircraft, the aeroacoustics has a great influence on the interior noise. The in-flight noise test campaign carried out on board of the AW609 LHD tiltrotor is described in this thesis. These tests were performed with the main goals to validate an experimental setup in a fully new environment and the assessment of a data analysis procedure and to better investigate the problem of noise and then obtain satisfactory levels of comfort for passengers of the NGCTR.
The use of the lightweight composite could lead to enhanced flexibility of the wing, which may cause many aeroelastic problems such as large deflections, the onset of flutter and whirl flutter, loss of control, etc.
Whirl flutter clearance, crashability requirements and, wing box structural layout design are all considered to address some of these problems through multidisciplinary design, analysis, and optimization studies in this work.
In this context, some laboratory activities on the sidelines of scalability were conducted to become more confident with the aeroelastic phenomena treated. In particular, a series of activities in the vibrations test field modal testing and experimental treatment of the whirl flutter phenomenon are presented.
Several numerical and structural dynamics tests were performed to confidently and validate the Multi-Input Multi-Output methods.
A section of the thesis shows the design, development, and testing of a small-scale unpowered experimental test rig with a multi-blade propeller to demonstrate the aeroelastic phenomenon of Whirl Flutter investigated by means of Operational Modal Analysis. The discussion experimentally and numerically introduces the sensitivity analyses as the shaft inertia and stiffness parameters and, the air stream speeds vary and the definition of the whirl flutter stability diagram, identifying for which speed conditions the shaft-propeller system is free from flutter.
The best solution of the NGCTR wing while satisfying different design constraints is

investigated employing a multi-objective optimization process implemented in the Multicella tool. Research studies show the possible benefits of using Multicella for wing preliminary design in terms of time-saving with respect to the Finite Element Model approach. Several optimization studies are conducted to show the influence of different composite materials to achieve the optimal stiffness distribution to reach the total structural weight minimization and maximum margin of safety requirements.

Acknowledgements

This research work has been funded by the European H2020 Clean Sky 2 FRC IADP NextGenCTR, dedicated to the design, construction, and flying of an innovative Civil Tiltrotor technology demonstrator.
The financial support from the CIRA Italian Aerospace Research Center and T-WING project was important for the research and my Ph.D. Thanks to the many training, meeting, and network activities organized by the various academic and industrial partners, I could get in touch with highly diverse research fields, enriching my knowledge. It was a unique and great experience to be part of these interdisciplinary projects.

Quella dei ringraziamenti è sempre la pagina più lieta ma anche la più difficile da scrivere anche se a valle di un dottorato di ricerca. Ecco alcune delle persone a cui va la mia più sincera riconoscenza.

Alla mia tutor aziendale Marika, Per la stima e l'affetto che mi ha sempre dimostrato. Sei stata per me esempio di grande tenacia e sensibilità.
A tutti i colleghi del consorzio T-WING, Posso considerarmi molto fortunato ad avere avuto l'opportunità di collaborare con voi tutti. Siete stati per me fonte di motivazione e coraggio. Avete condiviso con me le vostre esperienze lavorative ed il vostro modo di fare. Ho apprezzato tutto di voi, le competenze tecniche ed il lato umano, privato. Lo avete fatto sempre con estrema gentilezza e disponibilità e per questo, so di certo che sentirò la vostra mancanza.
Ai miei colleghi che compongono il gruppo di ricerca LIFE Lab, Oggi il mio Dottorato lo condivido con tutti voi che ne siete artefici almeno quanto me: senza LIFE Lab nella mia vita nessuna delle indimenticabili esperienze che ho vissuto durante questi tre anni sarebbe mai accaduta. Grazie alle persone che ne hanno fatto parte. A chi si è trattenuto per qualche giorno, a chi per il solo tempo di un caffè o per la durata del lavoro di tesi. Grazie a chi c'è sempre stato, Grazie a chi non c'è più ma che di LIFE LAB ne è le fondamenta. Un grazie particolare a Michele Guida e Tiziano Polito, i pilastri principali di questo gruppo. Grazie ai più giovani, Gennaro, Giuseppe e Vincenzo. Sono ben consapevole di aver avuto la rara fortuna di trovare in voi degli amici veri, prima che colleghi. Grazie oggi e sempre.
Al mio tutor, Ringrazio il Professor Marulo, per essere stato oltre che il mio mentore, per me, un secondo padre. Gli scambi di idee ed i momenti di riflessione che hanno costellato questi anni di lavoro e ricerca sono un tesoro inestimabile che porterò sempre con me. Grazie per avermi indotto a mettere a fuoco la strada migliore, in accademia così come fuori. Lei mi ha insegnato non solo ad affrontare la tesi, ma la vita. Porterò nel cuore per sempre questi suoi insegnamenti. Grazie immensamente.

Ai miei zii, Anna e Luigi, che nel mio cuore hanno sempre un posto. Li ringrazio per l'interesse sempre avuto nei miei confronti soprattutto durante questo percorso.
Grazie Silvia, grazie amica mia, per tutto. Per aver condiviso le cose belle e quelle brutte, in questi anni di dottorato, a volte bui, a volte meravigliosi ma sempre così pieni. Grazie per le centinaia di ore condivise in ufficio e non solo. Grazie per avermi sempre incoraggiato ogni volta prima delle conferenze, ed a guardare avanti a testa alta lungo questo percorso che, senza te, sarebbe stato sicuramente molto meno divertente. So che a parole non riesci ad esprimere il bene che mi vuoi. Grazie.
A mia sorella, che ha sopportato amorevolmente scleri e frustrazioni (ma soprattutto scleri), ansie e paure negli anni di laurea prima e durante quelli del dottorato poi. A te che hai gioito per ogni mio piccolo traguardo che raggiungevo come se fosse il tuo. Ora che ho finalmente raggiunto la meta so con certezza che non sarei mai riuscito a salire in vetta, senza quella tua gioia, quei tuoi sorrisi, non sarei mai riuscito a terminare questa tesi e di questo te ne sarò per sempre grato.
Alla persona che amo, da quando ti ho conosciuta sei sempre al mio fianco, non mi hai mai lasciato solo e mi hai sempre fatto sentire quanto tu credessi in me, ogni giorno. Con la tua dolcezza hai saputo ridimensionare ogni volta le mie preoccupazioni, ed ispirare con il tuo amore puro, ogni mia singola scelta. Grazie infinitamente ed eternamente mio Amore.
Ai miei genitori, Grazie è una parola troppo scarna per esprimere la mia gratitudine nei vostri confronti. Non c'è parola di questa tesi che in qualche modo non racchiuda il bene che provo per voi, per la vostra dolce presenza nei miei giorni, per il vostro sostegno molto spesso silenzioso ma sempre tenace. Grazie per la vostra costante vicinanza. Grazie per avermi amato e sostenuto ogni giorno della mia vita. Grazie per avermi permesso di studiare, di assecondare le mie inclinazioni, di scegliere infine la mia strada. La vita spesso non è facile, ma avere dei buoni genitori semplifica decisamente molte cose. Grazie di cuore.

Daniele

Contents

List of Figures

List of Tables

List of Abbreviations

BL	**B**uttock **L**ine
BPF	**B**lade **P**assage **F**requency
BW	**B**ackward **W**hirl mode
DMU	**D**igital **M**ock **U**p
DOF	**D**egree **O**f **F**reedom
EMA	**E**xperimental **M**odal **A**nalysis
ESDU	**E**ngineering **S**ciences **D**ata **U**nit
FRC IADP	**F**ast **R**otor**C**raft **I**nnovative **A**ircraft **D**emonstrator **P**latform
FEM	**F**inite **E**lement **M**ethod
FRF	**F**requency **R**esponse **F**unction
FFT	**F**ast **F**ourier **T**ransform
FW	**F**orward **W**hirl mode
GTOW	**G**ross **T**ake **O**ff **W**eight
LHD	**L**eonardo **H**elicopters **D**ivision
LSCF	**L**east-**S**quare **C**omplex **F**requency
MAC	**M**odal **A**ssurance **C**riterion
MIMO	**M**ulti **I**nput **M**ulti **O**utput
MPF	**M**odal **P**artecipation **F**actor
NGCTR	**N**ext **G**eneration **C**ivil **T**ilt **R**otor
NGCTR-TD	**N**ext **G**eneration **C**ivil **T**ilt **R**otor **-** **T**echnology **D**emonstrator
OASPL	**O**ver**A**ll **S**ound **P**ressure **L**evel
ODS	**O**perating **D**eflection **S**hape
OMA	**O**perational **M**odal **A**nalysis
RMS	**R**oot **M**ean **S**quare
RPM	**R**ound **P**er **M**inute
PSD	**P**ower **S**pectral **D**ensity
SBN	**S**tructure **B**orne **N**oise
SIMO	**S**ingle **I**nput **M**ulti **O**utput
SISO	**S**ingle **I**nput **S**ingle **O**utput
SPL	**S**ound **P**ressure **L**evel
TA	**T**est **A**rticle
TBL	**T**urbolent **B**oundary **L**ayer
VTOL	**V**ertical **T**ake **O**ff **L**anding
WAL	**W**ork **A**rea **L**eader
WF	**W**hirl **F**lutter
WFSD	**W**hirl **F**lutter **S**mall **D**emonstrator
WRT	**W**hit **R**espect **T**o

Physical Constants

Reference value of the sound pressure $p_{ref} = 2 \times 10^5$ Pa

List of Symbols

Θ	Engine angular displacements around horizontal axis	rad
Ψ	Engine angular displacements around vertical axis	rad
Ω	Propeller angular rotational speed	rad/s
J_X	Propeller mass moment of inertia about x-axis	$\mathrm{kg\,m^2}$
J_Y	Mass moment of inertia about y-axis (propeller + nacelle)	$\mathrm{kg\,m^2}$
J_Z	Mass moment of inertia about z-axis (propeller + nacelle)	$\mathrm{kg\,m^2}$
J_+	Additional moment of inertia provided in experimental testing	$\mathrm{kg\,m^2}$
j	Imaginary unit	
K_Θ	Rotational stiffness of engine attachment in pitch	N m
K_Ψ	Rotational stiffness of engine attachment in yaw	N m
l	Distance between joint and spring attachment	m
m_+	Additional mass provided in experimental testing	kg
$M_{Y,P}$	Aerodynamic moment around y axis in propeller disc plane	N m
$M_{Z,P}$	Aerodynamic moment around z axis in propeller disc plane	N m
P_Y	Propeller aerodynamic forces in y direction at propeller disc plane	N
P_Z	Propeller aerodynamic forces in z direction at propeller disc plane	N
u_0	Spring initial stretching	m
u	Spring instant stretching	m
V_∞	Air velocity, flight speed	m/s
V_{FL}	Flutter speed	m/s
X, Y, Z	Deflected x, y and z axis	
x, y, z	Undeflected x, y and z axis	

Dedicated to Paolo Russo …
… Engineer, colleague, FRIEND.

Chapter 1

Introductory remarks

1.1 Introduction

Tiltrotor is a hybrid aeronautical system due to its capability to take off and land like a helicopter and, by means of configuration change in flight, it acts like a turboprop aircraft with a much higher cruise speed than a helicopter.
One absolute requirement for defining an aircraft as a tiltrotor is that the vehicle's rotors must tilt through a range of approximately ninety degrees, from near-vertical rotor rotational axes for hover and takeoff and landing to nearly horizontal for higher speed cruise in forward-flight. Thus, the main difference between the two operating configurations is essentially marked by the direction of the thrust generated by the rotors.
When the rotors are in a vertical position tiltrotor operates like a helicopter and the rotor serves both to generate the lift and to control the aircraft. When the rotors are rotated downwards, the aircraft begins to accelerate and a part of the lift is generated directly from the rotor while another part is provided from the wing. Finally, when the rotors are in the horizontal position, the lift is generated by the wing alone and the control delivered to the traditional control surfaces (stabilator, ailerons, and rudder), leaving all engine power to overcome aerodynamic drag in high-speed cruise.
In the last few years, for a fast and reliable point-to-point connection or intercity flights and to solve the runway congestion problem, the Runway-Independent Aircraft concept is increasingly becoming more prominent in civil aviation. Moreover, the market prospects predict an increasing demand for Disc-Rotor technologies in the Civil field [1]: business flights, air medical, search and rescue applications, and others.
The helicopter is currently the best solution in all operative conditions where low-speed capabilities are essential mainly thanks to the efficiency connected to the physics of low disk loading, the high-payload carriers, due to efficiency and low empty weight, and the high maneuverability and agility, using thrust for control power. For instance, the military helicopter's ability to take off and land vertically and the low-speed maneuvering and agility are of great strategic and tactical value in military missions. Nevertheless, the moderate speed and altitude at which the helicopter usually flies make it more susceptible to enemy fire than aircraft.

Another significant helicopters limit derives from their lack of ability to counteract the roll at a higher speed that results from the rotor advancing into the airflow on one side while retreating on the other.
On one hand, an important effort to neutralize the rolling tendency at higher speeds was the compound helicopter that uses small wings to pick up the flight loads as forwarding speed increases, by reducing the loading on the rotor. On the other hand, a valid alternative solution was identified in the concept of Tilt Rotor aircraft.
The vertical lift efficiency of a Vertical Take-Off Landing (VTOL) vehicle is not the only interesting capability of this aircraft. The challenge has been to extend the capabilities of the standard helicopter to those of a conventional aircraft, in terms essentially of maximum cruising speed, range, and autonomy. Indeed, the intrinsic characteristics of rotor aerodynamics limit both the maximum reachable speed from the helicopter, about 350 km/h, and the maximum altitude and service ceiling of around 3.000-6.000 m, as well as autonomy. It is usually less than fixed-wing, conventional takeoff, and landing airplanes of similar weight.
The solution to the helicopter's limitations has been to combine the speed, range, endurance, payload, maneuverability, and superior survivability of the airplane with the vertical lift capabilities of a helicopter [2] and for this reason, much research worldwide has yielded many tiltrotor concepts and even construction, but very few have taken flight.
In NextGen, Tiltrotor is expected to have a wider range of capabilities than today and support varying levels of total system performance. In terms of flight operational performance, a wider range of capabilities regarding cruise speed, cruise altitudes, climb and descent rates, noise, and emissions will exist. A key aspect of NextGen Civil Tiltrotor is providing environmental protection that allows sustained aviation growth.
With NextGen, significant community noise and local air quality impacts are reduced in absolute terms compared to today, even with the increase in growth. The energy use and climate effects of aviation are addressed and mitigated. This is accomplished with advanced technologies and operational capabilities, environmental improvements in airframe and engine technology resulting from a robust research and development program, and appropriate policy approaches and financial support.
The T-WING project is placed in this challenging context. The main challenges of the Horizon 2020 (H2020) Research and Innovation Framework Program are:

- Safe, Reliable and Competitive mobility of passengers, goods and public services
- Eco-Design and Minimal impact of transportation on the environment
- Low Cost (Operational and Maintenance costs) and Risks Mitigation
- High Quality and Building industrial leadership in Europe

- Low Weight

In particular, H2020 Clean Sky 2 FRC IADP NextGenCTR is dedicated to the design, construction, and flying of an innovative Civil Tiltrotor technology demonstrator [3, 4], the configuration of which will go beyond current architectures for this type of aircraft.

NextGenCTR's demonstration activities, led by Leonardo Helicopters, will aim to

FIGURE 1.1: NGCTR-TD.

validate its architecture, technologies/systems, and operational concepts, with significant improvement concerning the current state-of-the-art tiltrotors.
In addition to an advanced fly-by-wire system for the flight control and a cutting-edge nacelle that will integrate both the engine and the tilting gearbox in a compact, streamlined configuration, the NGCTR-TD is characterized by a different concept for the tilting mechanism for the upcoming Leonardo civil tiltrotor platform: a fixed engine installation with a split gearbox to provide the proprotor tilting mechanism, based on new capabilities in aerodynamic and structural analysis, design, and next-generation manufacturing and assembly principles.
As regards the propulsion system, the choice fell on a fixed engine that improves maintainability and reduces the need for a complex certification program. This will also allow important operational cost reduction to address the competitiveness of the architecture and solutions adopted. The NGCTR-TD needs to be equipped with a tilt-wing that does not lose too much performance in helicopter mode.
As for the wing design of the NGCTR, the above challenging objectives required:

- the development of a new high lift and low drag wing which is optimized to improve downwash impingement in hovering. Downwash impingement is improved by the introduction of two surfaces, an outboard flaperon and a large morphing surface which rotates downwards in helicopter mode to reduce the wing area beneath the rotors;

- the development of a highly integrated composite wing structure with a compact structural wing box, since almost half of the wing chord length is dedicated to the moveable surfaces.

T-WING consortium is working on the composite wing of the NGCTR-TD planned to be flying in 2023. The consortium, led by the Italian Aerospace Research Center (CIRA), is composed by industrial partners Magnaghi Aeronautica and Salver (IT), Step Sud Mare (IT), SMEs Officine Meccaniche Irpine (IT) IBK Innovation (DE) and Università degli Studi di Napoli Federico II (IT).
The task undertaken by the consortium is aimed at designing, manufacturing, qualification, and flight-testing of the wing and moveable surfaces of the NGCTR-TD. The logic behind the development of wing and moveable surfaces, which is illustrated in Figure 1.2, foresees a design phase based on the requirements, driven by airworthiness and defined in cooperation with the Work Area Leader.
Once the design phase was completed, the toolings to be used for the manufacturing of the wing were designed and produced and the wing itself will be manufactured and qualified. After successful qualification, the wing will be assembled to all the other components of the NGCTR-TD. The last step of the development is the instrumentation of the wing, by the use of accelerometers and strain gauges, and the flight test campaign which will lead, among others, to the validation of the flight loads used for the preliminary design of the wing.
One of the bullets to be covered in the project is to perform Scalability assessments to investigate the scalability potential of the NGCTR-TD proposed structural concept and technologies up to on the larger NGCTR aircraft.

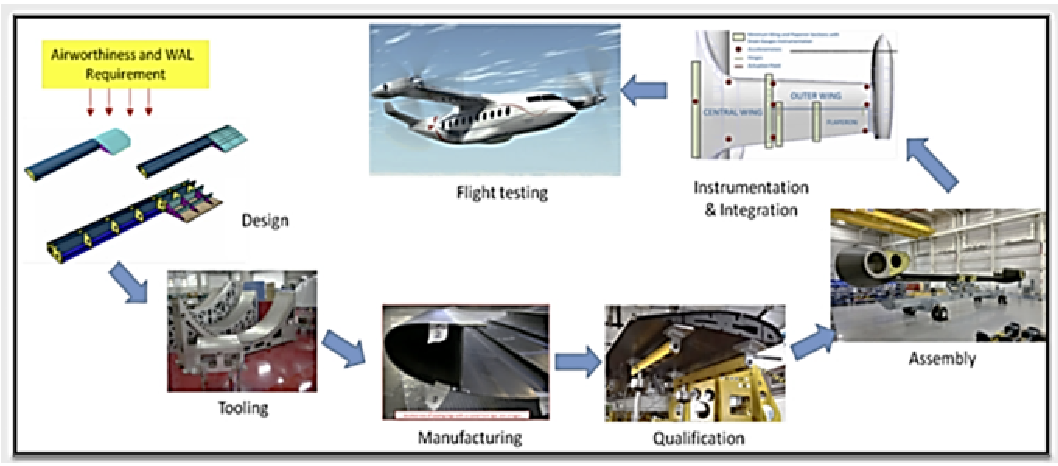

FIGURE 1.2: NGCTR-TD wing development logic.

1.2 State-of-the-Art Assessment

Much research worldwide has yielded many tiltrotor concepts but very few have taken flight, including some NASA prototypes, the pioneer XV- 3 and then the successful XV-15 program, the Bell's military tiltrotors V22 and V280 and, finally, the AW609, currently subjected to the certification process for use in the civil sphere.
The Table1.1 summarizes some important performances in terms of GTOW (Gross Take-Off Weight), disk loading, maximum and cruise speeds, service ceiling, and range to provide an approximate comparison between the main design parameters of the aforementioned tiltrotors .
Generally, the Preliminary Tailored Wing Design depends on the specific tiltrotor flight mission, in terms of payload, range, and cruise speed, and consists of an iterative process during which a design concept is settled to match the potential customer's requirements. The design concept is then subjected to design analysis and the results, in terms of a trade-off and optimization, output a reviewed design solution. This process is repeated until a solution deemed to be the best is economically sustainable and meets the desired requirements. So, the final design proposal only evolves after a systematic interaction between the requirements, detailed design tools and historical database of similar existing works produced and/or in operating conditions.
The design of a composite wing for a tiltrotor aircraft is strongly connected to the flight mission requirements so the fuel tanks, the rotor drive system and other components must be included inside of the wing structure preliminary sizing.
Sometimes, because related to project requirements or manufacturing technologies, it could be required that geometric configurations are kept fixed, such as the spar location, when other components location or shape change.
For this reason, to find the best design solution that minimizes the structural weight of the wing while satisfying a series of design constraints, an optimization process is necessary. It also expected that the best design solution must also minimize costs, time, and computational efforts.

1.3 NGCTR-TD Wing Structure Preliminary Design

Basing on the architectural layout of the NGCTR-TD wing structure set by LHD an iterative and novel optimization process has been necessary. This optimization process was aimed at finding the optimal composite thickness distribution at minimum weight. The preliminary structural design strategy is based on a two-level optimization.
The first-level optimization, is based on engineering models, used to perform a multi-objective optimization by means of genetic algorithms, also taking into account the aeroelastic stability.
The first-level optimization aims to have, at the very beginning of the project, i.e., at

TABLE 1.1: Main performances and maximum take-off weight of existing tiltrotors.

	XV-3	XV-15	V22	V280	AW609
$GTOW_{Max}$	4,890 lb	13,248 lb	52,600 lb	57,320 lb	16,799 lb
	2218 kg	6009 kg	23859 kg	26000 kg	7620 kg
Disk loading	5.66 lb/ft^2	13.2 lb/ft^2	20.3 lb/ft^2	16 lb/ft^2	15.9 lb/ft^2
	27.5 kg/m^2	64.3 kg/m^2	99 kg/m^2	78 kg/m^2	77.4 kg/m^2
Maximum speed	160 kts	300 kts	305 kts	304 kts	275 kts
	296 km/h	557 km/h	565 km/h	560 km/h	509 km/h
Cruise speed	145 kts	165 kts	241 kts	278 kts	260 kts
	269 km/h	425 km/h	446 km/h	520 km/h	482 km/h
Service ceiling	15,000 ft	29,500 ft	25,000 ft	15,092 ft	25,000 ft
	4600 m	8840 m	7620 m	4600 m	7620 m
Range	255 mi	515 mi	1,011 mi	2,485 mi	863 mi
	411 km	825 km	1627 km	4000 km	1389 km

the concept design level, a safe structural configuration, which is free from flutter at minimum mass.
The second-level optimization is based on a 1D and 2D elements Finite Element Model (FEM) built based on the selected first-level structural optimization.
The composite parts (skin and spars) of this structural configuration are then subjected to optimization employing commercial FEM software.
To speed up the optimization process and to evaluate different design choices, the equivalent laminate theory is applied to model the composite properties of the finite elements, also giving an advantage in the computational effort.
The results of this two-level optimization, in terms of wing-box sizing, has been transferred into higher fidelity models, detailed FEM and digital mockup (DMU), to verify compliance with all the remaining requirements, such as stress and fatigue, crashworthiness, accessibility, assembly and integration, and manufacturability.
After that, the final wing configuration was launched for manufacturing.
For the NGCTR-TD, the requirements derived from airworthiness specifications are drawn from EASA (European Aviation Safety Agency) large airplanes (CS-25), and large rotorcrafts (CS-29), for the particular nature of the tiltrotor. In addition to that, tailored requirements are necessary, since not all the airplane and rotorcraft requirements encompass all the possible scenarios which characterize this vehicle.
Regarding the structural architecture, LHD has fixed several technical and functional requirements, in terms of the location of the spars, ribs, and moveable surfaces' geometry.
The fuel capacity of the Technological Demonstrator is a crucial aspect and it affects the space available for the fuel bladders.
Given the architecture, the wing structural design, in terms of skin and spar web thicknesses and stringers and spar cap areas, has to cope with strength and buckling

requirements, at the lowest possible weight, and more predominantly, with stiffness requirements.
Stiffness requirements are of paramount importance when designing the wing of a tiltrotor, making the task quite challenging also because of other requirements such as weight and accessibility (numerous and wide access holes and removable panels, which tend to reduce torsional stiffness). Stiffness requirements are expressed in terms of limitations on the frequency values of the airframe elastic modes to avoid.
There is also a requirement on the lowest elastic airframe mode frequency, which shall not be lower than a minimum value, to avoid whirl flutter stability issues and coupling with aeromechanical modes, due to the presence of big masses at the wingtip (nacelles, engine, and propellers).
Based on the above-mentioned requirements, the design strategy in the preliminary phase is composed of two main phases/levels as shown Fig.1.3.

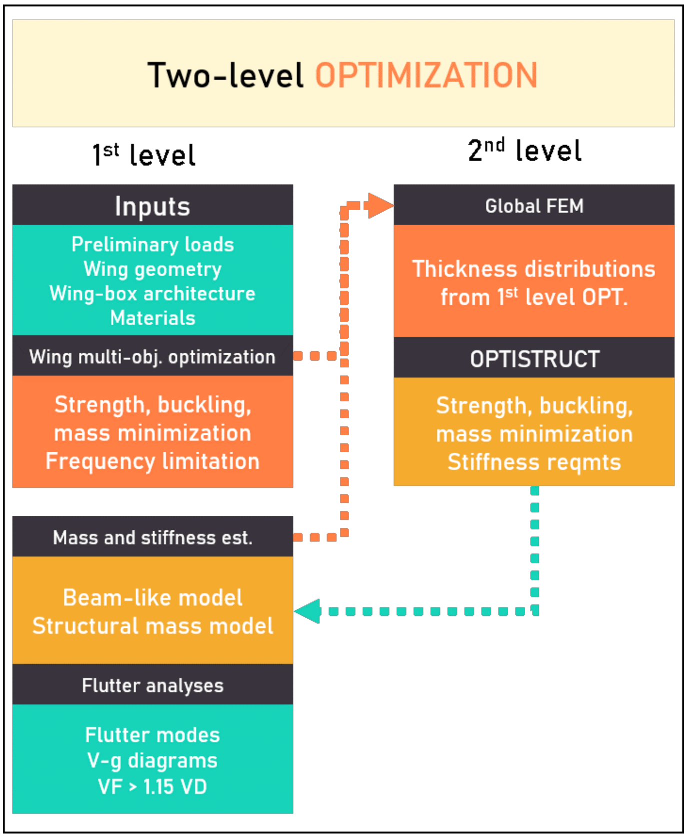

FIGURE 1.3: Design strategy flowchart.

1.4 Objectives and outline of the thesis

This thesis consists of several parts and presents the problems not only of noise and vibrations, of experimental modal analysis and vibration tests but also of aeroelastic and structural scalability.

The first part shows a series of activities in the vibrational field (Part I, Ground Vibration Test on the NextGen Tiltrotor Wing): several numerical and experimental modal analysis tests were performed to confidently and validate the Multi-Input Multi-Output methods. This activity was necessary with the aim of becoming confident with these methods in anticipation of the tests that will be performed on the test articles of the T-WING as part of the research project.
The second part shows the in-flight noise measurement test on a Leonardo Helicopters existing tiltrotor (Part II, Tiltrotor Acoustic Data Acquisition and Analysis). The third section regards the Whirl Flutter phenomenon investigation (Part III, Numerical and Experimental Investigation of Whirl Flutter), and a final part concernes the Structural Scalability by taking in account Stiffness, Crash and Whirl flutter requirements (Part IV, Wing Structure Scalability).

1.4.1 Part I: Ground Vibration Test on the Next Generation Tiltrotor Wing

A vibration test is the most commonly used method for an economic modal analysis of a structure. The purpose of the vibration test is to determine information such as the stiffness, natural frequencies, and mode shapes inherent to the dynamic response of a test article (TA) or flight article.
A ground vibration test has a unique combination of the importance of structural dynamics in aircraft and safety requirements. A vibration test on large structure always involves multiple inputs and multiple outputs (MIMO) frequency response testing. Random excitation is sometimes used, but most often stepped sine techniques are used to supply the required energy for the system. Stepped sine testing allows the user to obtain test results by exciting a single frequency at a time and sweeping through frequencies. Stepped sine testing is particularly useful when testing systems that contain composites and display non-linear behavior or require larger force levels for adequate excitation.
The main objectives of T-WING vibration test are:

- to characterize the dynamic behaviour of the primary structure and its movable surfaces;
- to validate the FE models;
- to gather auxiliary data for flight flutter tests;
- to contribute to the wing qualification.

The Part I of this work contains a preliminary numerical activity consisting in the building and use of a simplified FEM model that reproduces the dynamic behavior of the T-WING, a satisfactory sensitivity analysis to verify the changes by varying masses and constraint conditions. Then a experimental test campaign was execute to manage the MIMO procedures until to define the planning of the real full-scale tests, and the test setup, as well as preliminary experimental activities concerning both the primary structure of the T-WING and movable surfaces.

1.4.2 Part II: Tiltrotor Acoustic Data Acquisition and Analysis

In the aeronautical, railway, and automotive industries, noise and vibration are important for many reasons and in many different, more specialized, disciplines, such as *Structural Dynamics field* where vibration problems occur because resonances amplify the vibrations of the structure to very high levels (resonance condition); *Environmental Engineering, Vibration Monitoring, and Fatigue Analysis fields* concerned with the prediction of the vehicle's ability to sustain the vibrations it will encounter during its lifetime and by measuring with accelerometers and strain gauges vibrations, fatigue cracks and other deteriorating effects in the structures; and obviously the *Acoustics*, discipline very close to noise and vibration analysis as the cause of acoustic noise is often vibrations.

As mentioned above, high speed and maneuverability, and at the same time, low vibration and noise are the most important features of the new generation rotorcrafts and tiltrotors. Rotorcraft manufacturers are trying to bring tiltrotor technology to the civil aviation market by reducing the interior vibration and noise level so to make the competitiveness of tilt-rotor aircraft greatly improved for this purpose.

The interior noise characteristics of tilt-rotor aircraft are different from those of ordinary helicopters or propeller aircraft. For helicopters, engines and the gearbox are usually installed right above the cabin, while the blade tip is relatively far away from the cabin. So the engine and the gearbox, instead of the rotor, are the main source of helicopter interior noise.

For tilt-rotor aircraft, however, the engine and gearbox are located at the tip of the wing, far away from the fuselage. So the engine and gearbox affect less the interior noise. While the blade tip is very close to the fuselage in both aircraft mode and helicopter mode, so the aeroacoustics has a greater influence on the interior noise [5, 6].

Moreover, in the view of the frequency domain, because the rotor diameter of the tilt-rotor is between the main rotor of the helicopter and the propeller of the aircraft, the frequency of the aeroacoustics is higher than that of the helicopter, which is more sensitive for the human ear.

In the second part, the in-flight noise test campaign carried out on board an existing LHD tiltrotor is described.

These tests were performed to better investigate the problem of noise and then obtain satisfactory levels of comfort for passengers of the NGCTR. Pressure load measurements in operative conditions represent a fundamental parameter for improving the knowledge of the in-flight forcing generation and transmission. Furthermore, it is a fundamental step for assessing the validity and confidence of numerical methods able to predict such pressure loads, usually generated by propulsion and Turbulent Boundary Layer (TBL).

Exterior noise was measured at fixed values of engine rpm before in ground tests and then at forwarding speeds up to 98 m/s in-flight tests. Propeller noise levels, spectra, and vibrations correlation were determined using a horizontal array of

seven surface microphones and a vertical array of four surface microphones in the propeller plane.
The data acquired are used to describe the propagating and rotating characteristics of the propeller noise field on the fuselage.
About the most interesting results, the measurements in terms of Overall Sound Pressure Levels (OASPL) make clear that the correspondent levels increase according to aircraft speed and that they show the highest values in the propeller plane.
The spectra of exterior and interior noise are dominated by tones at low frequencies (up to about 400 Hz) due to the passage of the propeller blades while at greater frequencies, the contribution from the TBL is predominant.
Moreover, comparisons between the data of internal and external pressure sensors show a significant noise reduction due to the soundproofing material.
Finally, because the measurements time histories present a high dispersion level it was very useful to provide an interval of confidence and statistical evaluation on the measurements.

FIGURE 1.4: Tiltrotor surface microphones locations.

1.4.3 Part III: Numerical and Experimental Investigation of Whirl Flutter

Part III summarises the activities performed for improving the understanding of the Whirl Flutter instability and its most sensitive parameters. Clearance from such aeroelastic instability is required by airworthiness rules for turboprop-powered aircraft and must be cleared for tilt-rotor vehicles. It may be also a required check to be carried out for windmilling propellers.

FIGURE 1.5: WFSD Whirl Flutter Small Demonstrator.

In this chapter, the design, development and testing of a small demonstrator (Figure 1.5) are presented and results are discussed with reference to existing literature. The initial focus is on the governing equations and identification of parameters that affect the aeroelastic behaviour of the propeller-engine installation. Ground vibration tests, at zero airspeed, have been performed to validate numerical models for the mass/inertia and stiffness distribution. Several measurements have been further carried out at different configurations, changing the airspeed, the stiffness, the mass and the propeller in order to setup a sensitivity analysis and create a database for further improvements, mainly for a basic computation of unsteady airloads of the propeller. These analyses confirm expected results, allow interesting and confident conclusions and are able to help for showing compliance with current airworthiness rules for propeller-driven aircraft.
The results presented in this work will also represent the basis for asserting the range of validity of scaling effects for realistic applications.

1.4.4 Part IV: Wing Structure Scalability

The tiltrotor wing is one of the most critical and heavily investigated structures in the design due to the fundamental need to consider the interaction between the wing, pylon, and rotor systems to achieve aircraft aeroelastic stability. In high-speed forward flight, wing flexural and torsional stiffness has a fundamental role in pitch-whirl stability.
Another specific concern of the tiltrotor is the dynamic mode placement: it is necessary to properly place wing bending modes away from prop-rotor forcing frequencies.
In the attempt to reach the satisfaction of the main aeroelastic stability and dynamics requirements, the use of composite materials plays a fundamental role with the perpetual aim of minimizing the structural weight.

An overview of the basic T-WING configuration and the specifications design starting point of the upscaled wing are provided. After the adopted optimization methods, genetic algorithm and tool explanation, the main part of the effort focuses on the scalability process to obtain the best structural compromise, with an acceptable weight penalty, through the comparison of different composite materials (mechanical properties) and layouts.

1.4.5 Appendix C

The current design process of a new aircraft includes several modeling and testing steps. The main purpose of the Ground Vibration Testing is to achieve experimental vibration data of the whole aircraft structure, in terms of frequencies, damping factors, and mode shapes to ensure that the aircraft will be free from any aeroelastic instability and safe to fly in the desired flight envelope. GVT results are also mainly used for validating and eventually improving FEM models of the aircraft examined. On the other hand, structural dynamic models are used to predict the flutter behavior and carefully plan the in-flight flutter tests, and lead to mitigation of the risks related to them. This paper aims to compare different aeroelastic methods outcomes achieved using two diverse commercial software: the widely used NASTRAN™ and the most recently developed Zonatech ZAERO. The flutter computation results are obtained by means of P-K, K, and G methods. The first case presented is the aeroelastic analysis of a forward-swept wing whereas the second case concerns the stabilator of a two-seater ultralight aircraft, for which the results of an experimental campaign of vibrations test were available. The structural mode shapes at each generated frequency mode are also visually presented.

1.5 What this Thesis Includes

Chapters – The thesis, divided into 5 chapters, collects a series of works by the author in different disciplines and contributions which, originally partially written in the form of independent scientific works, are coordinated and linked together in an overall design, aimed at the Vibroacoustic Optimal Design and Structural Scalability of Composite Wing for the Next Generation Civil Tiltrotor.

- Chapter 1: Introduction to the thesis topics
- Chapter 2: Ground Vibration Test on the Next Generation Tiltrotor Wing
- Chapter 3: Tiltrotor Acoustic Data Acquisition and Analysis: theoretical background and discussion of the experimental results
- Chapter 4: Numerical and Experimental Investigation of the Whirl Flutter phenomenon
- Chapter 5: Structural Scalability

- Chapter 6: Conclusion and future directions

This chapter layout is specialised for the experimental sciences, your discipline may be different.

Appendices – Some appendices are added at the end of the volume intended to clarify some points not covered in detail in the text or to complete information such as the supply of Matlab codes used for data processing. Some other appendices contain other works carried out during the author's years of research. These research activities are not directly related to the TWING project but can be strongly contextualized in the same field of application of the topics covered in the rest of the thesis.

- A: Tiltrotors 3 view drawings and dimensions
- B: DNA - Data Noise Analyzer code
- C: Comparison of aeroelastic problems calculation methods based on numerical and experimental results. Overview of Nastran and ZAERO Aeroelastic Capabilities

Bibliography – The last appendix contains some references to good sources for more information within the aeroelasticity and structural dynamics, noise and vibration community, with hope reader can benefit from this list, as it has been for me.

Thesis written by —
Aniello Daniele Marano
0000-0002-2118-0974
www.linkedin.com/in/aniello-daniele-marano

Chapter 2

Ground Vibration Test on the Next Generation Tiltrotor Wing

2.1 Introduction

The main objective of the work presented in this chapter is to verify the effectiveness and limits of the Multi-Input Multi-Output (MIMO) technique compared with the better manageable Single-Input Multiple-Output (SIMO) procedure.
Although the use of a single shaker implies a minimum effort and management difficulty procedure, for large test structures, such as a wing, this approach could exhibit some strong limitations connected to the internal damping: the structure is able to dissipate the vibrational energy that shaker provide to it. The points nearest to the excitation absorb the most energy and this can distort the measurements and affect the engineering modal data. Moreover, for the single-point excitation testing, the forcing excites any mode that has a natural frequency nearby the excitation frequency, and so there will be a mixture of modal responses within the range of test frequencies. To adequately excite every mode of interest and collect FRF data sets, a multi-point excitation approach or MIMO method represents the best solution.
Multiple-Input Multiple-Output methods offer some distinct advantages for the measurement and extraction of basic modal parameters, especially for large structures [7].
Compared to SISO techniques, MIMO allows for more uniformly distributed energy across the structure, force levels can be kept lower for each shaker, modal test parameters can be obtained in one single shot, while nonlinearities are less likely to be excited. In the case of light structures, the use of stingers can provide constraints between the excitation system and the structure itself. Thus, using more electrodynamic shakers could locally affect and modify the stiffness of the structure by altering the test results.
In this study, we investigate the feasibility of using a MIMO modal testing technique on two beams of different material and weights to investigate the excitation method that produces less interference with the suspension modes of the free–free test article (TA). The first step of this test is a preliminary numerical study to investigate the excitation method and the suspension system that produce less interference with the

dynamic behaviour of the TA.
The global purpose is to demonstrate that the use of multiple actuators properly excites the global modes of larger structures and distinguishes between pairs of modes at nearly identical resonant frequencies.
The overall aim was to achieve a high level of confidence with practical aspects of multi-shaker and excitation signal management, reciprocity checks, and the basic principles behind MIMO technique and its capability to resolve closely spaced modes and repeated time-consuming tests.
Following these activities, it was possible to plan what will be the tests to be carried out on the T-WING TA.
After a first introductory, theoretical part, about the methods of experimental modal analysis, the SIMO and MIMO methods are introduced and compared.
The experimental laboratory activities and the numerical activities related to them are then shown.
As for the tests, two different metallic beams of comparable size but different weights are tested in a free-free constraint condition. The outcome of this vibration test is a comparison between the results obtained via SIMO and MIMO. Further analysis is the evaluation of the effects of an increase in the weight of the TA on the MIMO results by installing known masses at the end of the beam.
From the numerical point of view, through the creation and use of a simplified FEM model that reproduces the dynamic behavior of the wing, some sensitivity analyzes were carried out to varying masses and constraint conditions.
Finally, the lesson learned, the planning of the real full-scale tests, and the test setup are shown, as well as preliminary experimental activities concerning both the primary structure of the T-WING wing and its movable surfaces.

2.2 Theoretical and Practical Aspects of MIMO Testing

The main scopes of the experimental modal analysis (EMA) are the characterization of the dynamic behavior of a structure to avoid resonance phenomena with consequent damage or failure, durability test of systems or structures, the validation of FEM models but also reasons for prevention and maintenance.
It is common in many vibration applications to compute Frequency Response Function (FRF) from measurements [8, 9].
In most cases, during Ground Vibration Test (GVT) the structure is excited by known forces applied by an impulse hammer or by a shaker. In some cases, for Operational Modal Analysis (OMA) and Operating Deflection Shape (ODS), the FRF are measured between response signals which are due to natural excitation by for example wind or traffic loads on buildings or bridges.
Refer to the scheme of a typical modal shaker test setup configuration (Fig.(2.1)), the signal is generated from the data acquisition system and fed into the shaker amplifier.

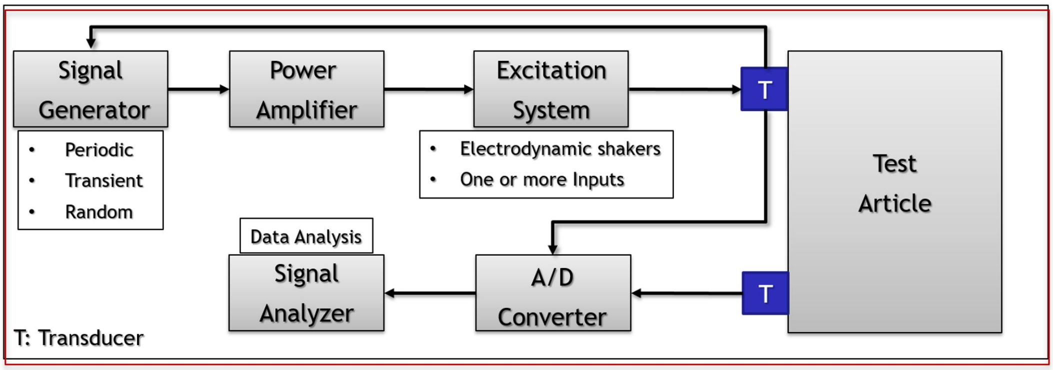

FIGURE 2.1: Typical modal shaker test setup configuration.

The top of the shaker is attached using a stinger, which is attached to an impedance head or force sensor and linked to the structure at the excitation location. The input signal generated by the excitation system and measured by the force sensor and the output signal measured by the acceleration sensors, flow into the acquisition system for data processing.

In the EMA, it is common to use several shakers to excite the test structure, and simultaneously to measure a large number of response signals. In this case, frequency response functions must be estimated using a MIMO model.
The response of the excited structure under examination is acquired in terms of accelerations, velocities, or displacements in the time domain. The data are reported in the frequency domain by Fourier transform and by the frequency response functions, applying parametric extraction models, to obtain the modal parameters. For a real multi-degree of freedom system, the stabilization diagram helps to select the poles that have a physical meaning and not a purely mathematical one.

Basic assumptions in the modal analysis are:

- Linearity
- Time invariance
- Reciprocity
- Observability.

Linearity has two aspects. The first one is that the response is proportional to the applied force. So the larger force is applied to the structure, the larger amplitudes will occur. The second aspect is that we can apply the principle of superposition. It means that the resulting response is equal to the sum of the individual responses to each of the forces acting on a structure.
In general, a system with an input signal and output is considered to be time-invariant if the coefficients of the system of differential equations that describe the system do not change with time: the system parameters, for example, mass, damping, and stiffness, do not change during the time we measure the system.

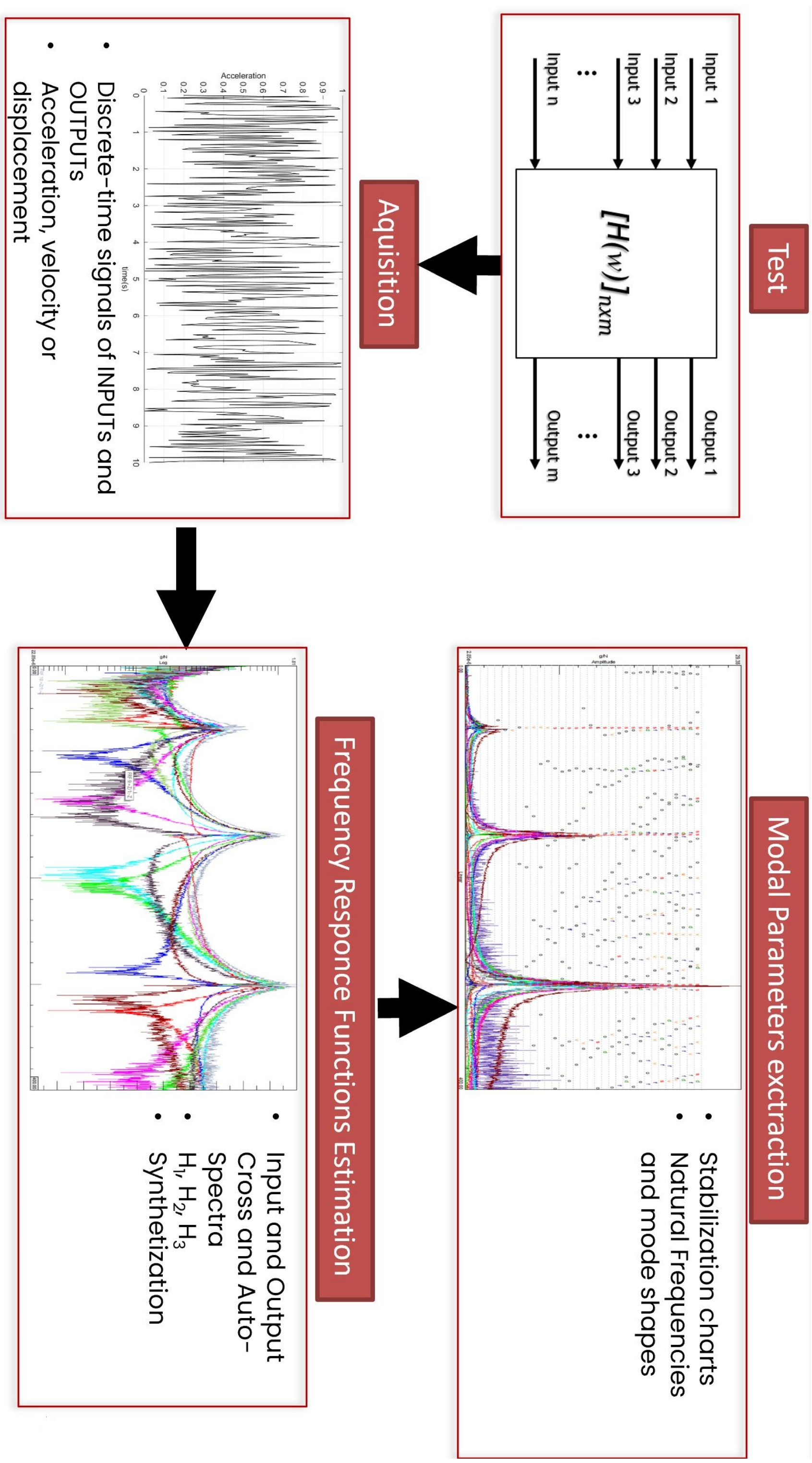

FIGURE 2.2: Experimental Modal Analysis Process Scheme.

The next assumption is reciprocity. Reciprocity means that force applied at degree-of-freedom P causes a response at degree-of-freedom Q that is the same as the response at degree-of-freedom Q caused by the same force applied at degree-of-freedom P. A consequence of the principle of reciprocity is that the FRFs acquired in the two configurations must be the same.
The last assumption in modal testing is observability. It means that measurement data contain enough information to generate an adequate model of the structure.
Real-life systems are rarely completely linear. During all measurements of FRF, we need to investigate if the conditions of linearity are satisfied otherwise the modal analysis assumptions fail, and the classical methods could not be appropriate.
In real-life measurements, particularly in the field of noise and vibrations, we are not able to measure input and output signals without at least one of these signals being contaminated by extraneous noise from the sensor and input electronics in the measurement system.
To overcome or mitigate this problem, in the SIMO approach, we introduce different estimators, H_1 or H_2, depending on the noise in the input signal or the output signal is negligible. Thus, neglecting the term of cross-spectrum (between input and noise or between noise and output), we consider the uncorrelated signals and from the relationship that links output and input, we can easily derive the FRF and the modal parameters.
Furthermore, when we estimate the frequency response with the H_1 or H_2 estimators, we can compute the coherence function. If coherence is = 1, then $H_1 = H_2$ which implies that we have no extraneous noise, the measured output derives only from the measured input. The coherence function is a quality measure of the estimated frequency response, regardless of which estimator we use. The coherence function drops below unity if there is contaminating noise on either the measured input signal or in the measured output signal or both signals.
In the case of MIMO, each output is caused by a linear combination of all the inputs, and there are no relations between any of the outputs.
A general MIMO system can be seen as many parallel multiple-uncorrelated input and single-output systems.
In the frequency domain, a MIMO system is described by systems of matrix equations, and instead of computing FRF as scalar quantities, matrix processing of data is required. If we consider many averages of the measurements, the cross-spectra terms linked to the noise approach to zero, and this allows us to simplify the resolution models. To solve the system of Equations you need to diagonalize it to produce a system where each of the estimators is separated into one row. This is usually obtained through the Gaussian elimination procedure that provides a well-conditioned solving system.

In vibration test analysis, matrix processing of data is required [10]. The response $[G_{XF}]$ of a generic TA, obtained through accelerometers, could be defined by means

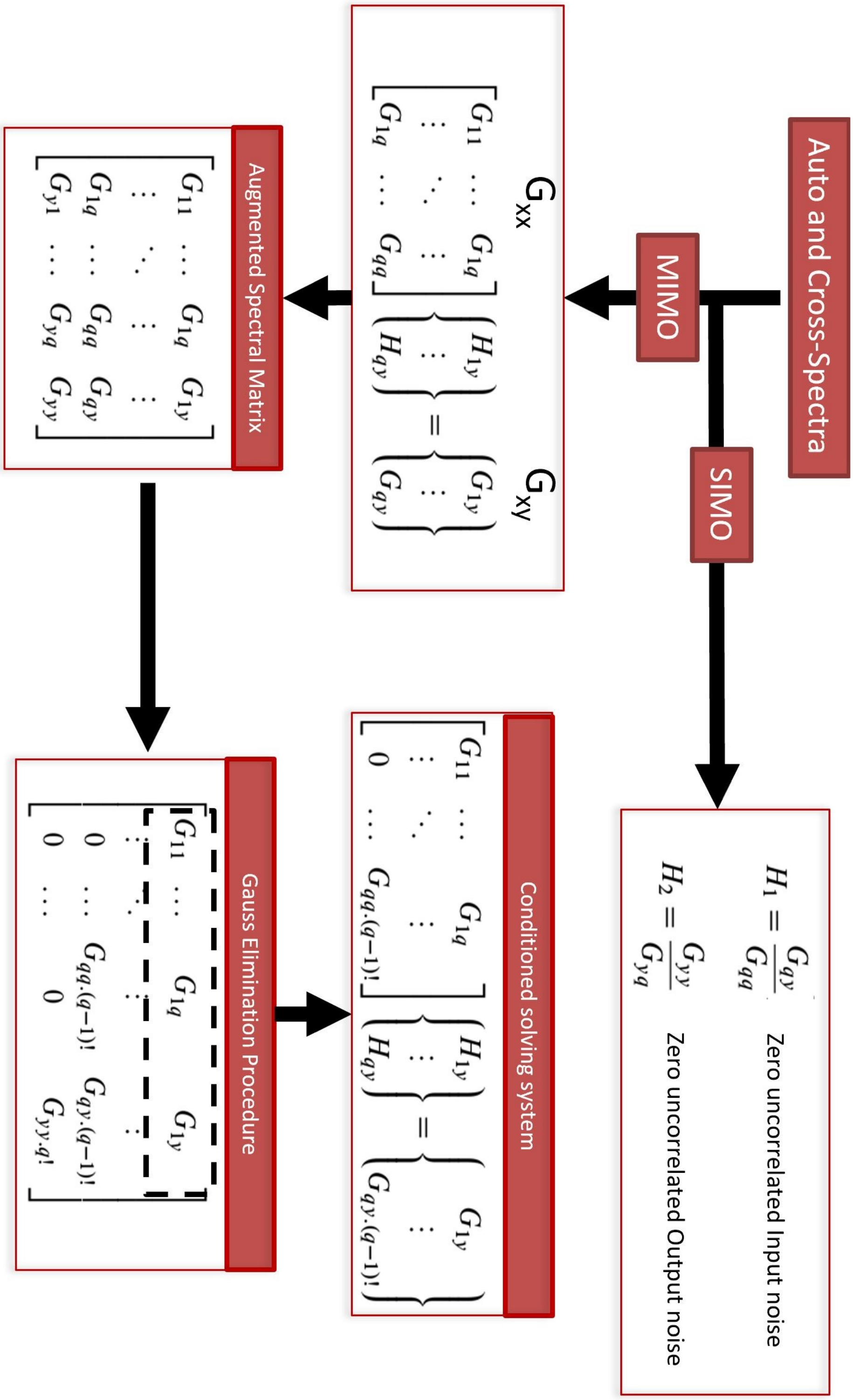

FIGURE 2.3: MIMO Analysis Process Scheme.

of the modal model as

$$[G_{XF}] = [H][G_{FF}] \tag{2.1}$$

From a theoretical point of view, the assumption on which multi-input testing is based is that each of the know inputs must be uncorrelated with the other ones so that can be invert the input matrix $[G_{FF}]$ otherwise the inverse matrix is not accurate and this effects the extraction of the modal parameters from FRF matrix $[H]$:

$$[H] = [G_{XF}][G_{FF}]^{-1} \tag{2.2}$$

Although the data collection time for MIMO is the same as SISO/SIMO, with respect to Single excitation test, the MIMO approach allows for the simultaneous collection of multiple columns of the FRF matrix providing a more uniform and reliable definition of the FRFs.

$$[H] = \begin{bmatrix} H_{11} & H_{21} & \cdots & H_{1,Ni} \\ H_{21} & H_{22} & \cdots & H_{2,Ni} \\ \vdots & \vdots & & \vdots \\ H_{No,1} & H_{No,2} & \cdots & H_{No,Ni} \end{bmatrix} \tag{2.3}$$

Where N_o is the number of outputs and N_i is the number of inputs.

From a practical point of view, in the EMA field, the use of shakers is the most widespread among the methods to excite a structure due to its ability to reproduce a wide range of excitation signals as periodic, random, or transient [11]. The most common signals are random or burst random for non-deterministic signals and sine chirp or pseudo-random for deterministic signals.

If on the one hand, the shakers offer a lot of flexibility, on the other hand, they involve several issues to which particular attention must be paid during the tests.

First of all, the execution of a vibration test implies some preliminary considerations such as the best location for placing the shakers to avoid the impedance mismatch. Indeed, while the accelerometer is located on the structure where the response is large for all its modes, the location of the shaker is not as simple as the measurement sensor. The shaker has a limited stroke and velocity (typically around 1.8 m/s for commercial electrodynamic shakers) along with a maximum force rating which controls the maximum acceleration. So, if a shaker is mounted to the structure at a point where the displacement is large or the velocity response is high, then the shaker will not be able to follow the structure response; the shaker excites the structure partially or not at all following its response instead. This causes a force dropout in the force spectrum at the resonances of the structure and the FRF and coherence may not be good for measurement.

In general, before to carrying out an experimental test, it is advisable to perform a numerical analysis. For both beams presented in the following chapters, to individuate the best location of the shakers and force the structure with a satisfactory and wide-ranging flat input force spectrum over the frequency range of interest, before the vibration test was performed, a preliminary numerical investigation and a hammer modal test have provided useful information to better understand the mode shapes of the TAs.

In addition to verifying the correct alignment of the stinger to the structure so that the impedance head measures the axial load normally imparted to the surface of the TA at the attachment point and to checking that the vibrations are not transmitted back through the base on which the shaker is placed, other considerations concern the setting of the appropriate level excitation of the shakers. Large force levels tend to overdrive the structure and can excite nonlinear characteristics of the structure and provide overall bad measurements.

To identify system characteristics by means of modal testing, to avoid exciting nonlinear characteristics of the structure under test, the levels of input excitation are generally low. The excitation levels dependent essentially on the nature of the structure is being tested [12]. In the case of simple and linear structures, it is possible to use a single shaker with an appropriate force level whereas when the structure presents many assembled components and higher damping, it may be more difficult to provide an adequate level of energy from one shaker to identify the global mode shapes. The necessary signal increase to obtain measurable vibrations in all response positions implies an increment of noise and probable excitation of the nonlinearities and the overall measurement could be corrupted.

From a purely theoretical standpoint, modal parameters can be extracted from any reference location as long as it is not at the node of a mode by moving a single shaker. But from a practical point of view, while the structure may be time-invariant, the test setup can affect the measured FRFs when the measurements are obtained from separate tests. In general, therefore, in these cases, it is advisable to use several shakers in different positions with a lower level of excitation and collect data simultaneously in a MIMO test to make acceptable FRF measurements and following modal parameters estimation [13].

Figure 2.4 summarizes some conclusions from the comparison between the SIMO and MIMO methods.

2.3 In-depth study of the methodology

2.3.1 Modal Model, Response Model and Spatial Model

In this section, two crucial phases of EMA that follow the acquisition of the input and output temporal signals are presented: the process of estimating the FRFs and extracting the modal parameters [14].

For the current work, both phases are managed by the same software Testlab, which also manages the excitation and the acquisition of the vibrational levels of the structure.

Starting from the discrete temporal input and output signals, the modal parameters

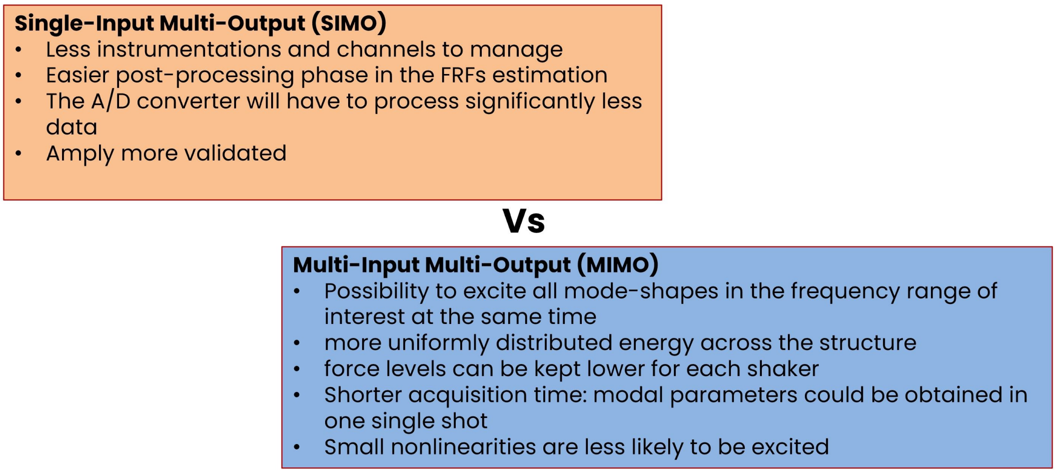

FIGURE 2.4: SISO *vs.* MIMO methods.

in the form of natural frequencies, modal shapes, and damping ratios are obtained to realize the response model of the TA. In the modal analysis it is possible to define three types of models:

- the *spatial model* in which the system is described by the properties of mass, stiffness, and damping;
- the *modal model* consisting of eigenvectors and eigenvalues;
- the *response model* defined by the frequency response curves.

The three models are dependent on each other and generally, a complete analysis involves the determination of all three. According to the order in which they are evaluated, two possible "paths" can be distinguished. Figure 2.5 shows two different paths to proceed to describe the dynamics of a structure. In the numerical procedure, starting from a FEM model, the modal parameters could be determined by utilizing the assembly of the mass and stiffness matrices, and by applying one of the various numerical techniques for estimating the FRFs. On the other hand, one could start from the experimental acquisitions, obtaining an estimate of the FRFs from which to extract the modal parameters and finally arriving at the properties of mass and stiffness (this last step is generally neglected). In reality, the classical and widespread used procedure, involves using both numerical analysis and an experimental test.

Following this double approach, generally, the first step is represented by the realization of a numerical finite element model which preliminarily provides useful information regarding some key phases of the experimental test. Firstly, it provides an overview of what the dynamic behavior of the TA will be in the the frequency range of interest in terms of modal shapes, approximate natural frequencies and modal density. Preliminary knowledge of how the structure will deform allows a conscious choice of measurement points. It is good practice to position the transducers in the probable points of maximum deflection to obtain a Signal-to-Noise

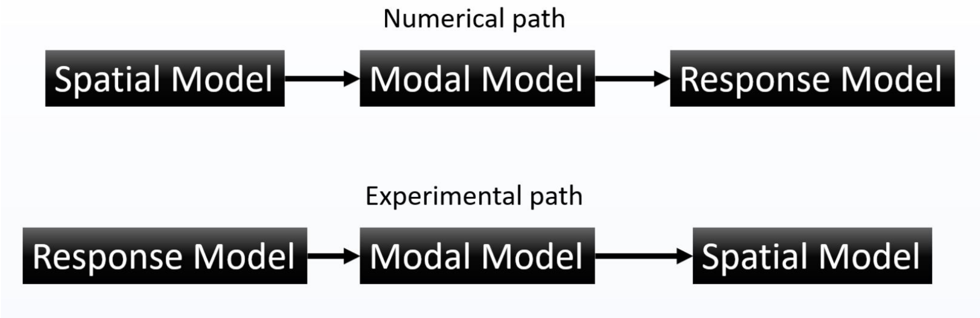

FIGURE 2.5: Two typical ways of proceeding in modal analysis.

ratio, between the measured output and any external noise, as high as possible. On the other hand, the measurement points must be evenly distributed on the TA in such a way as to have a good set of descriptors in the modeling phase. Ultimately, the position of the sensors also depends on the type of dynamics to be analyzed for instance the allocation changes radically if the analysis also takes into account the torsional modes.
As shown in figure 2.6, another fundamental difference between the numerical and the experimental approach lies in the determination of the damping ratios. If on one hand the damping ratio can be measured downstream of the modal parameter extraction phase in modal testing, on the other hand, especially for complex structures, it is not possible to include a realistic damping law in a first FEM model. For this reason, the modal parameters obtained numerically do not include damping at least at a first iteration. The numerical and experimental determination of the modal parameters allows to carry out the so-called correlation phase. The just-described process is iterative as the correlation phase is generally followed by an updating of the numerical model. In the following subsections, the three key steps that characterize the experimental path will be analyzed, namely the estimation of the FRFs, the extraction of the modal parameters, and the numerical-experimental correlation.

2.3.2 FRF estimation and synthesization

The process of estimating an FRF can be applied according to one a multitude of different techniques but all are characterized by common aspects. The first problem is represented by the fact that obtaining the input e output spectral components through the operation of the Fourier transform into its discrete Fourier transform (DFT) and The Fast Fourier Transform (FFT) algorithm is limited to the analysis of perfectly deterministic signals. In practice, whatever the configuration tested, the measurements of the aforesaid quantities will always be subject to an additional unwanted noise component. This can come from external sources (poor isolation of the TA) or interference between the instrumentation. as shown in Figure 2.7, with the introduction of noise, the system is not excited with the nominal excitation profile $f(t)$ but with a different function $f'(t)$.

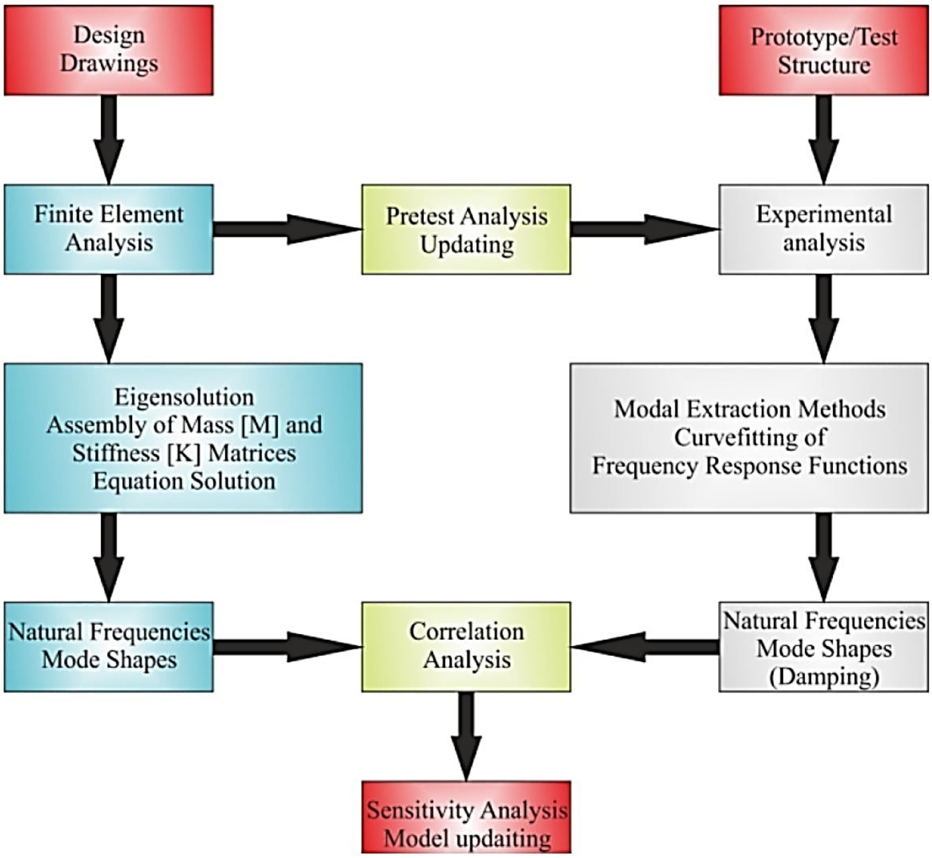

FIGURE 2.6: Experimental Modal Analysis workflow

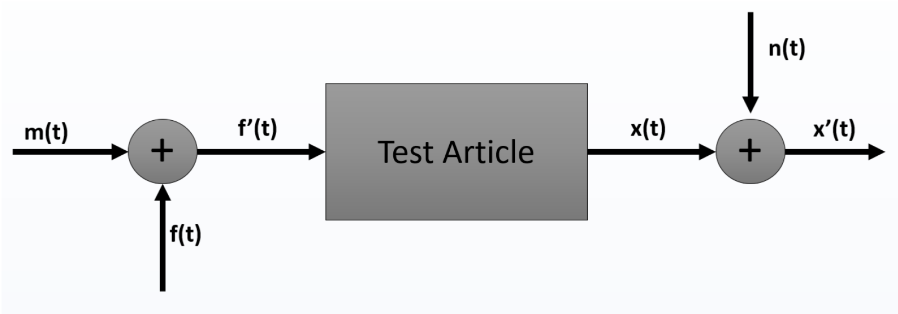

FIGURE 2.7: Noise afflicting input and output measurements.

This also applies to the output measurement, modified by the presence of the noise function *n(t)*. The functions *m(t)* and *n(t)* are intrinsically unknown but if the error is systematic it can be eliminated once it has been identified.
In most cases, these functions are not systematic but it is possible to assume the hypothesis of non-correlation of the noise signals with a reference signal. In other words, it is assumed that *m(t)* and *n(t)* are random and not associated with the input and output signals *f(t)* and *x(t)*. The aforementioned absence of correlation is the basis of a reasonable measurement setup.
The FRFs in the form of the *Receptance* (Displacement/Force) is not usable in this case as the Fourier transform of the signal affected by noise is very different from that of the nominal signal. This affects the ratio of the input and output frequency spectra does not lead to the actual FRF. It is necessary the use estimators whose purpose is to "clean" the signals from the noise components.
In this context, to provide the estimators it is necessary to introduce some basic operations used in signal theory.
Some of the functions introduced below will be resumed in chapter 3 in which vibroacoustic and not only vibrational phenomena are described and studied.
The first function introduced is the *autocorrelation function* $R_{xx}(\tau)$:

$$R_{xx}(\tau) = \int_{-\inf}^{+\inf} x^{'}(t)x^{'}(t+\tau)dt \tag{2.4}$$

It allows to relate a function with a copy of it after a certain period of time. Similarly, the *cross-correlation function* can be defined, $R_{xf}(\tau)$.

$$R_{xf}(\tau) = \int_{-\inf}^{+\inf} x^{'}(t)f^{'}(t+\tau)dt \tag{2.5}$$

The *cross-correlation* operation has an important property: in the hypothesis of systematic noise this operation returns the same result if applied to the two pairs of signals (*x′(t)*,*f′(t)*) and (*x(t)*,*f(t)*). It represents a way of evaluating the systematicity of the noise functions. Finally, the following operation is defined as a convolution integral.

$$x(t) = \int_{0}^{+\inf} h(t-\tau)f(\tau)d\tau \tag{2.6}$$

It is now possible to introduce two other frequency functions obtained through a Fourier transform of the auto and cross-correlation, namely auto-power-spectral density (APSD), S_{xx}, and cross-spectral-density (CSD), S_{xf}.
The APSD is a real function and it has the dimensions of a quantity squared (eg acceleration) over a frequency.
The CSD is generally complex (usually between input and output there is a certain phase difference) and it expresses the correlation between input and output in the frequency domain.
By multiplying 2.6 to the left and right by $x(t+\tau)$ and $f(t+\tau)$ respectively, it yields

a linear relationship between the autocorrelation $R_{xx}(\tau)$ and the crosscorrelation $R_{xf}(\tau)$. If we then apply the Fourier transform to all the members we arrive at the following equations:

$$S_{xx}(w) = H(w)S_{xf}(w) \tag{2.7}$$

$$S_{fx}(w) = H(w)S_{ff}(w) \tag{2.8}$$

$H(w)$ represents the Fourier transform of the term $h(t-\tau)$ in relation 2.6. More in detail, $H(w)$ is:

- the *accellerance* if $x(t)$ is an acceleration;
- the *mobility* if $x(t)$ is a velocity;
- the *receptance* if $x(t)$ is a displacement.

$H(w)$ is therefore an estimator of a FRF.
Two relations have been written, 2.7 and 2.8, since the CSD is a complex function and it is not possible to invert the subscripts without altering the function. Indeed S_{fx} is the conjugate complex of S_{xf}. It is, therefore, necessary to distinguish the two possible expressions of $H(w)$.

$$H_1(w) = \frac{S_{xx}(w)}{S_{xf}(w)} \tag{2.9}$$

$$H_2(w) = \frac{S_{fx}(w)}{S_{ff}(w)} \tag{2.10}$$

$H_1 = H_2$ only if the noise is zero ($m(t) = n(t) = 0$). Since the CSD is defined as the Fourier transform of the cross-correlation signal, when the two noise signals were supposed to be uncorrelated, it is reasonable to assume that the cross-correlation and therefore the CSD are not affected by error (due to the properties of the cross-correlation function).
A possible error in the estimation of the FRF is necessarily due to the autocorrelation function and consequently to the Power-Spectral-Density (PSD). In these hypotheses, H_1 takes the following form:

$$H_1(w) = \frac{S'_{xx}(w)}{S_{xf}(w)} \tag{2.11}$$

Where $S'_{xx}(w)$ is equal to the sum of the nominal part plus the noise contribution, $S'_{xx}(w) = S_{xx}(w) + noise$.
On the other hand if we consider the formulation of H_2:

$$H_2(w) = \frac{S_{fx}(w)}{S'_{ff}(w)} \tag{2.12}$$

Where $S'_{ff}(w)$ is decomposable as the sum of two parts, $S'_{ff}(w) = S_{ff}(w) + noise$. These observations provide with a selection criterion for the estimator to use. If we assume the non-correlation hypothesis of noise signals, using H_1 means considering the error attributed to the input while using H_2 means to consider that relating to the output. Since the measurement of the input is generally considered more reliable, the estimator H_1 is used in most cases.
A third kind of estimator H_3 exists. It is defined as the ratio of two CSDs, eliminating both the unrelated input and output errors.

$$H_3(w) = \frac{S_{xv}(w)}{S_{fv}(w)} \tag{2.13}$$

As can be seen in 2.13 such the two CSD refer to three different signals. Indeed the use of H_3 is linked to the introduction of an additional reference signal *v(t)* and this is where the drawback hides. Using this solution even for a one DOF system we must use at least three different channels, this could represent the problem because as repeated several times the number of data that can be managed at the same time is limited to the number of available channels in the signal analyzer.
All the equations written up to now refer to a SISO test. When we introduce more measurement points, the determinations of the estimators must be repeated for each output and obviously repeated for each frequency. On the other side, for a multi-input test like the MIMO one, the equations expressing the estimators H_1 and H_2 are the following:

$$[H_1(w)] = \left[S'_{xx}(w)\right]\left[S_{xf}(w)\right]^{-1} \tag{2.14}$$

$$[H_2(w)] = \left[S'_{ff}(w)\right]^{-1}\left[S_{fx}(w)\right] \tag{2.15}$$

PSD matrices will always be square while CSD matrices will be square only if the number of inputs is equal to the number of the outputs.
Generally in a MIMO test, the number of acquisition points is always much greater than the number of excitation points so you will almost always have to deal with rectangular matrices. This can be a problem when inverting the matrix. Furthermore, it should not be forgotten that, also, in this case, the operation is repeated for all the analysis frequencies. The problems are mainly related to the possibility that the matrices are singular not allowing the inverse operations. For these reasons, multiple techniques use different resolution methods. In this context, one of these techniques, the so called Gauss elimination procedure, is shown in the follow paragraph.

2.3.3 FRF estimation in MIMO test

Suppose we have q points of excitation and the same number of measurement points (this hypothesis does not affect the generality of the method since matrix inversions are not required). For simplicity, we will consider one output at a time: the procedure must be repeated for each measurement point.

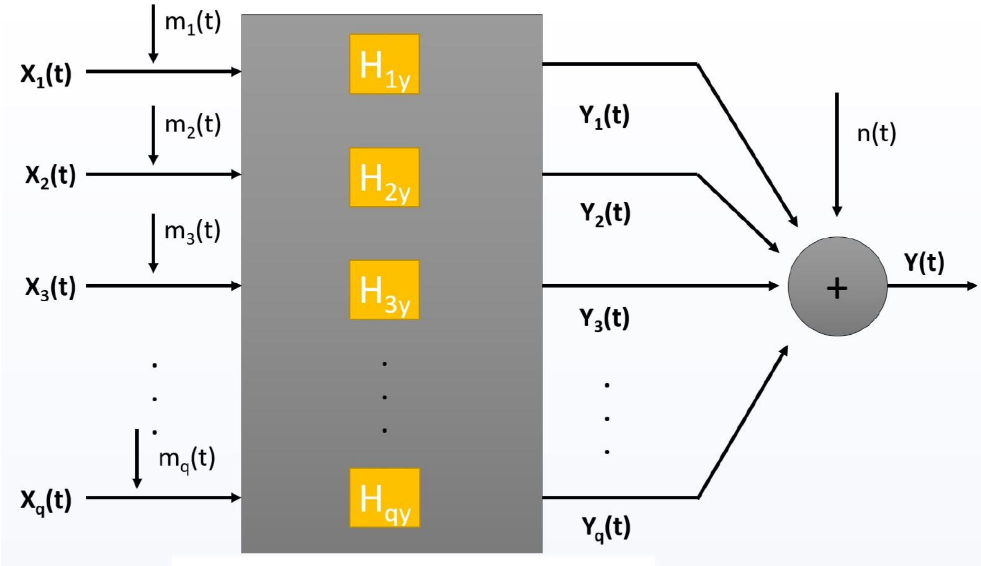

FIGURE 2.8: Multi Input Single Output configuration

The general equation governing the system shown in figure 2.8 is the following:

$$Y(f) + N(f) = \sum_{i=1}^{q} H_{iy}(f)\left[X_i(f) + M_i(f)\right] \tag{2.16}$$

Assuming no input noise, we are considering the estimator H_1. In this case, the equation 2.14 becomes:

$$\begin{bmatrix} S_{11} & \dots & S_{1q} \\ \vdots & \ddots & \vdots \\ S_{1q} & \dots & S_{qq} \end{bmatrix} \begin{Bmatrix} H_{1y} \\ \vdots \\ H_{qy} \end{Bmatrix} = \begin{Bmatrix} S_{1y} \\ \vdots \\ S_{qy} \end{Bmatrix} \tag{2.17}$$

In the 2.17, the matrix of the PSD and CSD of the input and the vector of the unknown terms can be identified at the first member, while at the second member there are the input and output CSD. The technique consists in first constructing the augmented spectral matrix, G_{xxy} starting from the two matrices of the auto and cross-spectra appearing in the 2.17.

$$\left[G_{xxy}\right] = \begin{bmatrix} G_{11} & \dots & G_{1q} & G_{1y} \\ \vdots & \ddots & \vdots & \vdots \\ G_{1q} & \dots & G_{qq} & G_{qy} \\ G_{y1} & \dots & G_{yq} & G_{yy} \end{bmatrix} \tag{2.18}$$

The Gauss elimination procedure is now applied to the previous matrix. This technique consists of the recursive application of the so-called "Gauss moves", which can be summarized as follows.

- Step 1: If the first row has the first null element, it must be swapped with a row that has the first non-null element. If all rows have the first non-null element, go to step 3.

- Step 2: For each row G_i with the first non-null element, except the first (i > 1), multiply the first row by a coefficient chosen in such a way that the sum between the first row and G_i has the first null element. Replace G_i with the sum you just got.

- Step 3: Now on the first column all the figures, except perhaps the first, are null. At this point, we return to point 1 considering the submatrix obtained by deleting the first row and the first column.

The application of the above technique leads to a new formulation of the G_{xxy} matrix:

$$\left[G_{xxy}\right] = \begin{bmatrix} G_{11} & \dots & G_{1q} & G_{1y} \\ \vdots & \ddots & \vdots & \vdots \\ 0 & \dots & G_{qq\cdot(q-1)!} & G_{qy\cdot(q-1)!} \\ 0 & \dots & 0 & G_{yy\cdot q!} \end{bmatrix} \tag{2.19}$$

The matrix has become upper triangular, so it is now possible to return to the starting equation by replacing the submatrixes by the augumented spectral matrix.

$$\begin{bmatrix} G_{11} & \cdots & G_{1q} \\ \vdots & \ddots & \vdots \\ 0 & \cdots & G_{qq\cdot(q-1)!} \end{bmatrix} \begin{Bmatrix} H_{1y} \\ \vdots \\ H_{qy} \end{Bmatrix} = \begin{Bmatrix} G_{1y} \\ \vdots \\ G_{qy\cdot(q-1)!} \end{Bmatrix} \tag{2.20}$$

At this point, starting from the last line of the system of conditional equations 2.20 that has been created, it is possible to find the H_{iy} unknowns using back substitution. The procedure must be repeated for each of the measured outputs and each frequency. In this way, we obtaine the estimators that minimize the error of the output *n(t)*.

2.3.4 Modal Parameters Extraction

In this section, the methods of extraction of the main modal parameters are introduced and, by providing a general overview valid for the different, several, available techniques [15]. These techniques can be classified according to different criteria. A first differentiation can be made relative to the type of domain in which the analysis is carried out:

- Frequency Domain Techniques

- Time Domain Techniques

In the first category, we find all those techniques that analyze the FRF synthesized directly in the frequency domain while in the second, before conducting the analysis, it is necessary to move to the time domain. To do this, the so-called Impulse

Response Functions (IRFs) are used, obtained from the inverse Fourier transform operation.
A second classification can be made based on the frequency range considered. Two sub-categories can be distinguished.

- SDOF techniques - the modal parameters are evaluated peak by peak;
- MDOF techniques - the modal parameters are simultaneously evaluated by considering more peaks in a larger frequency range.

Single DOF techniques are only applicable under certain conditions. Recalling the generic expression of a FRF as a function of modal parameters:

$$\alpha_{j,k}(w) = \sum_{r=1}^{\infty} \frac{A^r_{j,k}}{\omega_r^2 - \omega^2 + i\eta_r\omega_r^2} \tag{2.21}$$

Assuming we can isolate one of the *r-th* term of the summation, 2.21 becomes:

$$\alpha_{j,k}(w) = \frac{A^r_{j,k}}{\omega_r^2 - \omega^2 + i\eta_r\omega_r^2} + \sum_{s\neq r} \frac{A^s_{j,k}}{\omega_s^2 - \omega^2 + i\eta_s\omega_s^2} \tag{2.22}$$

The 2.22 allows us to make an important consideration: the closer we are to the frequency $r - th$, the more the dynamics of the system can be expressed by the contribution of the $r - th$ mode plus a constant summation in frequency. This consideration is as true as the more distant the modes of the structure are (separated peaks, low damping).
So the SDOF techniques analyze the modes individually and extract the modal parameters starting from portions of FRF synthesized around the peaks.
The simplest applications based on a direct analysis of the portions of FRF (peak picking, half-power bandwidth), whereas the circle fit and the line fit techniques are the most used modal parameters extraction methods belong to SDOF category.
On the other hand, MDOF techniques take into account the FRFs in their entirety in the range of analysis chosen. In this case, it is not necessary to assume the hypotheses underlying the SDOFs for which the range of applicability increases.
Finally, the third and most important classification is based on the dataset that the evidence returned. We can distinguish the single-FRF techniques from the multi-FRFs techniques. As said in the previous chapter, what distinguishes a Single-Input approach from a Multi-Input one is the number of rows/columns of the FRF matrix that we estimate. In a SISO test, we can only analyze a single FRF with an SDOF or MDOF technique depending on how the dynamics of the system are presented. For MIMO or SIMO tests we can instead consider all the FRFs at the same time. In particular, in the context of multi-FRFs methodologies we can distinguish the global techniques generally referred to SIMO tests (number of FRFs equal to the number of outputs measured) and the poly reference techniques that instead refer to MIMO tests (number of FRFs equal to the product between the number of Inputs and the number of Outputs measured).

The type of technique used in a test can be defined as a particular combination of the just introduced subcategories. The choice must be made wisely. For example, if we suppose that, downstream of the acquisition process, we have 128 FRFs that describe 10 modes of vibration each and we hypothesize the time of a single analysis equal to 1 minute, we understand that if we use an SDOF technique, the total analysis time is unbelievably large (1 min. x 10 modes x 128 FRFs = 21 hours).
A global technique on the other hand analyzes all FRFs simultaneously, drastically reducing analysis times. It should also be considered that single-FRF SDOF / MDOF techniques lead to as many sets of modal parameters as there are FRFs and a final averaging process is required. This is difficult to automate in a single algorithm. Another advantage of using global / poly reference techniques is that they can easily handle coupled and strongly damped modes. On the other hand, they also present several problems related to their complexity:

- Formulation/programming difficulties;
- Considerable computational power and fast A/D required;
- Prone to computational modes;
- Possible to miss modes;
- Ideally, all the FRFs should be measured simultaneously.

In the next paragraph an overview of PolyMAX is provided. PolyMAX is one of the techniques used by the TestLab software to manage the tests object of this work. Before giving an overview of PolyMAX, it is useful to introduce two further concepts:

- Modal Participation Factor (MPF);
- Stabilization Chart.

The MPF describes the displacement rate with which a particular mode contributes to the total response of the structure under test.
The Stabilization Chart, used in identification techniques, is a standard tool to estimate the modal parameters. The main purpose of using the stabilization diagram as a post-processing place for parameter identification is to distinguish physical modes and spurious (or mathematical) modes.
There are three main causes for spurious modes. First, numerical mathematical spurious modes will arise due to an overestimation of the system order. Second, noise spurious modes will arise due to physical reasons, e.g. excitation and noise color. Finally, analog or digital filtering of the data also produces numerical spurious poles. A stabilization diagram is simply a plot of different model orders(in this particular context the interpolating polynomial order) versus the frequencies identified at each of the model orders. Generally, the typical stabilization diagram is a graph where the frequency is plotted as the x-axis and the model order as the y-axis.

2.3.5 PolyMAX

The fundamental premise of the class of techniques adopted in this work is the use of polynomial functions for the representation of synthesized FRFs.

$$H_{jk}^{s}(w) = \frac{b_0 + b_1(iw) + b_2(iw)^2 + \ldots + b_{2N-1}(iw)^{2N-1}}{a_0 + a_1(iw) + a_2(iw)^2 + \ldots + a_{2N}(iw)^{2N}} \tag{2.23}$$

The PolyMAX method is a further evolution of the so-called Least-Squares Complex Frequency-domain (LSCF) method [16]. In particular, it represents its poly reference version which improves the estimation of close poles through the implementation of the so-called right matrix-fraction model [17]. Using this pattern the 2.23 can be rewritten as:

$$[H(w)] = \sum_{r=0}^{p} z^{r}\left[\beta_r\right]\left(\sum_{r=0}^{p} z^{r}\left[\alpha_r\right]\right) \tag{2.24}$$

where $[H(\omega)]$ is the matrix containing the FRFs, $\left[\beta_r\right]$ is the numerator matrix of the polynomial coefficients, $[\alpha_r]$ is the denominator matrix of the polynomial coefficient and p is the model order. z is a frequency-domain variable derived from a the discrete-time model t through the following transformation.

$$z = e^{jw\Delta t} \tag{2.25}$$

Δt represents the sampling time related to the sampling frequency of the acquisition. The coefficients matrix $\left[\beta_r\right]$ and $[\alpha_r]$ are found as the least-squares solution of these equations after the linearization process. Once the denominator coefficients are determined the poles (natural frequencies) and modal participation factors are obtained evaluating the eigenvalues and the eigenvectors of the companion matrix of the denominator polynomial.

$$\begin{bmatrix} 0 & I & \cdots & 0 & 0 \\ 0 & 0 & \cdots & 0 & 0 \\ \ldots & \cdots & \cdots & \cdots & \cdots \\ 0 & 0 & \cdots & 0 & I \\ -\left[\alpha_0^T\right] & -\left[\alpha_1^T\right] & \cdots & -\left[\alpha_{p-2}^T\right] & -\left[\alpha_{p-1}^T\right] \end{bmatrix} \cdot P = P\Lambda \tag{2.26}$$

The matrix Λ contains the poles $z = e^{jw\Delta t}$ on its diagonal. The eigenfrequencies ω_i and the damping ratios ζ_i are related to the values of λ_i.

$$\lambda_i, \lambda_i^* = -\zeta_i w_i \pm j\sqrt{1-\zeta_i^2}\,w_i \tag{2.27}$$

This procedure allows constructing a stabilization diagram for increasing model orders p and using stability criteria for eigenfrequencies, damping ratios, and modal participation factors.

An example of stabilization chart is shown in figure 2.9. It refers to one of the tests

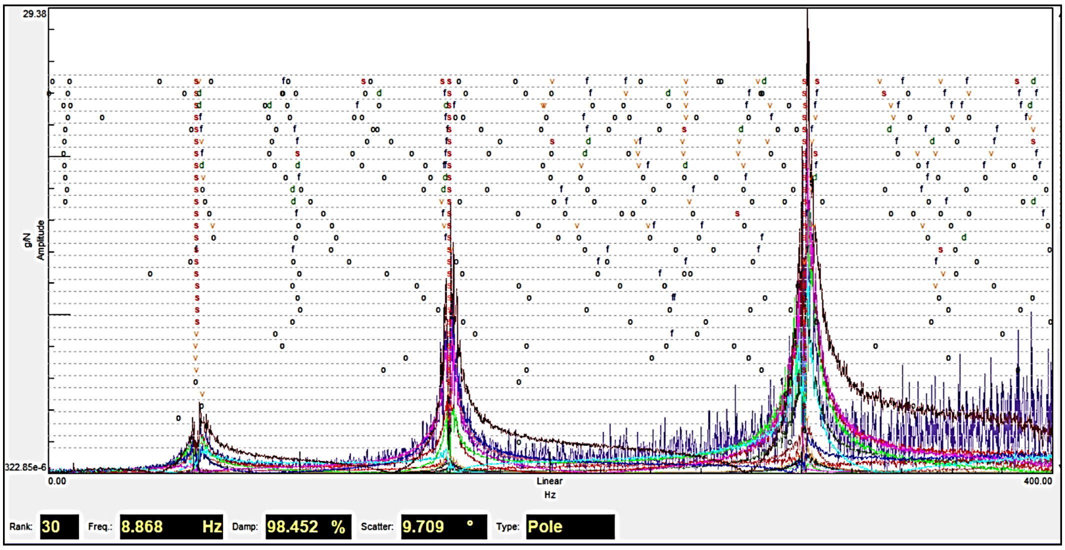

FIGURE 2.9: Stabilization Diagram of a MIMO test obtained in Test-Lab

that is presented in the chapter 2.4.2. It is possible to notice the presence of letters in correspondence of the peaks. These letters indicate how the algorithm has evaluated that mode, whether stable or not. More in details, the symbols have following meaning: "o": new pole, "f": stable frequency, "d": stable frequency and damping, "v": stable frequency and eigenvector, "s" all criteria stable. From the stabilization diagram it is possible to choose the modes to be included in the analysis to be able to determine the response of the system and the relative mode shapes.

Once the modal parameters have been obtained, it is possible to proceed with the correlation phase. This represents one of the final stages of an EMA and consists in comparing the experimental results with those obtained from an analytical, numerical model or deriving from another experimental test. In most cases, the comparison concerns numerical and experimental results.
As regards the numerical path, it is possible to build the modal model in terms of eigenvectors and eigenvalues that define the numerical natural frequencies and the numerical mode shapes of vibration. From the modal testing, it is possible to extract the experimental natural frequencies, damping, and mode shapes. If on one side it is relatively simple to compare the values of natural frequencies since they are scalar values, on the other side, the mode shapes comparison is not really easy because they are vectors, generally complex. The problem lies in the different information densities of the two models. Generally, a FEM model is described with several nodes much higher than the measurement points of the TA. In this regard, two possible solutions can be used.

1. Condensation of the FE model

2. Extrapolation of the experimental test results

Generally, the first solution is the most used. Once two equal-sized mode shapes are obtained it is possible to compare them. The most used descriptor to perform a comparison is the Modal Assurance Criterion or MAC. It can be defined with several equations but in this regard, we refer to the MAC as the normalized one. It can be expressed as follow:

$$MAC = \frac{\left|(\Psi_{ex})^T \cdot (\Psi_{num})\right|^2}{\left[(\Psi_{ex})^T \cdot (\Psi_{ex})\right]\left[(\Psi_{num})^T \cdot (\Psi_{num})\right]} \tag{2.28}$$

Even if the modes are complex, the MAC value will be scalar, in particular between 0 and 1.

The operation must be repeated for each possible pair of numerical/experimental modal vectors until the complete MAC matrix is built. MAC values are usually shown in histogram form. If the MAC value is close to 1 there is a linear relationship between the two considered mode shapes while if it is close to 0 they are linearly independent. In particular, figure 2.10 shows the trend of the autoMAC in which the experimental or numerical modes are related to themselves. Consequently, all the elements of the diagonal will assume unitary value. The autoMAC is used to verify the orthogonality properties of the modes or to analyze the consistency of the points chosen to represent the modal deformations. In the general case of numerical-experimental correlation, the value of the MAC rarely reaches a unitary value (identical modes) so conventions must be adopted to establish when a good correlation is reached. The choice of the lower limit beyond which to accept the good correlation depends on various factors, in a plausible choice it can be 0.8.

The non-achievement of the unit value on the diagonal is interpreted, as an imperfect correlation due to different causes, for example:

- non-linearities in the test structure;
- noise on the measured data;
- poor modal analysis of the measured data;
- inappropriate choice of DOFs included in the correlation.

Therefore, once the correlation has been made, it is possible to hypothesize what it was the source of the error in the test activity and act accordingly.

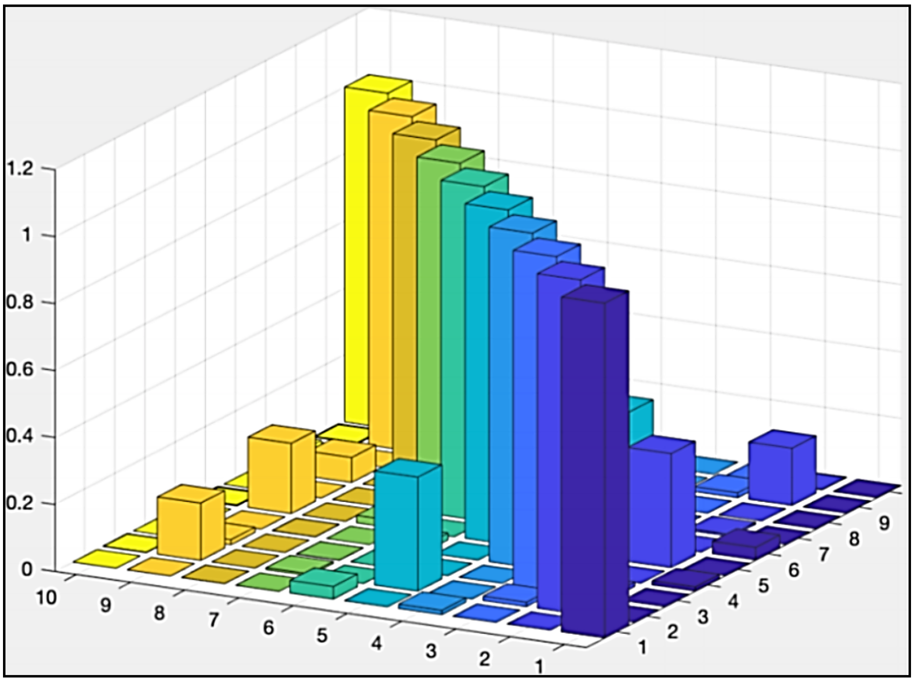

FIGURE 2.10: Histogram of the autoMAC values

2.4 Vibration Test

2.4.1 Test set-up

In this section, the tests carried out and the results are presented. The goal was to conduct a series of vibration tests on the two uniform cross-section beams by means SIMO and MIMO approaches. The properties and sizes of the two TAs are indicated in Table 2.1 and Figure 2.11.

To set an adequate setup, an initial step is to identify the number and arrangement of the measurement points through a FEM analysis. Mono-dimensional elements are used for both beams models. The numerical activity provided a preliminary assessment on the frequencies and the mode shapes and it represented a reference for the position of the accelerometers: twelve measurement points were located along the beams.

From a practical point of view, by taking into account the problems illustrated in the previous paragraph, in the organization of the test setup, particular attention was paid to the shaker-structure rigid connection, the free-free condition simulation, and the instrumentation isolation.

Regarding the first point, a connection via double-sided tape with dual lock technology was made, as shown in Figure 2.12.

The free-free constraint condition was obtained through the use of suitable bungee cords of known stiffness, able to guarantee that the natural frequencies of the mass-spring system were at least 10% than the first natural frequency of the structure [18]. During shaker excitation, there is a potential error source to avoid. This error arises

TABLE 2.1: TAs. Properties and sizes.

Properties and sizes	TA 1 - Aluminium	TA 2 - Iron
Young Modulus, E, [GPa]	69	196
Shear Modulus, G, [GPa]	27	80
Poisson Ratio, ν	0.33	0.3
Mass Density, ρ, $[kg/m^3]$	2700	7874
Length, L, [m]	2	2
Mass, m, [kg]	0.8	7.9

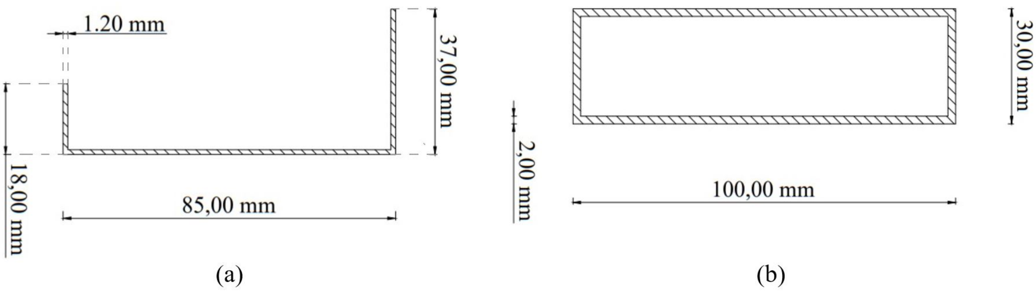

FIGURE 2.11: Cross sections of TA 1 (a) and 2 (b).

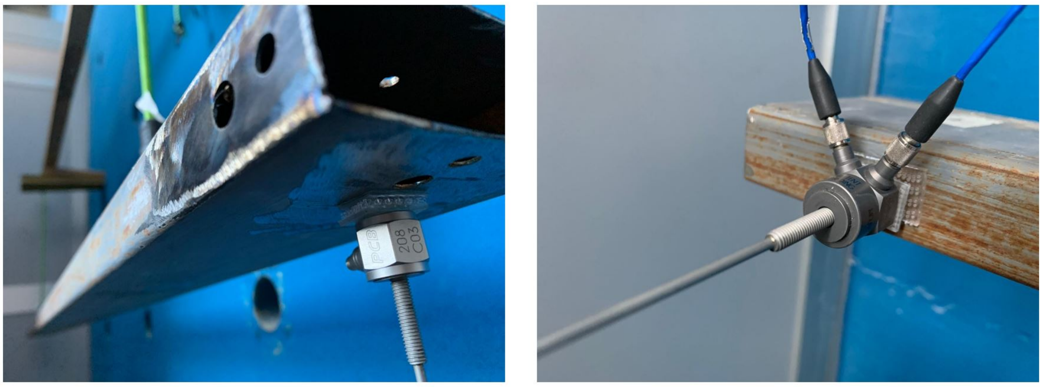

FIGURE 2.12: Double-sides tape solution.

if the shaker causes vibrations which propagate into the structure through a different path than through the stinger. These vibrations make the linear system incorrect according to the model we assume. The input forces to the structure via the wall, floor, frame, and suspension are highly correlated with the force measuring by means the force transducer. Therefore, this type of error is not discovered by the coherence function, since the measured response signal is correlated with the measured input. So, as regards the isolation of the instrumentation from the floor, panels of viscoelastic material were used to avoid interference in the FRF acquisitions due to the vibrations of the base of the shaker.

For all tests, the data acquisition was carried out running LMS TestLab ®v.19 software while the spectral data system was an LMS SCADAS Mobile 05. The excitation signal is true random. The data acquisition parameters are a resolution of 0.46 Hz, 1024 spectral lines, a number of 20 averages, and exponential windowing. One or two electrodynamic shakers (445 N peak force - Modal Shop 2100E11) and two roving unidirectional accelerometers (ICP®333B32) were used to carry out the vibration test.

For the directions of the shaker axes and the description of the modal shapes, we consider a reference system in which the x-axis is along the beam, y horizontal and parallel to the floor while z is orthogonal and vertical.

The second preliminary operation was to investigate the reciprocity and non-linearity of the structures under study to verify the invariance of the FRF by respectively swapping the input and output points location and varying the voltage of the signal power amplifier.

When multiple SISO/SIMO testing are performed, the theory of modal testing states that reciprocity must hold true between the results from different single input runs. Practically, there may be differences due to the effects of stiffness and shaker mass. The Figure 2.13 shows the reciprocity and non-linearity test results for both TAs limited to the first natural modes of vibrations. In the case of the aluminum structure, the test outputs a satisfactory result for a relatively low level of power amplifier voltages. The beams under study have modes that are quite directional in nature. In our investigation, we consider the first four modes. There are some modes that have predominant motion in the setup vertical direction and other modes that have predominant motion in the setup horizontal direction. But while two shakers could be used to excite the structure in the x and y-directions separately, the test could also be conducted with just one single shaker that would be set at a skewed angle to the y- and z- directions, such that the four modes are excited; if other modes were of interest, the shaker would need to be moved to a different skewed location and to not be at one node of the mode.

MIMO provides the opportunity of exciting all modes of the structure simultaneously in a certain frequency range. In the latter case, the structure must be adequately constrained to be able to undergo oscillation in several directions at the same time [19]. This advantage is independent of the size of the structure and favors the

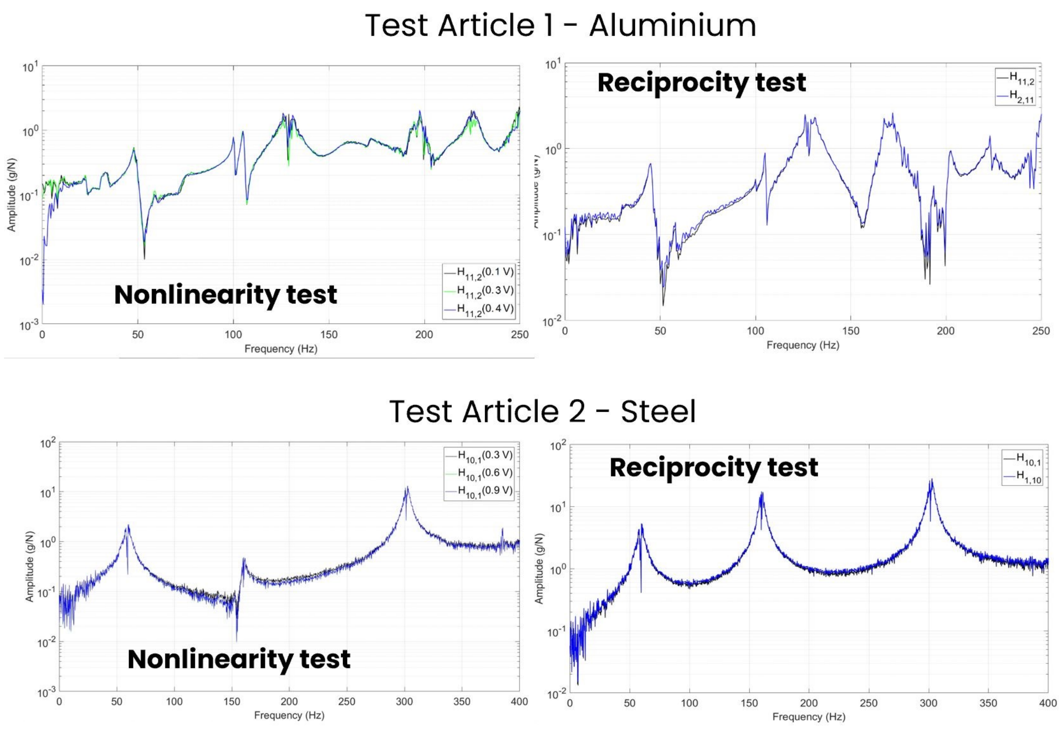

FIGURE 2.13: Reciprocity and Non-linearity: TA 1 (top) and TA 2 (bottom).

time saving of the tests.

2.4.2 Test results and conclusions

A numerical modal analysis has been carried out using the dynamic analysis of NASTRAN solver to perform a numerical and experimental comparison above all in terms of natural frequencies. The real structure is discretized in the FEM model with 41 geometrical grid points and 40 1D bar elements, as shown in figure 2.14.
The topic of the experimental-numerical comparison was the first 4 flexural mode shapes so bar elements was able to describe the dynamic behaviour of the TA. For the first 4 modes of vibrations, the mode shapes and natural frequencies are reported in Figure 2.15 and Table 2.2.

TABLE 2.2: Dynamic analysis results for the first 4 modes of the 1D bar element FEM model.

FEM Results	TA 1		TA 2	
No.	**Mode**	**Frequency**	**Mode**	**Frequency**
1	1Z	39.88	1Z	58.91
2	1Y	109.8	1Y	154.59
3	2Z	143.8	2Z	158.86
4	3Z	205.	3Z	301.58

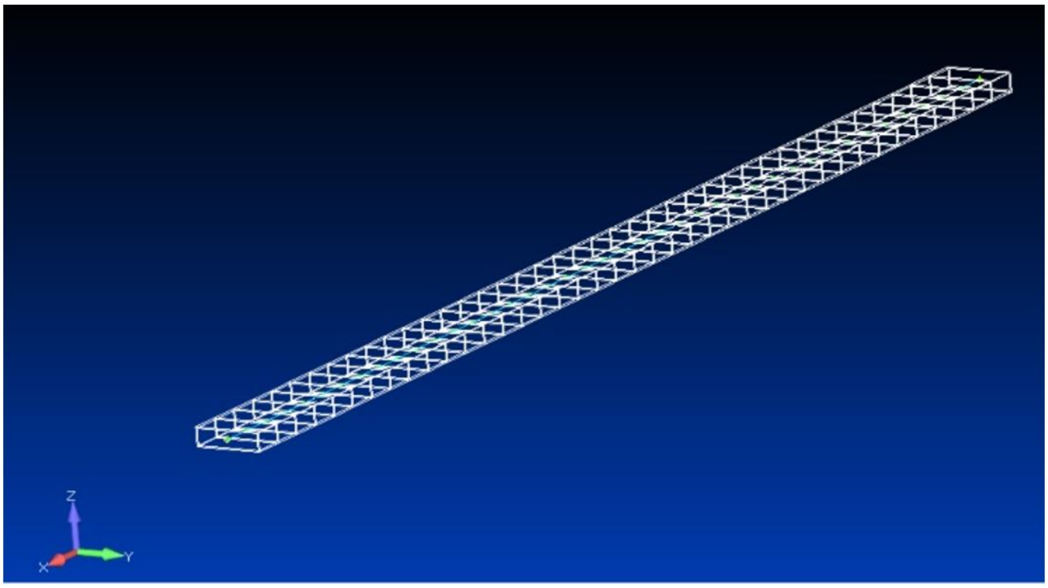

FIGURE 2.14: 1D bar element FEM model.

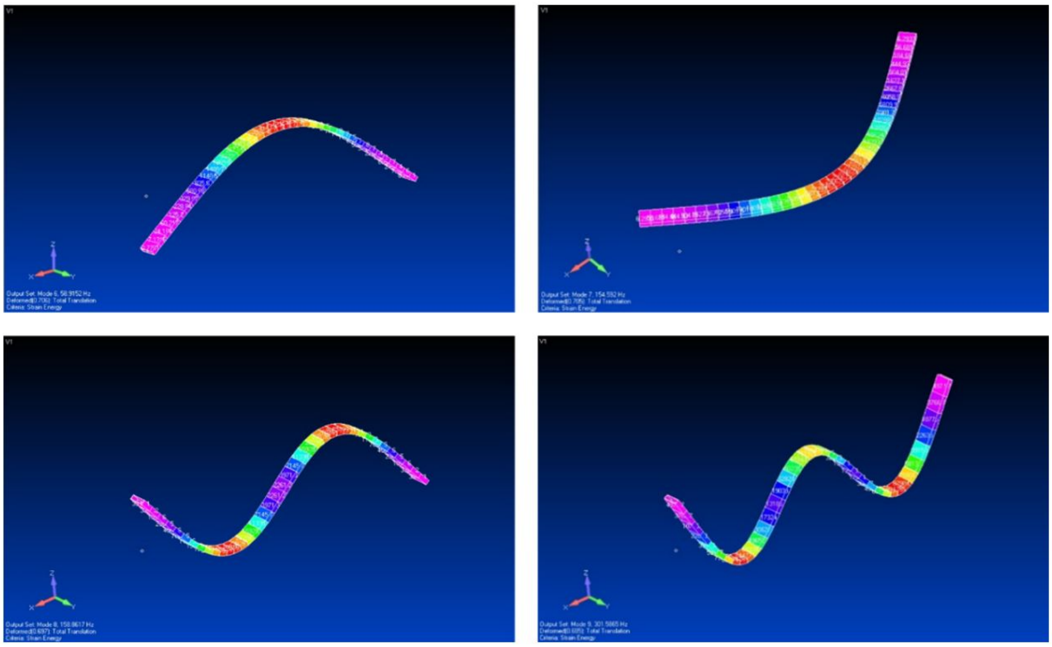

FIGURE 2.15: First 4 mode shapes of the 1D bar element FEM model.

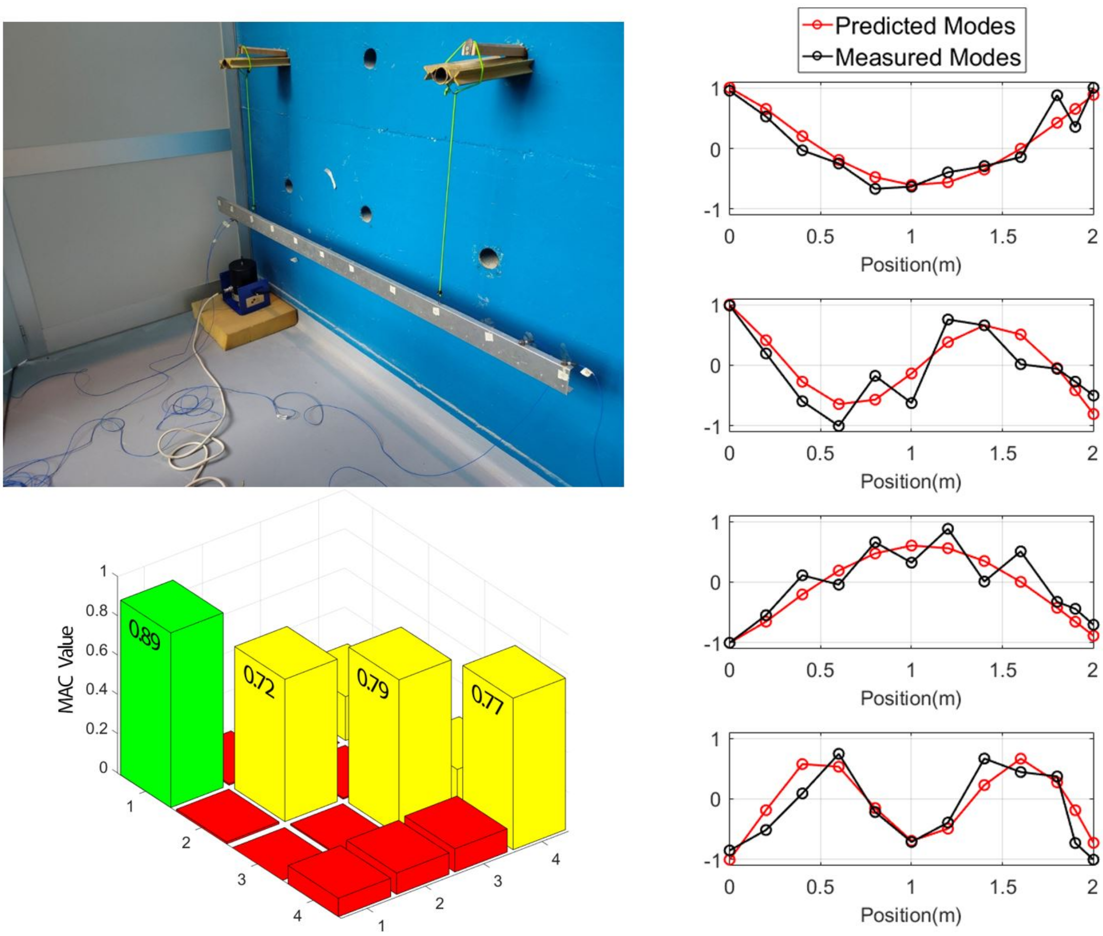

FIGURE 2.16: TA 1, SIMO Test.

For the aluminum TA, the results are not satisfactory. It is observed that the percentage error between numerical and experimental results is high enough. In this case, the MIMO works worse than the SIMO because of too light structures, stingers locally modify the stiffness of the structure and affect the test results.
The numerical-predicted and experimental-measured mode shapes are compared through the MAC. In this case there is a good correlation in the estimation of the mode shapes.
Moving to the iron TA, it can be seen that the MIMO approach gives much better results than the SIMO for all the flexural modes along the z-direction.
To investigate a trend between the weight increase of the TA and improvement of the experimental results, we added masses at the end of the beam: two 1 kg masses in the first test and 2 kg masses in the second one. Thus doubling the additional masses at the ends of the beam there is a satisfactory improvement in the results both in terms of frequencies and in the estimation of mode shapes [20, 21].

To conclude and summarize, some advantages of MIMO over SIMO have been experimentally investigated: more uniformly distributed energy across the structure, force levels can be kept lower, modal test data can be taken in one single shot,

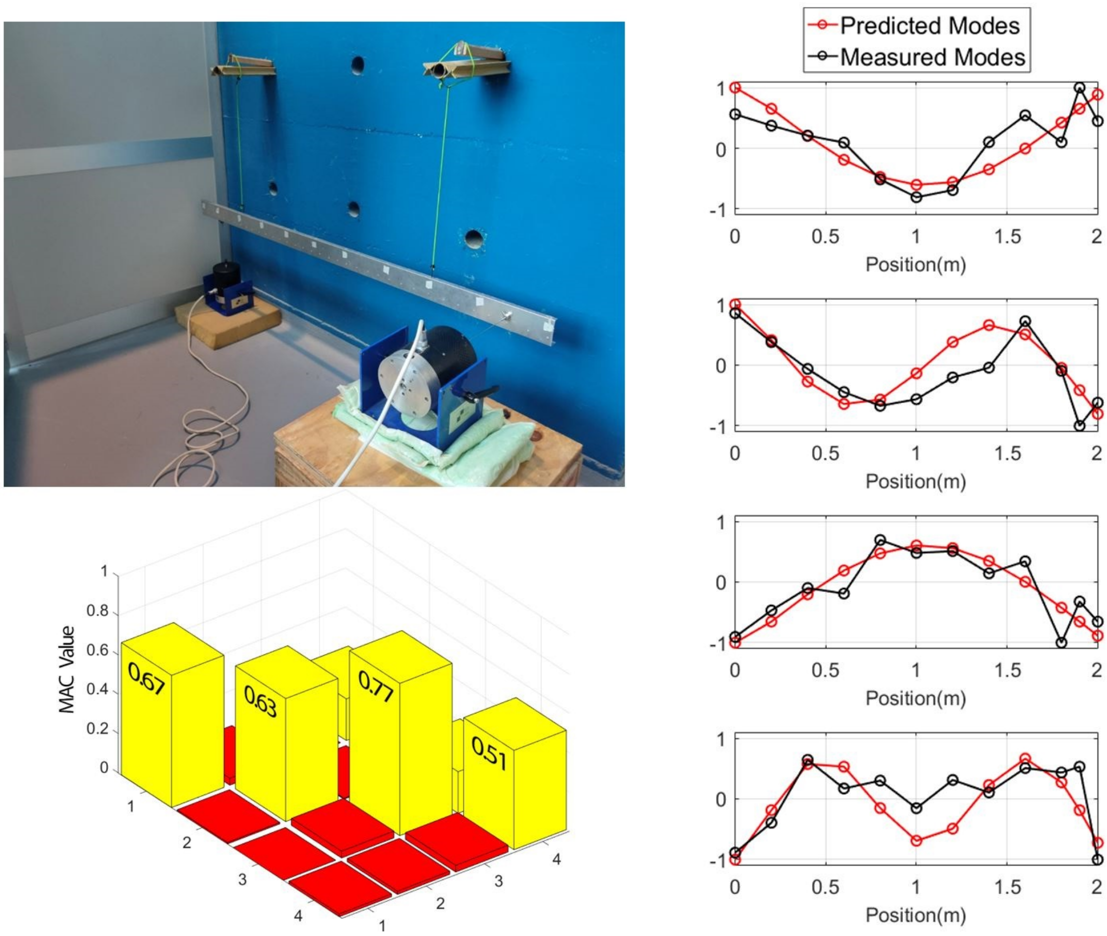

FIGURE 2.17: TA 1, MIMO Test.

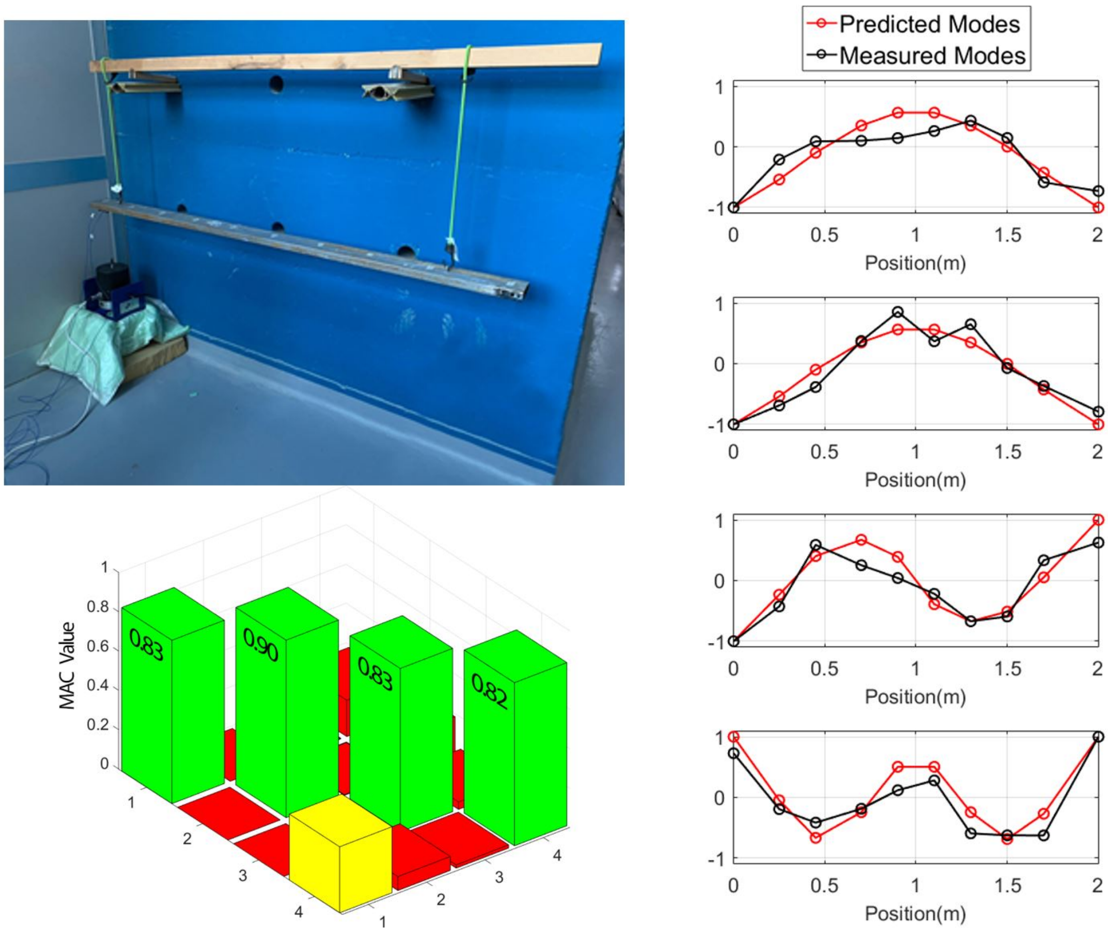

FIGURE 2.18: TA 2, SIMO Test.

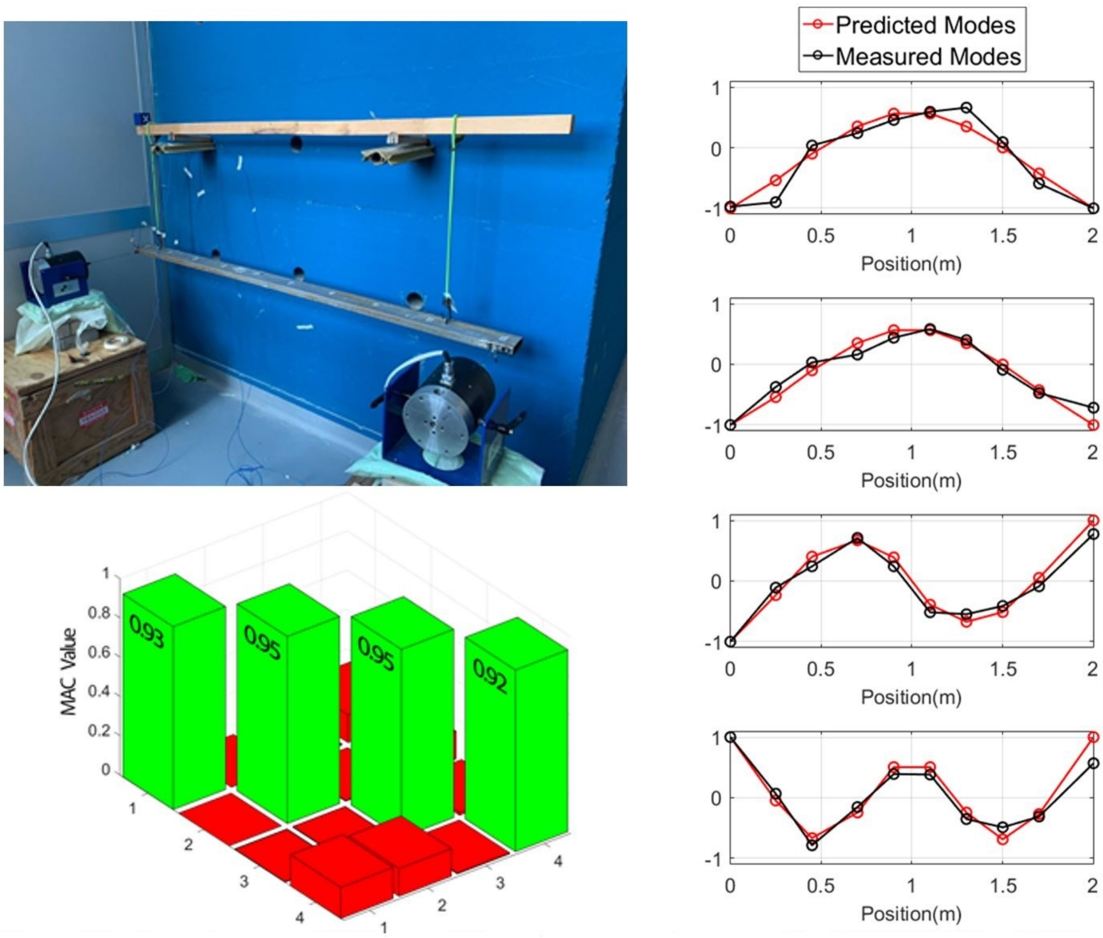

FIGURE 2.19: TA 2, MIMO Test.

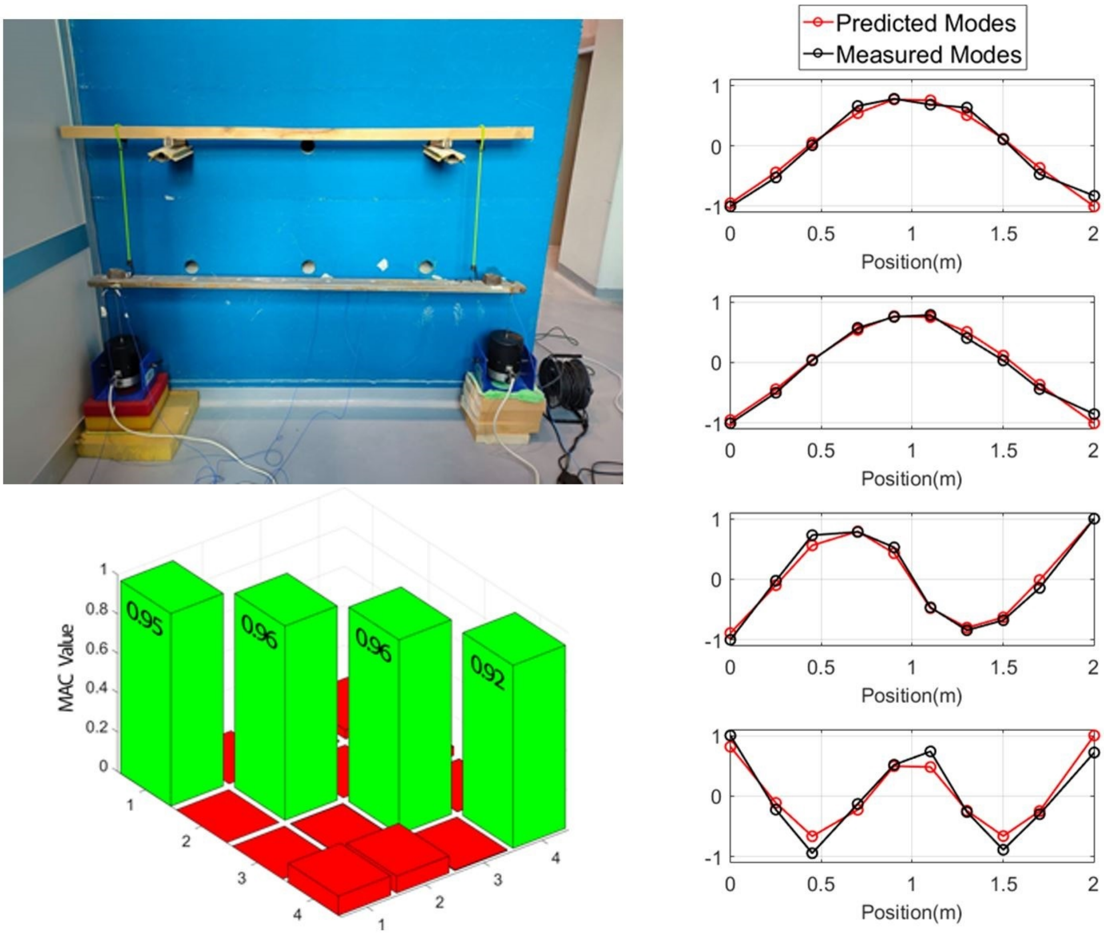

FIGURE 2.20: TA 2 + two 1 kg masses at the ends, MIMO Test.

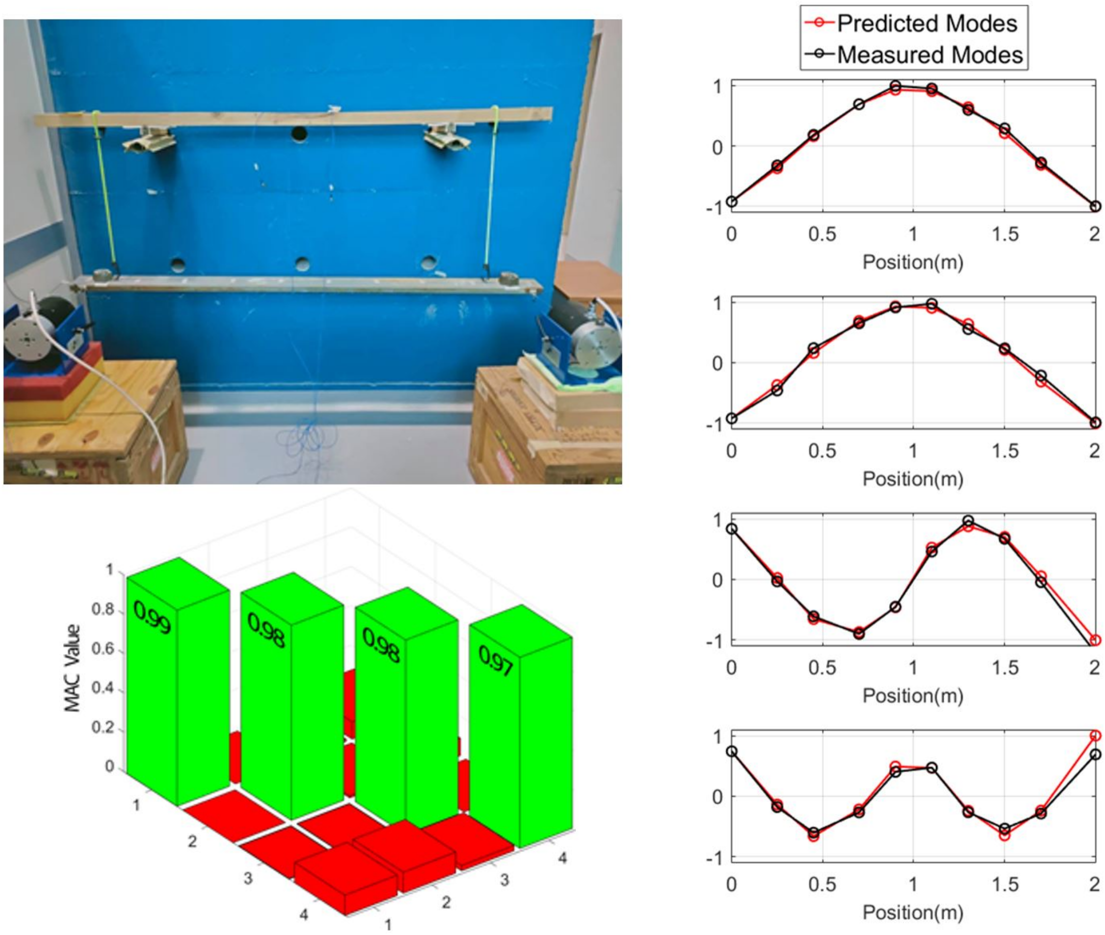

FIGURE 2.21: TA 2 + two 2 kg masses at the ends, MIMO Test.

TABLE 2.3: SIMO and MIMO test results - TA 1.

Mode	Numerical (Hz)	SIMO (Hz)	Error (%)	MIMO (Hz)	Error (%)
1^{st} Flexural Z	39.88	41.4	3.8	37.62	5.7
1^{st} Flexural Y	109.8	105.7	3.7	102.3	6.8
2^{nd} Flexural Z	143.8	135.8	5.6	133.8	7.
3^{rd} Flexural Z	205.	200.7	2.1	224.2	9.4

TABLE 2.4: SIMO and MIMO test results - TA 2.

Mode	Numerical (Hz)	SIMO (Hz)	Error (%)	MIMO (Hz)	Error (%)
1^{st} Flexural Z	58.91	56.5	4.1	60.16	2.1
1^{st} Flexural Y	154.6	152.9	1.1	152.	1.7
2^{nd} Flexural Z	158.9	162.2	2.1	159.9	0.6
3^{rd} Flexural Z	301.6	304.7	1.0	300.6	0.3

TABLE 2.5: MIMO test results - TA 2 with two masses at the ends.

Mode	Numerical (Hz)	SIMO (Hz)	Error (%)	Numerical (Hz)	MIMO (Hz)	Error (%)
1^{st} Flexural Z	51.95	50.12	3.5	43.49	43.92	1.
1^{st} Flexural Y	132.3	130.1	1.7	124.2	123.3	0.7
2^{nd} Flexural Z	148.3.9	146.9	0.9	148.8	146.1	1.8
3^{rd} Flexural Z	288.7	285.9	1.0	292.1	290.4	0.6

while nonlinearities are less likely to be excited. To demonstrate them, two different beams, in a free-free boundary condition, are subjected to single and multiple shaker tests. For the first, lighter TA, the error between numerical and experimental natural frequencies does not drop below 2% with a maximum value of 5% on the third mode shape. As the non-linearity test suggested, the errors are most likely attributable to the excessive influence of the inertia of the instrumentation on the dynamics of the TA. The percentage error increases when a second shaker is added to the setup.
As regards the second heavier TA, SIMO led to worthy results in the correlation of numerical natural frequencies. The main difference, however, lies in the results of the multiple-input technique which has returned excellent results both in terms of natural frequencies, mode shapes, and MAC values.
In Modal Testing distributed smaller forces are generally better than having a single strong one. The modal parameter estimation performed on the six data sets has confirmed the growing trend in terms of the goodness of the numerical-experimental correlation, revealing quite some advantages of the MIMO over the SIMO, as the weight of the TA under test increases.

2.5 Further Numerical Considerations

During the preliminary study of the state of the art of vibration tests and theoretical-numerical-experimental correlations, a reference was of particular interest: A. Erturk and D. J. Inman "On the Fundamental Transverse Vibration Frequency of a Free-Free Thin Beam With Identical End Masses". This paper shows that the commonly accepted and frequently quoted fundamental natural frequency formula (2.29) for a beam with identical end masses stemming from the work of Haener [22] is incorrect.

$$f_1 = \frac{\pi}{2}\sqrt{\left[1 + \frac{5.45}{1 - 77.4\,(M/m_b)^2}\right]\frac{EI}{m_b L^3}} \tag{2.29}$$

This formula, reported in many handbooks, tabulations and structural dynamics reference books [23, 24] was examined and was shown to be accurate only for the extreme case of very large end mass to beam mass ratios. The 2.29 represents the fundamental transverse vibration frequency of a free-free slender (Euler–Bernoulli) beam with identical masses at both ends. In the Formula, E is Young's modulus, I is the cross-sectional area moment of inertia, L is the length, m_b is the total mass of the beam, and M is the mass rigidly attached to each end of the beam. This form of Eq.2.29 gives the natural frequency in hertz and it can be converted to rad/s according to ω_1=$2\pi f_1$.

After rearranging Eq. 2.29 by separating the dimensionless frequency term from the material and geometric parameters, one can obtain the following equation, which gives the resulting natural frequency in rad/s:

$$\omega_1 = \pi^2\sqrt{1 + \frac{5.45}{1 - 77.4\,(M/m_b)^2}}\sqrt{\frac{EI}{m_b L^3}} \tag{2.30}$$

It is clear from Eq.2.30 that it may yield imaginary numbers and may even tend to infinity for certain values of M/m_b end mass to beam mass ratio. For this fundamental natural frequency expression to yield a finite positive real value, the following inequality must be satisfied:

$$1 + \frac{5.45}{1 - 77.4\,(M/m_b)^2} > 0 \tag{2.31}$$

which can be reduced to the following acceptable ranges of M/m_b:

$$0 \leqslant \frac{M}{m_b} < 0.1137 \quad \frac{M}{m_b} > 0.2887 \tag{2.32}$$

and for the following range of M/m_b, the expression suggested by Haener [22] results in imaginary numbers, which has no physical meaning:

$$0.1137 < \frac{M}{m_b} < 0.2887 \tag{2.33}$$

The natural frequency of the rth mode of an Euler–Bernoulli beam can be expressed as

$$\omega_r = \lambda_r^2 \sqrt{\frac{EI}{m_b L^3}} \tag{2.34}$$

where λ_r is well known as the dimensionless frequency parameter of the rth mode. Therefore, according to Eq. 2.30, the dimensionless frequency parameter of the first elastic mode suggested by Haener is:

$$\lambda_1 = \pi \left[1 + \frac{5.45}{1 - 77.4\,(M/m_b)^2} \right]^{1/4} \tag{2.35}$$

In [22], it was demonstrated that Eq. 2.29 yield incorrect results for the M/m_b regions given by Eq. 2.33 where it gives positive real numbers. In fact, by taking into account the simplest case M/m_b =0, which is the case when there are no end masses. In this particular case, the beam reduces to a uniform free-free Euler–Bernoulli beam without end masses, whose dimensionless frequency parameter for the first mode is λ_1=4.7300. However, when $M = 0$ is used in Eq. 2.29, one obtains

$$\lambda_1 = \pi[1 + 5.45]^{1/4} = 5.0066 \tag{2.36}$$

which has 5.8% relative error.

It should be noted from Eq. 2.34 that the natural frequency 1 is proportional to λ_1^2 and, therefore, the relative error in the resulting natural frequency predicted by using Eq. 2.29 for the particular case of $M = 0$ is about 12%.

The mathematical formulation, results and discussion are satisfactorily provided in [22]. Referring only to the new expressions identified for the first 4 natural frequencies, the correct dimensionless frequency parameter versus end mass M to

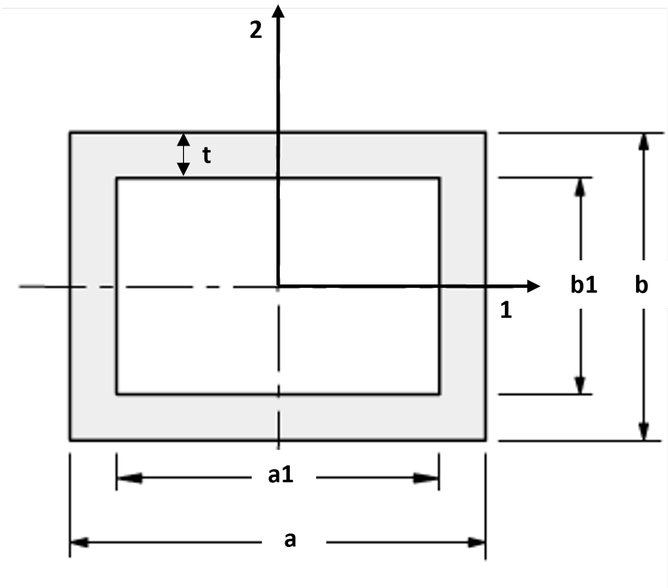

FIGURE 2.22: Cross-sectional beam, T-WING simplified model.

beam mass m_b ratio are:

$$\begin{aligned}
\lambda_1 &= \frac{3.1416\alpha^2 + 1.821\alpha + 0.2211}{\alpha^2 + 0.4783\alpha + 0.04674} \\
\lambda_2 &= \frac{6.2832\alpha^2 + 2.408\alpha + 0.2003}{\alpha^2 + 0.3579\alpha + 0.02551} \\
\lambda_3 &= \frac{9.4248\alpha^2 + 1.258\alpha + 0.04291}{\alpha^2 + 0.1222\alpha + 0.003903} \\
\lambda_4 &= \frac{12.5664\alpha^2 + 1.304\alpha + 0.03672}{\alpha^2 + 0.07888\alpha + 0.001745}
\end{aligned} \tag{2.37}$$

where $\alpha = M/m_b$.

2.5.1 T-WING Simplified FEM model and Sensitivity Analysis

The results obtained from the numerical analysys of the T-WING GFEM Nastran model cannot be made public for reasons of industrial secrecy. However, based on the project results, it was possible build a simplified FEM model, consisting of a simple beam able to check and resume the considerations, formula and data discussed in previous paragraph. The purpose is also to ascertain what happens when the masses, their positions, and the constraint vary.
After a few attempts in choosing the size and material to use, it emerged that a good compromise is represented by the beam with the following likely characteristics:

1. Geometrical data
   - Section Length: a=850 mm;
   - Section Height: b=320 mm;
   - Section Thickness: t=11 mm;
   - Cross-sectional Area: A=25,256 mm^2;

$$A = (ab - a_1 b_1) = [ab - (a - 2t) \cdot (b - 2t)] \tag{2.38}$$

   - Moment of inertia to axis 1: I_1=4.95x10^8 mm^4

$$I_1 = \frac{ab^3 - a_1 b_1^3}{12} \tag{2.39}$$

   - Moment of inertia to axis 2: I_2=2.28x10^9 mm^4

$$I_2 = \frac{ba^3 - b_1 a_1^3}{12} \tag{2.40}$$

   - Torsional Constant: C=1.29x10^9 mm^4

$$\mathrm{C} = \frac{2\mathrm{t}^2 \cdot (\mathrm{a} - \mathrm{t})^2 \cdot (\mathrm{b} - \mathrm{t})^2}{t \cdot (\mathrm{a} + \mathrm{b}) - 2t^2} \tag{2.41}$$

   - Radius of Gyration: I_ρ=2.77x10^9 mm^4
   - Beam Length: l=10,300 mm;
   - Beam Weight: m_b=1,053 kg.
2. Material data, Aluminum
   - Young's Modulus: E=7,000 kg/mm^2;
   - Lamé Constant: G=1,680 kg/mm^2;
   - Poisson's Ratio: ν=0.33;
   - Density: ρ=4.125x10^{-10} $kg\ sec^2/mm^4$;
3. FEM data
   - 105 nodes;
   - 104 CBEAM elements;
   - 2 CONM2 Concentrated Mass Element Connections.

Thanks to the use of the simplified model it was possible to carry out a sensitivity analysis by studying how the natural frequencies of the first 4 mode shapes vary, for the following configurations:

1. **CASE 1**: free-free beam of mass m_b with masses M equal at the ends;

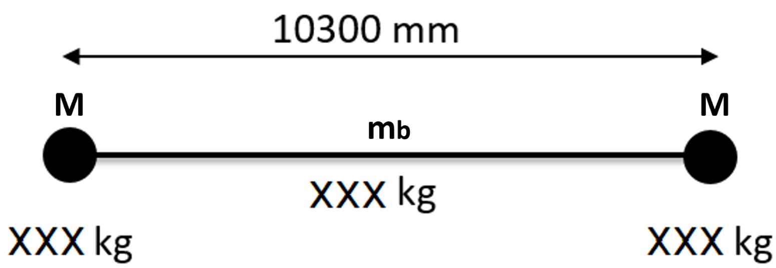

FIGURE 2.23: Simplified wing model - CASE 1.

2. **CASE 2**: free-free beam of mass m_b with one end fixed-mass $M = m_b$ and one end variable-mass M_v to the other end;
3. **CASE 3**: free-free beam of mass m_b, with equal end masses $M = m_b$, and, an additional variable mass m_c in the middle of the beam;
4. **CASE 4**: fixed half-beam with an end mass M at the free end;
5. **CASE 5**: fixed half-beam with an end mass M at the free end, and with variable offset in two directions, x and z.

CASE 1 In the CASE 1 the simplified beam of mass m_b representing the wing primary structure, has two masses M equal at the ends, representing the nacelle-engine-propeller group. A scheme of this model is shown in figure 2.23. The weight values are not provided.

The first 4 mode shapes are shown in the figure 2.24. The 4 mode shapes are described:

- 1^{st} wing symmetrical-bending;
- 1^{st} wing symmetrical Fore & aft;
- 1^{st} wing Anti-sym bending;
- 1^{st} wing Torsion.

It is interesting to observe from table 2.6 that the frequency of the 4^{th} mode does not vary as the ratio α varies.

CASE 2 In the CASE 2 the simplified beam has a fixed mass m_b and has one end fixed-mass $M = m_b$ on one side and one end variable-mass M_v to the other one as shown in figure 2.25. In this case $\alpha = M_v/m_b$.
The results in terms of natural frequencies are reported in table 2.7. Also in this case the frequency of the torsional mode does not change.

CASE 3 In the CASE 3 the beam of mass m_b, has two equal end masses $M = m_b$, and, an additional variable mass m_c in the middle of the beam (figure 2.26). In this case $\alpha = M_c/M = M_c/m_b$

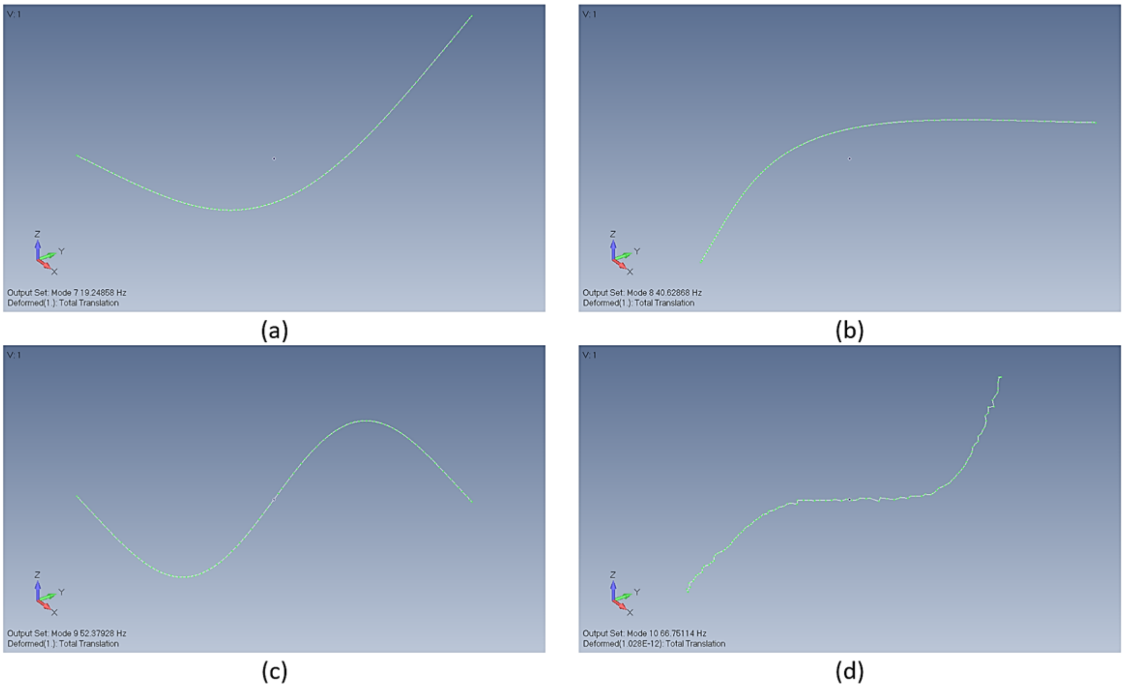

FIGURE 2.24: Simplified wing NASTRAN model.

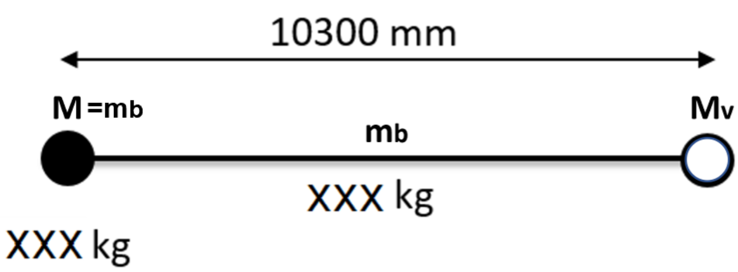

FIGURE 2.25: Simplified wing model - CASE 2.

TABLE 2.6: Simplified wing model. Natural frequencies vs. mass ratio α - CASE 1.

α	f_1 (Hz)	f_2 (Hz)	f_3 (Hz)	f_4 (Hz)
0.00	19.249	40.629	50.379	66.751
0.25	12.525	26.516	38.609	66.751
0.50	11.019	23.332	36.503	66.751
1.00	9.951	21.071	35.187	66.751
1.50	9.520	20.159	34.670	66.751

TABLE 2.7: Simplified wing model. Natural frequencies vs. mass ratio $\alpha = M_v/m_b$ - CASE 2.

α	f_1 (Hz)	f_2 (Hz)	f_3 (Hz)	f_4 (Hz)
0.00	14.062	29.718	43.284	66.751
0.25	11.221	23.756	36.904	66.751
0.50	10.484	22.198	35.846	66.751
1.00	9.951	21.071	35.187	66.751
1.50	9.735	20.615	34.942	66.751

The table 2.8 shows that in this case the frequency of the 3^{th} and 4^{th} mode shapes do not change. In particular, the third mode shape of the beam has a node in the center and therefore independent of the value of the central mass.

TABLE 2.8: Simplified wing model. Natural frequencies vs. mass ratio $\alpha = M_c/M = M_c/m_b$ - CASE 3.

α	f_1 (Hz)	f_2 (Hz)	f_3 (Hz)	f_4 (Hz)
0.00	9.951	21.071	35.187	66.751
0.25	8.419	17.820	35.187	66.751
0.50	7.545	15.961	35.187	66.751
1.00	6.564	13.877	35.187	66.751
1.50	6.017	12.716	35.187	66.751

CASE 4 The CASE 4 concerns the study of fixed free half-beam, adding the fixed joint constraint at one end and considering the mass M at the other end.

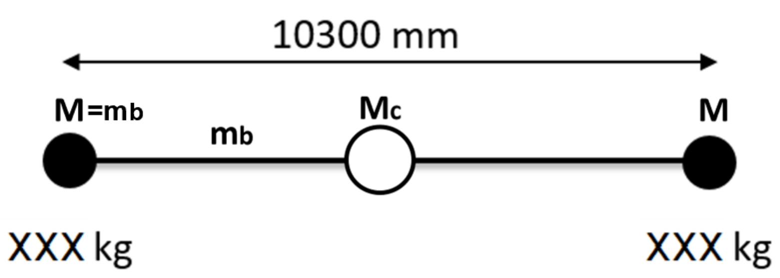

FIGURE 2.26: Simplified wing model - CASE 3.

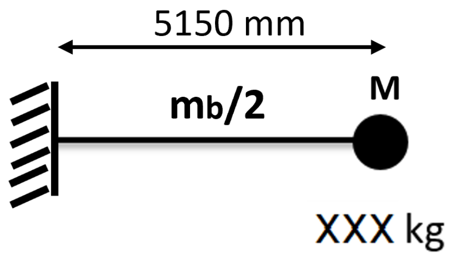

FIGURE 2.27: Simplified wing model - CASE 4.

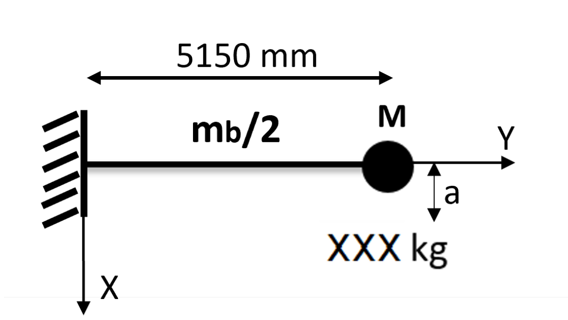

FIGURE 2.28: Simplified wing model - CASE 5.

From table 2.9 it is interesting to observe that the torsional frequency remains unchanged as α increase since it is that of an anti-symmetric torsion. The frequency of the 3^{th} mode, on the other hand, decreases by crossing the value of the torsional frequency, for $0.<\alpha<0.25$.

TABLE 2.9: Simplified semi-wing model. Natural frequencies vs. mass ratio $\alpha = M/(m_b/2)$ - CASE 4.

α	f_1 (Hz)	f_2 (Hz)	f_3 (Hz)	f_4 (Hz)
0.00	12.072	25.271	72.619	66.751
0.25	8.517	17.923	59.205	66.751
0.50	6.937	14.618	56.097	66.751
1.00	5.359	11.304	53.958	66.751
1.50	4.524	9.545	53.122	66.751

CASE 5 Finally, to conclude the sensitivity analysis phase of the simplified model, the CASE 5 of offset of the extremity mass was studied. The offsets are a along the X direction, transversal to the beam and b along the longitudinal direction Y. The results are shown in Table 2.10. If only a varies (b = 0), the frequency f_4 increases with the offset, unlike the others which decrease instead. If it also b increases, all frequencies decrease and the higher frequencies are more sensitive to the variation of the offset. With the same variation, f_1 has a variation Δf = 0.117 Hz while f_4 has a variation Δf = 16.827 Hz.

TABLE 2.10: Simplified semi-wing model. Natural frequencies vs. mass ratio $\alpha = M/(m_b/2)$ - CASE 5.

	$a = 0$ $b = 0$	$a = 100$ $b = 0$	$a = 250$ $b = 0$	$a = 500$ $b = 0$	$a = 100$ $b = 100$	$a = 250$ $b = 250$	$a = 500$ $b = 500$
f_1	6.937	6.934	6.919	6.866	6.932	6.907	6.820
f_2	14.618	14.614	14.595	14.527	14.586	14.423	13.851
f_3	56.097	55.246	51.641	43.582	54.974	49.830	39.270
f_4	66.751	67.111	68.351	70.119	66.016	62.976	55.060

The figure 2.29 graphically compares the resulting frequencies against mass ratio α for the four previous cases.

2.6 NGCTR-TD Wing Vibration Test

2.6.1 Vibration Test - T-WING Primary Structure

To facilitate an alignment on dynamic tests, the requirements of LHD and the objectives to be achieved, the work previously carried out and presented so far constitutes the lesson learned and the basics of the vibration test that will be performed on the TA of the wing T-WING and its moving surfaces. In other words, it could be used as a reference document for future activities for the NGCTR-TD wing when the TA becomes available. In this last section of the chapter, some preliminary considerations are given to what will be the aforementioned vibration tests.
The dynamic tests on the T-WING TA will be performed by using the methodology based on the transfer function analysis measured at several points on the structure, which is vibrating under a selected excitation function driven by two electrodynamic shakers [25, 26]. The main steps of these approaches are summarized below:

- Selection of suitable excitation and measured points;
- Evaluation of the transfer function between each couple of excitation and measured points by using the 24 channels acquisition system;
- Synthesis, by using TestLab software, of the previously acquired transfer functions for the calculation of the modal parameters.

Only the second item requires the structure, while the other steps may be performed at different times and places. A pre-test numerical activities allowed to better define the set-up of the vibrations tests in terms of:

- positions of Shakers;
- number and positions of accelerometers;
- there are no areas of the wing in which to carry out particular experimental modal analysis. there is no need to thicken the grid of the measurement points;

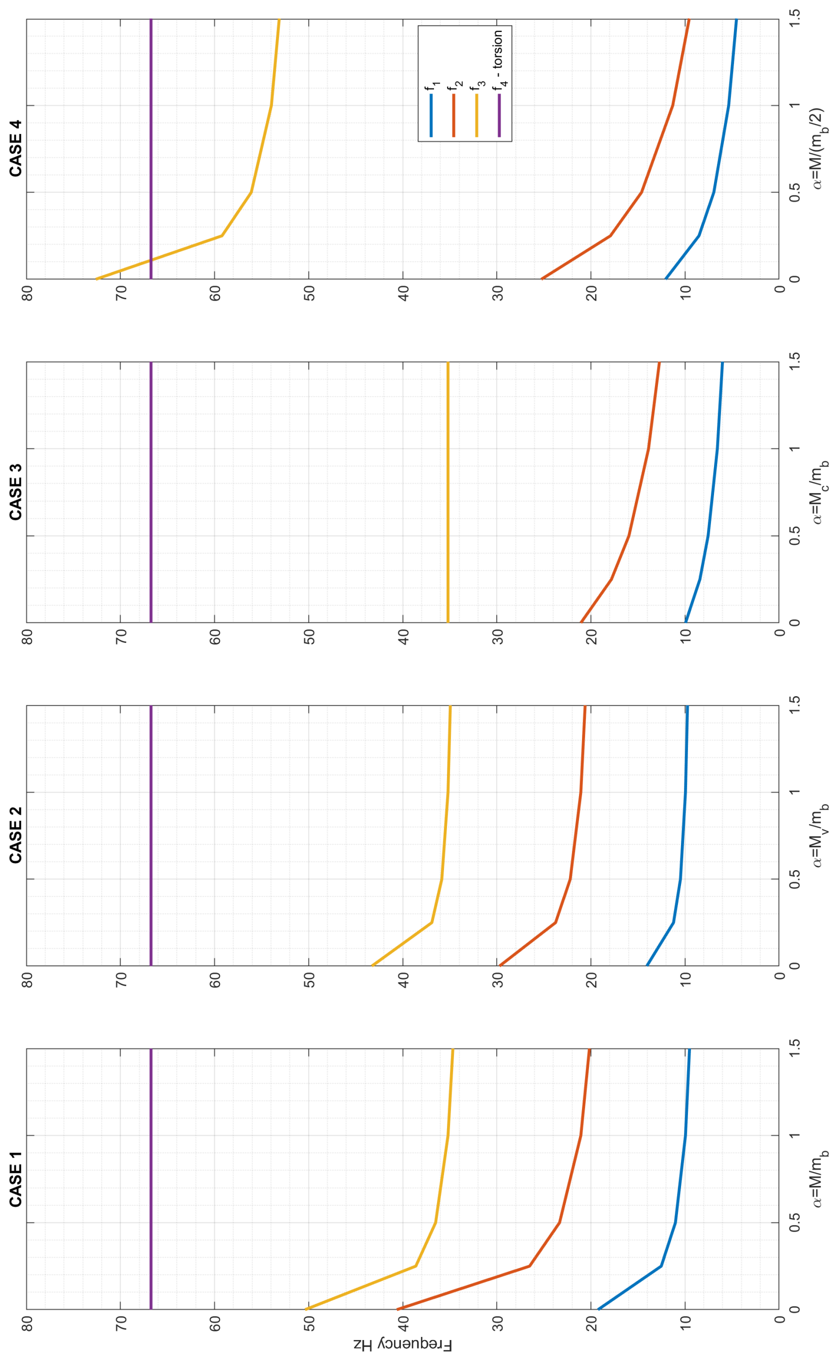

FIGURE 2.29: Numerical frequencies vs. mass ratio α.

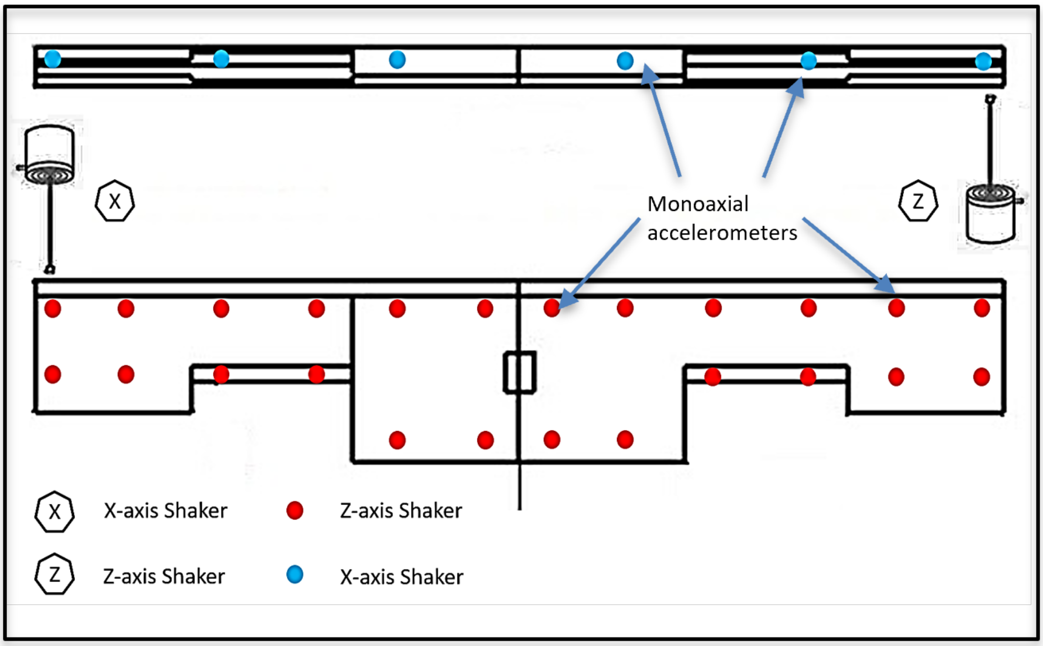

FIGURE 2.30: TWING - Location of the measurement sensors and shakers.

- frequency range (0-50 Hz).

The proposed excitation function will be Sine Sweep or Random at two points on the wing along with different directions:

- Along the z-axis at the wing tip;
- Along the y axis, at the wingtip.

The proposed accelerometers locations are:

- when exciting along the z-axis for Bending and Torsion modes along the z-axis no.2 accelerometers along the chord for a total of no.24 measurement points;
- when exciting along the x-axis for In-plane or Fore & Aft modes no.6 accelerometers along the wingspan.

About the boundary condition, the first conceptual test rig was a suspended system of two aluminum beams (Figure 2.31). The suspension system with bungee cords could be too rigid and the highest suspension mode could be too close to the first symmetrical wing bending so, for this and other reasons, the free-free condition will be realized using ground pneumatic support mainly consisting of air rides or air jacks (Figure 2.32).
The natural frequency of the air jack is easily regulated with a pressure gauge and it does not vary with load. So several mounts may be used to support a large structure, at 3 or 4 points, as shown in figure 2.33. Pneumatic supports are widely used in the aeronautical field for instance for GVT on large aircraft (Figure 2.34)[27–29].

This support is safer and easier to install, transport, and manage compared to the suspension system, by saving a big effort in the test set-up.
A pre-test numerical activities have also provided useful information about the use of some variants of elastic support systems.

These activities was mainly aimed at investigating, through numerical simulation, the influence of the presence of air jacks in the GFEM model of the wing. In particular, we established how the elastic modes of the wing vary due to the pneumatic system (make sure that there is sufficient difference between the first bending and fore and aft mode frequencies and the frequency of the support).
To simulate the pneumatic system consisting of the air jacks, 4 rigid elements were used in the wing GFEM model.
The vertical stiffnesses of air rides are known from the manufacturer's datasheet while the horizontal stiffnesses was obtained experimentally by arranging the supports in a horizontal position, by applying a known load and varying the internal pressure.

For the numerical analysis, three different horizontal stiffness values (700, 1000, and 1300 lb/in) of the air-rides have been assumed, to estimate the influence of ground pneumatic support on the dynamic behavior of the wing. Without going into the merits of the analyzes and without reporting the results or data on various elastic support systems, the numerical investigation outcomes the minimum ratio between the highest frequency of the pneumatic support system modes and the first elastic modes of the wing is determined: it is clear that, due to the hypothesized and used stiffnesses, the natural frequencies of the first 4 mode shapes do not change at all or remain approximately the same. The suspension system or the pneumatic ground support system chosen provide minimum impact on frequencies and mode shapes of lower elastic modes of the wing. The highest frequency suspension mode predicted was well below the first wing bending mode. This separation of the suspension modes from the wing dynamics is necessary to prevent coupling of the motion and an alteration of the T-WING dynamics.
The results of experimental research of elastic support system influence on wing modal parameters are briefly reported.
Some experimental tests were performed to validate the numerical results and calculate the in-plane (horizontal) stiffness of the air jack and to update the datasheet and the available FEM models.
The figure 2.35 shows the setup of the tests. The air jack was tied to a suitably fitted plate. A load applied to the air jack was progressively increased and the relative displacements were recorded utilizing photographic surveys. From the detection of the displacements and the known load applied it was possible to obtain two values of the stiffness for two different pressure values of the air ride: 60 and 80 psi. The two average values of the stiffnesses in plane obtained for the air jack are respectively:

- 58.6 lb/inch for 60 psi;

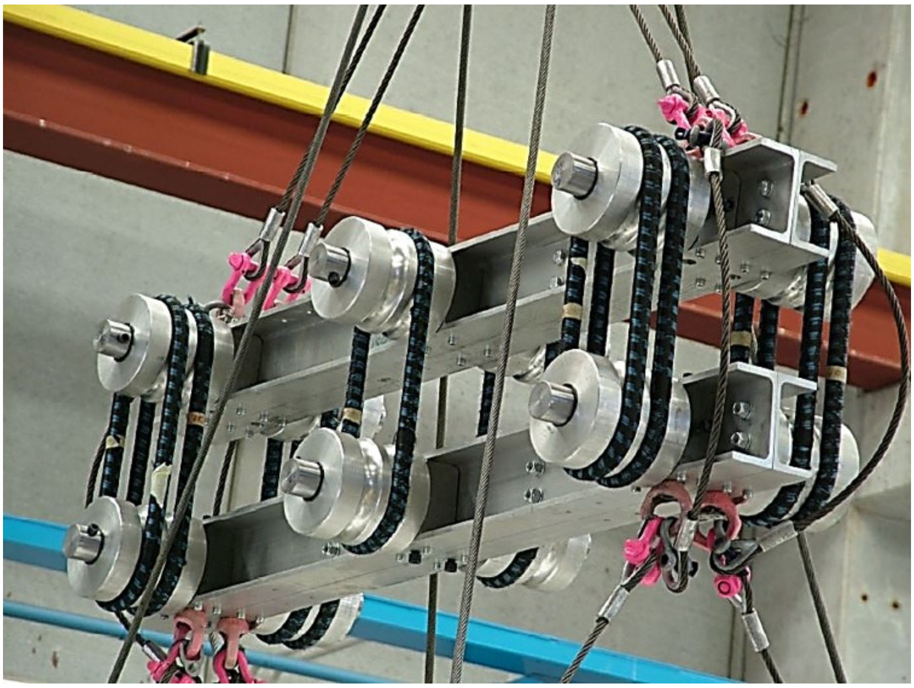

FIGURE 2.31: Elastic suspension system.

- 71.4 lb/inch for 80 psi.

To conclude, having found stiffnesses one or two orders of magnitude lower than those hypothesized in the numerical calculations, allows us to conclude that the stiffness of the air rides is such as to not affect the vibration tests: they do not affect the natural frequencies of the article examined.

2.6.2 Vibration Test - T-WING Movable Surfaces

Moment of inertia with respect to the hinge axis

To conclude this chapter on vibration tests, some preliminary activities are presented to the study of the structural dynamic behavior of the movable surfaces of the wing. In particular, some experimental laboratory methods, candidates for use on full-scale articles, are analyzed.
In this section, the focus is on the calculation of the mass moment of inertia with respect to the hinge axis and the position of the center of gravity of a movable surface. For the experimental estimate of the moment of inertia, a small laboratory device was created using 3D printing. The idea is to proceed experimentally with a small-scale model and once familiar with the methodology, move on to a preliminary experimental test with the use of real sizes movable surfaces.
The figure 2.37 shows the scheme of the lab device, where K is the linear stiffness of the spring, d is the distance between the spring and the hinge axis while x is the displacement. Θ is the angle of rotation of the movable surface about the hinge axis when the force F is applied to the surface.

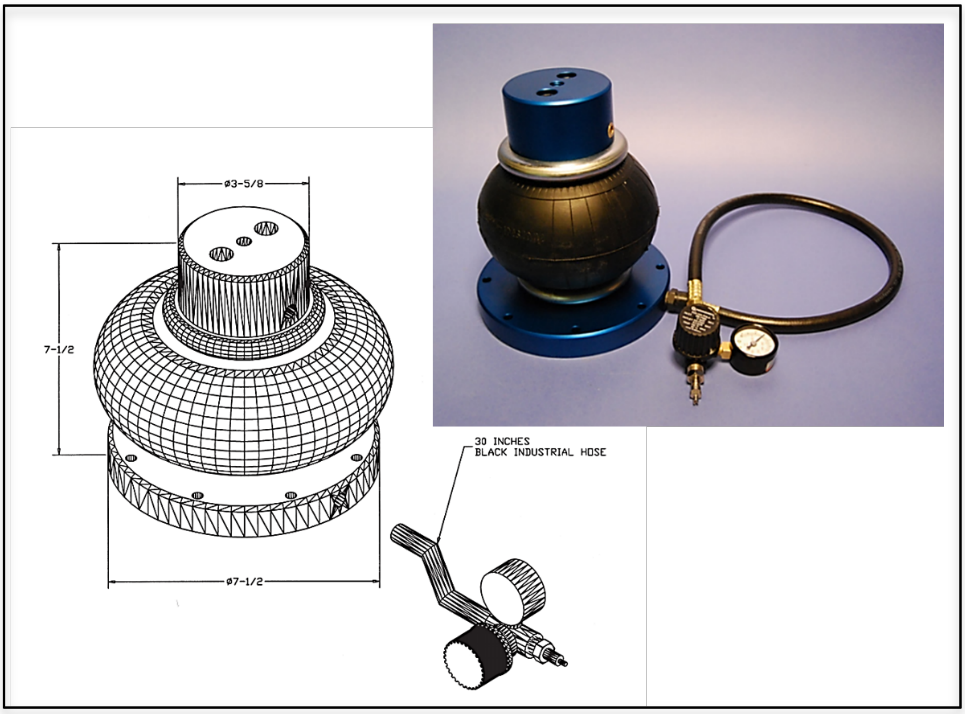

FIGURE 2.32: Air ride.

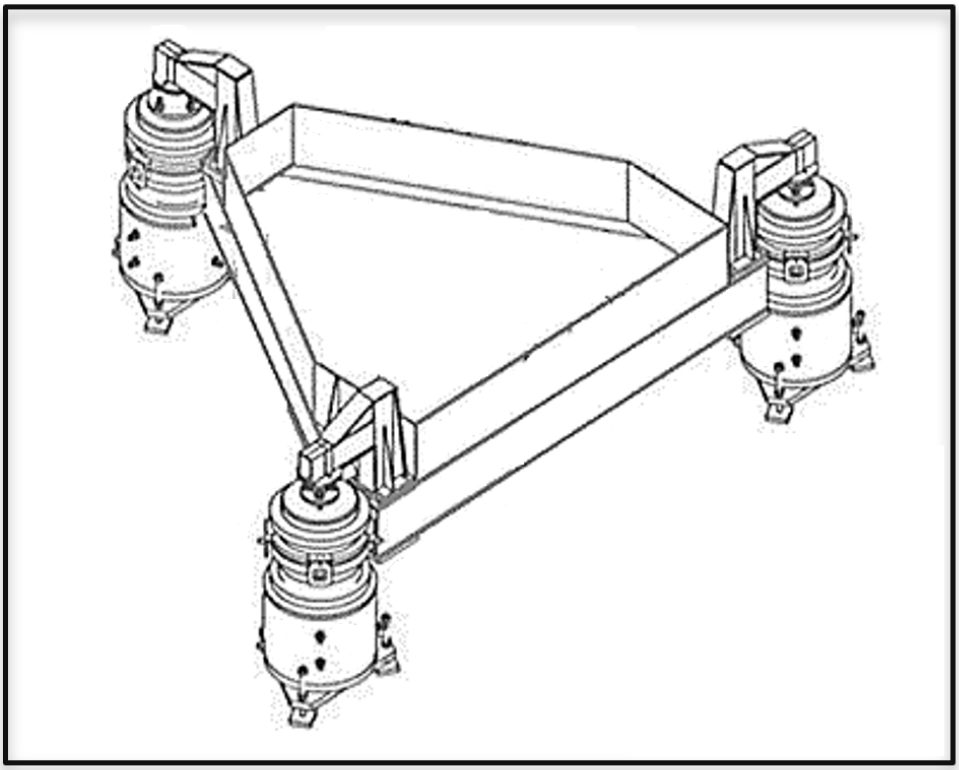

FIGURE 2.33: Pneumatic ground support system - drawing.

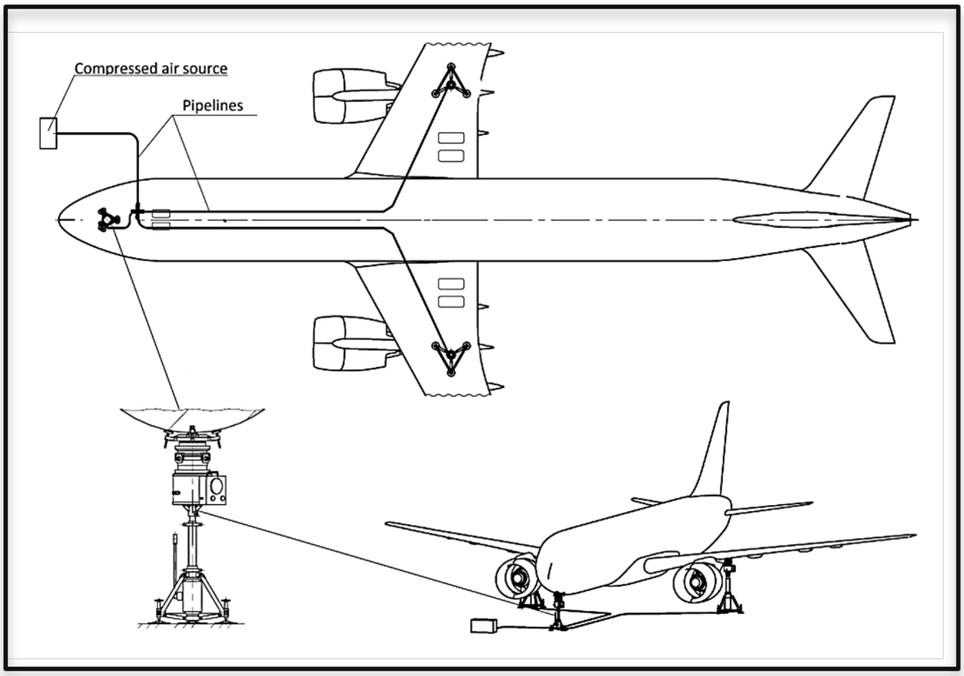

FIGURE 2.34: Pneumatic ground support system used for GVT tests on large aircraft - drawing.

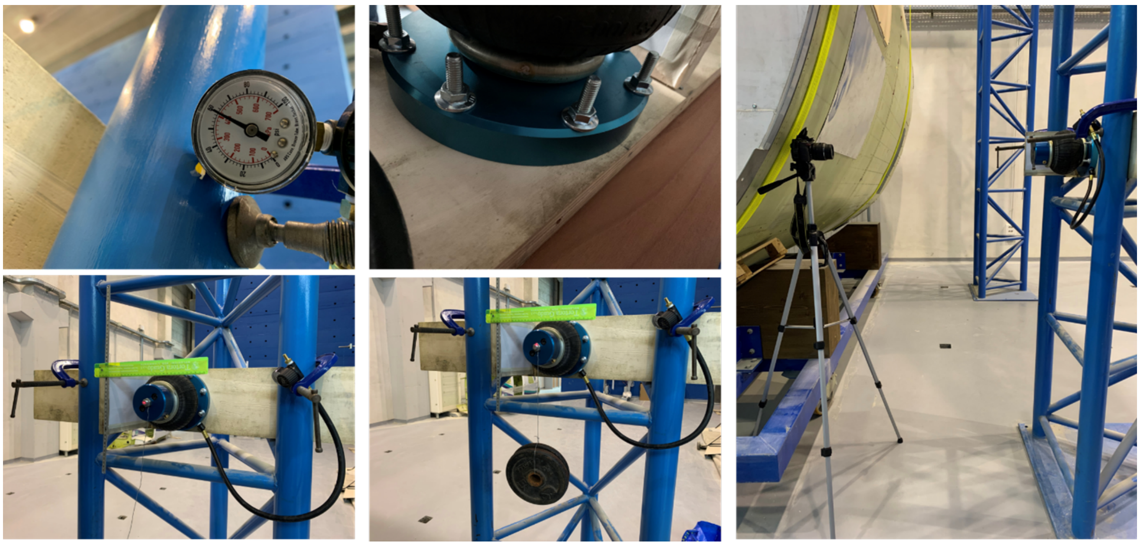

FIGURE 2.35: Experimental test setup to estimate the horizontal stiffness of the air jack.

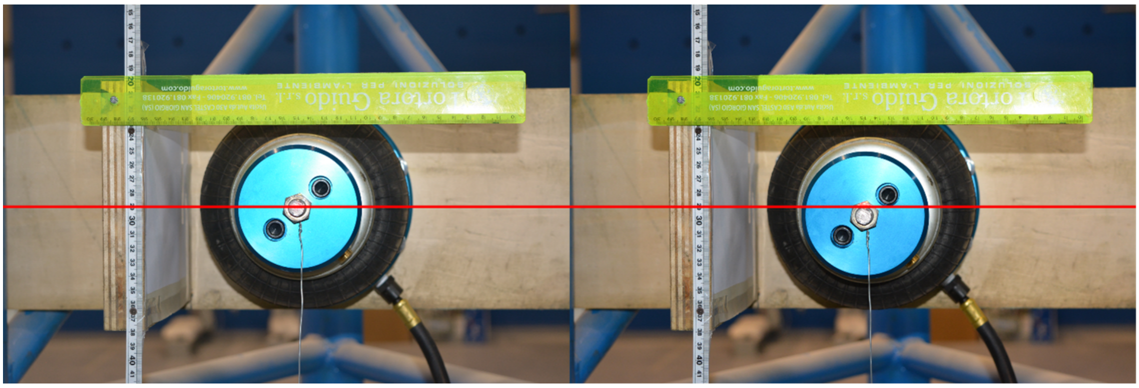

FIGURE 2.36: One of the test cases: 80 psi, 0 kg (left) – 10 kg (right).

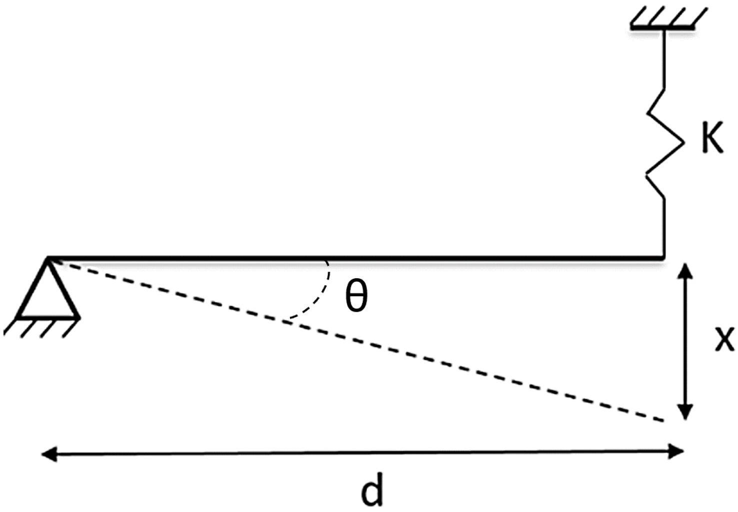

FIGURE 2.37: Spring-movable surface system scheme.

Starting from a hammer test, through the knowledge of the natural frequency (Eq. 2.42) of the test under study and the stiffness K of the calibrated springs used, it is possible to obtain the moment of inertia I of the movable surface model.

$$f = \frac{1}{2\pi}\sqrt{\frac{K_\theta}{I}} \tag{2.42}$$

The moment is given by the following expression:

$$M = K_\theta \theta \tag{2.43}$$

In the hypothesis of small angles, $\theta << 1$ we have:

$$\theta = \frac{x}{d} \tag{2.44}$$

and

$$M = \mathrm{F} \cdot \mathrm{d} = \mathrm{Kx} \cdot \mathrm{d} \tag{2.45}$$

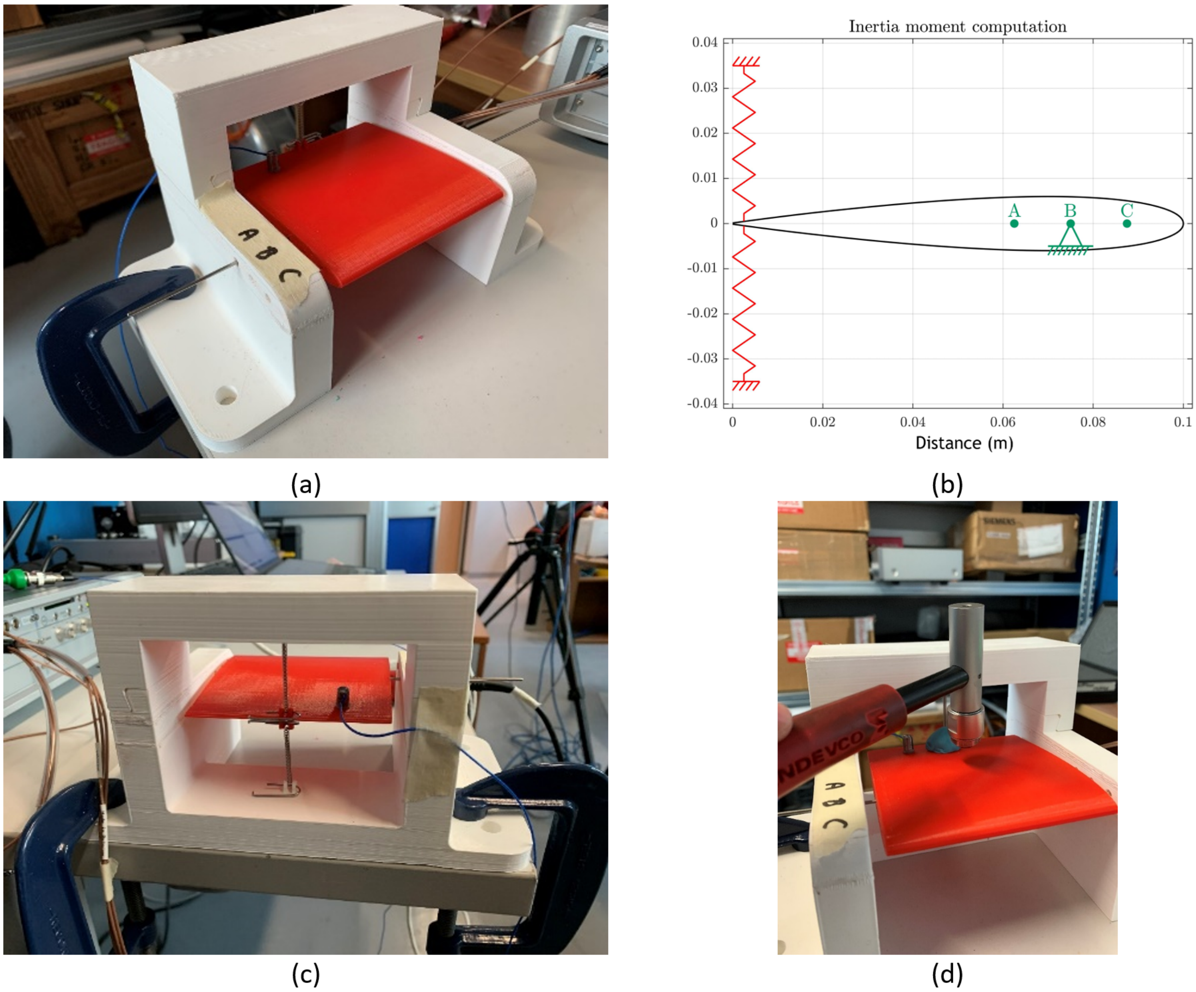

FIGURE 2.38: Device for measuring the moment of inertia of the moving surface and Hammer Impact Test set up

by equating Eqs. 2.43 and 2.45, and by considering the Eq. 2.44, we obtain:

$$\mathrm{Kx} \cdot \mathrm{d} = K_\theta \cdot \theta = K_\theta \cdot \frac{x}{d} \tag{2.46}$$

from which the torsional stiffness K_θ is obtained:

$$K_\theta = \mathrm{K}d^2 \tag{2.47}$$

Finally, from Eq. 2.42, we obtain the moment of inertia I:

$$I = \frac{Kd^2}{4\pi^2 \mathrm{f}^2} \tag{2.48}$$

The test setup is shown in the following figures 2.38
The response of the structure in terms of acceleration has been acquired employing a roving ICP piezotronic accelerometer (PCB 352B10) shown in figure 2.38(c) while

the energy is supplied to the TA through an impulsive excitation provided by the hammer, figure 2.38(d).
The movable surface has three different positions for the hinge axis A, B and C to be able to appreciate the effects due to the axis moving forward or backward. The effect of a plasticine mass simulating the balancing mass was also evaluated. The following tables show the data of the small-scale test setup, in particular in table 2.11 there are the positions of the hinge axis and the distances of the balancing mass from it. Table 2.12 shows the values of the masses of the mobile surface and the balancing mass and the stiffness of the springs. Finally, the results of the modal hammer test in terms of natural frequencies are shown in table 2.13. For these results A, B and C are the measurements relating to the three positions of the hinge axis while the subscript bm indicates that the measurement is performed, with the same position of the hinge axis, with the balancing mass on the movable surface.

TABLE 2.11: Spring-movable surface system, Distance hinge axis-balancing mass

Hinge axis position (m)		Distance hinge axis-balancing mass (m)	
dA	0.06	dPa	0.047
dB	0.0725	dPb	0.0595
dC	0.085	dPc	0.072

TABLE 2.12: Spring-movable surface system, Masses

Mass (kg)	
Movable surface M	0.0425
Balancing mass m	0.0037

TABLE 2.13: Spring-movable surface system, Stiffness

Stiffness N/m	
Spring K	60

TABLE 2.14: Spring-movable surface system, Hammer test natural frequencies

Hammer test natural frequencies (Hz)					
A	A_{bm}	B	B_{bm}	C	C_{bm}
18.74	16.78	18.74	16.78	17.60	15.74

Table 2.15 shows the results obtained. In particular, the first column represents the tests without balancing mass for the three positions of the hinge axes; the second column is the tests with the additional mass; the third column is the differences

between the results of the first two columns; the fourth column is the results theoretical by using the analytical formula and, finally, the fifth column represents the difference between theoretical and experimental results. It can be seen that the order of magnitude is the same and the deviation between the experimental and the expected result is very small.

TABLE 2.15: Spring-movable surface system, Inertial hinge moments

Inertial hinge moment $\left(\mathrm{kg} \cdot \mathrm{m}^2\right)$				
IA	IA_{bm}	ΔI_{Exp}	ΔI_{Th}	ΔI_{Exp-Th}
3.12×10^{-5}	3.89×10^{-5}	0.77×10^{-5}	0.82×10^{-5}	0.5×10^{-6}
IB	IB_{bm}	ΔI_{Exp}	ΔI_{Th}	ΔI_{Exp-Th}
4.56×10^{-5}	5.68×10^{-5}	1.13×10^{-5}	1.31×10^{-5}	0.18×10^{-5}
IC	IC_{bm}	ΔI_{Exp}	ΔI_{Th}	ΔI_{Exp-Th}
7.01×10^{-5}	8.87×10^{-5}	1.86×10^{-5}	1.92×10^{-5}	0.6×10^{-6}

As an example, the procedure of how the results of the first row of the table were obtained is shown. From Eq. 2.47:

$$K_{\theta A} = \mathrm{K}dA^2 = 2 \times 60\frac{N}{m}x(0.06m)^2 = 0.432\mathrm{Nm} \tag{2.49}$$

is obtained:

$$\begin{aligned} f_A &= \frac{1}{2\pi}\sqrt{\frac{K_{\theta A}}{I_A}} = 18.74 \text{ Hz} \\ f_{A_{bm}} &= \frac{1}{2\pi}\sqrt{\frac{K_{\theta A}}{I_{A_{bm}}}} = 16.78 \text{ Hz} \end{aligned} \tag{2.50}$$

Thus, by applying Eq. 2.48, is ontained:

$$\begin{aligned} I_A &= \frac{1}{4\pi^2}\frac{0.432\mathrm{Nm}}{(18.74/\mathrm{s})^2} = 3.12 \times 10^{-5} \text{ kg m}^2 \\ I_{A_{bm}} &= \frac{1}{4\pi^2}\frac{0.432\mathrm{Nm}}{(16.78/\mathrm{s})^2} = 3.89 \times 10^{-5} \text{ kg m}^2 \end{aligned} \tag{2.51}$$

Finally, as regards the differences between tests with balancing mass and without mass and the difference between experimental and theoretical values is:

$$\begin{aligned} \Delta I_{Exp} &= 0.77 \times 10^{-5} \text{ kg m}^2 \\ \Delta I_{Theory} &= m \times dP^2 = 0.82 \times 10^{-5} \text{ kg m}^2 \end{aligned} \tag{2.52}$$

So to conclude, the expected and confirmed results from small-scale tests are:

- By adding the balancing mass the moment of inertia increases.

Moreover, if the initial position of the hinge axis is identified in B, we have that:

- By moving the hinge axis towards the leading edge (position C) the moment of inertia increases as well as the difference ΔI_{Exp} the moment of inertia of the

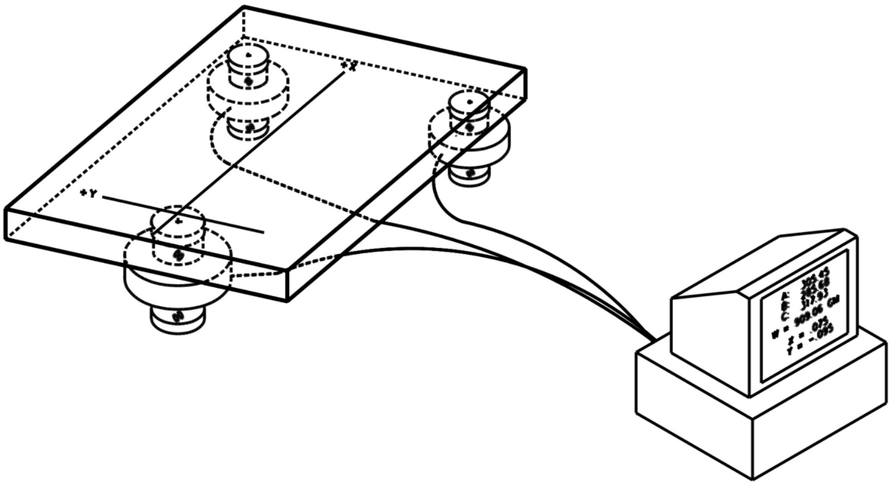

FIGURE 2.39: Multiple Point Weighing CG Machine

movable surface alone and the moment of inertia of the movable surface + the balancing mass (*bm*);

- Conversely, by moving the hinge axis back towards the trailing edge (position A), the moment of inertia decreases as does the difference ΔI_{Exp}.

Center of Gravity

The center of gravity (CG) of a movable surface can be determined by placing scales or load cell platforms under three points and calculating the CG location from the difference in force measurement at these three points as shown in the scheme 2.39. To determine part weight W and CG coordinates X and Y, three force transducers are typically used to support a frame which in turn supports the object [30, 31]. The weight is simply the sum of the force applied to the three transducers. W_T=W_A+W_B+W_C where W_A, W_B, and W_C are force readings on the three force transducers.

To determine CG, it is necessary to calculate the moments of the weight force W_A by means the following formula. Referring to figure 2.40, D and L are the known distance whereas X and Y are the CG coordinates.

$$\begin{aligned}
\Sigma M_X &= (W_B + W_C)L - W_T X = 0 \\
\Sigma M_Y &= \frac{W_C D}{2} - \frac{W_B D}{2} - W_T Y = 0 = \frac{D}{2}(W_C - W_B) - W_T Y \\
X &= \frac{(W_B + W_C)L}{W_T} \\
Y &= \frac{(W_C - W_B)D}{2W_T}
\end{aligned} \tag{2.53}$$

If all the transducers outputs are set to zero when fixturing is in place, the equations above can be used to determine the CG location of the test part. In practice, two measurements are made:

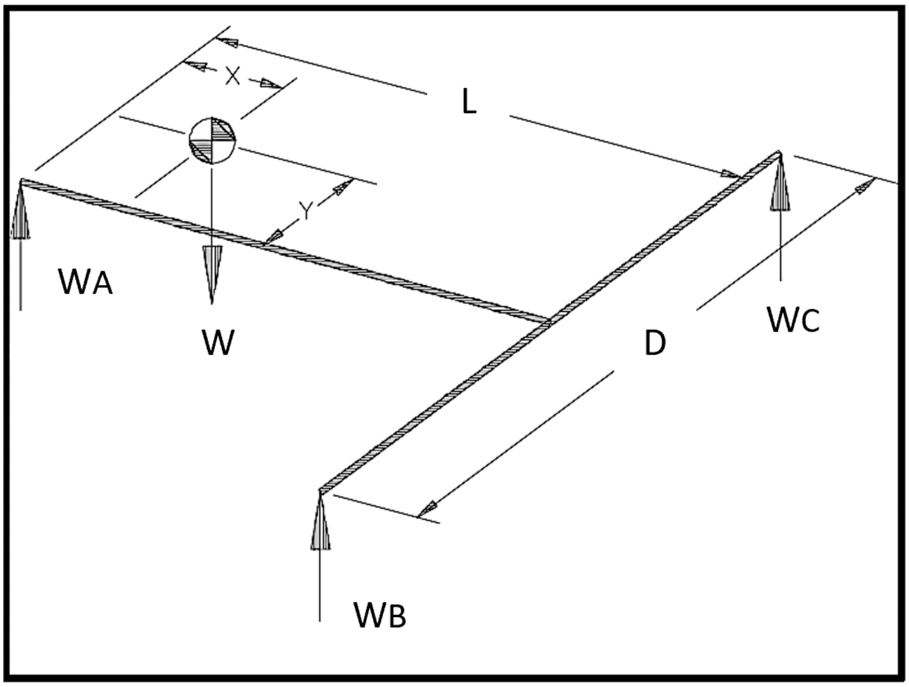

FIGURE 2.40: Measuring weight - distances, forces and coordinates scheme

1. First the tare value are measured, with the fixture in place;
2. then the test object is installed in the fixture, and a seconds set of W_A, W_B, and W_C force readings are made;
3. tare readings are then subtracted from the part measurements to yield the net value of W_A, W_B, and W_C for the test object;
4. the equations 2.53 are then use to calculate the X and Y coordinates of the test object CG. The sum of the net values of W_A, W_B, and W_C is the total weight of the test object.

Once obtained X and Y coordinates, the third CG coordinate Z may be measured by tilting the TA through a know angle as shown in figure 2.41.

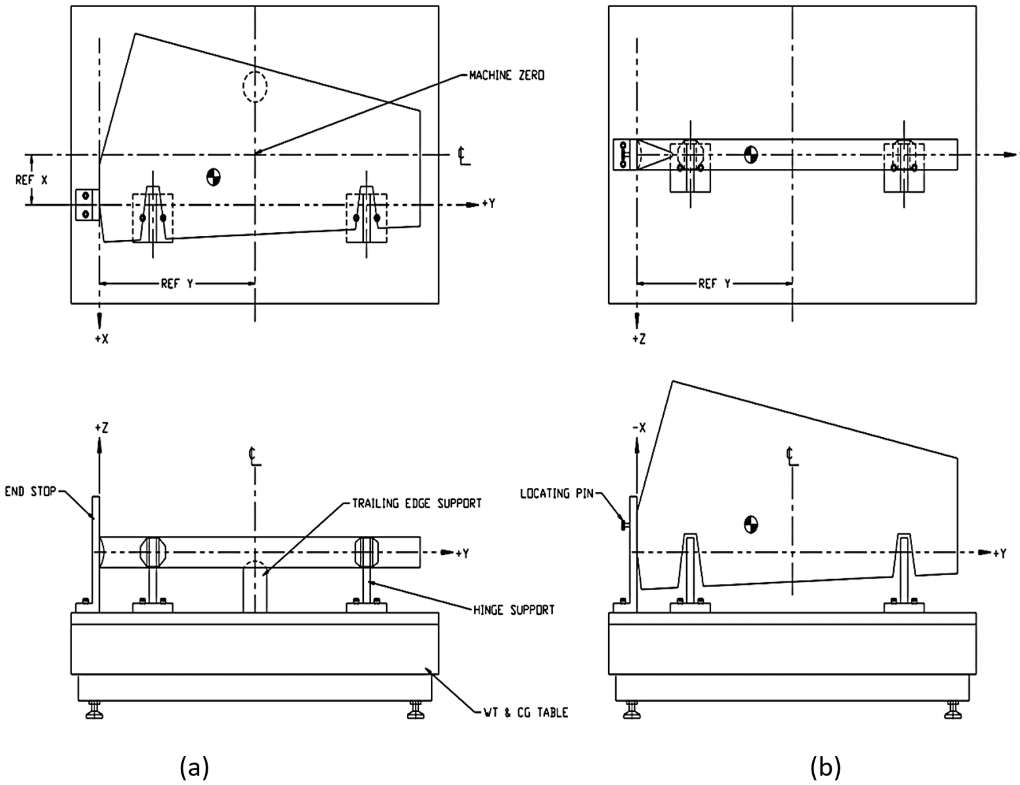

FIGURE 2.41: Measuring CG - X and Y (a). Measuring CG - Y and Z (b).

Chapter 3

Tiltrotor Acoustic Data Acquisition and Analysis

3.1 Introduction

The fluctuating pressures that act on the surfaces of flight vehicles due to propulsion systems and movable surface flows tend to induce oscillatory motions of the fuselage surfaces. These vibrations can induce structural fatigue, result in degradation of equipment performance and produce acoustic noise inside the aircraft. Too high a noise level can have adverse effects on the crew and passengers.
To avoid these problems, it must be taken into account the fluctuating pressures and their potential effects early in the design and development cycle or it is necessary to perform in-flight noise measurement on board of prototype vehicle once it is available.
The recent emphasis on the design and construction of next-generation tiltrotors and unmanned aircraft and the environmentally friendly solution of an electric or hybrid distributed propulsion is leading to a renewed interest in understanding propeller noise. For such vehicles to be working successfully and commercially viable, the interior noise levels must be acceptable to civil passengers.
Noise is the result of propulsion systems, the interaction between high-speed airflow and aircraft surfaces, and internal operation systems [32]. The noise is an important design and operation parameter of every aircraft because the effects of too intense levels can affect the crew and passengers' comfort and pose problems for on-board equipment and communication systems [33, 34].
Structural-acoustic measurements were taken aboard an existing tiltrotor aircraft to better investigate the physical mechanisms that originate the interior noise in the tiltrotor. The flight test measurements include structural accelerations, external and internal noise. The results presented in this chapter mainly focus on the exterior pressure loading on the fuselage [35, 36], the experimental in-flight measurements and analysis and numerical methods [37] and their correlation with the experimental measurements [38]. Both these activities are required as a starting point for studying the transmission mechanism through the fuselage. This transmission is responsible for the vibration and noise level which can be measured inside and for identifying

potential solutions for their mitigation [39].
The Knowledge of external pressure loads in flight is also required to replicate the flight conditions in a laboratory to test different solutions for improving passenger comfort and identify the most promising ones [40].
When considering propeller noise it is important to consider the effect of the installation, as this can have a significant effect on the noise generation process. This installation effect represents the difference between the laboratory environment and the real operational conditions. In a laboratory environment, noise calculation procedures and analyzes generally assume ideal conditions, such as the propeller is operating with perfectly uniform flow. For an operational propeller, the flow field always has some distortion due to wing upwash, aircraft angle of attack, or inflow turbulence. Since this distortion leads to additional noise, it is a factor that must be considered when defining the total noise of an operating propeller.
If a propeller is designed to meet certain noise targets, even with a comfortable margin of error, ignoring the effects of operating conditions can result in a substantial underestimation of system noise, with the strong possibility that the aircraft will not meet the noise requirements.
In this regard, the study of the aeroacoustic loads acting on the fuselage through in-flight noise acquisitions is also of fundamental importance for the design, manufacturing, testing and qualifying of new propellers.
The in-flight measurements have been first carried out on a flying Leonardo Helicopter tiltrotor, undergoing certification for use in the civil sphere.
The scientific literature concerning this flight vehicle is very reduced. An important reference is certainly the analysis of the XV-15 acoustic data performed by the Vehicle Technology Center of the NASA Langley Research Center [41].
For reasons of industrial confidentiality, sensitive data and graphs relating to measurements are masked: the qualitative sense of the analyses is provided rather than the quantitative and precise data.
The sources that induce pressure loads on the external fuselage of the tiltrotor are essential of two types: a rotor noise due to the presence of the large rotors located at the wingtips and the boundary layer noise. The acoustic loads produced by the propeller is mostly affected by the the power produced, forward and rotational tip speeds, number of blades, blade shape and thickness, and distance from the propeller. Propeller engines generate a noise field that is highly tonal in frequency content and highly directional in spatial distribution [42–44]. In high-speed flight, boundary layer noise can be a significant part of the noise perceived in the cabin.
The obtained results are interesting and promising: these measurement procedures could also be addressed to more traditional airplanes and, possibly, to ground vehicles for characterizing different transport systems from the structural-acoustic point of view.

3.2 Characterization of Aeroacoustic Loads

Generally, a noise field is ruled by the Sound Pressure Level (SPL) and the direction. The first quantity indicates the strength of the noise source while the second indicates the path along which the noise spreads.
In a free field, a vibrating sphere radiates sound in all directions whereas in a closed space the noise field is reflected off the walls from different edges. In case the noise strength is equally high all from all directions, the noise field is called diffuse or reverberant. On the assumption of reverberant noise field, the direction of noise is negligible and only the noise strength is important.
In a closed space, the sound consists of that coming directly from the source plus the amount reflected or scattered by the walls and the surrounding objects [45].
Complete characterization of the pressure field on an aircraft fuselage requires a description of both its temporal and its spatial variations. A satisfactory description is very complex due to random variations with space and time. Therefore, some rather limited descriptions of the average properties of the pressure fields of interest are usually employed.
The purpose of this paragraph is to introduce some temporal descriptive parameters of the pressure field as a function of time and frequencies at a point and widely used in the following paragraphs [46].

3.2.1 Autocorrelation function

Obviously, the most intuitive way to represent the variation of pressure at a point is as function of time *p(t)*. The extent to which the function *p(t)* repeats itself in a time interval τ is revealed by the *autocorrelation function* R(τ), defined by

$$R(\tau) = \lim_{T \to \infty} \frac{1}{T} \left[\int_{-\frac{T}{2}}^{\frac{T}{2}} p(t)p(t+\tau)dt \right] \tag{3.1}$$

and this function provides a simple and meaningful representation of the pressure variation. For $\tau = 0$ the autocorrelation represents the time-average value of the square of the pressure.

3.2.2 Power Spectral Density and Sound Pressure Level

A much more widespread and useful representation of the pressure distribution than that in terms of time periods is that in terms of its frequency components. This can be obtained by means the Fourier integral defined as

$$P(\omega) = \frac{1}{2\pi} \int_{-\infty}^{\infty} p(t)e^{(i\omega t)}dt \tag{3.2}$$

where $\omega = 2\pi f$ is the radian frequency.
For the practical applications of this work, in the Matlab® code it was preferred to

discard the phase information related to the complex function P(ω) and operate with the real function *Spectral Density* defined as:

$$S(\omega) = |P(\omega)|^2 \tag{3.3}$$

For a pressure *p(t)* that is sampled only for a time interval T_0 and that is assumed to vanish outside that time interval, Parseval's theorem indicates that

$$\frac{\pi}{2}\int_{-\infty}^{\infty} S(\omega)d\omega = \pi\int_{-\infty}^{\infty} S(\omega)d\omega = T_0\overline{p^2} \tag{3.4}$$

and it is possible to define the mean-square pressure:

$$\overline{p^2} = \frac{1}{T_0}\int_0^{T_0} p^2(t)dt \tag{3.5}$$

The quantity $\pi S(\omega)/T_0$ is interpreted as the contribution to the mean-square pressure at the radian frequency ω. Similarly, one may consider

$$\frac{\pi}{T_0}\int_{\omega_1}^{\omega_2} S(\omega)d\omega = \frac{2\pi^2}{T_0}\int_{f_1}^{f_2} S(f)df = \int_{f_1}^{f_2} s(f)df = p_{\Delta f}^2 \tag{3.6}$$

as representing the contribution to $\overline{p^2}$ made in the frequency interval between ω_1 and ω_2 (or f_1 and f_2).
The function $s(f) = 2\pi^2 S(f)/T_0$ is the *Power Spectral Density* (PSD) of the pressure. The PSD has the dimensions of $(pressure)^2$/Hz and represents the contribution of $\overline{p^2}$ per Hz made at the frequency *f*.
It is noteworthy that the spectral density and the autocorrelation function are a Fourier transform pair:

$$R(\tau) = \frac{2\pi}{T_0}\int_{-\infty}^{\infty} S(\omega)e^{(-i\omega\tau)}d\omega \tag{3.7}$$

3.2.3 Decibel: definition, formula and facts

The concept of decibels is central to noise and vibration analysis. The Bell unit was invented for use in telecommunications (at the Bell Telephone Labs) to make expressions independent of the context, that is, amplitude or power is used. In most fields it is most common to use the deciBell (dB), a tenth of a Bell. Another parameter that describes the acoustic field is the *Sound Pressure Level* (SPL) measured in dB and defined as a relative measure using a power ratio:

$$L_p = 10log\left[\overline{p^2}/p^2{}_{ref}\right] = 20log\left[\overline{p}/p_{ref}\right](dB) \tag{3.8}$$

where p_{ref} represents a reference pressure and p is the effective value of the occurring sound pressure. The standard value of p_{ref} is 2x10^{-5} N/m^2.
Examples of SPLs are given in Table 3.1.

TABLE 3.1: Examples of Sound Pressure Levels.

Examples	SPL (dB)
Near jet engine (at 3 m)	140
Threshold of pain	130
Rock concert	120
Accelerating motorcycle (at 5 m)	110
Pneumatic hammer (at 2 m)	100
Noisy factory	90
Vacuum cleaner	80
Busy traffic	70

3.2.4 Octave band, centre frequency and relative bandwidth

In Acoustics it is common practice to present data in terms of the SPL in contiguous standard octave or one-third octave bands. The corresponding plot of the SPL versus the band center frequency is called SPL spectrum.
As regards the octave bands, for a constant relative bandwidth, the ratio between two consecutive frequencies is defined as:

$$f_x/f_{ref} = 2^x \tag{3.9}$$

Distinguishing the two cases in which:

- $x = 1$, *octave band* and $f_x/f_{ref} = 2^1$
- $x = 1/3$, *one-third octave band* and $f_x/f_{ref} = 2^{1/3} = 1.260$.

Once the octave bands have been defined, it remains to introduce the central frequency and the relative bandwidth. The centre frequency f_{cent} is defined as:

$$f_{cent} = \sqrt{f_{min} f_{max}} \tag{3.10}$$

and represents the geometric mean of the minimum frequency f_{min} and the maximum frequency f_{max} in the relative frequency band. The centre frequency depends on the octave band adopted.
Table 3.2 shows the centre frequencies octave and one-octave frequency bands.
Finally, the bandwidth Δf is the difference between the maximum frequency f_{max} and the minimum frequency f_{min} and is defined by:

$$\Delta f = f_{max} - f_{min} \tag{3.11}$$

Considering the ratio between extreme frequencies within the band $f_{max}/f_{min} = 2^x$, it is effortless to derive the expression for the bandwidth in terms of the centre frequency:

$$\Delta f = (2^{x/2} - 2^{-x/2}) f_{cent} \tag{3.12}$$

TABLE 3.2: Centre frequencies octave and one-octave frequency bands.

Octave frequency band (Hz)	One-third octave frequency band (Hz)
	25
31.5	31.5
	40
	50
63	63
	80
	100
125	125
	160
	200
250	250
	315
	400
500	500
	630
	800
1000	1000
	1250
	1600
2000	2000
	2500
	3150
4000	4000
	5000
	6300
8000	8000
	10000

Any proportional frequency band is defined by its centre frequency and by x. The relative bandwidth for the one-octave and one-third octave bands are:

- $x = 1$, $\Delta f = 0.7071 f_{cent}$
- $x = 1/3$, $\Delta f = 0.2316 f_{cent}$

For instance, an octave band with a centre frequency 1000 Hz, the extreme frequencies of the frequency band are $f_{min} = 707$ Hz and $f_{max} = 1414$ Hz respectively and the relative bandwidth is $\Delta f = 707$ Hz.

3.2.5 Overall Sound Pressure Level

For a certain centre frequency with relative bandwidth Δf it is possible to define the power spectral density of effective sound pressure as:

$$W_p(f_{cent}) = p^2/\Delta f \qquad (3.13)$$

$W_p(f_{cent})$ is the PSD of the sound pressure defined in paragraph 3.2.2. Because the SPL is constant in the frequency bandwidth, the pressure is constant in the frequency bandwidth. As consequence, the PSD of the sound pressure is constant too in the frequency bandwidth. The square root of the mean value of the noise strength over the entire frequency band is calculated as:

$$p_{rms} = \sqrt{\int_{f_{lower}}^{f_{upper}} W_p(f)df} \tag{3.14}$$

Equation 3.14 can be simplified using 3.13:

$$p_{rms} = \sqrt{\int_{f_{\text{lower}}}^{f_{\text{upper}}} W_p(f)df} = \sqrt{\sum_k \frac{p_k^2}{\Delta f_k} \Delta f_k} = \sqrt{\sum_k p_k^2} \tag{3.15}$$

The last parameter to be introduced is the *Overall Sound Pressure Level* (OASPL) calculated as follows:

$$OASPL = 10log\left(p_{rms}^2 / {p^2}_{ref}\right) \tag{3.16}$$

3.2.6 Propeller and Rotor Noise Sources

A propeller can be generally described as an open rotor with fixed or adjustable-pitch blades. In general, the blades are designed to provide a region of low pressure on one side and high pressure on the other. The resulting forces induce air from the front and push it back, resulting in thrust. Because propellers impart a relatively small amount of velocity to a large mass of air, their efficiencies are high.

Propellers are used on small general aviation aircraft as well as small to medium-sized passenger airliners. In small general aviation aircraft, propellers operate with a fixed-blade pitch. In larger general aviation and commuter aircraft, they operate with an adjustable pitch to improve aircraft take-off and flight performance [47].

Smaller aircraft have two-blade propellers while larger aircraft have three or more blades.

The spectrum of the propeller noise has both discrete and continuous components. The discrete frequency components are called tones while the continuous ones are called broadband noise.

Although there are many differences in details among various designs and applications, such as number of blades, blade shape, and airfoil section, the noise-generating process is basically the same for all.

Propeller noise can be classified into three categories: harmonic noise, broadband noise, and narrow-band random noise. Harmonic noise is the periodic component, that is, its time signature can be represented by a pulse which repeats at a constant rate. Typically the generated pulse is not a pure sinusoid, so that many harmonics exist. These occur at integer multiples of the fundamental frequency. The first harmonic is the fundamental, the second harmonic occurs at twice the fundamental frequency, and so on [48].

For a single propeller, tones are generated, which are harmonics of the blade passing frequency. The fundamental blade passage (BPF) is the product of the shaft frequency and the blade number [49].

Theoretically, the BPF is a discrete frequency that is related to the number of blades N, and the engine rpm, R, and is given by $f_{BPF} = NR/60$ Hz. Thus, blade passing harmonic tones occur at frequency $f_{BPn} = nNR/60$ Hz, where n is an integer, 1, 2, 3, 4 etc., and represents the number of propeller blades.

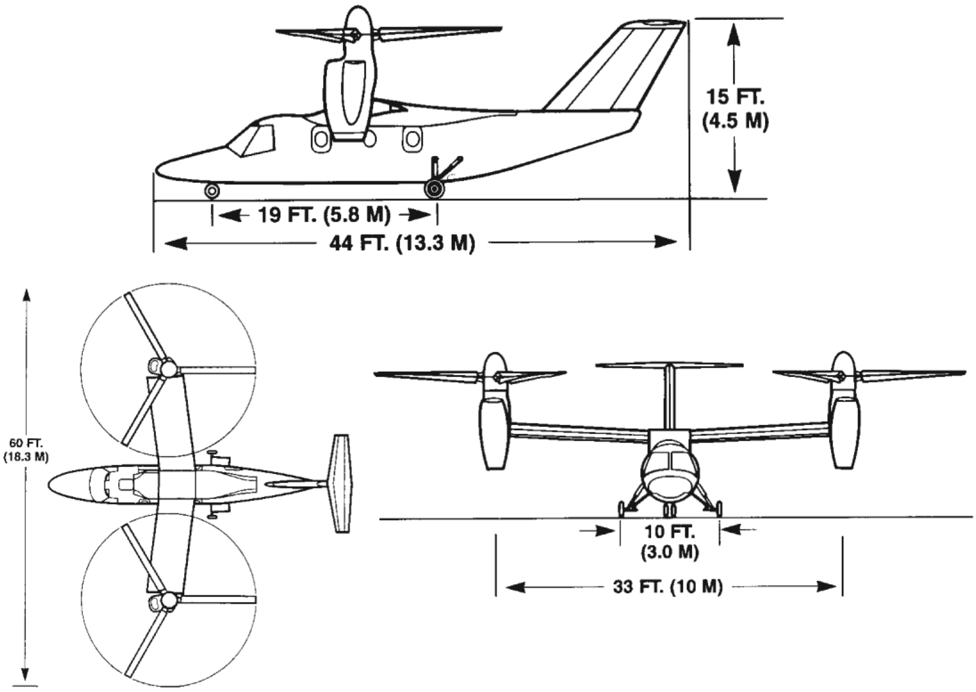

FIGURE 3.1: Sketch of tiltrotor used in in-flight noise studies.

3.3 Flight Test Set-up

Measurement and Analysis of noise is a powerful diagnostic tool in noise reduction for improving the quality of flights and to maximize passengers' comfort on board [50].

The Tiltrotor under test is shown in Figure 3.1. Nominally, this tiltrotor has a takeoff gross weight of 7620 kg and a cruise speed of 90 m/s. This tiltrotor is able to take few seconds to complete the conversation from helicopter mode to airplane mode but, in general, there is no need to rush to complete the conversion since the airspeed and climb rate achieved in airplane and VTOL/conversion mode overlap for some time during a standard departure profile. The maximum altitude at which the tiltrotor can reach VTOL/Conversion mode when moving and hovering is around 8,000 ft according to gross weight whereas the usual and maximum cruising altitude is around 20,000 ft up to a maximum of 25,000 ft.

The interest of the tests was mainly focused on altitude, usual, and cruising speeds for this reason the conversion phase was not taken into consideration for the acquisition of the noise data.

Noise data were acquired at the nine flight conditions indicated in Table 3.3.

The interest of the tests was also to study propeller noise and turbulent boundary layer effects rather than those related to turbine and compressor noise, which should be at higher frequencies.

The graphs in this work refer to lower frequency values. For a light twin-engine aircraft, for example, the cabin noise spectrum typically has an engine tone at around

700 Hz. On the other side, structure-borne noise (SBN) can be a major contributor to the SPL in the cabin of a helicopter. For example, an investigation of the noise sources contributing to the acoustic environment in an eight-seat helicopter showed that SBN from the engine and gearbox dominated cabin sound levels at frequencies above about 3000 Hz. The fundamental tonal component of the compressor and turbine could be appreciated in the cabin sounds level graph but not in the exterior noise because the nature of SBN is linked to this source.

Some components of the interior acoustic field are the result of mechanical forces acting on distant regions of the airframe. The resulting vibrational energy is transmitted through the structure and then radiated into the fuselage interior as noise [42].

The external acoustic measurements and analysis carried out on board the tiltrotor also show that the acoustic radiation from the engine inlet did not generate sufficiently high sound pressure levels to be a dominant source and the broadband SBN has not been identified, probably because of masking by broadband airborne noise.

Generally, when measuring sound pressure, specially developed condenser microphones are used. The principle behind the condenser microphone is that there are two plates, as in a capacitor, across which a DC voltage is applied. One plate works as the microphone diaphragm, and when it experiences air fluctuations, and consequently vibrates, the capacitance between the plates varies, as the distance between the plates varies. This variation in capacitance gives rise to a charge change, which converted to a voltage in the microphone's preamplifier.

As regards the test setup, the exterior spectrum levels were measured applying twelve surface pressure transducers with 13 mm diameter diaphragms and 3 mm height on the fuselage. These special microphones are designed and optimized to reduce wind induced noise during testing [51]. Eleven microphones were installed on the port side of the tiltrotor and one surface microphone (no. 12) was located on the right side to verify the symmetry of the results. A drawing with the dimensions of the microphones is shown in Figure 3.2. The exterior sensors installation scheme is shown in Figure 3.3. Since the pressure loads are much higher near the plane of rotation of the propeller and rapidly decrease both forward and aft, most of the sensors have been installed to form a 'T' as close as possible to the propeller disk when the tiltrotor is in airplane configuration. This arrangement was able to take into consideration both longitudinal and transverse variations in the distribution of acoustic loads. Figure 3.4 shows the surface pressure transducers locations.

The main purpose of the work was the experimental acquisition of external acoustic loads acting on the tiltrotor fuselage to carry on a comparison with the numerical results provided by noise prediction tools. However, during flight tests, in addition to acquisitions of external pressures, structural accelerations and internal pressure levels of the fuselage were acquired. Accelerations were measured on the inside of the skin at six locations far from the shell and vibrating panels and as close as possible to the fuselage frames and stiffeners. Piezoelectric accelerometers with a nominal

TABLE 3.3: Flight Test Conditions.

Flight condition	Speed (kt)	Altitude (ft)	RPM
I	150	20,000	478
II	155	20,000	478
III	160	20,000	478
IV	165	20,000	478
V	170	20,000	478
VI	175	20,000	478
VII	180	20,000	478
VIII	185	20,000	478
IX	190	20,000	478

sensitivity of 10 mV/g were used. Interior pressures at six locations were measured using half-inch condenser microphones of random incidence type with a nominal sensitivity of 50 mV/Pa. 30 sec of data were acquired.

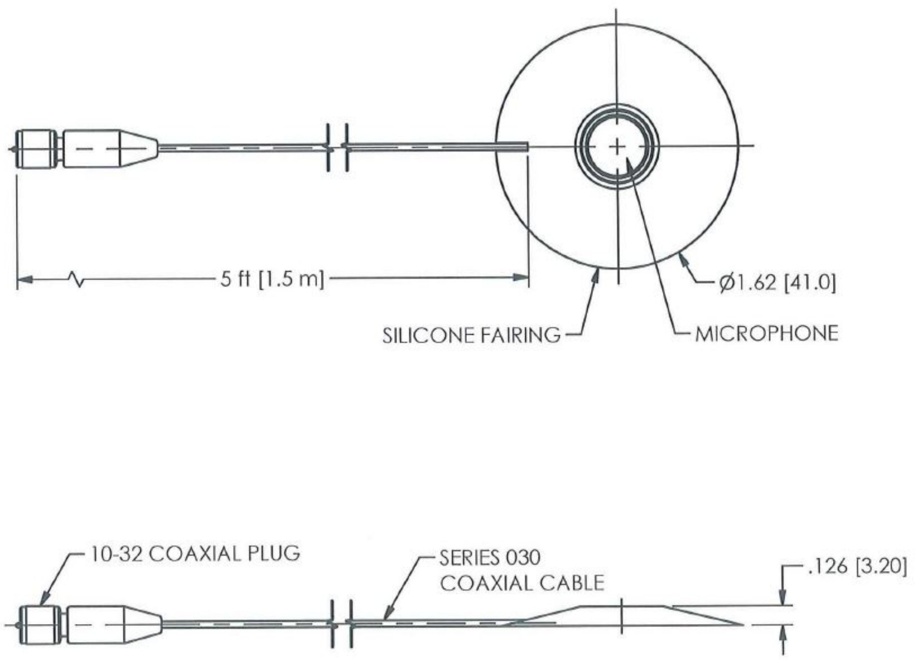

FIGURE 3.2: Surface microphone size.

3.4 Test Results

3.4.1 Time Domain Results

The acquired data were analyzed through DNA: a specially developed Matlab® code able to plot the LMS TestLab Spectral Testing results stored in a .mat file. DNA is

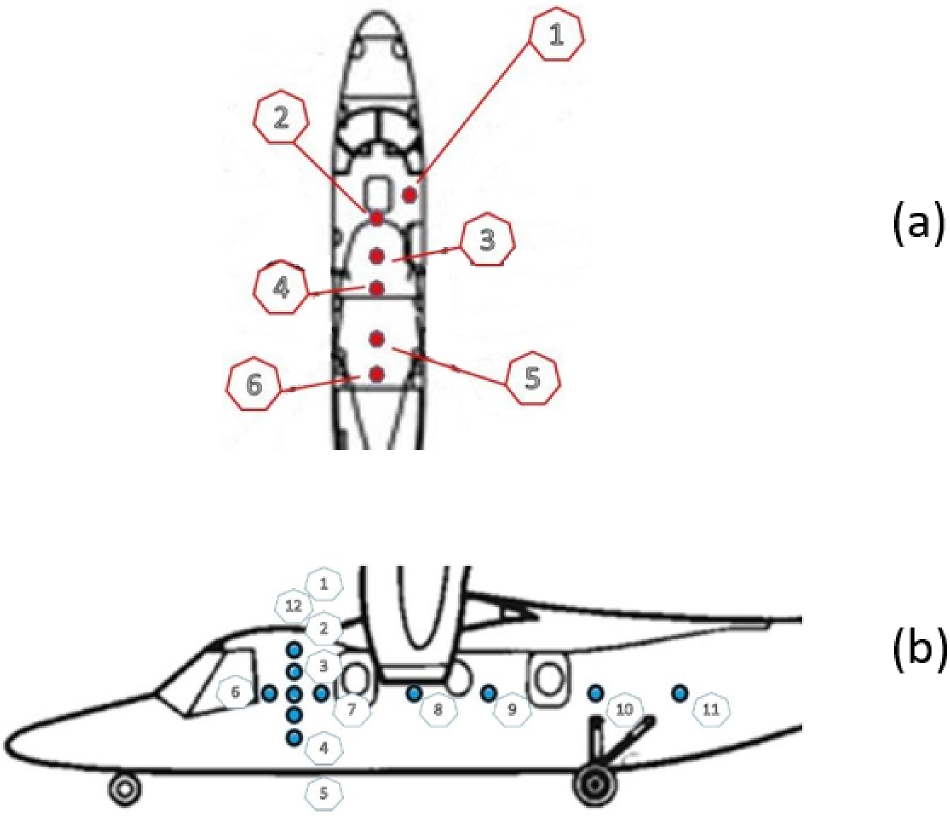

FIGURE 3.3: Layout diagram of the internal (a) and external (b) microphones.

FIGURE 3.4: Photograph of Exterior Sensors Locations.

short for Data Noise Analyzer. This tool was validated using a careful comparison with the results obtained through the commercial software.
During Flight Test the external surface microphone no. 11 did not work correctly. This anomaly could be due to an electrical problem. The plot related to this microphone showed very "wired" peaks, so it was decided to exclude it from the data process. However, the number of sensors adopted was enough to perform an excellent acquisition and analysis of the data and to output some fundamental conclusions about the noise.
The noise distribution pattern can be expected to be broader for larger propeller diameter and greater clearance between the propeller and the fuselage of the Tiltrotor. In addition, the directional characteristics may be affected by operational factors such as flight speed, by interactions with the fuselage flow field, and by interaction with a second propeller in a counter-rotating configuration.
The values and graphs shown in this report are mainly related to flight condition VI. The measured pressure fluctuations and noise levels are quantified from a subjective point of view by means the Overall Sound Pressure Level (OASPL) [35] and [43].
Figure 3.5 shows the OASPL plotted as a function of the flight speeds, with the twelve microphones indicated by different symbols. The OASPL is highest near the plane of rotation of the propeller and decreases rapidly in both forward and aft directions.
As expected the overall level shows a linear trend with the speed. It significantly increases when the flight speed increases.
It is interesting to note for condition IX at high flight speed, due to the increase of the aerodynamic noise, the OASPL of the microphone 11, located downstream of the wing, is comparable with the value relative to the microphone 6, near the cockpit.
Focusing of microphones 1, 3, and 5 it is possible to observe that in the circumferential direction the noise level decreases.
Sample time histories for the surface microphone no. 6 at the different flight speeds are shown in Figure 3.6 in which the time period represents one rotation of the propeller. In each subplot, the thin line represents the instantaneous response whereas the heavy line denotes the time-averaged response. The time-averaged response closely follows the instantaneous response and you can appreciate that the magnitude of the response changes quite whereas the shape of the time history does not vary significantly as a function of the flight speed: the periodic trend linked to the passage of the propeller blades is very clear.

3.4.2 Frequency Domain Results

Figure 3.7 shows the spectral shape for each microphone at the cruise speed of the tiltrotor. In general, the harmonic peaks of the exterior pressures due to the rotating propeller approaches the broadband noise floor between 300 and 400 Hz. By observing the data of the microphones 8, 9 and 10, located under the wing, we note that

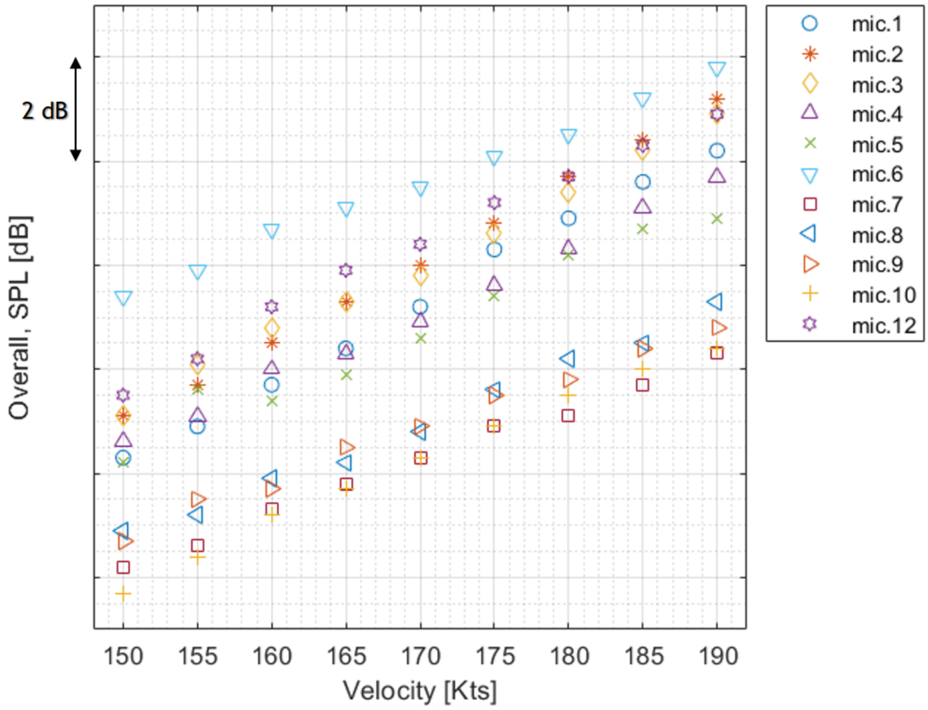

FIGURE 3.5: OASPL at different flight conditions.

only the first three harmonics of the fundamental blade passage frequency (BPF) are greater than the broadband noise. The presence of the wing considerably disrupts the flow and it probably increases the broadband level.

The symmetry condition can be verified from the autospectra plots related to microphones 3 and 12 in Figure 3.8.

Figure 3.9 shows the noise spectra taking into account the external microphones respectively in the longitudinal and transverse directions concerning the fuselage. It is clear that the tone at the first BPF has the highest level and succeeding tones decrease at a rate of about 2 dB per harmonic. BPF falls in the low-frequency range up to around 350 Hz whereas the boundary layer noise is dominant at the higher frequency.

Figure 3.10 illustrates sound spectrum of the external microphone no. 3 in the 1/3 octave band frequency for the whole speed range, with the frequency axis in logarithmic scale. The trend of the signal in 1/3 octave tends to increase the sound levels at the higher frequency and to attenuate them at lower ones, thus better representing human hearing.

The different characteristics of the noise can have important effects on the noise transmitted through the fuselage.

As can be seen from figure 3.13, which shows the exteriors pressure spectra exterior of the mic. 3 for the whole range of speeds, as the flight speed increase there is a significant contribution of broadband noise at higher speeds.

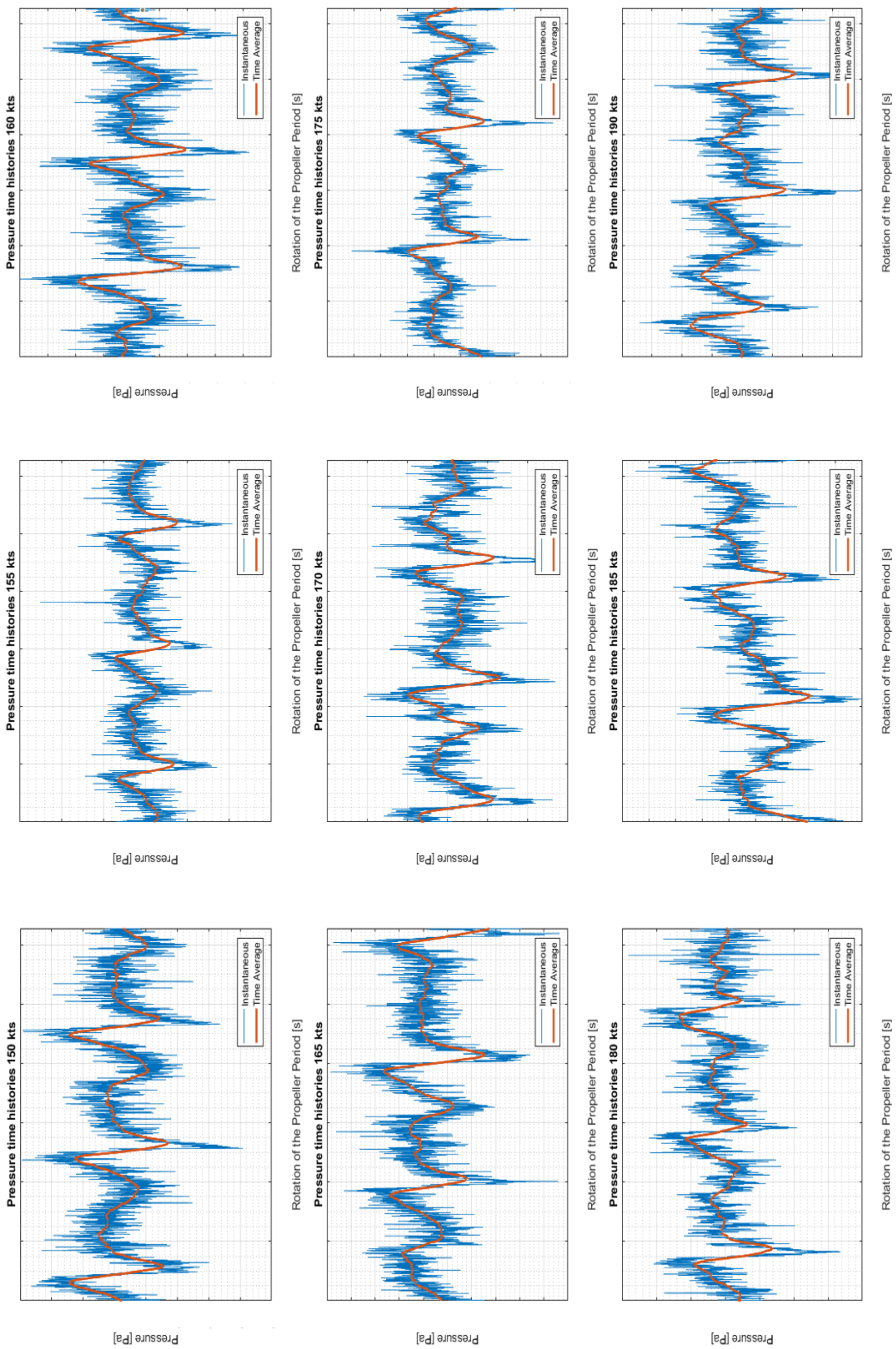

FIGURE 3.6: Acoustic pressures time histories.

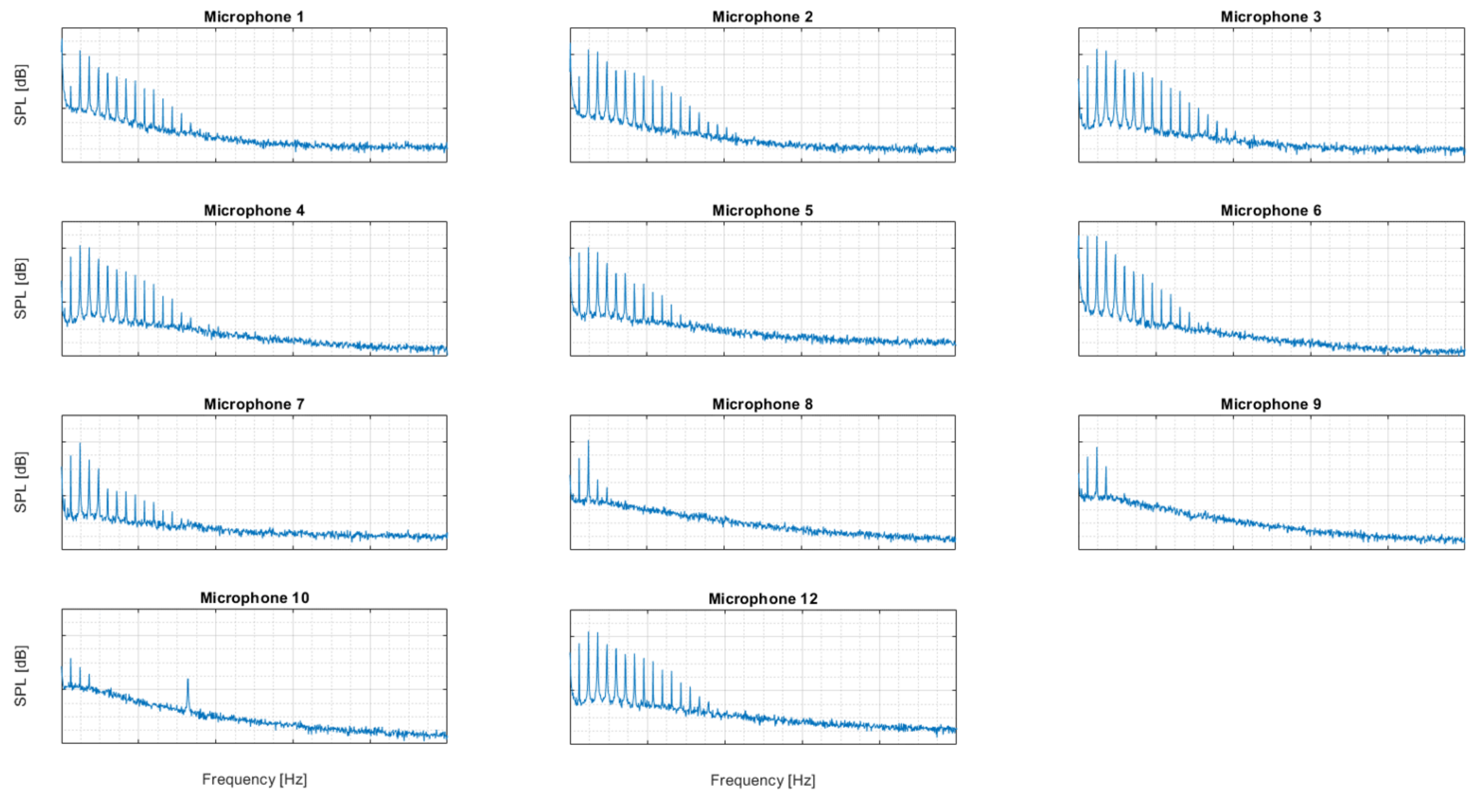

FIGURE 3.7: SPL Spectral shape for each external microphone, 175 kts

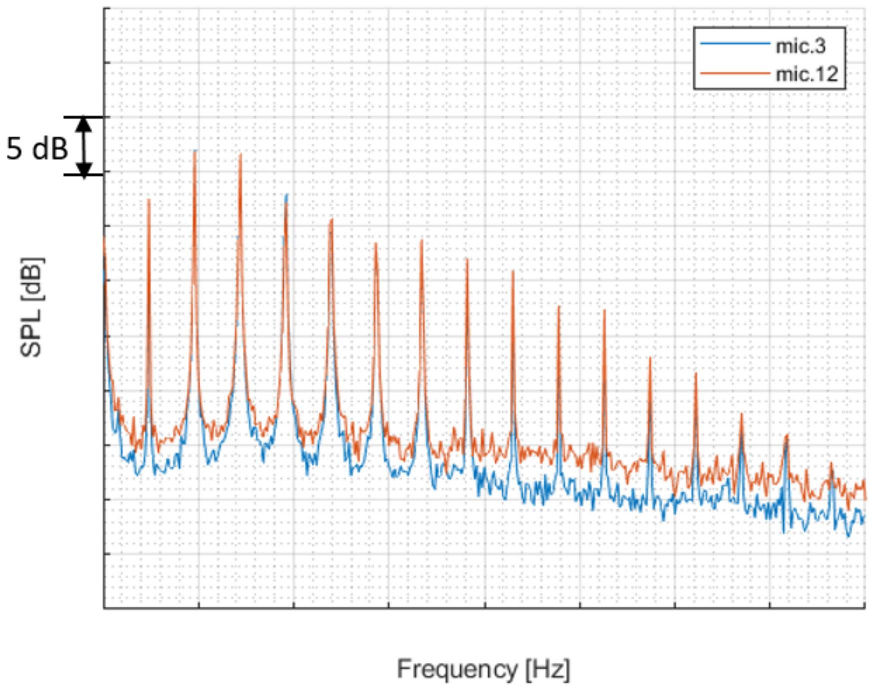

FIGURE 3.8: Noise spectrum-symmetry condition, 175 kts.

The fuselage noise reduction is shown in Figure 3.11 as the difference between the exterior overall SPL on the fuselage surface and the overall SPL transmitted through to the interior, for different flight speeds.
Figure 3.12 shows a comparison of the noise levels acquired simultaneously by the two microphones, respectively external (above) and internal (below), located in the fuselage section near the pilot's head. The levels in the cabin are significantly lower than the levels on the exterior indicating that the sidewall provides substantial noise reduction.
By focusing on the internal noise spectrum, some effects of sidewall transmission characteristics are evident in the measured cabin noise. Both the propeller tones and the boundary layer noise appear in the cabin with the propeller harmonics dominating, as they do in the exterior noise. Moreover, both the propeller tones and the boundary layer noise levels inside the cabin vary irregularly with frequency, in contrast to the smoother variations shown by the exterior noise levels. This frequency-dependent behavior is probably associated with fuselage shell, panel modal activity, and various experimental instruments on board the tiltrotor under test. Figures 3.14, 3.15 and 3.16 refer to the analysis of the signal in the frequency domain and in particular to the use of Power Spectral Density (PSD). This type of function allows the evaluation of the distribution of power in the acoustic signal to frequency by identifying and quantifying oscillatory components.
The graph 3.14 shows the shape of the signal obtained by applying Welch's Method. By applying this method and by overlapping the signal it is possible to reduce the

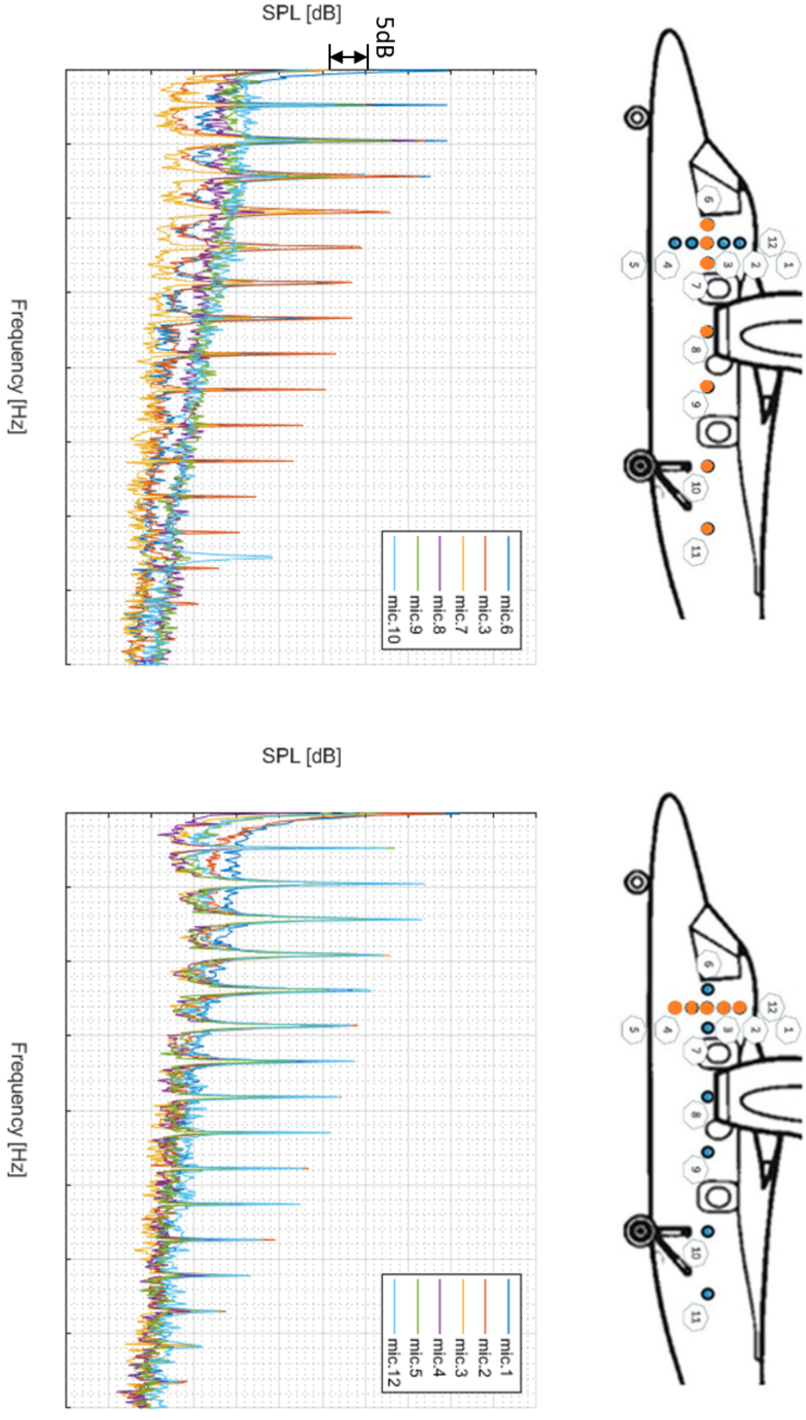

FIGURE 3.9: Noise spectrum-longitudinal and circumferential noise distributions, 175 kts.

FIGURE 3.10: SPL 1/3 octave band frequency, mic.3.

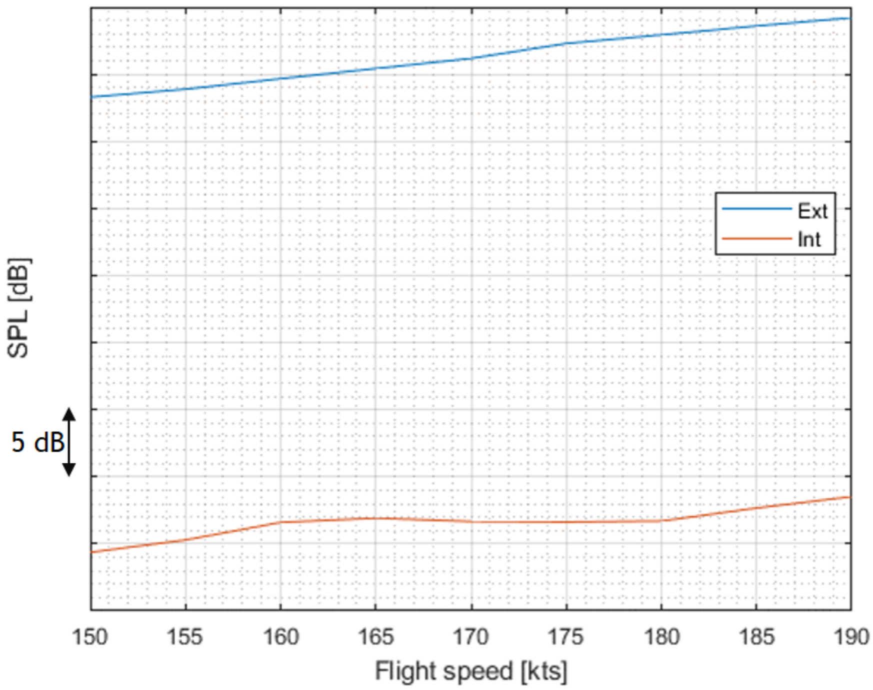

FIGURE 3.11: OASPL for increasing flight speed. Comparison between external mic. 1 and internal mic. 1

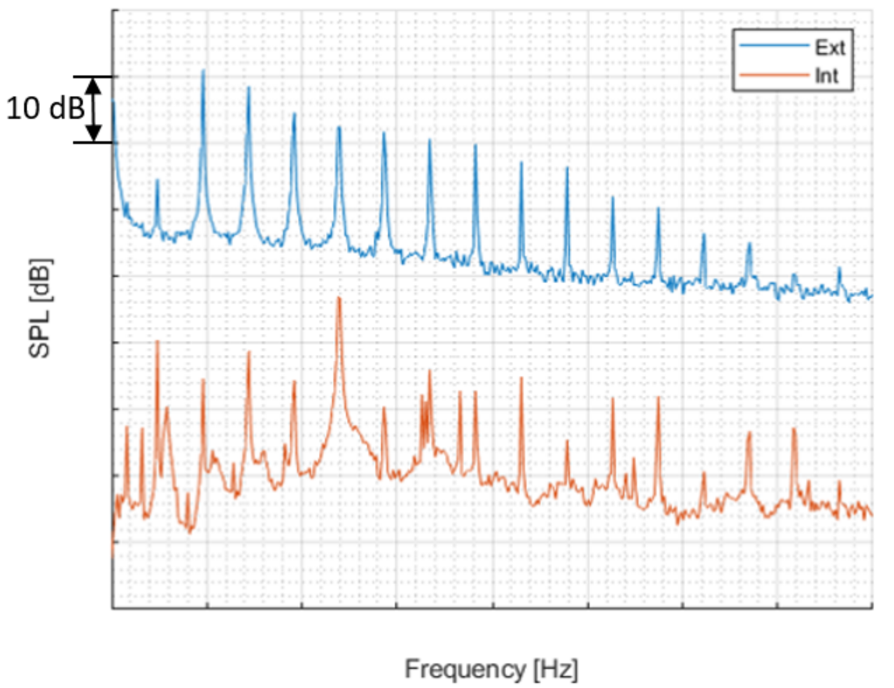

FIGURE 3.12: Noise Spectrum - Comparison between external mic. 1 and internal mic. 1, 175 kts.

spectral variance of the measurements. The time interval of the measure or a subinterval of interest is divided into k equal-length sections to which a window is applied. Then the Fast Frequency Transform (FFT) of each section is computed and an array of k signal segments in the frequency domain is obtained. Finally, by dividing by k and applying an appropriate scale factor, an improved estimate of the PSD is obtained (thicker line in the Figure 3.14). Obviously, as the number of averages (or sections, k) increases, the spectral variance decreases, at the expense of diminished frequency resolution.
With reference to Figure 3.16, it represents the PSD in terms of the cumulative distribution of the root mean square (RMS) plotted as a function of the frequency.

This graph quantifies the contributions of spectral components at and below a given frequency to the overall RMS pressure level for the time frame of interest. In other terms it highlights, how different portions of the noise spectrum contribute to the overall RMS noise level, quantitatively:

- steep slopes indicate relatively strong narrowband disturbance;
- shallow slopes indicate relatively quiet, broadband portions of the spectrum.

The first eight peaks of the figure on the left are representative of the contributions provided by the various tones due to the passage of the propeller blades. The magnitude of each step decreases with increasing frequency and, no longer providing appreciable contributions, the curve flattens starting from 350 Hz. The figure on the right is related to microphone 10 located in the fuselage section downstream of the wing where the tonal components of the noise are covered by the contribution of the Turbulent Boundary Layer (TBL) [40].
Boundary layers develop as a consequence of the effect of the viscosity. The structure of a TBL and thus the pressure it exerts on a surface to which it is attached depends not only on the Reynolds and Mach numbers, but also on the surface roughness, the pressure gradient, and the velocity field outside of the boundary layer.

The noise recordings were finally analyzed in the time-frequency domain. Other common ways to plot BPFs maps are the waterfall and color map plots. The waterfall is a three-dimensional diagrams with frequency on the x-axis, time on the y-axis and amplitude on the z-axis. The same representation can be reported in the two-dimensional plane through a color map.
As an illustrative example, a 30-seconds segment is taken from the noise recording of microphone 6 in cruise speed condition. Its time-frequency spectrogram is presented in the 2D and 3D view Figure 3.17 and 3.18. As expected, two major sound components can be recognized: a number of tonal components (from the propeller) and a broadband noise component (from airframe noise,...).
A series of spectrograms are shown in Figure 3.19 for different microphones and different flight speeds.

3.5 Statistics and Confidence Intervals

Noise and vibrations are often produced by sources with random behavior, for example by turbulence around the wing. In data quality assessment many statistical properties can be used to assess the quality of a set of acquired data.
In practice, it is not possible to estimate the probability distribution and density functions from real measurement signals but it is nevertheless possible to estimate the signal amplitude histogram. This graph consists of a discrete number of values, where each value is the number of samples of the signal in a certain amplitude range, for instance, the range between the minimum and maximum amplitude values of the signal. This amplitude range is then divided into several uniformly spaced intervals. Finally, we produce the histogram by counting the number of samples in the data that fall within each bin.
Figure 3.20 shows a distribution of the number of samples of the measurements and the SPL values in dB. The figure can be interpreted as a quality indicator about the number of samples acquired: histograms become smoother and more continuous when they are made from an increasing number of samples. In the limit when the number of samples is infinite, the resulting curve is a probability density function. The data acquired during the whole acquisition time, referring to a time equal to the propeller rotation period (0.126 sec.), are shown in Figure 3.21. This plot shows that with increasing speed there is a greater dispersion of the measurement: the data are less focused. Confidence intervals are an approach to impart a range of values that contains the test outcome with a degree of certainty given by the confidence level. The confidence level clearly defines the range of probable values and the risk of an incorrect conclusion. The general expression of confidence intervals is:

$$IC = Estimate \pm MoE$$

where MoE is the Margin of Error.

3.5.1 Time Domain

Figures 3.22 - 3.27 show the confidence intervals of microphones 6 and 10 for the three different flight conditions I, V, IX. The blue lines represent an estimated range of values which with a probability of 95% will include the average value of the measurements (red line) while the green lines are relative to a probability of 99%.
A higher confidence level will tend to widen the confidence level given a fixed sample size, as can be seen through the figures. The estimated range was calculated from a series of around 2500 sample data. The data refers to a time equal to the Propeller Rotation Period.
Figures 3.22 - 3.24 refer to the data recorded by external microphones 6 while figure 3.25 - 3.27 refer to mic. 10. It is clear that the signal has a tonal trend near the tiltrotor rotor disk whereas it has a random trend downstream of the wing due to the TBL

effect.
Finally, as expected, there is an increase in data dispersion with increasing speed. This trend is much more evident from figure 3.28 in which the exact values of the measurements, the average, and the confidence intervals are reported together and referring to the propeller rotation period.

3.5.2 Frequency Domain

This paragraph is focused on the spectra with the intervals of confidence. A first comparison was made to determine which probability distribution to choose. The results are shown in figure 3.29 and reported in table 4. Whereas the distinction between T-statistic and Normal statistics may not appear very great at first, relatively modest samples sizes could make a substantial difference at the 95% or 99% level. You must use the T-distribution table when working problems when the sample size is small (n<25). (**GUM**: **G**uide to the Expression of **U**ncertainty in **M**easurement - UNI CEI ENV 13005). On the basis of the comparison, it was decided to operate with the T-distribution.
The flight conditions II, IV, VI and IX were chosen to perform the analysis on the confidence intervals. The data were organized in a *MxN* matrix, where:

- $M = f_i, i = 0, 1, 2, ..., N = 10240\ Hz$ are the Frequencies rows;
- N =Δt are the Time intervals columns.

The figures below show some of the results obtained. The frequencies of the first ten BPFs were considered. It is possible to summarize some aspects of fundamental importance:

- At the BPF frequencies, the confidence intervals are narrower than the other frequencies.
- With the same flight condition, the measurement uncertainty increases moving longitudinally from the microphones near the rotor disk towards the tail of the tiltrotor.
- With the same microphone and flight condition, the measurement uncertainty increases for the harmonics following the first one.

3.6 Further Analyses

The Figure 3.30 shows a direct correlation between acoustic loads and vibrations recorded inside the fuselage. The blue curves indicate the acceleration levels while the orange curves represent the acoustic loads. Both curves are shown on the same scale.
The vibroacoustic data were acquired by sensors that are located in approximately

TABLE 3.4: T-Student and Normal distribution values. 150 kts, Mic. 1

BPFs	**AVG** (dB)	**T** **(α = 0.05)**	**N** **(α = 0.05)**	**T** **(α = 0.01)**	**N** **(α = 0.01)**
I	—	1.19	1.65	1.59	1.51
II	—	0.13	0.17	0.17	0.17
III	—	0.23	0.32	0.31	0.29

the same position, respectively inside and outside the fuselage. It is possible to appreciate how, even for accelerations, at low frequencies, the trend is highly tonal. It is possible to distinguish along the fuselage some areas in which the acoustics are strong and at low frequencies, which aspects the acceleration levels. At higher frequencies, where the contribution of the TBL begins to become predominant to the detriment of the excitation of the propeller, there is a response of the accelerometers which is of a structural type. This behavior is all the more evident in correspondence with the surface microphones 7 and 9: near the wing, there are peaks in the accelerations which represent structural modes.

When the fuselage is subject to acoustic loads excitation, the vibration characteristics and noise radiation characteristics show certain correlation with each other.

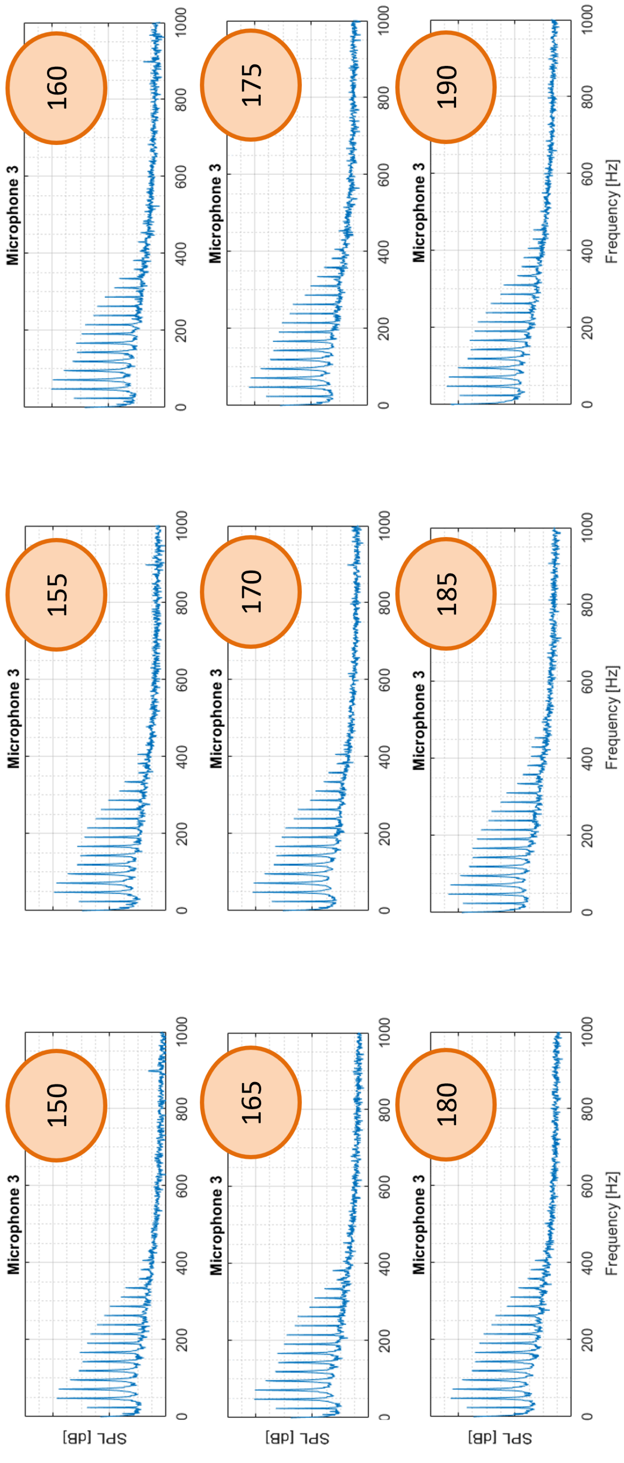

FIGURE 3.13: SPL Spectral shape for each flight speed, mic. 3.

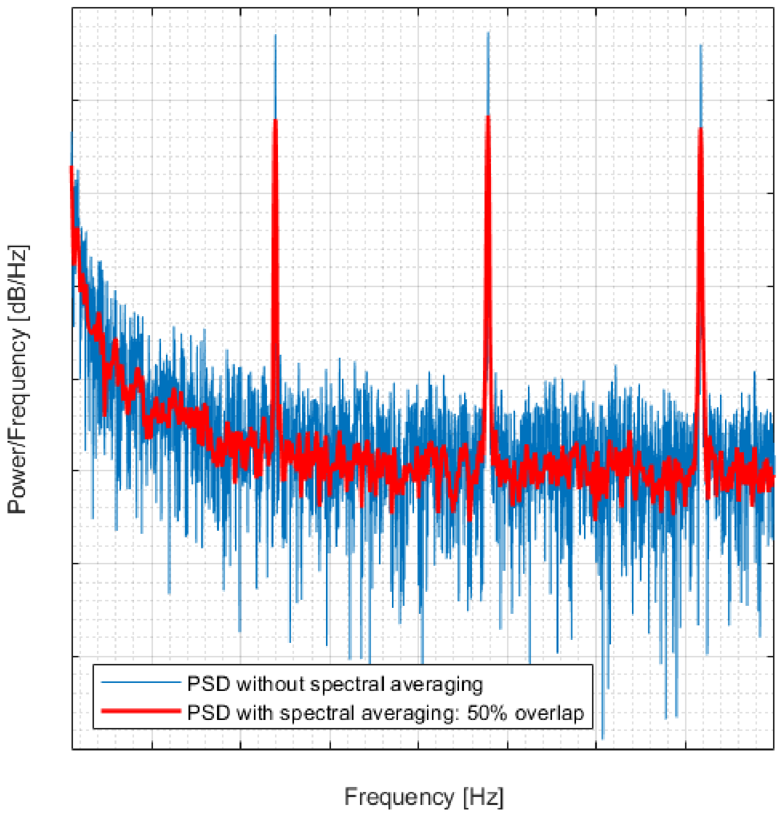

FIGURE 3.14: Power Spectral Density, mic.6, 175 kts.

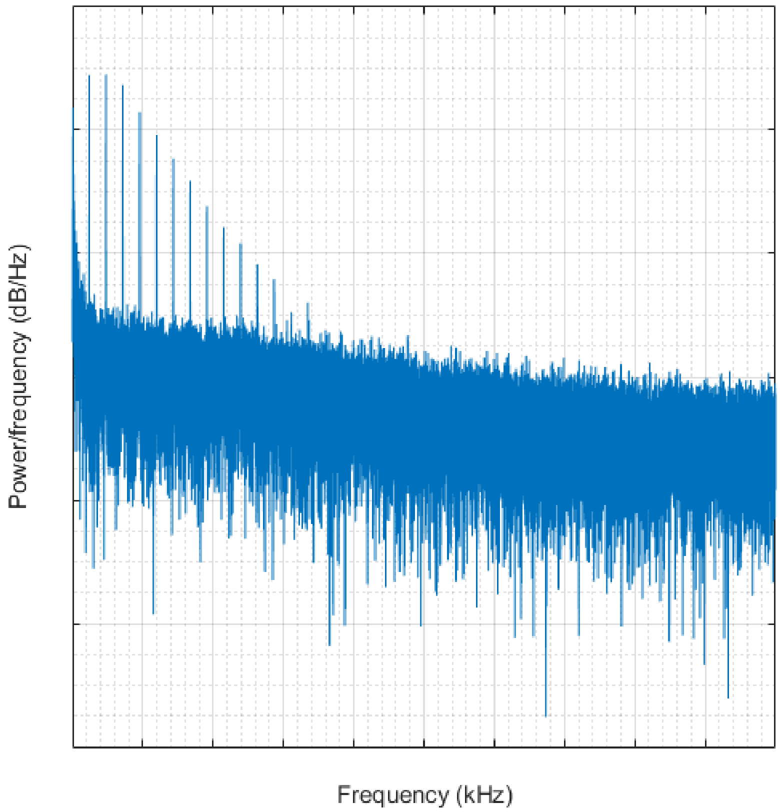

FIGURE 3.15: PSD Welch's (periodogram) Method.

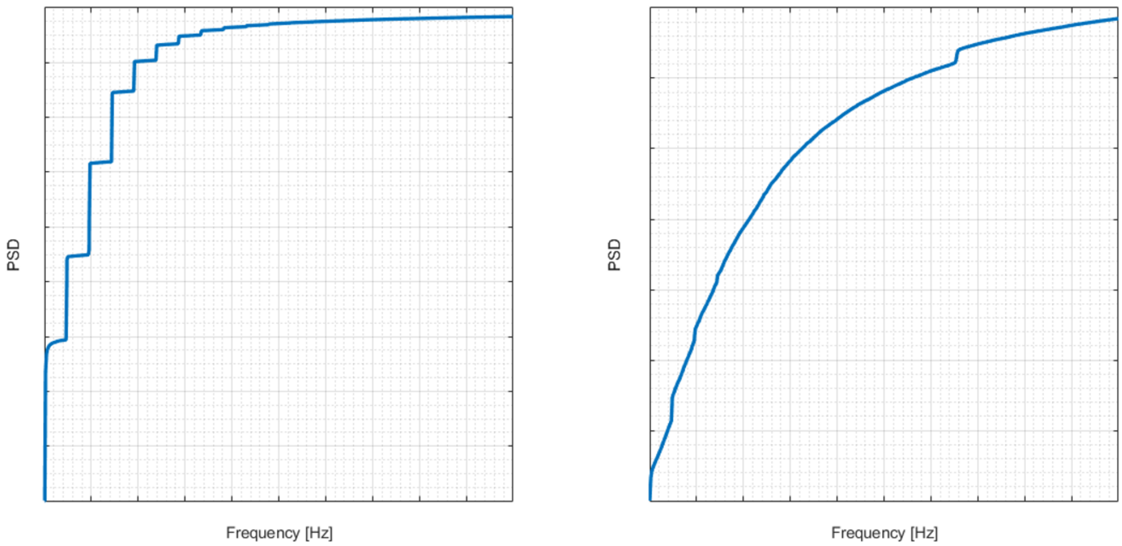

FIGURE 3.16: Cumulative Distribution Root Mean Square vs frequency, mic.6 (left) and mic.10 (right), 175 kts.

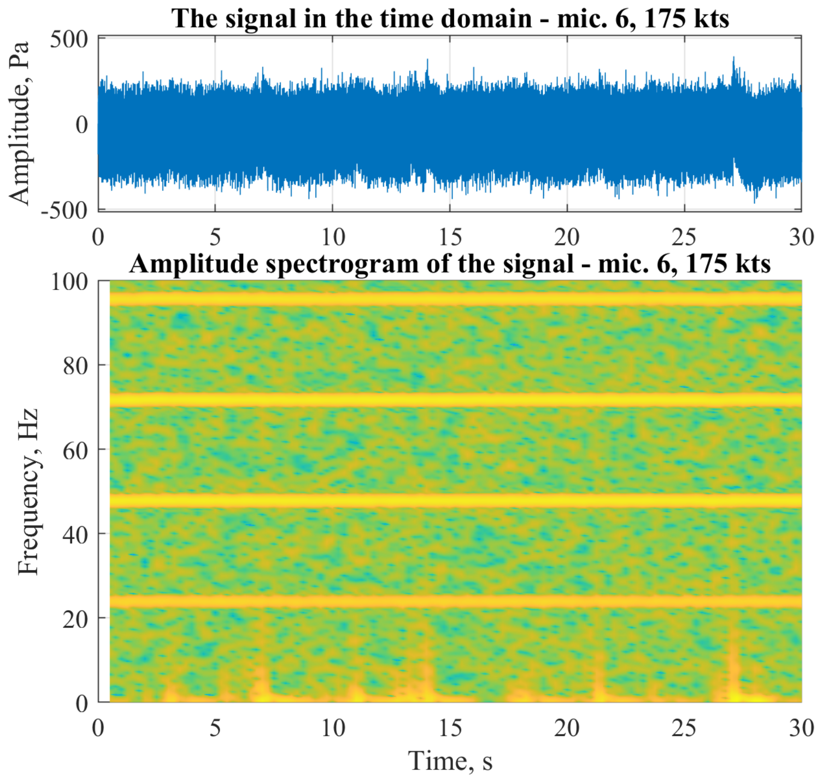

FIGURE 3.17: Signal track in the time domain (top) and 2D Spectrogram (bottom), mic.6, 175 kts

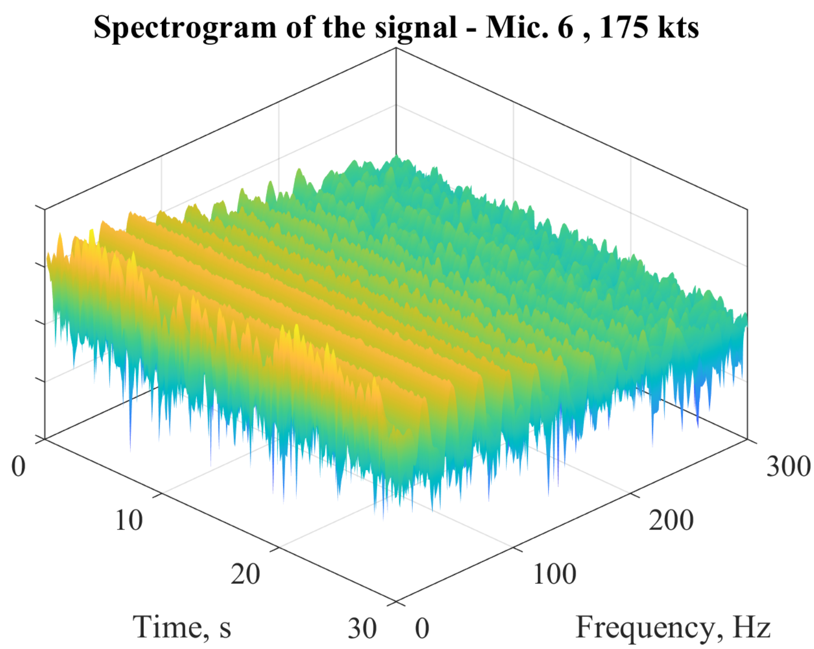

FIGURE 3.18: 3D Spectrogram, mic.6, 175 kts

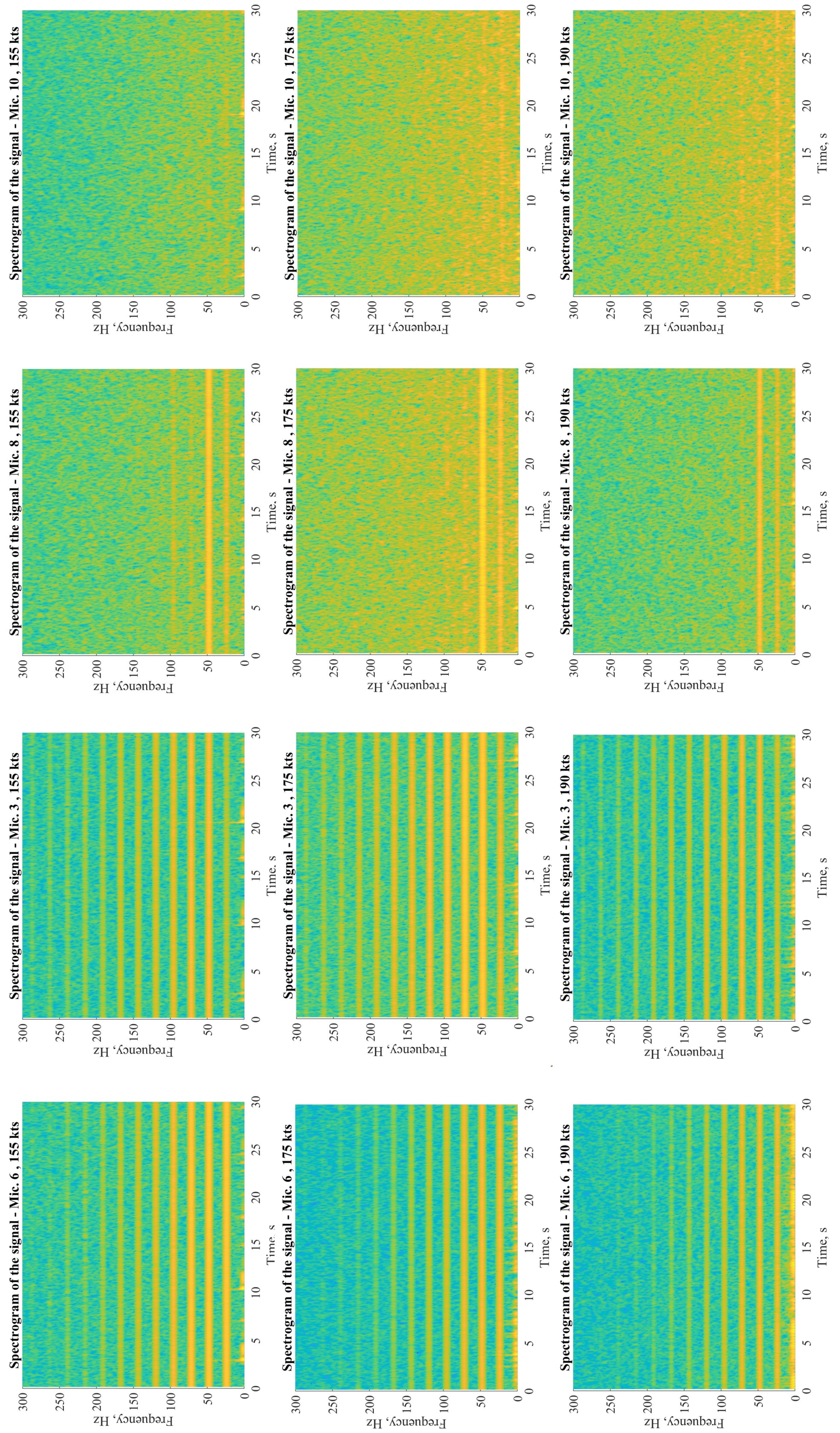

FIGURE 3.19: Spectrograms of the signal for different mics and flight speeds

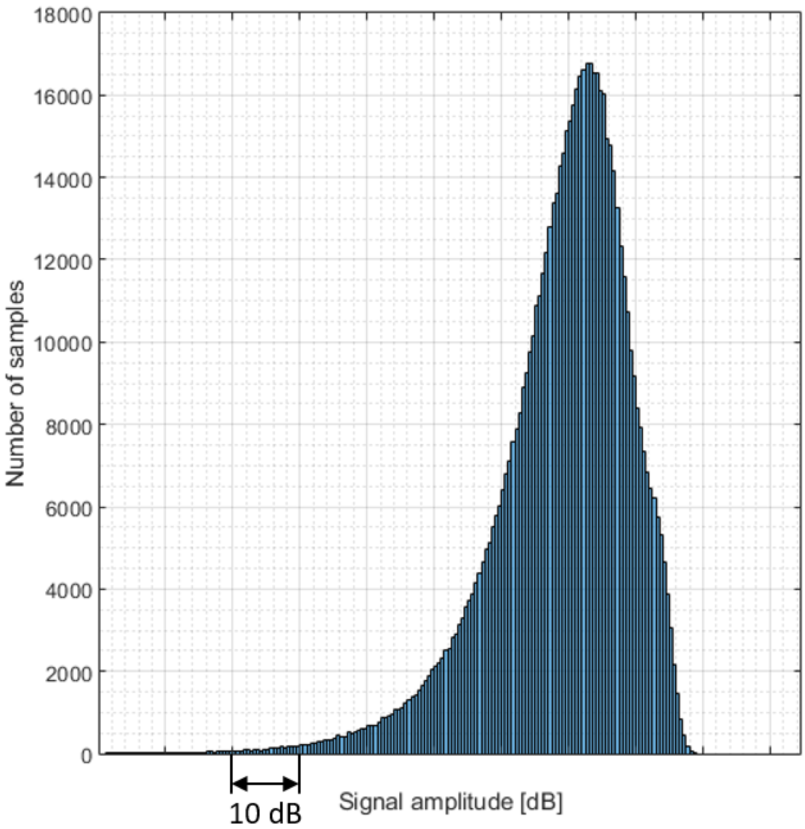

FIGURE 3.20: Probability distribution of the signal.

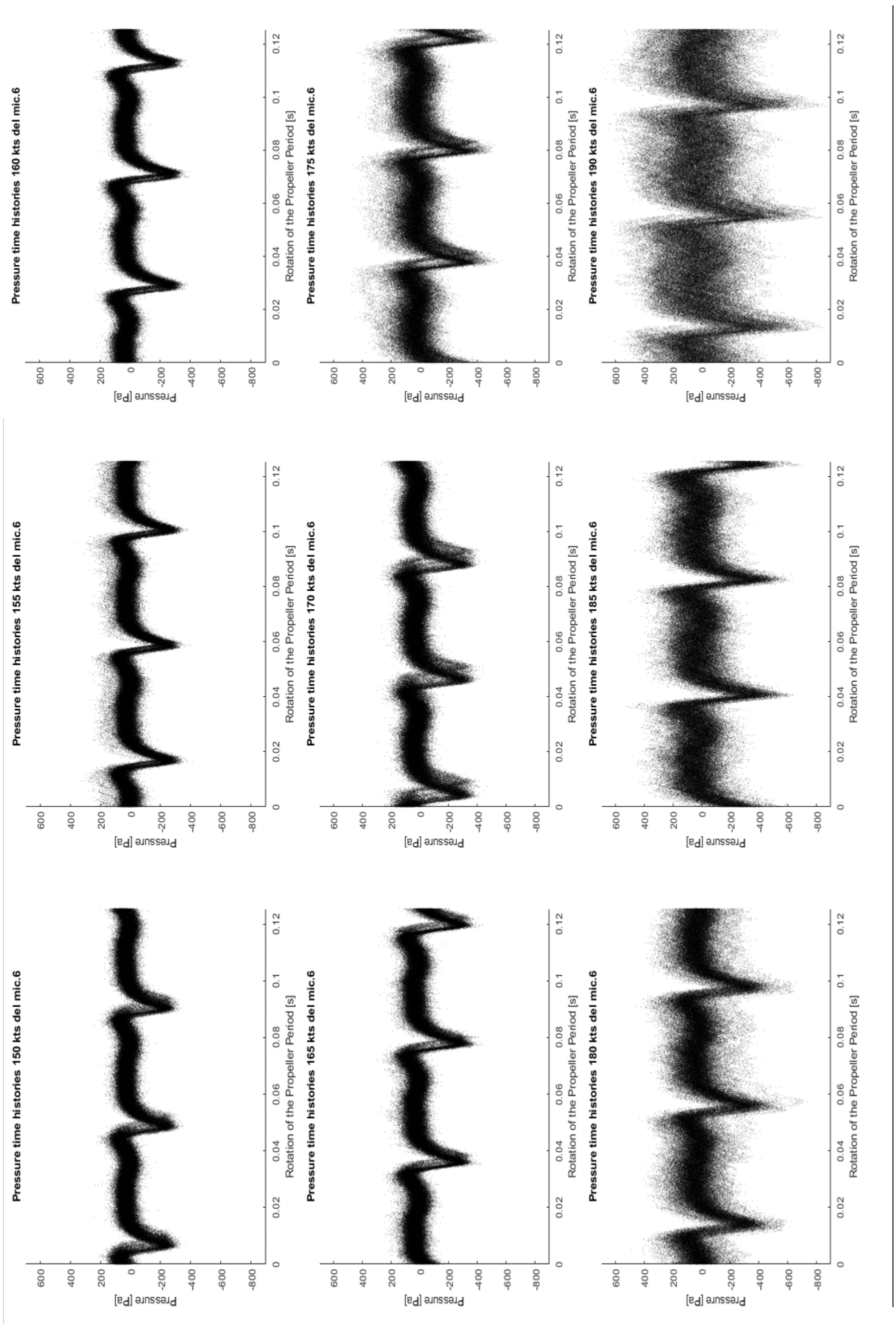

FIGURE 3.21: Pressure time history refer to propeller rotation period, mic. 6.

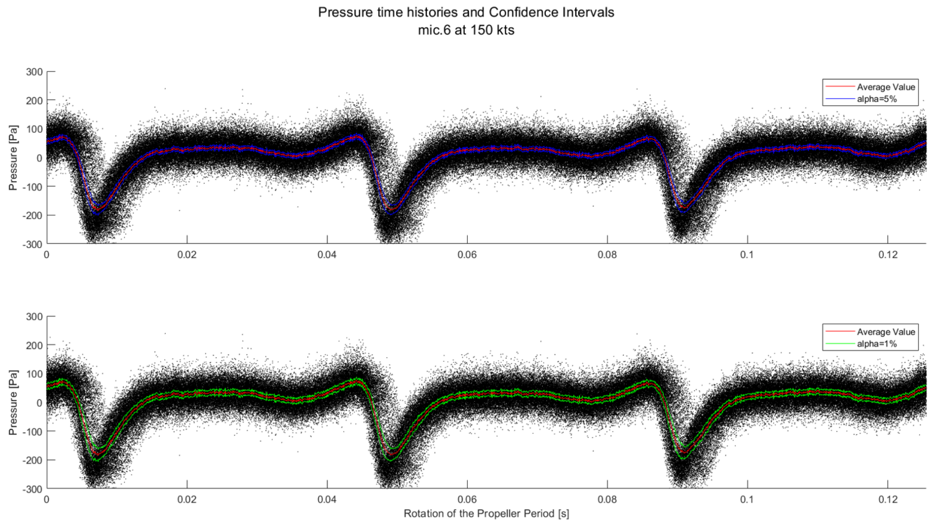

FIGURE 3.22: Confidence Intervals Time Domain - mic.6, 150 kts.

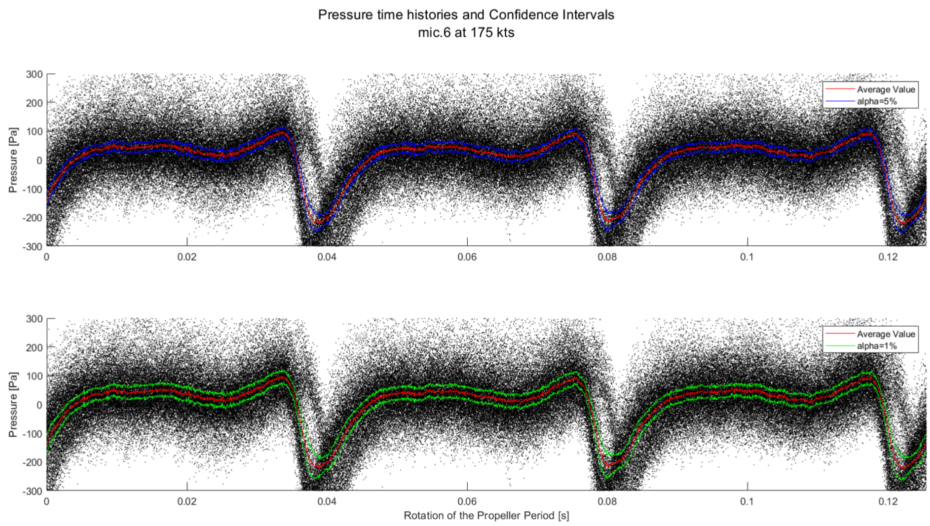

FIGURE 3.23: Confidence Intervals Time Domain - mic.6, 175 kts.

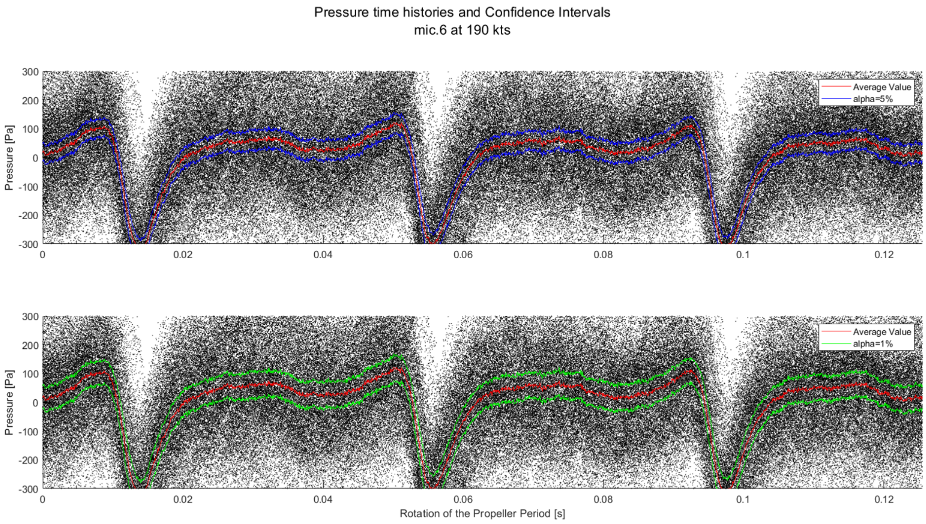

FIGURE 3.24: Confidence Intervals Time Domain - mic.6, 190 kts.

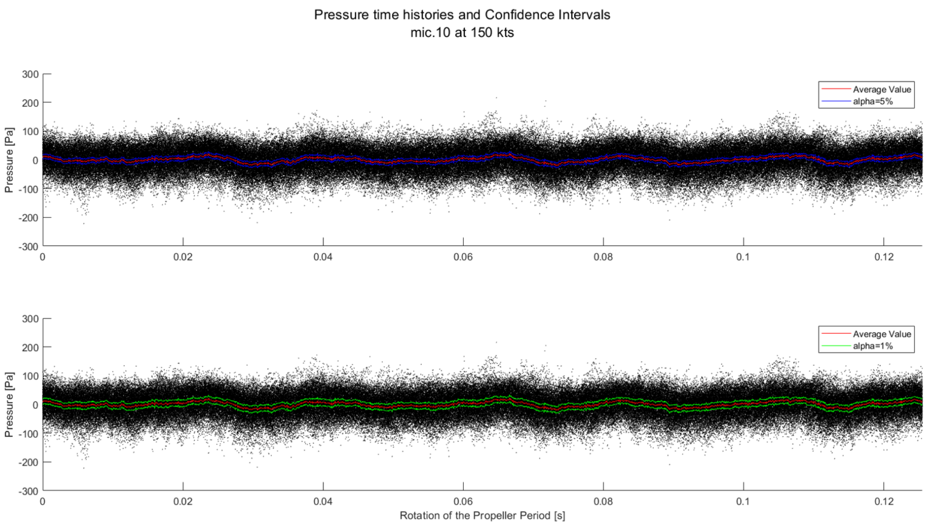

FIGURE 3.25: Confidence Intervals Time Domain - mic.10, 150 kts.

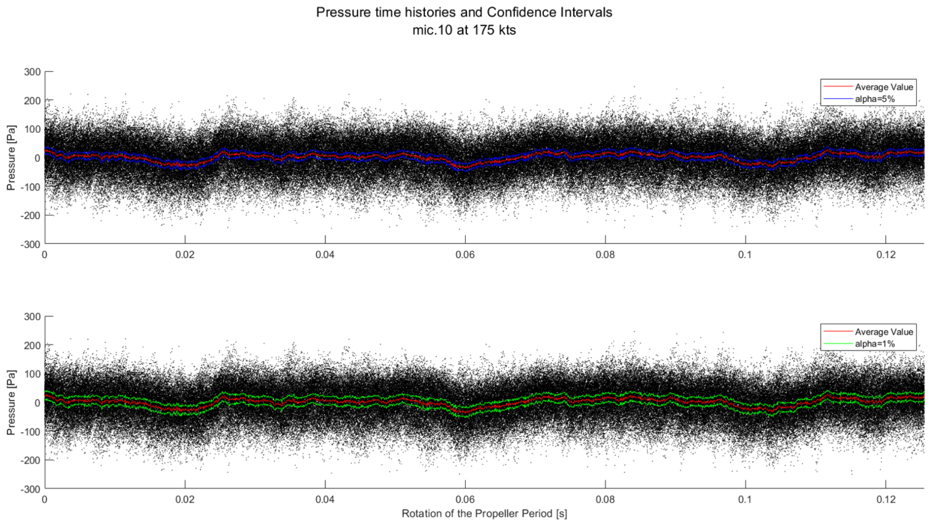

FIGURE 3.26: Confidence Intervals Time Domain - mic.10, 175 kts.

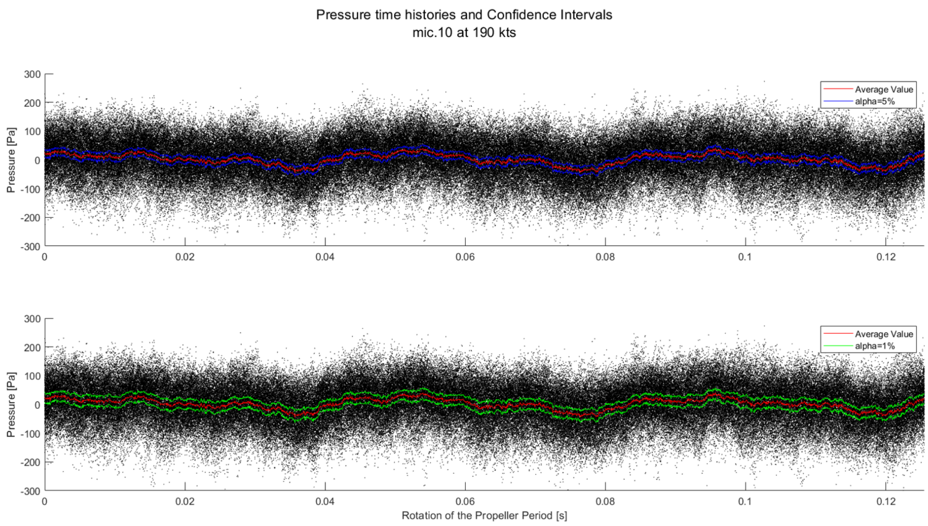

FIGURE 3.27: Confidence Intervals Time Domain - mic.10, 190 kts.

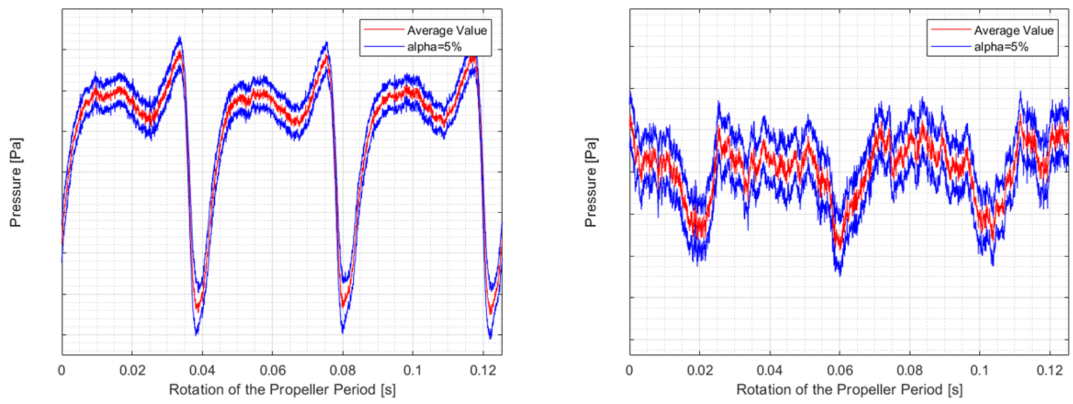

FIGURE 3.28: Averaged Value and Confidential Interval, external mic. 6 (left) and mic.10 (right), 175 kts.

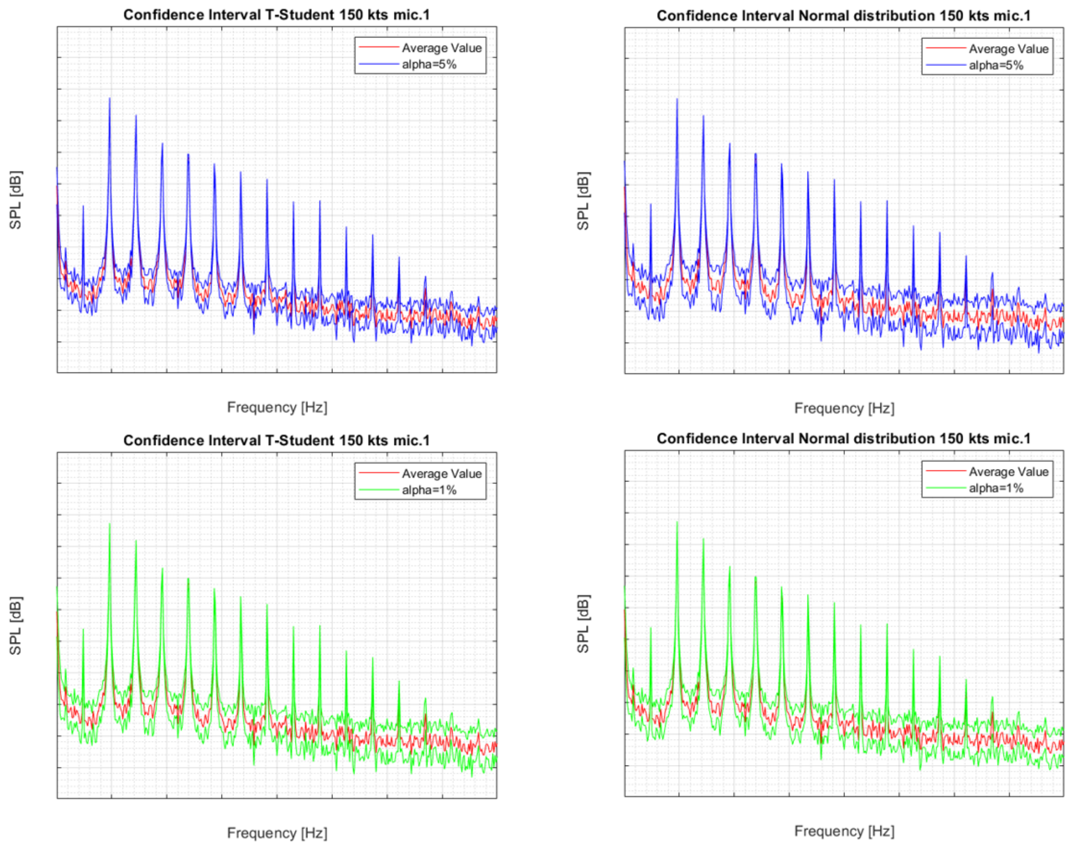

FIGURE 3.29: Comparison between T-Student and Normal distribution, Spectra.

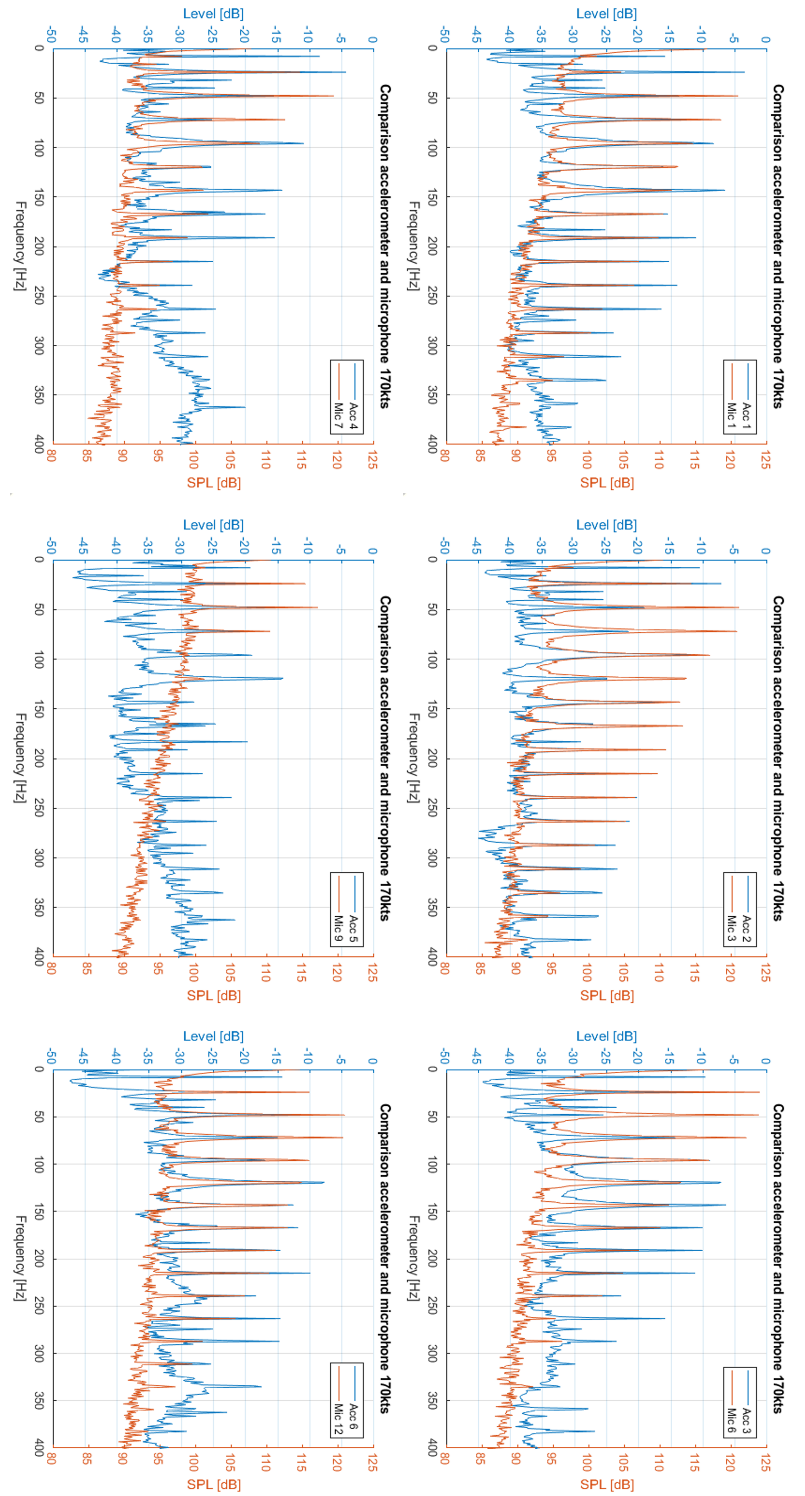

FIGURE 3.30: Vibroacoustic correlation.

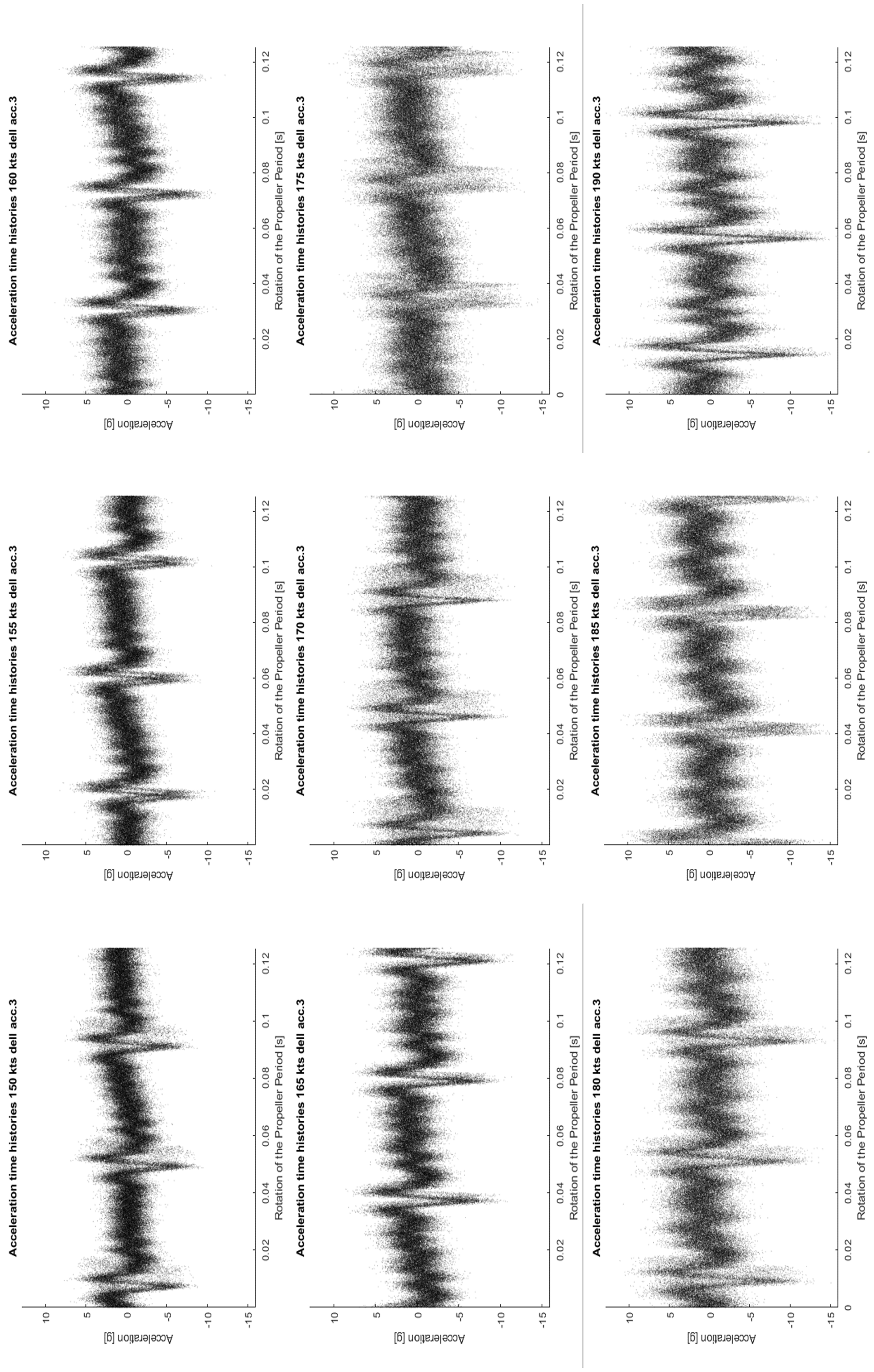

FIGURE 3.31: Accelerations time history refer to propeller rotation period, accelerometer no.3

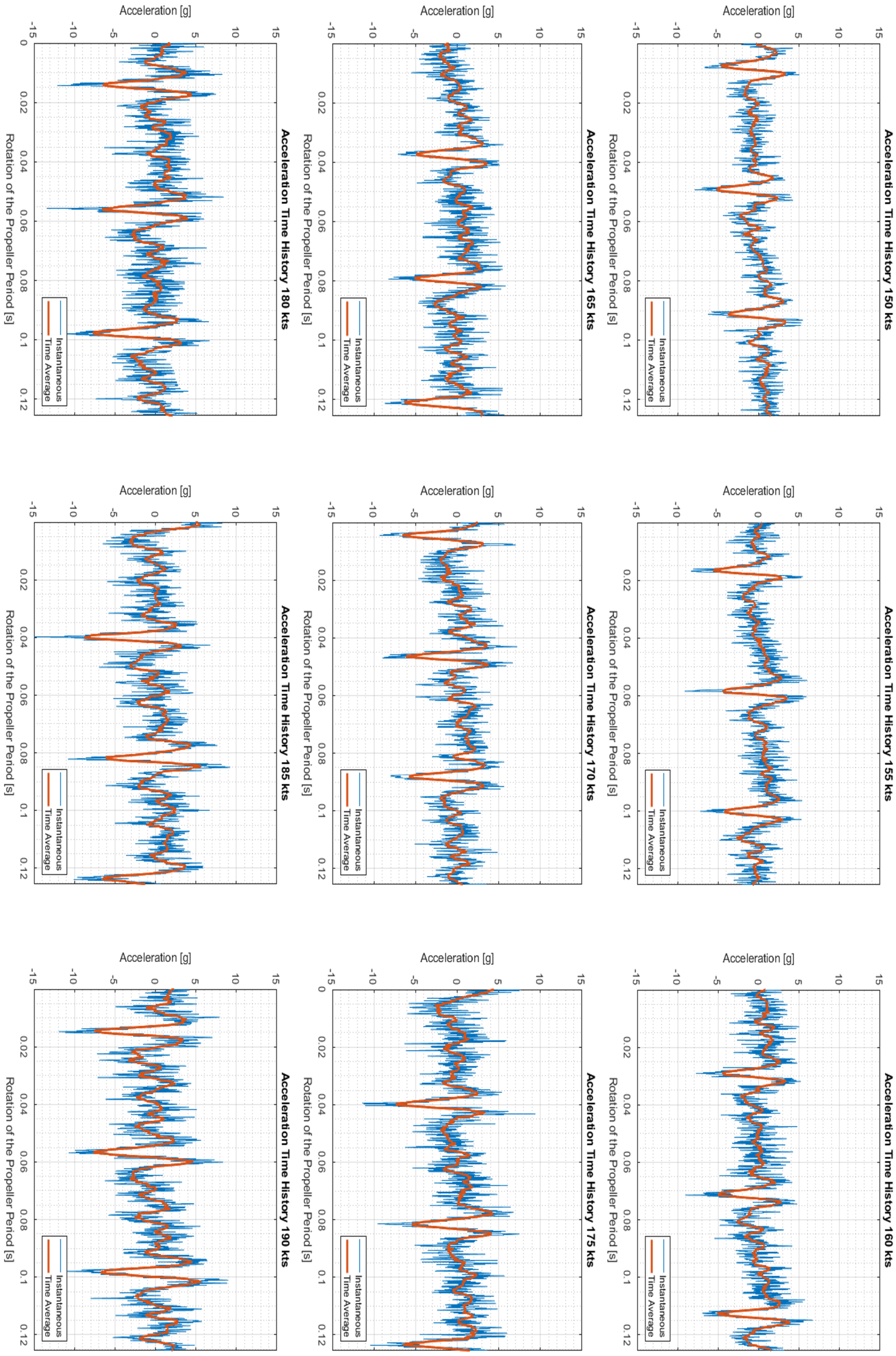

FIGURE 3.32: Accelerations time histories.

Chapter 4

Numerical and Experimental Investigation of the Whirl Flutter

4.1 Overview on the Aeroelastic problems

Before going into the specific topic of whirl flutter to which chapter 3 is dedicated and seeing the aeroelastic results of the upscaled wing in chapter 4, as per the tradition of every text concerning aeroelasticity, a brief introduction to aeroelastic problems is presented below through the well-known Collar diagram, that describes the aeroelastic phenomena by means of a triangle of forces (Fig. 4.1), distinguishing the aeroelastic phenomena of the static type from those of the dynamic type.
Aeroelasticity is the study of the interaction of aerodynamic, elastic, and inertia forces for a flexible structure and the phenomena that can result [61]. For fixed-wing aircraft there are two key areas:

- **Static aeroelasticity** - the deformation of the aircraft influences the lift distribution, which can lead to the statically unstable condition of torsional divergence and can reduce the control surface effectiveness, which can even lead to control reversal;

- **Dynamic aeroelasticity** - includes the critical area of flutter, where the aircraft become dynamically unstable in a condition where the structure extracts energy from the air stream. Aeroelastic problems would not exist if the aircraft structure is perfectly rigid. Modern aircraft structures are very flexible, and this flexibility is fundamentally responsible for various types of aeroelastic phenomena.

Structural flexibility itself may not be objectionable. However, aeroelastic phenomena arise when structural deformations induce additional aerodynamic forces. These additional aerodynamic forces may produce additional structural deformations which will induce still greater aerodynamic forces. Such interactions may tend to become smaller and smaller until a condition of stable equilibrium is reached, or they may tend to diverge and destroy the structure. Divergence can be exemplified easily considering Figure 2.2 that represents the increase of wing incidence due to wing twist. The moment of the lift vector about the center of twist causes an increase in wing incidence which produces a further increase in lift, leading to another increment in incidence so on [52].

At speeds below a critical value, called divergence speed, the increments in lift converge to a condition of stable equilibrium in which the torsional moment of the aerodynamic forces about the center of twist is balanced by the torsional rigidity of the wing. In the opposite case, speed above the divergence speed, the wing will exhibit a divergent behavior, causing structural failure. One can understand that the divergence speed will be higher for wings with greater torsional stiffness or with the aerodynamic center closer to the twist center; these are important factors indeed to consider in the structural project. Most aircraft are designed with swept-back wings. The reason for this is mainly aerodynamic, since for subsonic aircraft by sweeping back the wing the airspeed at which shock waves are formed on the wings increases, so delaying the associated increase in drag. Supersonic aircraft are designed with the wings swept inside the Mach cone, which also decreases the associated wave drag. Wright and Cooper et al. [53] explain that the divergence speed increases with swept-back wings and decreases for the swept-forward case. This reduction of the divergence speed becomes the limiting case for sweep-forward designs and consequently very few exist. Dynamic Aeroelasticity - Flutter So far, when considering static aeroelastic effects (see Section 2.2), the aerodynamic surfaces are in a steady condition and so the resulting forces and moments are steady (i.e constant with time). However, for flutter, maneuver, and gust response analyses the behavior of aerodynamic surfaces under dynamic motion is required. Flutter is arguably the most important of all the aeroelastic phenomena and is the most difficult to predict. It is an unstable self-excited vibration in which the structure extracts energy from the air stream and often results in catastrophic structural failure. Classical binary flutter occurs when the aerodynamic forces associated with motion in two modes of vibration cause the modes to a couple in an unfavorable manner. In aircraft design, flutter is a critical parameter that must be considered in the early stages of the design cycle. At a critical speed, known as flutter speed, the structure sustains oscillations following some initial disturbance. Below this speed, the oscillations are damped, whereas above it one of the modes becomes negatively damped and unstable oscillations occur. Flutter can take various forms involving different pairs of interacting modes, e.g. wing bending/torsion, wing torsion/control surface, etc. Flutter, like other aeroelastic phenomena, is very sensitive to the structure's normal modes of vibration. Some indication of the physical nature of wing bending-torsion flutter may be given from an examination of aerodynamic and inertia forces during a combined bending and torsional oscillation in which the individual motion is 90° out of phase. In a pure bending or pure torsional oscillation, the aerodynamic forces produced by the effective wing incidence oppose the motion; the geometric incidence in pure bending remains constant and therefore does not affect the aerodynamic damping force, while in pure torsion the geometric incidence produces aerodynamic forces which oppose the motion during one-half of the cycles but assist it during the other

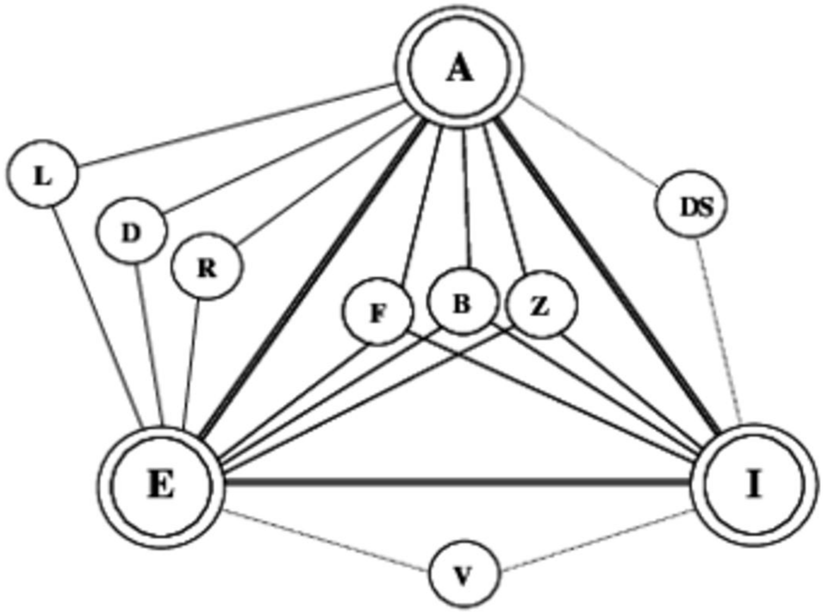

FIGURE 4.1: The aeroelastic triangle of forces

half so that the overall effect is nil. Thus, pure bending or pure torsional oscillations are quickly damped out. This is not the case in the combined oscillation when the maximum twist occurs at zero bending and vice versa; that is, a 90° phase difference [52]. The type of flutter described above, in which two distinctly different types of oscillating motion interact such that the resultant motion is divergent, is known as classical flutter. Other types of flutter may involve only one type of motion, which examples are the stalling flutter and aileron buzz. Stalling flutter of a wing occurs at a high incidence where, for particular positions of the spanwise axis of twist, self-excited twisting oscillations occur which, above a critical speed, diverge. Aileron buzz occurs at high subsonic speeds and is associated with the shock wave on the wing forward of the aileron.

4.2 Introduction: historical and theoretical background of whirl flutter phenomenon

Whirl flutter, also called gyroscopic flutter, is a dynamic aeroelastic stability phenomenon that may occur in a flexibly mounted engine and propeller system. The elastic modes of the system are coupled by the gyroscopic effects of the turning rotor disk, resulting in complex mode shapes of the mechanical system. The propeller vibration causes a change of propeller blades' angle of attack that will result in non-stationary aerodynamic forces generation. Due to that, the vibrations could become unstable and result in the failure of the engine, nacelle, or whole wing [54, 55].
After a historical and theoretical background of the aeroelastic phenomenon, this work illustrates the concept, development, and testing of a demonstrator for whirl flutter investigation.

The theoretical formulation of this complex dynamic aeroelastic phenomenon is preliminarily provided. Since this work concerns a propeller demonstrator, the experimentally observed phenomenon may be related to the instability affecting turboprop aircraft rather than the tiltrotor. All the demonstrator specifications have been investigated, especially the stiffness and inertia ones. Analytical and numerical models have been developed to predict the test rig modal characteristics. Good correspondence with experimental results has been achieved. For the numerical investigation, a beam-elements based model has been drawn up with two different ways of modeling the system stiffness. For the rotating propeller numerical investigation, the rotor gyroscopic effects and the propeller aerodynamic forces have been included to obtain whirl natural frequencies and mode shapes.
From a historical point of view, although whirl flutter was discovered analytically by Taylor and Browne in 1938, it acquired practical interest only after the two fatal accidents that involved the Lockheed L-188 Electra II aircraft, on 29 September 1959 in Texas and on 17 March 1960 in Indiana.
Electra II was designed with four Allison 501 turboprop wing-mounted power units installed into the lengthy nacelles, with large propellers placed quite far forward of the wing.
The nacelle was designed considering a case of large unbalancing, e.g. due to the loosening of the propeller blade. In one of the two cases investigated, it was found that the outboard engine nacelle was vibrating at an amplitude of 35 degrees around the neutral position. The nacelle attachment was undamaged while the whole wing had been torn away from the fusolage.
The investigational activities of the incidents report as a trigger a failure of the wing due to the forces coming from the whirl mode, i.e. the vibratory motion of the propeller was transmitted to the wing that was unable to dampen it.
Following the two incidents, the whirl mode study was introduced into the analytical flutter solution and wind tunnel tests were performed on the 1/8 scale aeroelastic model of the Electra aircraft, in order to evaluate the failure mechanisms.
Another incident directly caused by whirl flutter is the Beechcraft 1900C one, in 1991. Contrary to the Electras' events, the Beech 1900C crash occurred at the time when the whirl flutter issue was already well-known [56].
Figure 4.2 shows a simplified scheme in which the power plant or nacelle is idealized by two springs behind the propeller disk. The dynamic system can be modeled with a propeller, having the spin axis approximately oriented into the direction of the freestream velocity V_∞, horizontally supported by a pylon pivoted on the wing.

In this system, two independent mode shapes (pitch and yaw) will emerge, neglecting the propeller's rotation and aerodynamic forces. If the propeller has a certain angular velocity Ω, the two independent mode shapes merge into the whirl motion. The propeller axis is subjected to an elliptical motion and the orientation relative to its rotation is such to be backward for the lower frequency mode and forward for the higher frequency one.

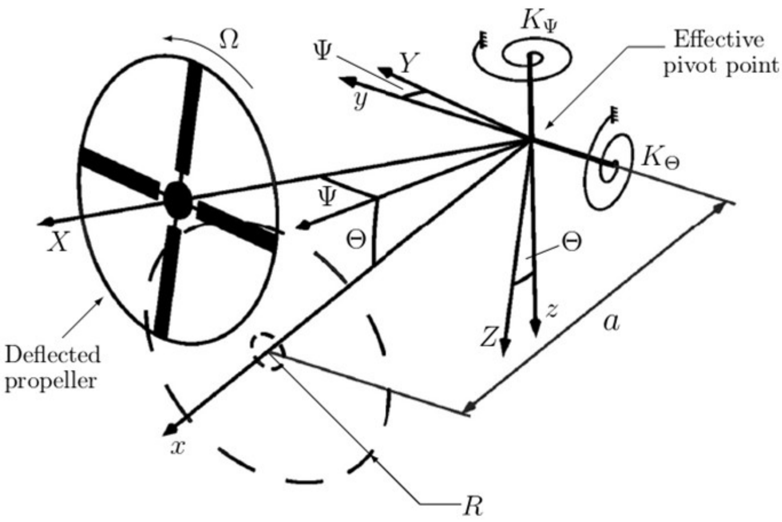

FIGURE 4.2: Schematic representation of basic features of the propeller-nacelle dynamic system

The equations of motion can be set up for the system through Lagrange's approach, using a kinematical scheme that includes the gyroscopic effects. The generalized coordinates are the pitch and yaw angles (Θ, Ψ).
The final whirl flutter equations are:

$$
\begin{aligned}
J_Y\ddot{\Theta} + \frac{K_\Theta \gamma_\Theta}{\omega}\dot{\Theta} + J_X\Omega\dot{\Psi} + K_\Theta\Theta &= M_{Y,P} - aP_Z \\
J_Z\ddot{\Psi} + \frac{K_\Psi \gamma_\Psi}{\omega}\dot{\Psi} + J_X\Omega\dot{\Theta} + K_\Psi\Psi &= M_{Z,P} - aP_Y
\end{aligned}
\tag{4.1}
$$

The equations refer to the effective pivot point. Also, structural damping has been considered. γ_Θ and γ_Ψ are the structural damping ratios for the engine pitch and yaw vibrations modes.
The gyroscopic terms model the pitch reactive moment due to yaw angular velocity and vice versa. These terms cause the equations to be coupled.
The aerodynamic effects due to the whirl motion can be divided into two categories: torques (M_Y and M_Z) and forces lying in the propeller disk (P_Y and P_Z). The forces normal to the disk plane are neglected because of their very low effects.
The yawing moment due to pitch angle $M_Z(\Theta)$ and the pitch moment due to yaw angle $M_Y(\Psi)$ are the driving moments of propeller whirl flutter. $M_Z(\Theta)$ may be interpreted as a cross-stiffness term. This moment is in the same direction as the yawing velocity for the backward whirl mode and acts as negative (destabilizing) aerodynamic damping. It must be compensated by other positive damping forces to set the system stable. The aerodynamic part of the total damping available for this purpose may be found in the force $P_Z(\dot{z})$ and in the moment $M_Y(\dot{\Theta})$ produced by the rate terms ($\dot{z}$) and ($\dot{\Theta}$), respectively, [54], [57–63].
The complicated physical principle of the phenomenon requires an experimental

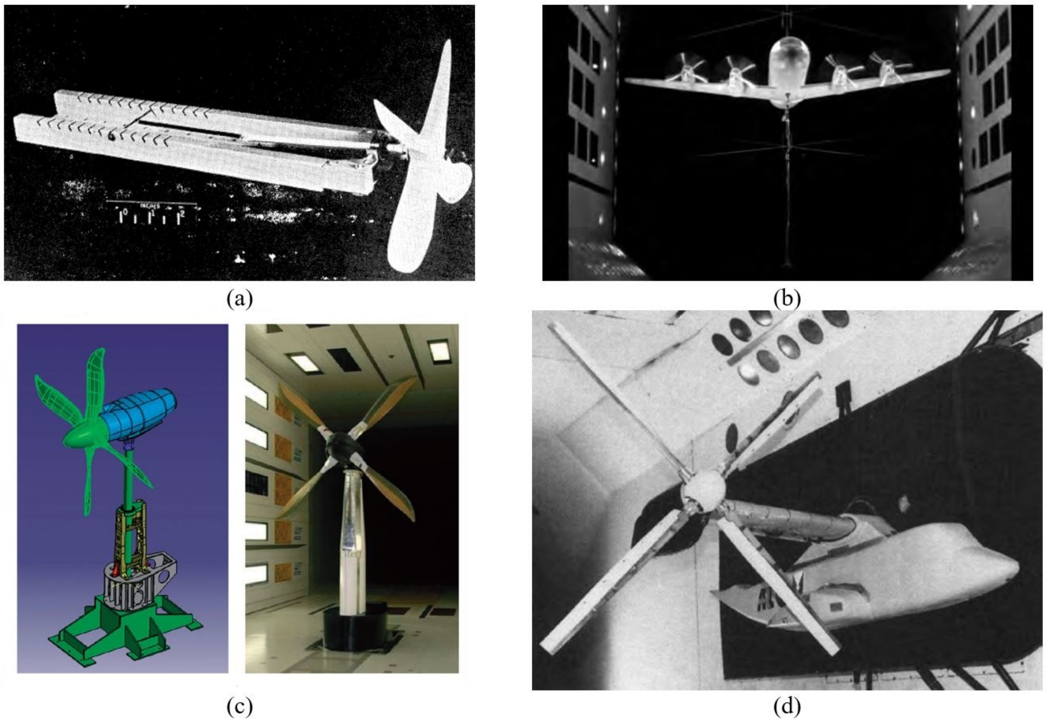

FIGURE 4.3: Example of propeller (a), aircraft (b), proprotor (c), tiltrotor aircraft (d) demonstrators.

validation of the analytical and numerical results. Experimental research activities are required especially because of the difficult computation of propeller aerodynamic forces. The main developments in the experimental research on the whirl flutter phenomenon were accomplished in the 1960s in direct connection with the Electra accidents.

As represented in Figure 4.3 [54, 55, 64, 65] the several whirl flutter demonstrators could be classified in:

- propeller demonstrators: simple tests on flexibly attached propellers in the windmilling mode;
- aircraft demonstrators: complex tests on the aircraft models or parts of the aircraft;
- proprotor demonstrators;
- tiltrotor aircraft demonstrators.

For tiltrotor aircraft, the whirl flutter is a relevant topic and its design has been one of the drivers of early whirl flutter investigation. Whirl flutter instability is the major barrier to increasing tiltrotor speeds. Increased power, thrust and rotor efficiency are of no avail unless the whirl mode stability boundary can be improved.

With current technology, very stiff, thick wings of limited aspect ratio are essential to meet the stability requirements [66–69].

TABLE 4.1: Mass and material characteristics of the WFSD components.

Item	Material	m [g]	ρ $\left[kg/m^3\right]$	E [GPa]	G [GPa]
Propeller	plastic	12.8	1450	3.0	1.0
Rod	PVC	28.7	1450	3.0	1.0
Cardan joint	steel alloy	9.6	7860	210	80
Hub	bronze alloy	11.5	8800	–	–
Spring	various	–	–	–	–
Tension variator	aluminium alloy	31.1	2700	70	27

The most recent and innovative whirl flutter applications regard proprotor and tiltrotor aircraft demonstrators. Very complex numerical tools have been developed which show consistently excellent agreement with each other for wide variations of design variables and operating conditions. Among them, it is possible to cite the Comprehensive Analytical Model of Rotorcraft Aerodynamics and Dynamics (CAMRAD II) and the Rotorcraft Comprehensive Analysis System (RCAS). The latest developments concerning the tiltrotor whirl flutter are deeply discussed in [70–75].

4.3 Whirl flutter demonstrator development

The model used for the current work, named "Whirl Flutter Small-Scale Demonstrator", is inspired by the classical two-DOF Houbolt and Reed's model [64].
WFSD has been devised to have a windmilling propeller attached to a rod simulating the engine's inertia.
The pitch and yaw degrees of freedom have been provided connecting the rod to the support through a Cardan joint. The stiffness of the system has been obtained by connecting the rod to a spring.
The support has been designed with a grooved surface to have an aluminium septum, fitted with a hook, inserted in. In this manner, it is possible to guarantee an adjustable stiffness.
The device has been equipped with two different propellers: a two-blade one simulating a piston engine propeller and a five-blade one simulating a high solidity multi-blade propeller.
The two versions of the demonstrator are shown in Figure 4.4.
The CAD model of the demonstrator is represented in Figure 4.5(a) with all various components mentioned, while the demonstrator technical drawing and its overall dimensions are reported in Figure 4.5(b). Components' masses values and main characteristics of the material (density ρ, Young's module E and Shear module G) are summarized in Table 4.1. The rod-propeller system and the total facility masses are reported in Table 4.2.

(a) (b)

FIGURE 4.4: WFSD equipped with a two-blade propeller (a) and a high-solidity five-blades propeller (b).

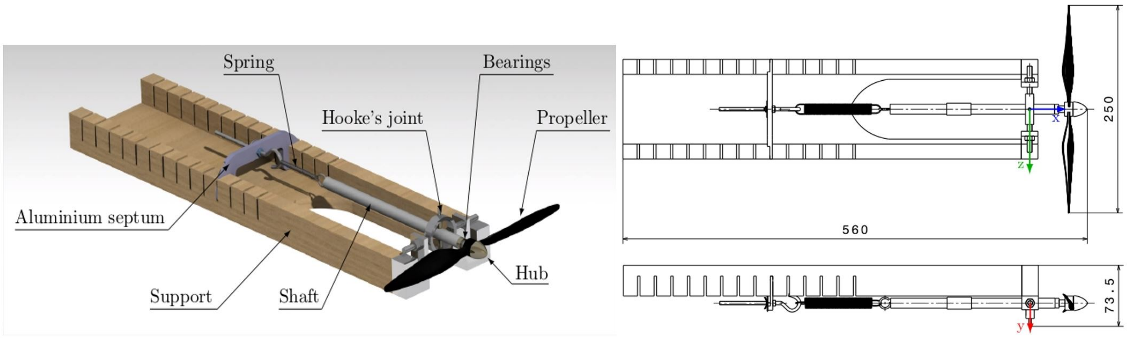

(a) (b)

FIGURE 4.5: Whirl Flutter Small-Scale Demonstrator (WFSD): CAD model (a) and technical drawing with overall dimensions specified [mm] (b)

TABLE 4.2: Rod-propeller system and total assembly masses, WFSD.

Element	**Mass** [g]
Rod-Propeller system	53.2
WFSD	822.9

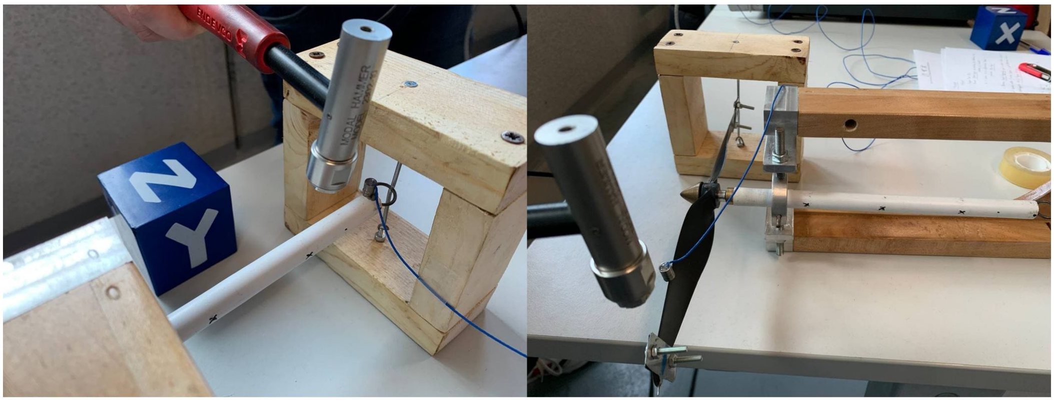

(a) (b)

FIGURE 4.6: Pitch (a) and propeller (b) moments of inertia measurement setup.

TABLE 4.3: Pitch, yaw and propeller natural frequencies and moments of inertia.

Type	**Natural freq.** [Hz]	**Analytical moment of inertia** $\left[\mathrm{kgm}^2\right]$	**Numerical moment of inertia** $\left[\mathrm{kgm}^2\right]$
Pitch (2-blade WFSD)	19.5	$2.74 \cdot 10^{-4}$	$2.63 \cdot 10^{-4}$
Yaw (2-blade WFSD)	18.3	$2.92 \cdot 10^{-4}$	$2.81 \cdot 10^{-4}$
2-blade propeller	16.2	$7.2 \cdot 10^{-5}$	–
Pitch (5-blade WFSD)	13.5	$5.76 \cdot 10^{-4}$	$5.23 \cdot 10^{-4}$
Yaw (5-blade WFSD)	12.9	$5.94 \cdot 10^{-4}$	$5.41 \cdot 10^{-4}$
5-blade propeller	9.72	$4.26 \cdot 10^{-4}$	–

4.3.1 WFSD Inertial characteristics

An experimental analysis has been conducted to find the two rod-propeller system moments of inertia and the propeller one, for both the configurations. For the rod-propeller system analysis, a known torsional stiffness has been provided utilizing two pre-stretched tension springs. The springs are represented in Figure 4.6.
A modal hammer testing was applied to find the pitch and yaw natural frequencies. By the knowledge of the torsional stiffness, it has been possible to find the two moments of inertia, both analytically and numerically. The pitch inertia measurement setup is shown in Figure 4.6(a).
For propeller modal testing, the shaft has been fixed and the blade has been connected to the springs employing a support, as represented in Figure 4.6(b).
The experimental natural frequencies and the analytical and numerical moments of inertia values are summarized in Table 4.3. In particular, the numerical inertia has been provided by employing a FE model. The mass distribution has been derived by attempts to obtain the experimental natural frequency. In the propeller case, only the analytical moment of inertia has been computed.

4.4 Analytical and numerical investigation

This section deals with the analytical and numerical analysis of the WFSD modal parameters. The aim was to achieve a model of the demonstrator allows the prediction of the device natural frequencies and vibration modes.
The analytical and numerical analysis has been performed for both rotating and non-rotating propeller. The numerical model has been developed using the Finite Element Method.

4.4.1 Stiffness modelling

To achieve the analytical and numerical models, it has been necessary to find a way to model the system stiffness. If modelled as a torsional spring, the stiffness has a non-linear behaviour. This is due to the contemporaneous increase of the return force of the spring and its arm as a consequence of pitch angle increase.
Figure 4.7 shows the conceptual schema of the system due to a pitch deflection. The non-linearity is mild due to the relatively low value of the spring elongation during the rotation $u \approx u_0$. For this reason, the spring elongation has been neglected and the return force has been considered by a constant value, equal to the initial one, during the rotation. In this way, a linear elasticity is achieved.
Therefore, the pitch and yaw torsional stiffnesses can be computed by means of the following equations:

$$K_\Theta = \frac{Fl}{\Theta}\left(1 + \frac{l}{u_0}\right); K_\Psi = \frac{Fl}{\Psi}\left(1 + \frac{l}{u_0}\right) \tag{4.2}$$

It is also possible to model the system stiffness taking advantage on a linear springs schematization:

$$K_Z = Fl\left(1 + \frac{l}{u_0}\right); K_Z = Fl\left(1 + \frac{l}{u_0}\right) \tag{4.3}$$

4.4.2 Analytical modelling

In the analytical approach, a rigid shaft and propeller have been assumed. This assumption implies the use of a torsional or linear stiffness indifferently. A torsional springs model has been assumed.
In the non-rotating propeller case, the dynamic behaviour of the system can be described by two independent degree of freedoms (DOF) as in Equation 4.4. Damping has not been taken into account.

$$\begin{bmatrix} J_Y & 0 \\ 0 & J_Z \end{bmatrix} \begin{Bmatrix} \ddot{\Theta} \\ \ddot{\Psi} \end{Bmatrix} + \begin{bmatrix} K_\Theta & 0 \\ 0 & K_\psi \end{bmatrix} \begin{Bmatrix} \Theta \\ \psi \end{Bmatrix} = \begin{Bmatrix} 0 \\ 0 \end{Bmatrix} \tag{4.4}$$

In the current case, pitch and yaw dynamics are decoupled and two independent modes emerge: pitch and yaw. Given the assumption of rigid propeller and shaft,

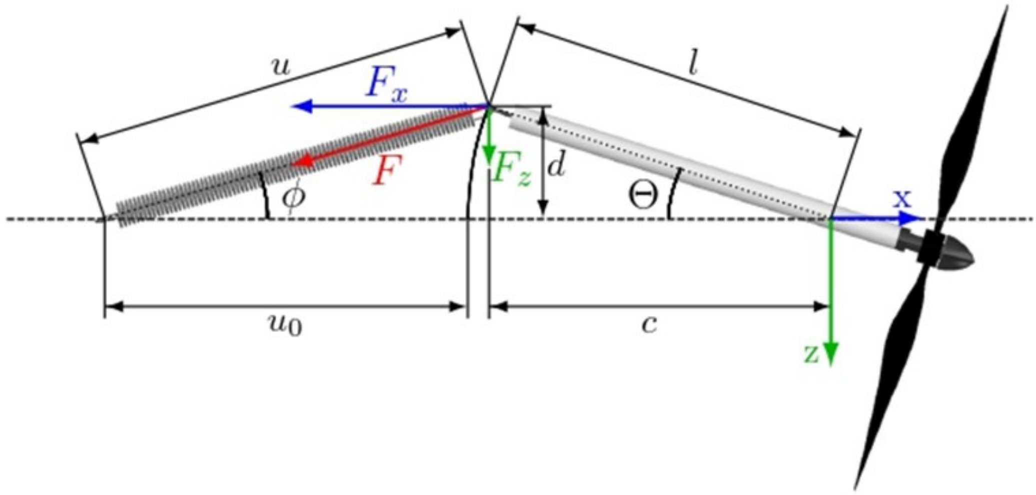

FIGURE 4.7: Schematic representation of the system as a consequence of a pitch deflection.

the analytical model provides only the first two natural frequencies. Of course, the real structure has several modes, but they have not been considered because they do not affect the whirl flutter phenomenon.
Rotating propeller analytical model has been achieved considering, in respect to the non-rotating case, the gyroscopic matrix $[G]$ and the propeller unsteady aerodynamic loads. The propeller aerodynamic derivatives have been calculated analytically by means of strip theory [76]. The dynamic behaviour of the coupled system is described by means of the Equation 4.5. The aim is to obtain the whirl natural frequencies and mode shapes.

$$[M]\{\ddot{q}\} + [C]\{\dot{q}\} + [G]\{\dot{q}\} + [K]\{q\} = [C_A]\{\dot{q}\} + [K_A]\{q\} \tag{4.5}$$

Whirl natural frequencies have been computed by solving the Equation **??** for various angular velocity values. In this manner it is possible to obtain the Campbell diagram [77, 78]. Figure 4.8 shows an example of the system Campbell diagram for a certain value of torsional springs stiffness.

$$\left(-\omega^2[M] + j\omega\left([D] + [G] + [D_A]\right) + \left([K] + [K_A]\right)\right)\begin{vmatrix}\bar{\Theta}\\ \bar{\Psi}\end{vmatrix} = \{0\} \tag{4.6}$$

4.4.3 Numerical modelling

To perform the numerical analysis in the non-rotating propeller case, two FE models were created. The analyses have been performed using the NASTRAN software. The two models differ concerning how the system stiffness has been modelled.
For both models, the shaft has been discretized employing one dimensional *BAR* elements.
The propeller has not been modelled, only its mass has been considered. No material

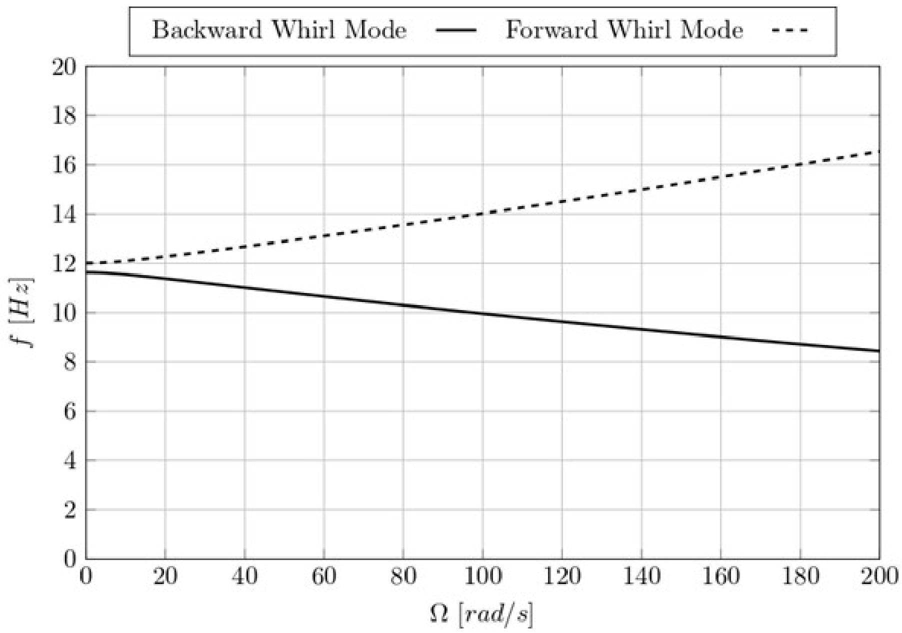

FIGURE 4.8: Analytical Campbell diagram, case K_{Θ}=K_{Ψ}=1.56Nm^2.

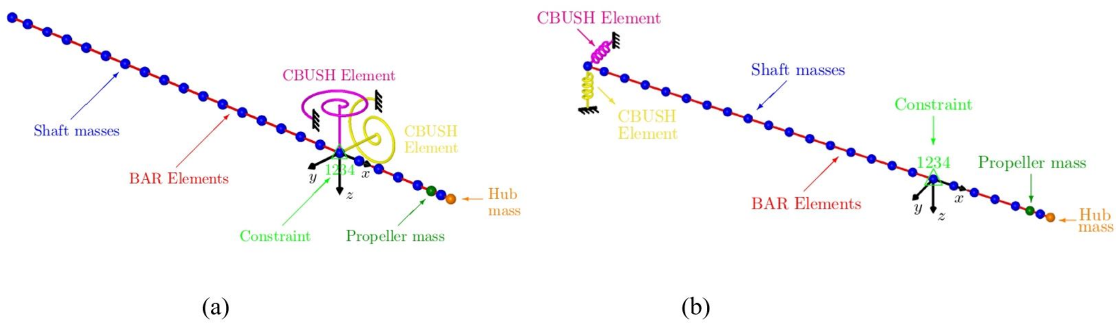

FIGURE 4.9: Torsional (a) and linear (b) springs FE models. Non-rotating propeller case.

mass has been provided: all the system's mass has been modelled through concentrated mass elements (*CONM2*) in correspondence of nodes. One of the *CONM2* mass elements has been also provided with and inertia terms to obtain different pitch and yaw moments of inertia, as evidenced in experimental measurements.
The elastic elements have been modelled through two zero dimension generalized spring *CBUSH* elements.
A modal analysis (*SOL 103*) has been made to obtain natural frequencies and mode shapes. Figure 4.9 represents the torsional and linear springs FEM models.
Figure 4.10 shows the torsional springs model first four modes.

To investigate whirl natural frequencies and mode shapes a rotordynamics analysis was performed.
Compared to the non-rotating propeller model, two cross-damping terms have been considered to simulate the rotor gyroscopic effect. The rotor effect has been modelled by explicitly inserting the damping matrix terms. In particular, the damping coefficients relate the fifth and sixth DOFs of the propeller node. They have opposite

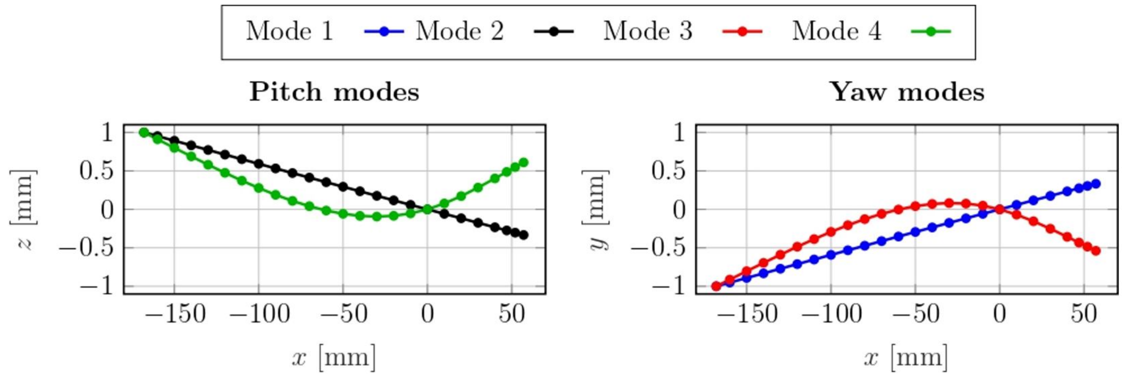

FIGURE 4.10: Torsional springs FEM model first four mode shapes. Non-rotating propeller case.

sign (c_{56}=c_{65}=$J_X\Omega$). These terms model the yaw moment due to the pitch angular velocity and the pitch moment due to the yaw angular velocity caused by the gyroscopic effects. Furthermore, all the analytically computed aerodynamic terms have been inserted.

The cross-damping and the aerodynamic terms have been inserted through the *DMIG* instruction: it allows direct input of matrices. In this manner, it has been possible to insert the gyroscopic matrix and the stiffness and damping aerodynamic matrices. A Direct Complex Eigenvalues Analysis (*SOL 107*) has been made up.

This method does not need a specific rotordynamics tool and allows to find whirl natural frequencies and mode shapes with a very low computational cost. Furthermore, it is possible to employ the same *BAR* elements used in the previous analysis. There is no need to use *CBEAM* elements or the J_X component of the *CONM2* mass elements because in this case the total $J_X\Omega$ cross-damping term is explicitly inserted. Moreover, the aerodynamic terms have been included without the need of complicated aeroelastic tools.

In Figure 4.11 the first four whirl modes for the torsional springs model are reported. Modes have been normalized such as the maximum was $0.1m$. In this way the graphic representation is meaningful.

4.5 Experimental Modal Analysis

This section considers the WFSD Experimental Modal Analysis (EMA) through impact testing. Two experimental campaigns have been carried on, concerning the two-blade propeller demonstrator and the five-blade one respectively. For both cases, analyses with varying stiffness and inertia characteristics have been performed. To find pitch and yaw natural frequencies, the structure was excited utilizing a modal hammer. The impact point was fixed while the accelerometer location has been varied. The impact and acquisition points positions are outlined in Figure 4.12.

The response of the structure in terms of acceleration has been acquired employing a roving ICP piezotronic accelerometer (PCB 352B10). Given the lightness of

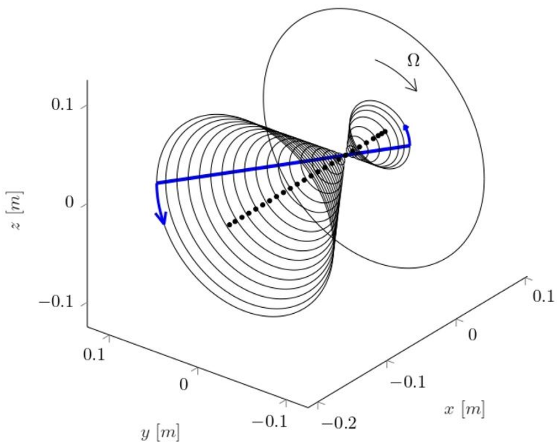

(a) BW1

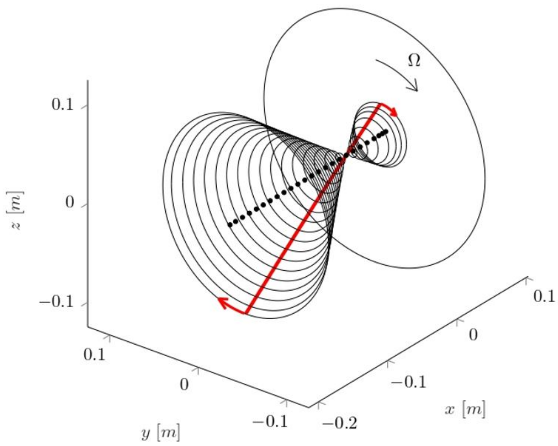

(b) FW1

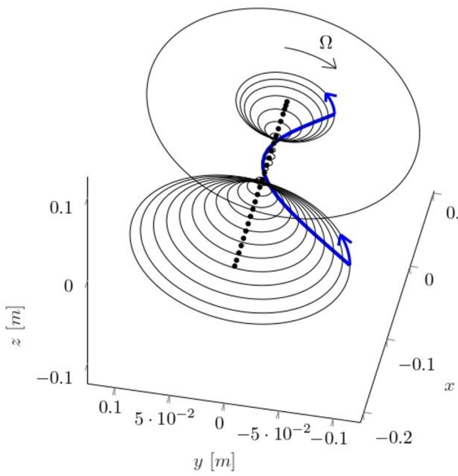

(c) BW2

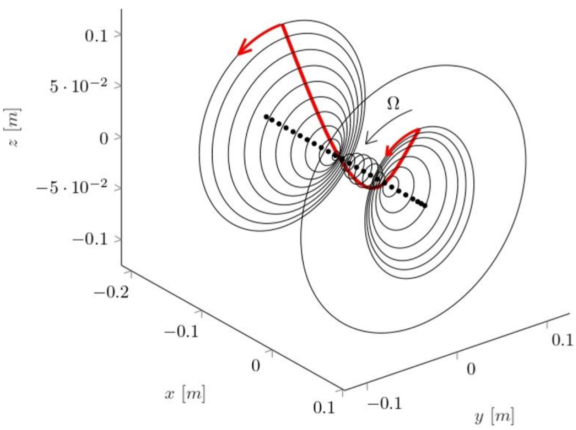

(d) FW2

FIGURE 4.11: First four complex mode shapes. Torsional spring model.

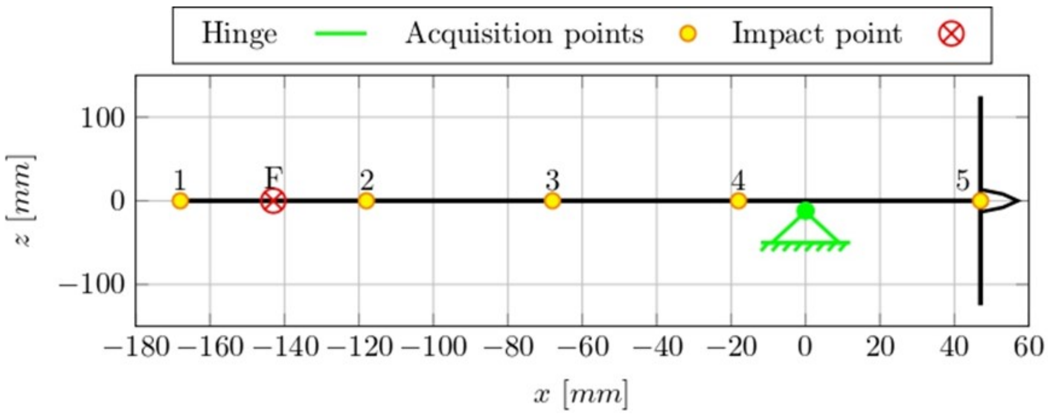

FIGURE 4.12: Schematic representation of impact point and acquisition points.

the structure, a miniature single-axis accelerometer with a weight of about 0.7g was used. An LMS Scadas mobile 05 has been employed. Modal testing acquisition and post-processing have been made using Simcenter Testlab software.

4.5.1 Sensitivity Analysis

Varying stiffness and inertia investigations have been conducted for both the two-blade and five-blade configurations. In the first case, different types of elastic elements have been used: both rubber bands and calibrated steel springs.
For the varying inertia analysis, the additional moment of inertia has been provided adding some plasticine masses to the shaft. Each of the analyses includes two impact tests, one regarding the pitch dynamics and the other concerning the yaw one.
In Figure 4.13 the experimental setup for a varying stiffness test (a) and a varying inertia one (b) are reported. In Figure 4.14(a) the pitch and yaw natural frequencies trend by varying the system torsional stiffness is represented. The experimental results are well approximated by the analytical and numerical curves.
Figure 4.14(b) shows the pitch and yaw natural frequencies plot as a function of the system moments of inertia. It is possible to observe an increase in the distance between experimental and analytical/numerical results increasing the added mass. This behaviour is due to the influence of the added masses on the stiffness of the shaft. The ballast provides both inertia and stiffness to the shaft because it has a larger local cross-section.
Adding more and more masses, the portion of the shaft affected by the variation in stiffness is even larger. That explains why the error between the results increases by raising the additional inertia.

The sensitivity analyses have been conducted also concerning the high solidity propeller version of the demonstrator. The analyses include both varying stiffness tests and varying inertia ones. Figure 4.15 (a) shows the pitch and yaw natural frequencies trend as a function of the stiffness. In Figure 4.15 (b) it is represented the

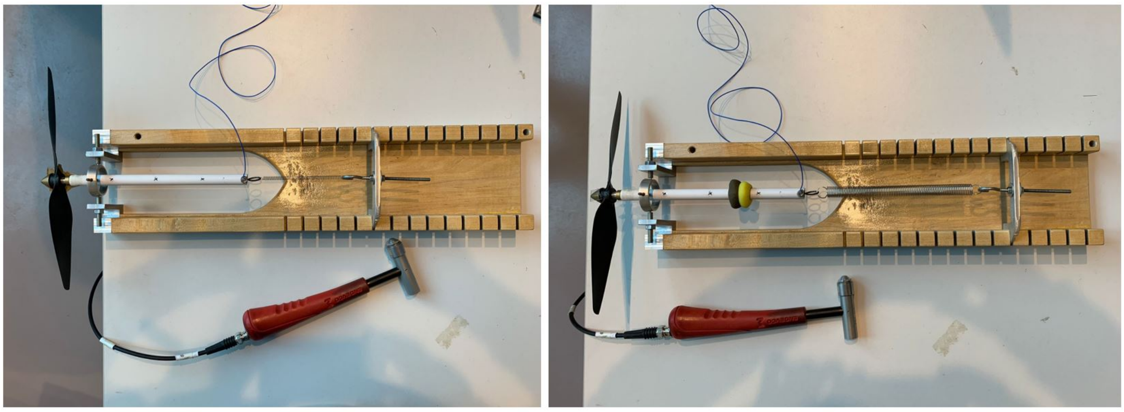

(a) (b)

FIGURE 4.13: Experimental setup for modal hammer testing. Varying stiffness (a) and varying inertia (b) analysis.

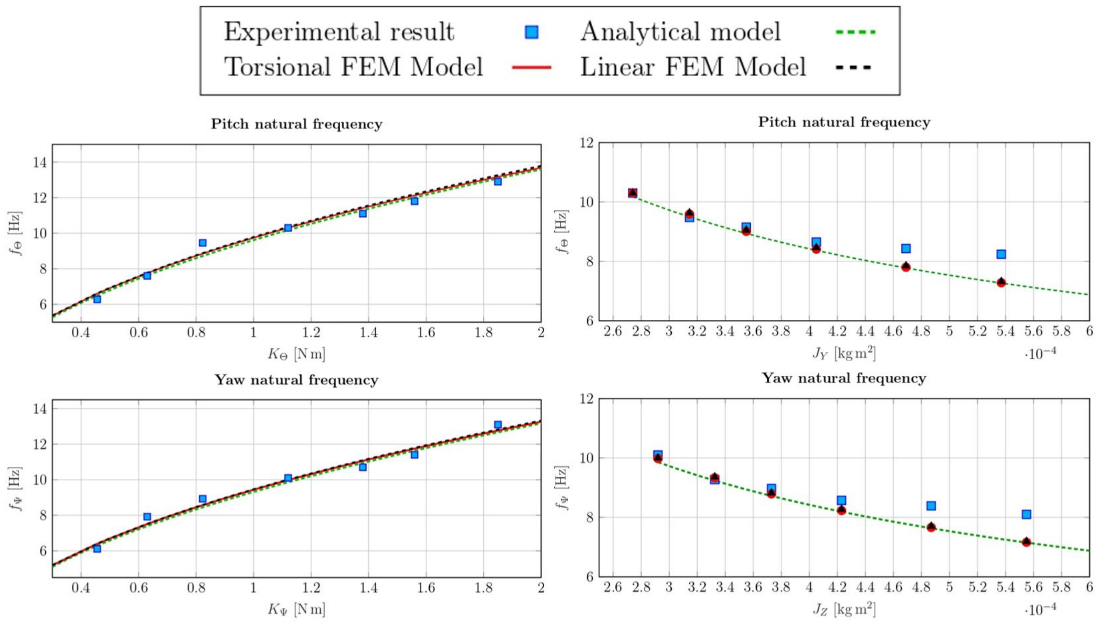

(a) (b)

FIGURE 4.14: Pitch and yaw natural frequencies trend varying the stiffness (a) and inertia (b). Comparison between experimental, analytical and numerical results. WFSD, two-blade propeller version.

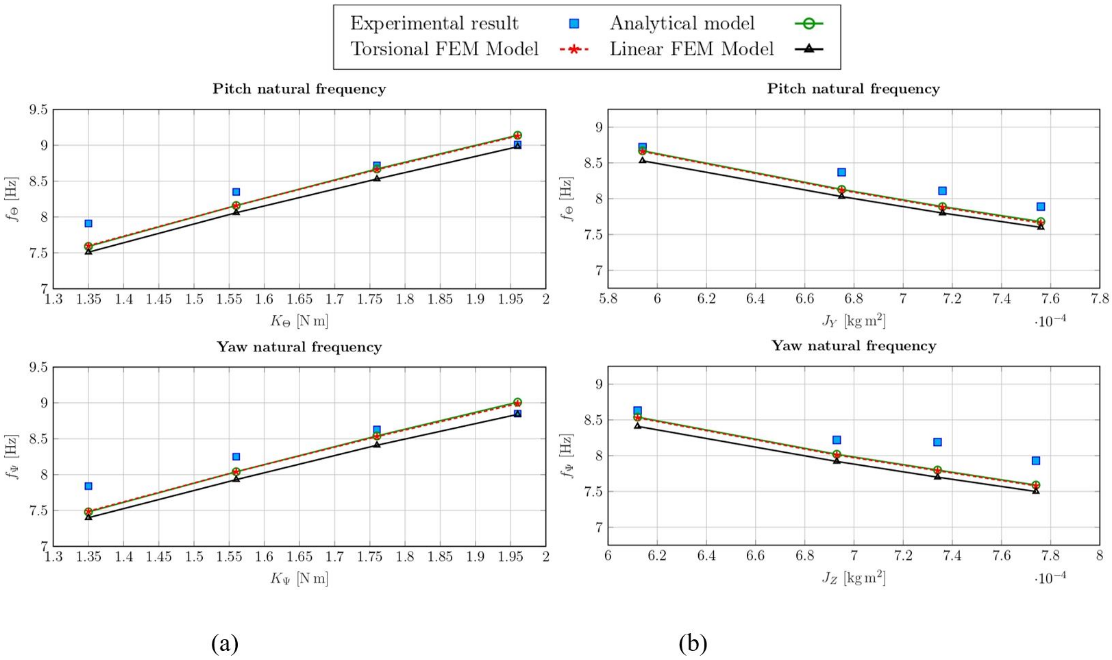

FIGURE 4.15: Pitch and yaw natural frequencies trend varying the stiffness (a) and inertia (b). Comparison between experimental, analytical and numerical results. WFSD, five-blade propeller version.

pitch and yaw natural frequencies trend as a function of the system moments of inertia. The trends are very similar to the two-blade propeller one. Thus, it is possible to derive very similar conclusions.

4.6 Operational Modal Analysis

This section is focused on the Operational Modal Analysis of the demonstrator in the case of rotating windmilling propeller. The airstream has been provided utilizing a centrifugal fan. The fan, with the indication of the various components, is represented in Figure 4.16. The electric engine of the fan is provided by a four-grooves multiple pulley. In this manner, it has been possible to obtain several values of the stream velocity. The freestream velocity has been measured by employing a digital anemometer, while the propeller angular velocity has been measured using a tachometer.
In Figure 4.17 the propeller angular velocity trends for each freestream velocity for the two-blade propeller and the high solidity one are reported.
To acquire the acceleration in both y and z directions, two piezotronic accelerometers were employed.

4.6.1 Experimental testing

The first investigation concerned the determination of the stability boundaries in the two-blade propeller and the high-solidity cases. As expected, it has been found that

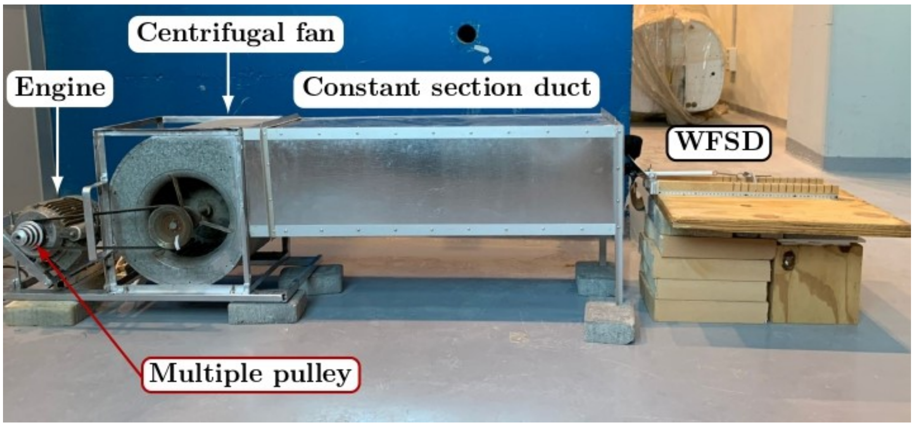

FIGURE 4.16: Centrifugal fan with main components' indication..

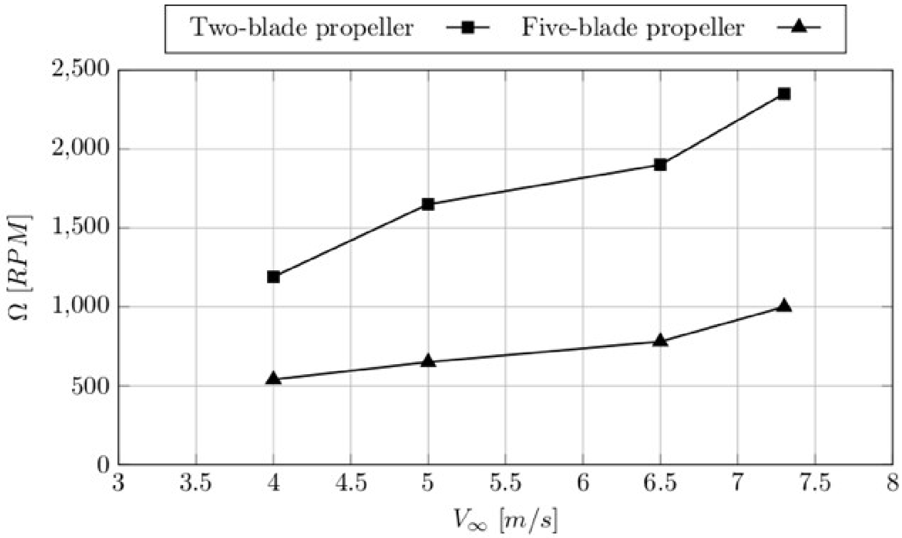

FIGURE 4.17: Centrifugal fan with main components' indication.

the two-blade propeller configuration was unable to show the instability with the available flow rates, even providing very low stiffnesses. This is due to the low moment of inertia of the propeller. It has a very low gyroscopic inertia and is not able to guarantee the modes coupling. Therefore, the first conclusion is that to have the whirl flutter instability, a large gyroscopic inertia is needed.

This fact explains why the whirl flutter phenomenon, as recalled by airworthiness rules, is very important for turboprop aircraft. Usually, they are equipped with heavy propellers in respect to piston aircraft that are equipped with lighter propellers. Consequently, the OMA has not been performed in the two-blade propeller case. Concerning the high solidity propeller version, it has been found the instability for each freestream velocity.

The stability boundary is represented in Figure 4.18. The stiffness behaviour as a function of the freestream dynamic pressure is well approximated by a linear trend, as evidenced in similar experiments found in the literature [79, 80]. It is possible to observe how, under a certain freestream velocity, the whirl flutter phenomenon does not occur.

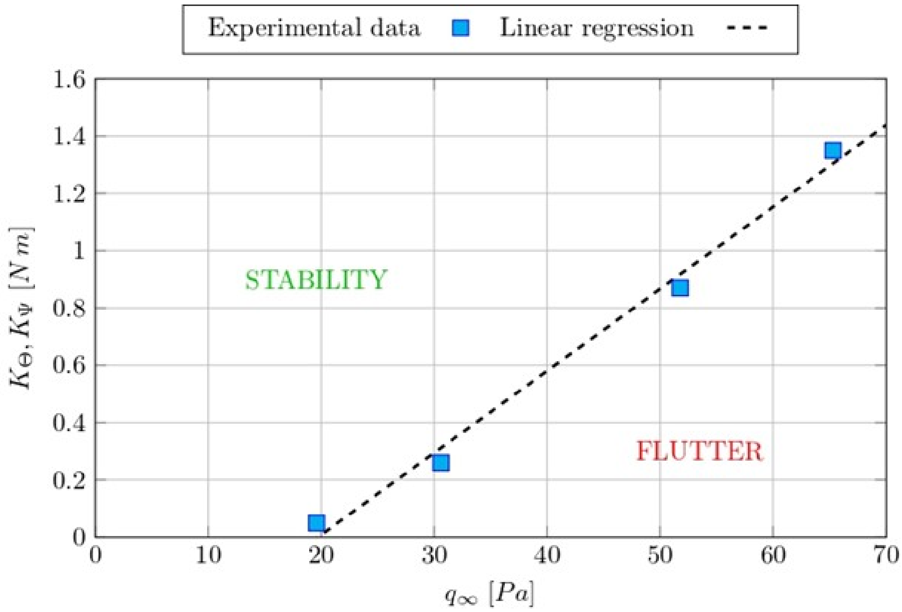

FIGURE 4.18: Experimental whirl flutter boundary. WFSD, high solidity propeller version.

4.6.2 Sensitivity Analyses

Some analyses have been conducted to acquire whirl modes and natural frequencies. In particular, it has been employed the WFSD high solidity propeller configuration. The analyses have been conducted at different stiffness, inertia and freestream velocity values to acquire the natural frequencies trend as the main parameters vary. First of all, a varying freestream velocity investigation is discussed.
In Figure 4.19 the backward and forward whirl natural frequencies behaviour as a function of the freestream velocity is represented. In particular, increasing the flow velocity the propeller angular velocity increases and the two whirl natural frequencies move away from each other.
More in detail, the backward natural frequency decreases and the forward one increases. These frequencies have been also compared with numerical and analytical ones. In particular, they have been plotted as a function of the propeller angular velocity, in the Campbell diagram 4.20. A quite good matching between analytical, numerical and experimental results has been achieved. Furthermore, the natural frequencies behaviour with varying stiffness has been analysed (Figure 4.21(a)). A good correspondence between the results has been obtained. Finally, the whirl natural frequencies behaviour with varying inertia has been analysed. In Figure 4.21(b) the whirl natural frequencies behaviour as a function of the added inertia has been graphed.
A good matching between the results has been achieved for the backward natural frequency behaviour. On the other hand, the experimental trend of the forward natural frequency is slightly decreasing, while the analytical and numerical curves have a larger slope.

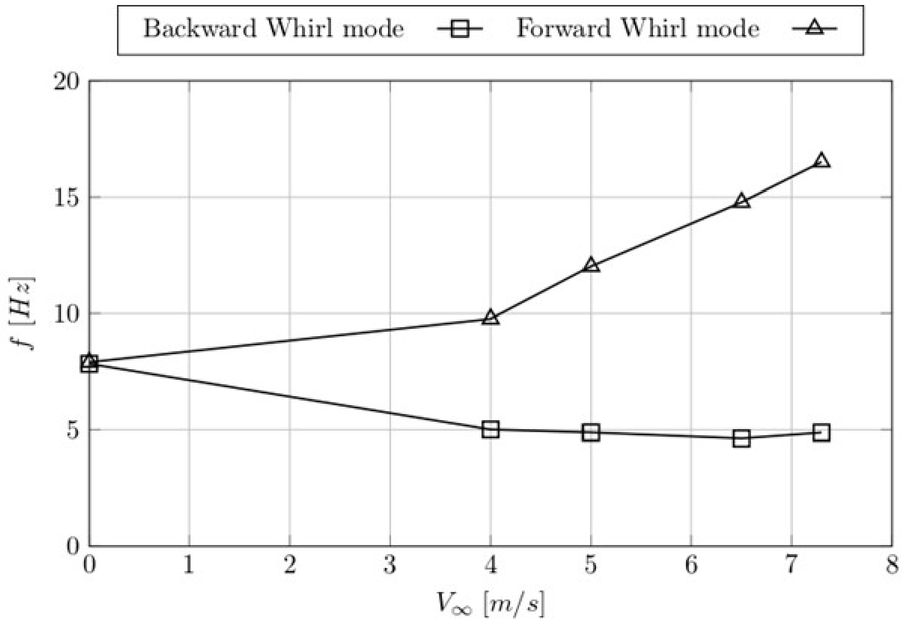

FIGURE 4.19: Backward and forward whirl natural frequencies experimental profile as function of freestream velocity.

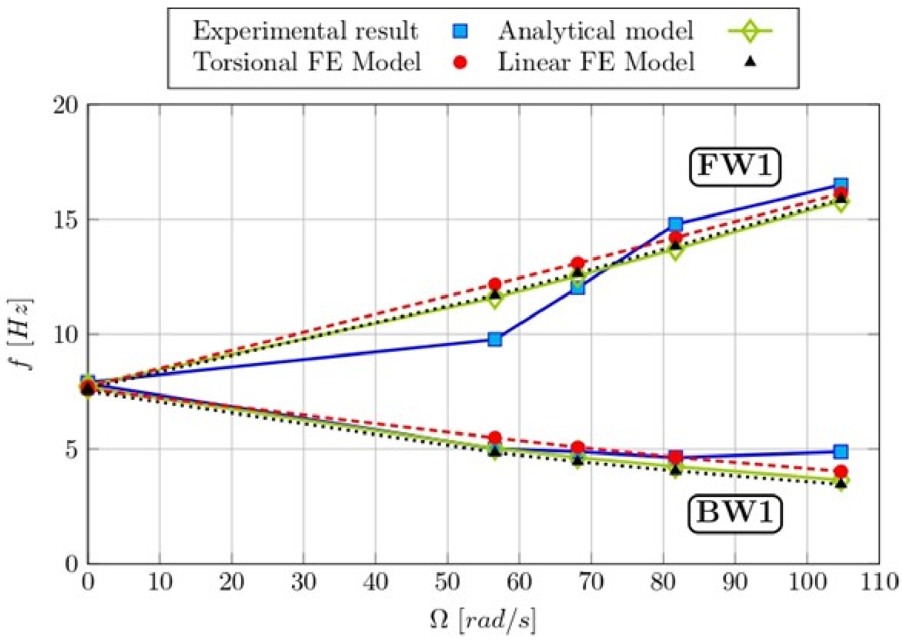

FIGURE 4.20: WFSD - high solidity propeller Campbell diagram. Comparison between experimental, analytical and numerical results.

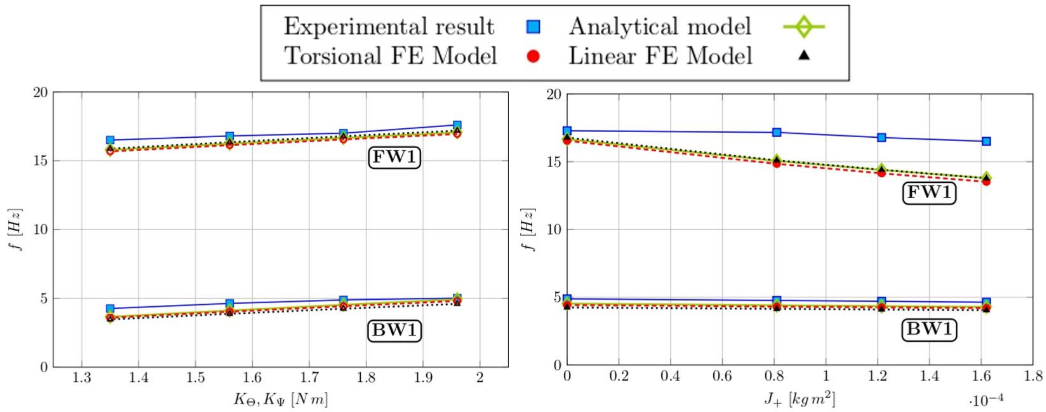

(a) (b)

FIGURE 4.21: Backward and forward whirl natural frequencies behaviour as function of the system stiffness (a) and inertia (b). Comparison between experimental, analytical and numerical results.

4.7 Conclusions

This work had the aim of studying the complex dynamic aeroelastic stability phenomenon of whirl flutter utilizing an in-house designed and developed small-scale demonstrator. Several experimental investigations were made up for both rotating and non-rotating propeller case. Numerical and analytical tools were developed to predict natural frequencies and mode shapes. For the numerical investigation, a one-dimensional beam elements-based model was used. For the rotating propeller numerical investigation, the rotor gyroscopic effects and the propeller aerodynamic forces were included to obtain whirl natural frequencies and mode shapes. Initial experimental studies included non-rotating propeller impact testing. The first lateral mode shapes (pitch and yaw) were detected for both two-blade and five-blade propeller cases. An Operational Modal Analysis of the demonstrator with a rotating windmilling propeller in airstream was performed. Among the most important outputs of the whirl flutter investigation, the first two whirl natural frequencies were detected and plotted as a function of the propeller angular velocity in the Campbell diagram. Finally, an experimental whirl flutter boundary diagram was achieved. Further future improvements will regard the application of a properly aeronautic multi-blade propeller on the WFSD and the deployment of a wind tunnel. Also, a larger version of the demonstrator could be developed. Another future application is the development of methodologies to be used with standard Nastran Doublet Lattice Method aeroelastic solver to obtain a more reliable solution of propeller aerodynamic forces. It would also be interesting to vary the freestream velocity continuously and to create a spectrogram to observe the evolution of the whirl natural frequencies as the freestream velocity varies. Finally, another future application will regard a non-linear analysis to take into account the stiffness and especially damping non-linearity.

Chapter 5

Structural Scalability

5.1 Introduction to Scalability

The tiltrotor wing structure is one of the most critical and heavily analyzed structures in the design due to the fundamental need to consider the interaction between the wing, pylon, and rotor systems to achieve aircraft aeroelastic stability. Indeed, in high-speed forward flight, wing bending and torsional stiffness have a fundamental role in the pitch-whirl stability.
Another specific concern of tiltrotors is the dynamic mode placement: it needs to properly place wing bending modes away from proprotor forcing frequencies [81].
A wing can be considered essentially as a beam able to transmit and concentrate the applied air load to the central attachment to the fuselage. As well as the wings of conventional aircraft, also the wings of high-performance tiltrotors, they require longitudinal members to withstand the bending moment which is greatest during flight, both cruise and maneuvers, and upon landing.
The basic shape of the wing for a tiltrotor is mainly driven by mission requirements. In the specific case of the NGCTR-TD the main objective was to design and realize a new high lift, low drag wing optimized to improve downwash impingement in helicopter mode and to increase the total fuel capacity. Downwash impingement is improved by the design of two movable surfaces, an outboard flaperon, and a morphing surface. The rotation of the morphing surface exposes a curved architecture that improved downwash impingement too. Such curved architecture maximizes available internal space to increase fuel capacity to match the requirement of extending the range of the tiltrotor. Space requirements for the housing of fuel tanks and the driving shaft are the main reason for the three-spar wing box configuration. The design of the wing must be compatible with strength, stiffness, and lightweight structure requirements and at the same time to offer a minimum of manufacturing problems.
This extremely challenging and critical aspect from the design point of view is very evident for the installation of the various access holes contained in the wing box structure.

For the wing of the tiltrotor, structural integrity and maintenance are aspects of fundamental importance. T-WING project could be considered a multidisciplinary development involving several research/technical topics such as the structural design, modeling, physical test, full-scale tests, system for loads in-flight monitoring, manufacturing, integration, airworthiness, and so on, performing at the same time studies on the scalability potential of the proposed solutions for the exploitation of the technologies on , the NGCTR.
The present chapter contains an assessment of the scalability of the NGCTR-TD composite wing-box up to the NGCTR (MTOW = 14000 kg), by taking into account the most relevant requirements that had a big impact on the design of the NGCTR-TD, namely the whirl flutter and the crashworthiness requirements.
Starting by presenting the TD wingbox and scaling objectives, this chapter will introduce the scaling methodology and the adopted optimization routine. Due to the complexity of the structure in the study, it was decided that a commercial code should be used to calculate the flutter speed and characteristics. The program used to perform these tasks was the Nastran^{TM} software, which integrates the essential disciplines required by aeroelastic design and analysis.
(...) Scalability is an important concept which runs parallely with aircraft family.
For a successful result it is necessary to move gradually, iterating and providing trade-offs step by step: by moving too much forward or backward from the starting point may result in wrong decisions.
Starting from the data related to the reference tiltrotor, some wing characteristics can be calculated, such as structural efficiency of the primary structure, weight of non-structural items and movable surfaces, initial stiffness estimate.
There are not enough detailed tiltrotor wing designs to establish a statistical database for wing weight prediction.Unlike the large availability of data about weights, MTOW, etc. concerning classical aircraft, given the peculiarity of the tiltrotors, a detailed preliminary research on the weights of the tiltrotor wings existing or in the design or prototyping phase was necessary [82–91]. Table 5.1 summarizes the results of this research. It shows the data found: the maximum take-off weight of the tiltrotor W_0, the structural weight of the wing W_w, the ratio between the two weights W_w/W_0. It can be seen how the ratio between the two weights is kept almost constant as the tiltrotor considered varies. This value is included in a range from 6.1% to 7.3%.

5.2 Basic T-Wing Configuration

The wing design is very peculiar to the tiltrotor aircraft. It features characteristics and constraints which are very different from conventional fixed-wing aircraft and therefore it presents specific challenges.
A key goal is to reduce the complexity of the wing making it straight with no dihedral or sweep, and so providing easier assembly of the interconnecting shaft and eliminating the need for a mid-wing gearbox.

TABLE 5.1: Weight of wings and maximum take-off weight of some tiltrotor of reference

	W_0 **(kg)**	W_w **(kg)**	W_w/W_0
I	5,896	429	0.073
II	7,322	521	0.071
III	10,000	680	0.068
IV	48,842	3,012	0.062
V	56,035	3,992	0.071
VI	66,832	4,042	0.061
VII	66,958	4,076	0.061

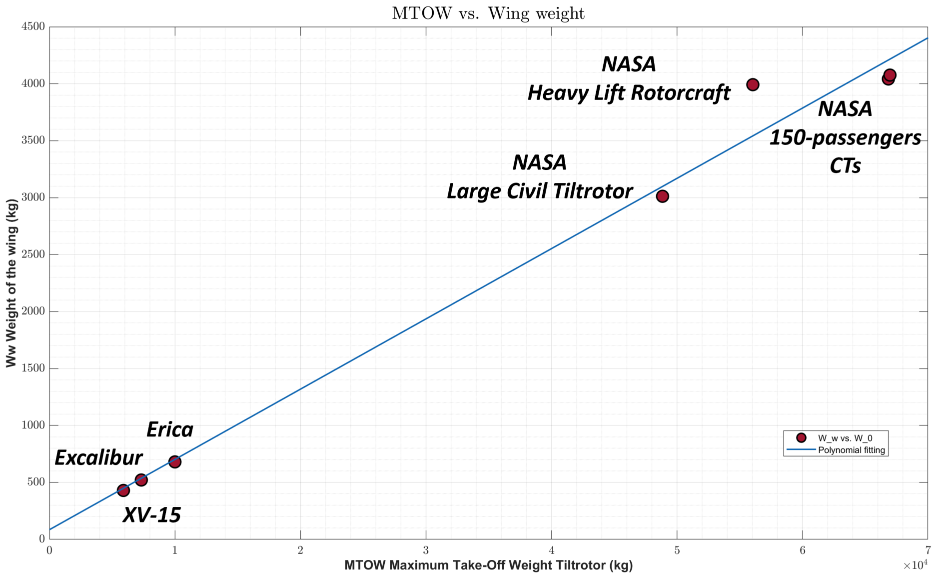

FIGURE 5.1: Weight of the wing vs. Maximum take-off weight tiltrotor

The TD wing will use flaps much larger than those of any prior tiltrotor. These devices are required because of the fixed engine configuration and the huger download from rotors. In addition, a quite important challenge will be to provide maximum wing aerodynamic efficiency in flight while taking into account all the required equipment and specific sub-systems functions to be maintained.
Downwash impingement is improved by the design of two movable surfaces: an outboard flaperon (blue in fig. 5.2), about 28% of total chord and about 32% semi-wingspan, which rotates downwards by 70° and upwards by 30° and a morphing surface (green in fig. 5.2), about 45% of total chord and about 32% semi-wingspan, which rotates downwards by 80° and upwards by 5° in helicopter mode to reduce the wing area beneath the rotors. The rotation of the morphing surface exposes a curved architecture that improved downwash impingement too. Such curved architecture maximizes available internal space to increase fuel capacity. Between front

spar and middle spar, an interconnect driveshaft which connects together both gearboxes runs along connected to the middle spar. Several Leading Edge sheet metal removable panels, which are resistant to bird-strike, compose the leading edge. No anti/de-icing provisions are foreseen on the TD. The outboard end of the main wing box provides the attachments for the prop rotor gearbox, engines and nacelle structure.

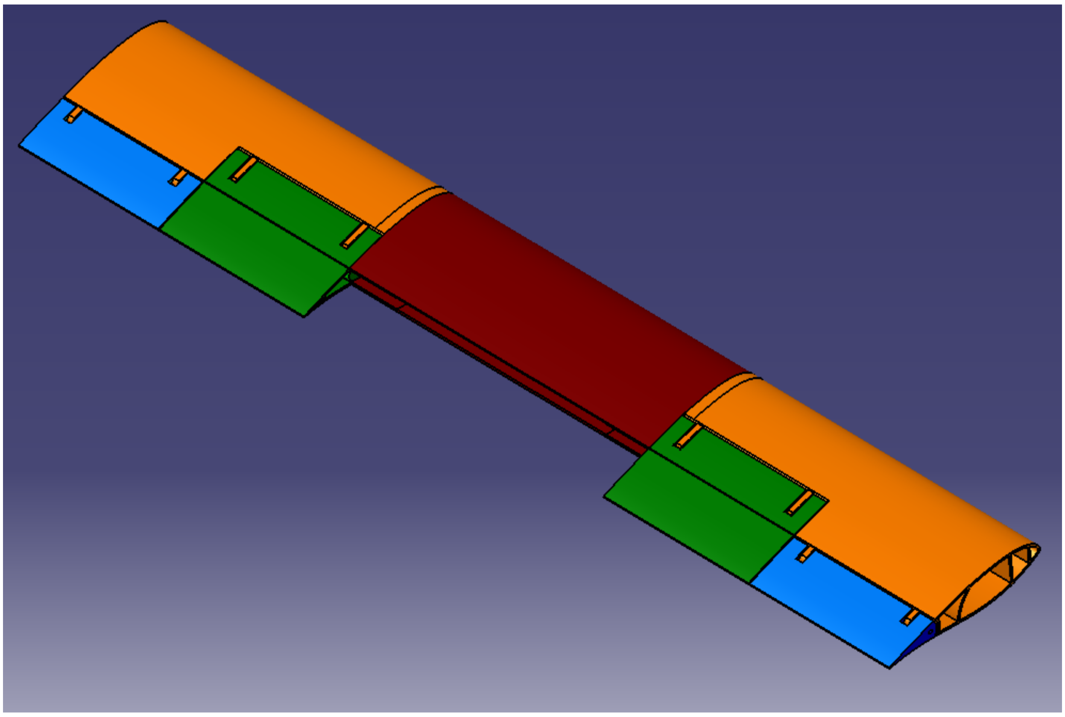

FIGURE 5.2: NGCTR-TD Wing General Layout.

The NGCTR-TD Wing is a multi-cell torque box constructed primarily of composite materials. The wing has a chord of 75 inches (1905 mm) and is divided into two half wing, linked by an upper splice fitting, each one has a span of 237.6 inches (6035 mm).

The upper skin panel is a single continuous composite panel running from tip to the aircraft centerline. Front and Middle spar are co-cured with the upper panel. Two continuous composite Ω stringers are co-bonded to the uncured upper skin. The lower skin panel is divided into three parts, one central and two lateral. On each lateral lower panel, one composite Ω stringer is co-bonded. The lower skin has structural access panels to accommodate the internal fuel bladders. To allow accessibility for inspection, repair and maintenance, structural composite removable panels, five per side, attached to lower skin, compose the wing box.

The composite spars, front and middle, are located at 7% and 19.1% chord. Each of these spars is composed of two separate sections, running from Buttok Line (BL) 24 to BL 237.6. Composite middle spar is spliced by clips at the side of body metallic ribs. From BL24 LH to BL24 RH, aligned with front and middle composite spar, two

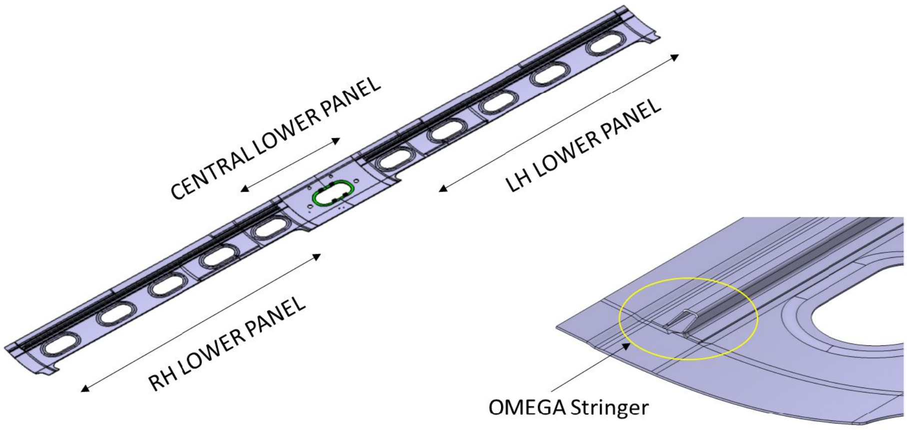

FIGURE 5.3: Composite Lower Panel Section

metallic spars are jointed to ribs and composite spars. A third metallic spar (rear) is located at 45.8% chord.

5.3 Up- scaling T-Wing Layout

The up-scaled wing design has to take into account many aspects: planform, spar and stringer location, morphings and flaperons, and many other spaces hosting shafts, fuel bags, mechanical, hydraulic, and electrical systems, and so on.
It was necessary to carry out a preliminary investigation to locate the main elements of the wing structure to define a geometric configuration subject to the study of the structural optimization process.
The logical flowchart was to draw the planform of the up-scaled wing with the necessary dimension to satisfy the wingspan and wing area provided by LHD. Locate the front, middle and rear spar at the same percentage of the chord adopted for TWING. The rear spar is located so that the up-scaled movable surfaces can be accommodated.
Ribs are used to hold the cover panel to contour shape and to limit the length of skin-stringer panels to an efficient column compressive strength. Ribs are likely to be located at each morphing and flap hinge.
The ribs spacing is determined from panel-size considerations, to which reference should be made. Some adjustments in the rib spacing may be desirable to get hinge-rib locations to coincide with the rib stations [81].
With a view to preliminary structural optimization, since the weight of the ribs is a significant amount of the total wing box structure, it is important to include the ribs in the overall optimization consideration of the structure. This is illustrated in Figure 5.4 where the relative weight of ribs and cover panels refer to the spanwise. It is advantageous to select a larger rib spacing.

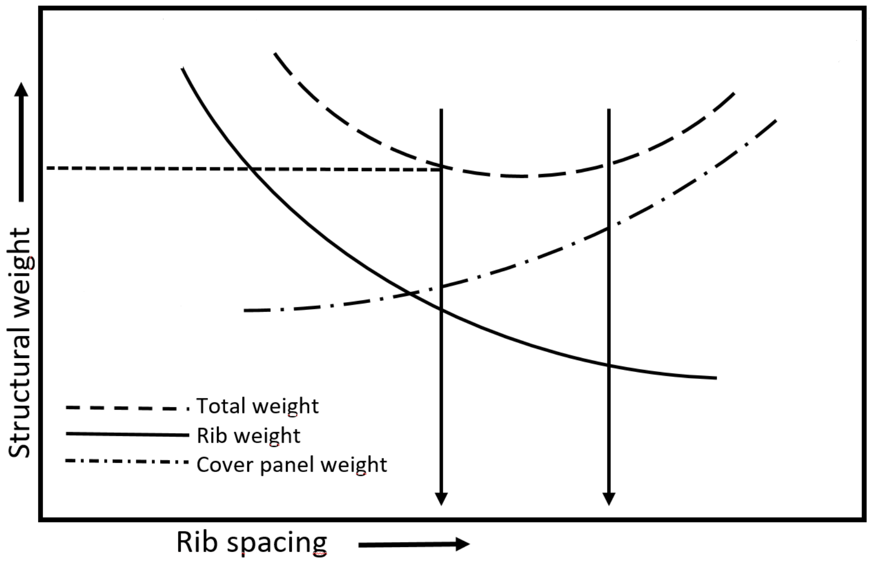

FIGURE 5.4: Determination of rib spacing by structural weight comparison

Once the primary wing structure has been defined, based on a set of load conditions, the stress analysis and optimization are started to define the distribution of the thickness of the covers along the wingspan. A first general expected result about the wing covers, considering that the wing bending loads that cause compression at the upper surface of the wing are generally higher than those causing compression at the lower surface. This requires that the stiffening elements along the upper surface be more efficient and also more closely spaced than those on the lower surface. The torsional moments are primarily resisted by the skin and the front and rear spars. The air loads act on the wing panels which transmit them to the ribs. The latter transfer them as shear loads to the main spar structures distributing the load in proportion to the stiffnesses of the webs. The use of multi spar allows a reduction in rib stresses and better support for the spanwise bending material.

5.3.1 Up-Scaled Structural Architecture

Among the various optimization process inputs, there is also the rib spacing defined based on preliminary calculation runs and to move within the range for which the overall weight of the wing structure does not increase. Also comparing the LHD's size requirements, it was possible to find a geometric scaling factor of 1.289.
The up-scaled wing has a chord of 96.7 inches (2456 mm) and is divided into two half wings, linked by an upper splice fitting, each one has a span of 289.8 inches (7360 mm). NGCTR wing has two movable surfaces: an outboard flaperon, about 28% (27.1 inches - 687.6 mm) of total chord and 83.98 inches (2113 mm) span and a morphing surface, about 45% (43.5 inches - 1105 mm) of total chord and 86.26 inches

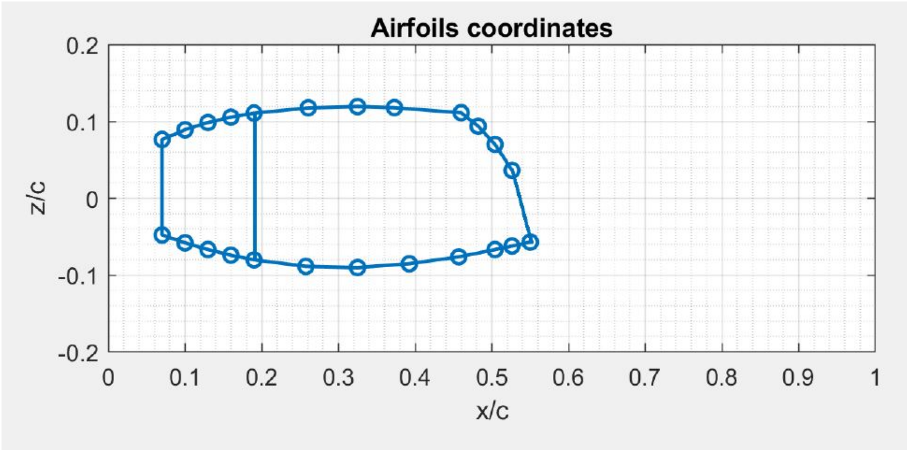

FIGURE 5.5: Up-scaled wing Airfoil coordinates

TABLE 5.2: NGCTR - wingspan % Rib Spacing

RIB 1	RIB 2	RIB 3	RIB 4	RIB 5	RIB 6
11.96%	29.08%	47.13%	63.27%	80.35%	100%

(2191 mm) span.
The airfoil of the NGCTR Wing is assumed to the same as the T-Wing airfoil, as well as the architecture of the wing box and the percentage wingspan and chord occupied by the moveable surfaces. Therefore NGCTR wing is a multi-cell torque box (Figure 5.5).

The same number of ribs along the wing was assumed for the up-scaled NGCTR wing. The first rib is located 30.9 inches from the wing-fuselage attachment. The tip rib is positioned, at 258.3 inches from the wing-fuselage attachment. Rib spacing is listed in Table 5.2 and shown in Figure 5.6. The number of wing-box stringers considered in the present study is equal to 9.

5.3.2 Up- scaled stiffness Data

In addition to a target weight requirement of the wing, the whirl flutter requirement is expressed as minimum flexural and torsional stiffnesses to comply with in the optimization problem.
The two distributions of flexural stiffnesses (bending and fore and aft) and the torsional stiffness have been provided by LHD. They are constant spanwise and equal to: EI_{xx} = 1.65E10 $Lbsxin^2$ (out-of-plane flexural stiffness), EI_{zz} = 4.83E10 $Lbsxin^2$ (fore-and-aft flexural stiffness), GJ = 1.65E10 $Lbsxin^2$ (torsional stiffness).
The Figure 5.7 shows the wing model whose stiffness and mass distributions are such as to consider the wing free from whirl flutter.

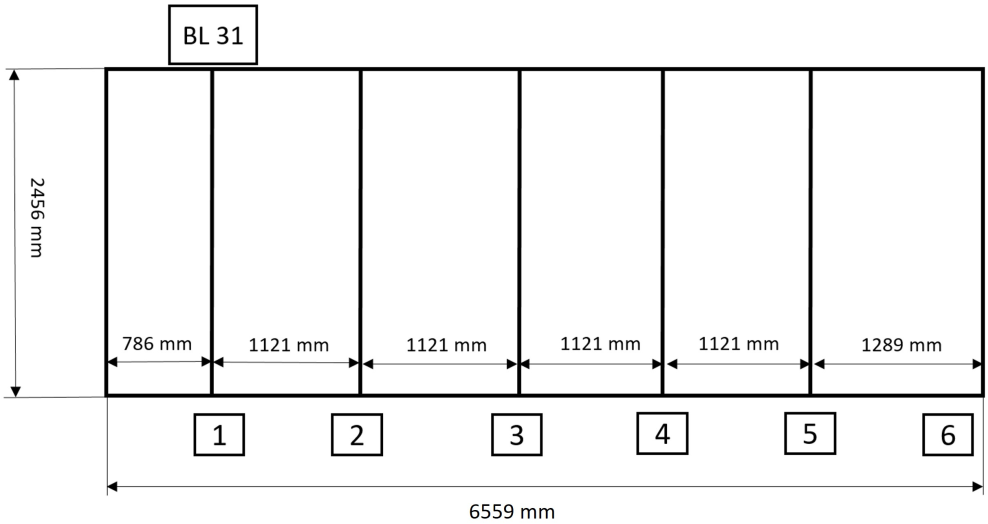

FIGURE 5.6: Rib spacing - NGCTR up-scaled wing

5.4 Materials

As regards the materials, for the optimization purpose, five different materials, reported in Table 5.3 were considered. More in detail, MAT01, and MAT05 are composite materials of the fabric type. MAT03 and MAT04 are unidirectional tape laminates whereas MAT02 is a unidirectional tape plus woven fabric impregnated. It is worthwhile to note that, according to T-WING consortium heritage, the only qualified materials are MAT 01 and MAT 02 for the T-WING wing box.
In other words, MAT01 and MAT02 are materials whose stacking sequence is known. The remaining materials are considered eligible for Scalability purposes and would require the qualification path in case if they were selected for the up-scaled configuration.
Optimization of composite structures considers the stacking sequence as a key parameter.
For the database of materials to be supplied to the Multicella tool, some assumptions have been made for the new materials such as tape and fabric. In particular:

- for tape-type MAT03 and MAT04, the allowable strain values are assumed to be equal to the average of the allowable strain values of MAT02. The allowable stress values were calculated by multiplying the allowable strain values for engineering properties (E11 and G12) known from commercial data-sheets.
- for fabric-type MAT05, the same stacking sequences and allowable strain values of MAT01 have been assume. The allowable stress values have been calculated by multiplying the allowable strain values by the corresponding engineering properties (which for fabric-type materials are the average between E11 and E22 and, G12).

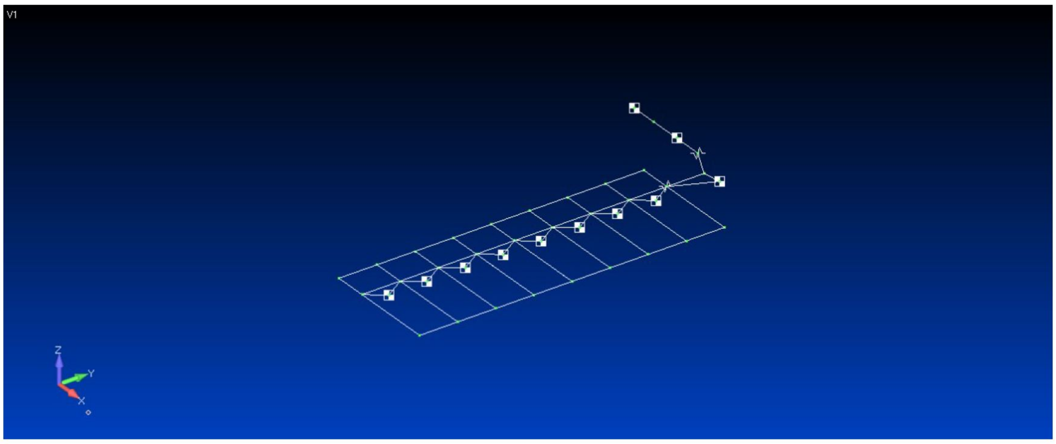

FIGURE 5.7: Dynamic model of the NGCTR up-scaled wing (stiffness and mass distributions)

TABLE 5.3: Materials used in the Optimization Process.

	Materials
MAT 01	Solvay CYCOM® 977-2A HTA
MAT 02	Solvay CYCOM® 977-2/IMS UD
MAT 03	Toray M60J
MAT 04	Toray M46J Tape
MAT 05	Toray M46J Fabric

All the allowable values are finally scaled by a factor 1.5 to be able to work at load limit (not at the ultimate load).

5.4.1 Crashworthiness

The crashworthiness requirements are taken into account in a successive step of the up-scaled optimization, nevertheless how the requirement will be implemented in the optimization, is briefly recalled herein. The requirement will be implemented based on the experience developed with the NGCTR-TD wing.
In the NGCTR-TD wing, to obtain the frangible section failure before the full acceleration level is achieved, an analysis was performed, based on linear calculation, aimed at demonstrating a progressive failure of the wing section under investigation and at evaluating the load factor at which the wing fails without endangering all the other operative and emergency conditions, i.e. a load factor well beyond the ditching load case. The procedure was set up starting from LHD's experience and considering the specific characteristic of the NGCTR-TD wing.
The process flow of the crash analysis for the frangible section is depicted in Fig. 5.8. It can be considered a general method to be applied for the tilt-rotor crashworthiness requirements during the sizing phase, and it is performed on the standalone wing constrained in correspondence of junction with the fuselage. This process will be

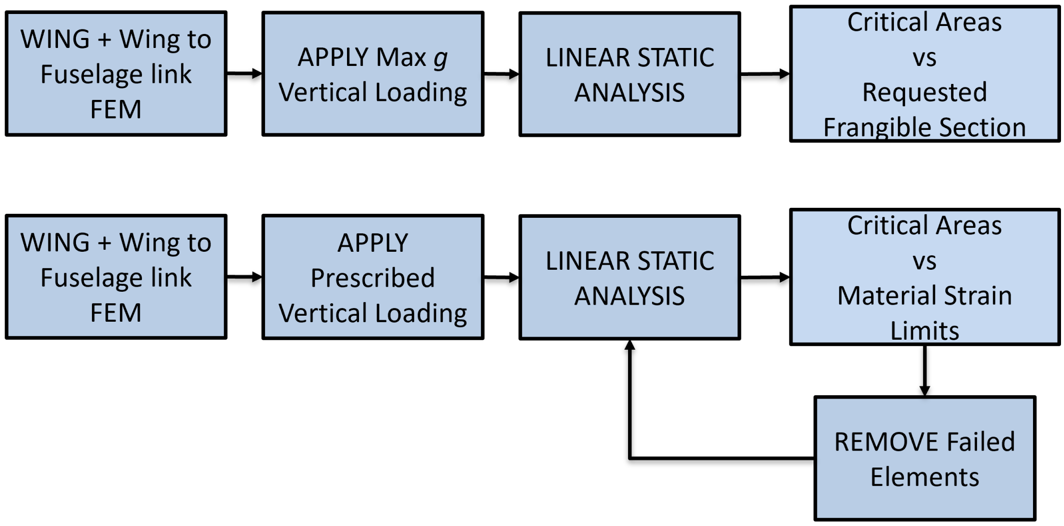

FIGURE 5.8: Stage 1 crash: selection of critical wing section; Stage 2 crash: demonstration of progressive failure of frangible section.

repeated in the 2^{nd} phase of the scalability study (Figure 5.9).
To define the crashworthiness requirement for the NGCTR wing the first step was to identify the desired frangible section. The same vertical load factor at crash ($n_z = 5$) was assumed for the up-scaled wing crash loads. A Matlab tool has been developed which, starting from the distribution of the masses, calculates the load acting along the wing during the crash load condition factor ($n_z = 5$), by integrating the inertia forces, and provides the shear and bending moment diagrams.
For the calculation of the inertia forces on the wing, the mass of the entire structure is considered (wing box, movable surfaces, fuel, and systems). The Matlab function outputs forces and moments (F_x, F_y, F_z, M_x, M_y, M_z). Starting with mass distributions of the dynamic model in the figure 5.7, the distributions of Shear Force and Bending Moment along the NGCTR-TD and NGCTR up-scaled wingspan are obtained (Figs. 5.10 and 5.11).
To implement the crash requirement in the optimizer, it will be imposed as constraint, the failure of the structure around the frangible section, whilst maintaining a minimum Margin of Safety elsewhere in the wing.
The simplified choice of the optimization constraint of having a low margin of safety in the so-called frangible section and a higher margin of safety in the other locations was based on the preliminary information coming from linear static crash analyses executed by another partner of the consortium T-Wing. Of course this is a low fidelity approach that is meant to be the starting point of the subsequent phase of design, relying on more refined models and tools to properly catch the phenomena with higher fidelity. The plan is to validate the crash linear static analyses with non-linear dynamic analyses and currently a detailed model of the wing plus the fuselage is work in progress by another partner.

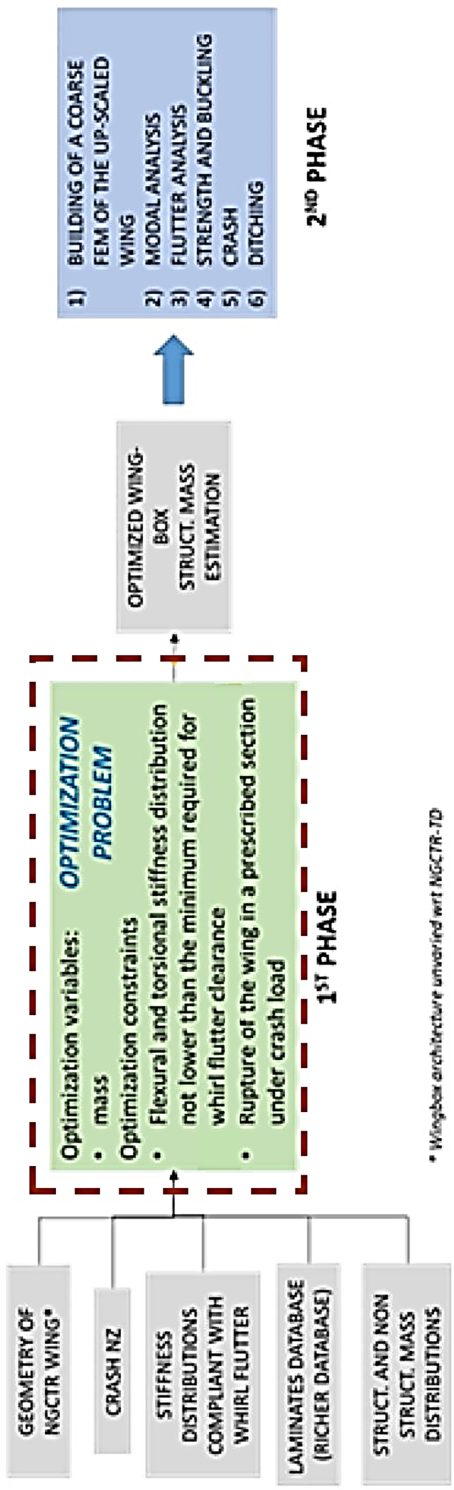

FIGURE 5.9: Diagram of the two phases of the optimization process.

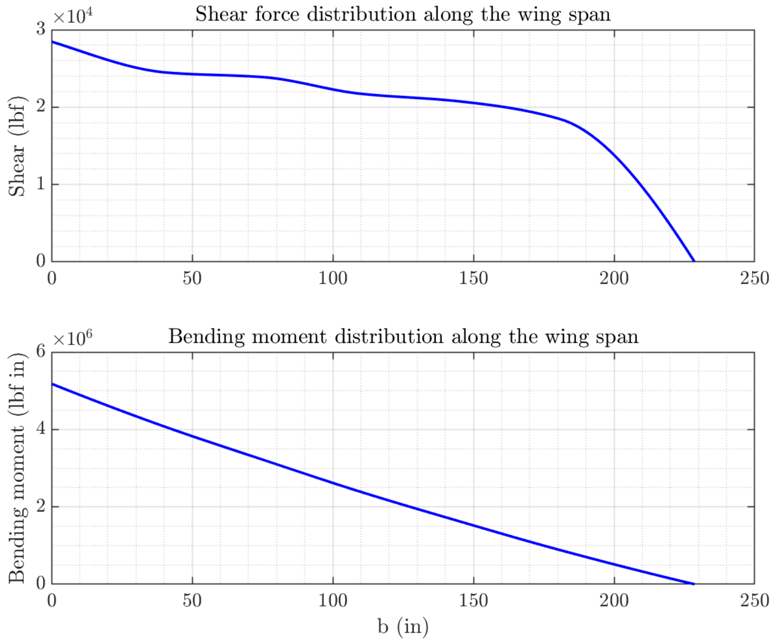

FIGURE 5.10: Shear Force and Bending Moment along T-WING wingspan.

5.5 Input for Scalability assessment

In order to perform a satisfactory Structural Scalability of the wing from NGCTR-TD to NGCTR, some inputs pertaining the NGCTR are needed. In the following a quite exhaustive list is reported:

- Geometry of NGCTR wing (wingspan, chord, movable surfaces wingspan and chord extension);
- Wing-span structural and Non-Structural Mass Distribution (primary structure, fuel, systems);
- Wing-span stiffness Distribution (Compliant with Whirl Flutter);
- NGCTR Data (MTOW, Fuselage radius, etc.).

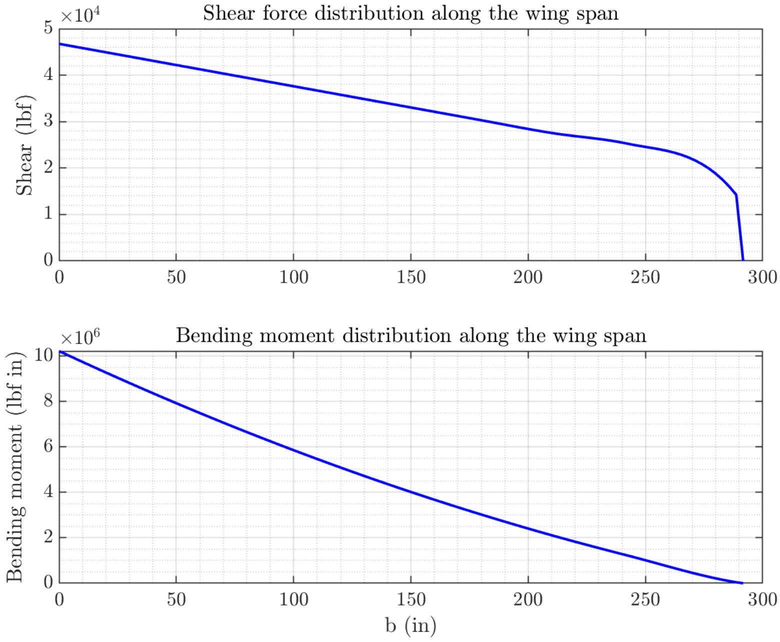

FIGURE 5.11: Shear Force and Bending Moment along up-scaled wingspan.

5.6 Tools and methods for Multi-objective Optimization

Within the T-WING project, an optimization tool has been set up, starting from a Matlab code, named Multicella. In its original version, Matlab code was originally aimed at performing a preliminary sizing of a composite wing box structure, basing on composite strength and buckling.
Through a further implementation of the Multicella, a Multi-Objective Genetic Algorithm optimization code has been included in the tool. Thanks to this optimization tool, it was possible to size skins, spars, and stringers of the NGCTR-TD pre-defined wing box architecture at minimum structural mass.
A brief description of the tools and methods used for Multi-objective optimization is provided hereafter.

5.7 Multi-Objective Optimization Tool - Multicella

When you have several objective functions that you want to optimize simultaneously, these solvers find the optimal tradeoffs between the competing objective functions.
Multi-objective optimization (MOO) involves minimizing or maximizing multiple objective functions subject to a set of constraints. Example problems include analyzing design tradeoffs, selecting an optimal product or process design, or any other application where you need an optimal solution with tradeoffs between two or more conflicting objectives. MO is widely used in many fields, such as:

- Engineering (Construction Design, Chip Design, Chemical Process, Manufacturing, Engine Design...);
- Finance (Risk return in portfolio management);
- Economics (Consumer demand supply study, Monetary policy, Production possibilities frontier...).

The wing box structure can be considered a compound engineering system which design has many objectives to be minimized or maximized. This leads to a MOO problem. Multicella was used to optimize the up-scaled wing box architecture. Multi-Objective optimization, based on a Genetic Algorithm, is written in Matlab language and used to optimize the wing-box structure. This robust and efficient tool provides a set of optimal solutions for a MOO problem since the final decision is always a trade-off. Multicella output is a Pareto front, constituted of design points of non-dominated optimal solutions: on the Pareto front, a solution that best fits the requirements of the design can be chosen (performing a-posteriori trade-off between non-dominated solutions). Figure 8 shows the block diagram of the Multicella code operational flow. As optimization variables, the thicknesses and areas of the different structural parts (wing box panels and stringers) of the wing box are chosen. Optimization objectives are the wing structural mass (to be minimized), and the strength and buckling Margin of Safety (MS) (to be maximized). In addition, the points on the Pareto front are labeled with the wing box torsional stiffness and the wing box first bending normal mode (calculated off-line, at the end of the optimization phase) to restrict feasible solutions to comply with other design requirements. The optimization phase is based on a Genetic Algorithm due to its capabilities to explore a huge space constituted by a lot of design variables with numerous local maxima and minima. The following input data are needed by the program:

- Semi-wing plan form;
- Aerofoil shape;
- Loads beam characteristics (Shear, Tension, Bending and Torque, i.e. F_x, F_y, F_z, M_x, M_y, M_z at each section where the stress has to be evaluated) at representative buttock lines of the wing span;
- Material database that is used for structural elements in the section (caps and panels modelling spars and skins). The database is constituted of:
  1. Density, Elastic and Shear moduli, the lamina material;
  2. the composite stacking sequences for skin and stringers;
  3. the composite material strength characteristics (tensile, compressive, shear allowables) and buckling loads.
- Caps chord wise length (that multiplied by thickness gives their areas);

- Wing buttock lines at which the output has to be calculated.

As regards material data, if the material is orthotropic (e.g. CFRP laminate) the properties are inputted as laminate equivalent engineering properties (preliminary calculated by means of the classical lamination theory -once lamina level properties and lamination sequence are known- by using a dedicated spreadsheet named laminate.xls, and introduced in the optimization-input database). The optimization tool is able to calculate, for a multiple-cell wing box section, the following quantities:

- Internal normal and shear stresses and corresponding margins of safety;
- Buckling margins of safety;
- Torsional and flexural stiffness;
- Total and span wise structural mass estimation, with also a subdivision among the structural components (skin, spar, stringer, webs).

5.7.1 Multi-Objective Optimization Tool Technical Description

The structural analysis and optimization process can be considered split into different phases. At each step, a dedicated set of files is used. The various phases can be summarized as follows:

5.7.2 Wing Geometry

Wing box geometry is expressed through a series of input files. These files are red by the main Matlab code before the optimization on skin thickness and cap areas is started. The names of the files used in the current tool release are listed and described below:

- *prof.dat*

It contains information on the geometry of the wing profile in terms of normalized points coordinates with respect to the chord (x/c and z/c), in a suitable reference system. The origin of the reference system is placed on the leading edge. The x axis is along the wing cross-section chord and directed from leading edge to trailing edge; the vertical z axis is directed upwards.

- *panel.dat*

Identifies the connections between the points of *prof.dat* making up the profile; that is, the front spar, the middle spar, the rear spar, the lower skin and the upper skin of the section are defined.

- *corde.dat*

This file contains the variation of the chord along the wingspan (y axis), starting from the root and moving towards the tip of the wing. The coordinates of the leading edge and trailing edge are expressed in meters; the x axis is positively oriented from the leading edge towards the trailing edge.

- *stringer.dat*

This file indicates the points of *prof.dat* where the stringers are positioned and their corresponding lengths (mm).

5.7.3 Wing Segmentation

The second step consists in dividing the wing into structural groups whose thicknesses will be optimized. This makes the structural analysis and the optimization processes easier and more efficient. The files containing the grouping information are listed below:
1. Grouping for strength analysis:

- *stazioni_calcolo.dat*:

this files contains the sections along wingspan where the tension and shear stresses will be calculated. This file subdivides skin and stringers spanwise. Generally, ribs and other "discontinuities" (like start and end of a movable surface) define the spanwise segmentation;

- *panelGrouping.dat*: each line of this file corresponds to a group of panels defined in *panel.dat* that define a part of the skin whose thickness is intended to be optimized as a whole.

- *Spanwise.dat*: this file contains the identification of the sections (along the wing) and defines the segments for the buckling analysis. The segment ends where the next one begins. 1 refers to the first section defined in *stazioni_calcolo.dat*, 2 to the second section and so on.

2. Grouping for buckling analysis:
For wing skin supported by stiffeners, the buckling can be considered to arise in panels delimited by the stringers and the ribs of the wing box; Therefore, it is convenient to have files that identify the panels to be analyzed for Buckling purpose. The following two files are intended to provide the panels to be analysed, respectively along the chord and the wingspan:

- *panelBucklingChordwise.dat* is similar to *panelGrouping.dat*. It groups panels contained in *panel.dat* to identify panels for buckling analysis;

- *panelBucklingSpanwise.dat* basically identify the wing sections where ribs are present.

5.7.4 Material Database

EGnu.dat This file contains the homogenised values of the mechanical properties (Elastic modulus along both direction, Shear modulus and Poisson's ratio) for several laminates that can be used for wing panels and caps (different thicknesses and different fibers orientation and layups). Lamina mechanical properties can be derived from experimental tests for various temperature conditions.

5.7.5 Wing Loading Conditions

WingLoad4Optxxx.mat It is a matlab file consisting of an array containing, for various wing stations, the six beam load components F_x, F_y, F_z,M_x, M_y, M_z (forces and moments with respect to the 3 axes of the cross-section: x axis from the leading to the trailing edge, y axis spanwise from root to tip and z axis upwards). This file is generated from the load conditions provided by LHD (Shear, Bending, Torsion, etc.).

5.7.6 Buckling Limit Loads

Buckling is the failure of a structural element when a portion of the element moves normal to the direction of primary load application. The deformation alters the mechanism by which loads are transmitted. It is the combined loading with compression and shear stress components that forces the buckle to occur. When the skin is not thick the buckling stress of the skin may be comparable to the yield stress of the material.
Calling θ the angle obtained from the composition of compression and shear loads, two extreme cases emerge:

θ=0 when a compressive force alone is applied to the panel;

θ=90° when a shear force alone is applied to the panel;

0 <θ< 90° for combined load conditions.

For a fixed θ angle, the compression and shear forces are defined by a certain gain between them. The buckling limit loads are calculated offline for the laminates that will be used in the optimization process and are the stored in a Matlab®file:

- *BucklingPreProWing.mat*. This file is a 5D multidimensional matrix. It contains buckling loads for:

1. the two dimensions of the panels tested at Buckling in the optimization process (derived from panelBucklingChordwise.dat and panelBucklingSpanwise.dat files);

2. the angle θ: from 0°to 90°with a step of 1°;

3. the lay-ups database used for panels (expressed as number of plies of laminates database);

4. the load conditions (CTD or ETW).

For each panel under investigation, the buckling MS is calculated as the ratio between the buckling limit load for the direction θ given by the compression and shear force acting on the panel and the magnitude of the vector composed from this two forces, minus 1.

5.7.7 Optimization Process versus strength or crash

Of the various T-wing design conditions, the one of overriding importance is that the structure should have adequate strength. The primary purpose of the optimization process is to determine the structure which has a minimum weight, sufficient strength (MS at least equal to 0 everywhere) for each assigned load conditions. The last step of the process is to identify the best solution among the various structural configurations obtained on the Pareto front: the one that maximizes the MS and minimizes the overall weight of the wing.

5.8 Genetic Algorithm

The Genetic Algorithm provides several potential solutions to a given problem [92–94]. It is a stochastic global search method that, through the use of probabilistic transition rules, simulates the mechanism of natural biological evolution. GAs operate on a population of potential solutions applying the principle of survival of the fittest to produce better and improved approximations to a solution. At each generation, a new set of approximations is created by the process of selecting individuals according to their level of fitness in the problem domain and breeding them together using operators borrowed from natural genetics. This process leads to the evolution of populations of individuals that are better suited to their environment than the individuals that they were created from, just as in natural adaptation. In the natural world, each individual has a distinguishing ability to survive in its existing environment. Within the operational flow of the GA, the objective function (or fitness function) characterizes each individual's performance in the problem domain and assigns them a fitness value. So, the objective function establishes the basis for the selection of pairs of individuals that will be coupled together during "reproduction": the GA selects certain individuals in the current population, called "parents", and uses them to create individuals in the next generation, called "children" [95, 96]. In other terms, once the individuals have been assigned a score, they can be chosen from the array of individuals, and the mating process continues through subsequent

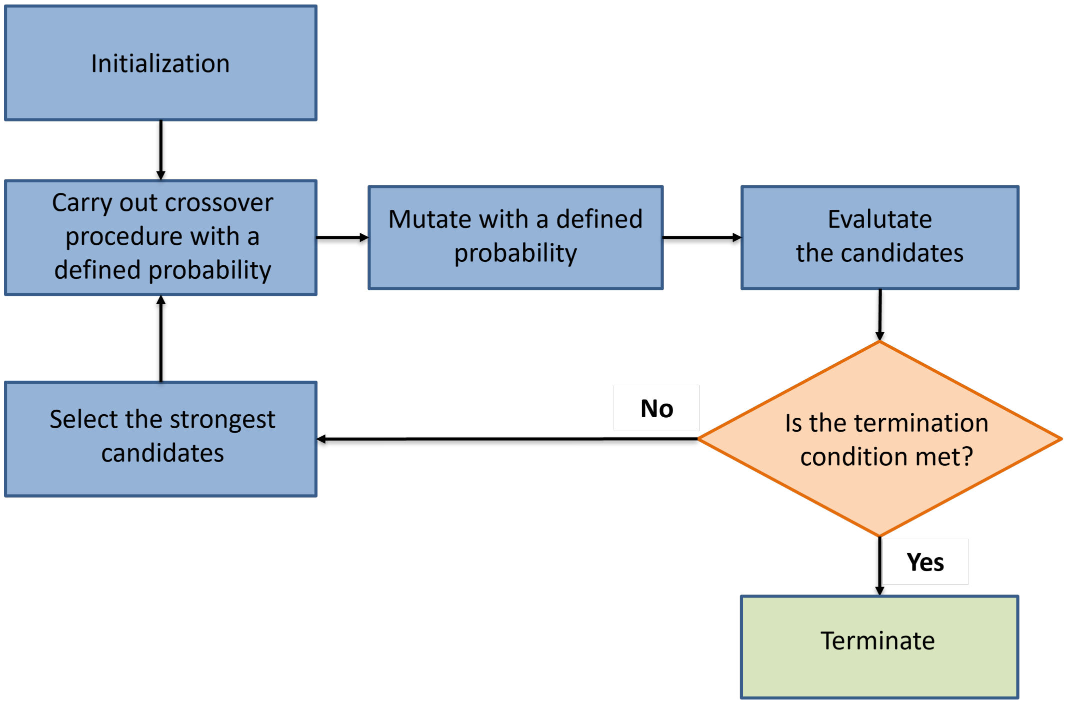

FIGURE 5.12: Flow chart of a general form of the genetic algorithm.

generations. The objective function and corresponding fitness levels influence the directions of the global optimum search. The average performance of individuals in a population is expected to increase, as good individuals are preserved and bred with one another and the fewer fit individuals die out. The GA is terminated when some criteria are satisfied, e.g. a certain number of generations, a mean deviation in the population, or when a particular point in the search space is encountered [97]. A common practice is to terminate the GA after a pre-specified number of generations and then test the quality of the best members of the population against the problem definition. If no acceptable solutions are found, the GA may be restarted or a fresh search initiated. The GA has the significant advantage to search a population of points in parallel, not a single point, making the optimization process very fast. The T-WING preliminary design and the structural scalability process are multi-objective optimization problems, then there is not one individual solution but a family of Pareto-optimal solutions. The GA is potentially useful for identifying these alternative solutions simultaneously however the choice of an ultimate better solution is left to the user. The general form of GAs is presented in Figure 5.12.

The first step of the GA algorithm is the initialization [98]. In the initialization, one generates, often randomly, a population from which new generations are formed. At this point one also needs to define the terminating condition so that the algorithm stops running once an acceptable solution is found [99].
The second step is the Crossover. Crossover is one of the genetic operator used in producing new candidates using the features of the existing ones. The crossover

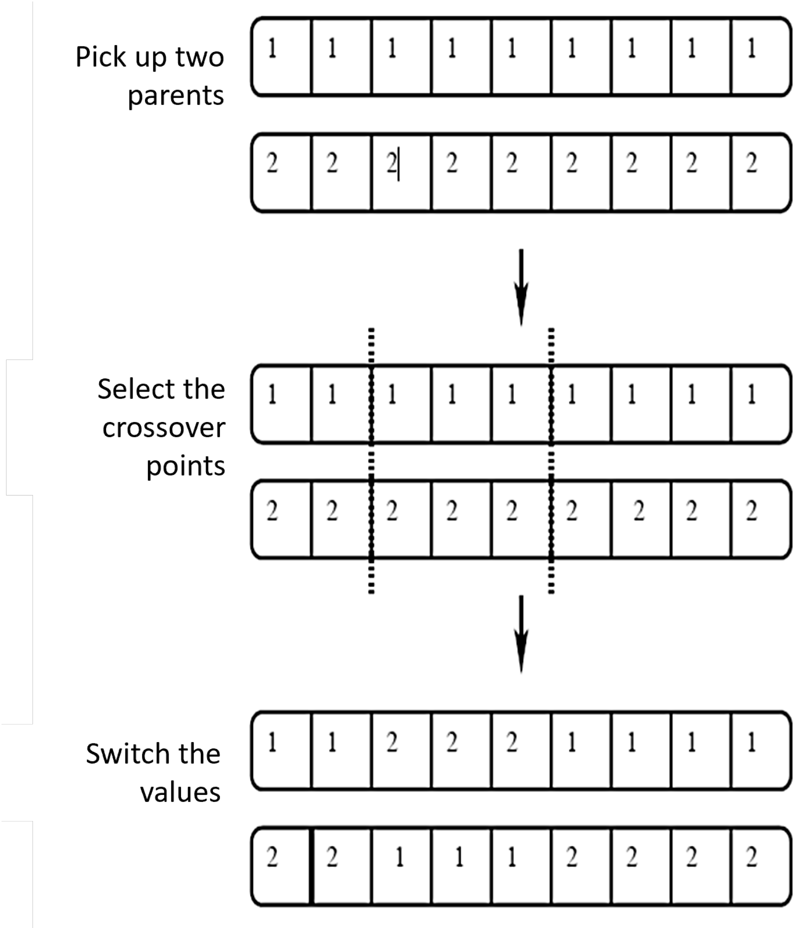

FIGURE 5.13: Crossover procedure.

procedure consists of three parts. First one selects two parents from the population. Then the crossover points are selected. The selection of crossover points is done at random, usually so that the distribution from which the points are drawn from is uniform [100]. In Figure 5.13 two crossover points are marked with dotted lines. Once the points are defined two off springs are generated by interchanging the values between the two parents as illustrated in the figure. In the genetic algorithm crossover is the operator that spreads the advantageous characteristics of the members around the population. Focusing on the third step, in the genetic algorithm mutation is the operator that causes totally new characteristics to appear in the members of the population. In many cases the mutations, of course, result in off springs that are worse than the other members, but sometimes the result has such characteristics that make it better. Figure 5.14 below demonstrates the mutation operation. First, one selects a member from the population to be mutated and a point of mutation. Then the values at the point of mutation is replaced by another value that is picked randomly from the set of all possible values. After the population is manipulated using the genetic operators, the fitness of each of the new off springs is evaluated. For this one needs to have a numerical function and fitness function.

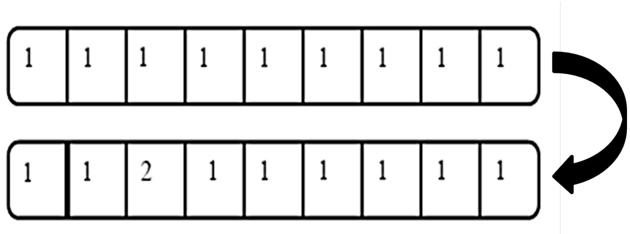

FIGURE 5.14: Mutuation.

In the selection the weakest individuals in the population are eliminated. The fit off springs survive to the next generation.

5.8.1 gamultiobj Matlab toolbox - Introduction

Common approaches for multiobjective optimization include:

- Goal attainment: reduces the values of a linear or nonlinear vector function to attain the goal values given in a goal vector. The relative importance of the goals is indicated using a weight vector. Goal attainment problems may also be subject to linear and nonlinear constraints.

- Minimax: minimizes the worst-case values of a set of multivariate functions, possibly subject to linear and nonlinear constraints.

- Pareto front: finds noninferior solutions—that is, solutions in which an improvement in one objective requires a degradation in another. Solutions are found with either a direct (pattern) search solver or a genetic algorithm. Both can be applied to smooth or nonsmooth problems with linear and nonlinear constraints.

Both goal attainment and minimax problems can be solved by transforming the problem into a standard constrained optimization problem and then using a standard solver to find the solution. Matlab offers various functions for solving optimization processes. The two most popular are:

- *Gamultiobj* - Find Pareto front of multiple fitness functions using genetic algorithm;

- *Paretosearch* - Find points in Pareto set.

The first approach was used for the work presented in this thesis. The gamultiobj Matlab toolbox uses an elitist and controlled genetic algorithm to create a set of points on the Pareto front (Genetic Algorithm TOOLBOX For Use with MATLAB). In general, an elitist GA always favors individuals with better fitness value or rank while a controlled elitist GA also favors individuals that can help increase the diversity of the population even if they have a lower fitness value. In order to describe

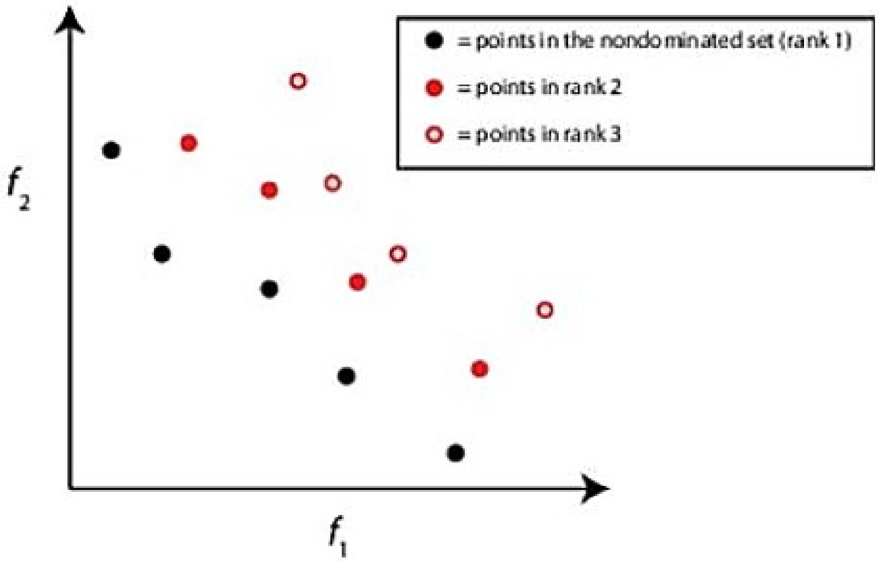

FIGURE 5.15: Dominant points and rank.

the algorithm on which the gamultiobj function and the plot of the Pareto front are based, it is necessary to introduce some definitions:
Dominance — A point x dominates a point y for a vector-valued objective function f when:

$$f_i(x) \leq f_i(y) \tag{5.1}$$

for all i.

$$f_j(x) < f_j(y) \tag{5.2}$$

for some j.
The term "dominate" is equivalent to the term "inferior:" x dominates y exactly when y is inferior to x.

Rank — For feasible individuals, there is an iterative definition of the rank of an individual. Rank 1 individuals are not dominated by any other individuals. Rank 2 individuals are dominated only by rank 1 individuals. In general, rank k individuals are dominated only by individuals in rank $k - 1$ or lower. Individuals with a lower rank have a higher chance of selection: lower rank is better. The gamultiobj function uses rank to select parents. The Figure 5.15 helps to better understand the definitions of dominance and rank. $f1$ and $f2$ are the two generic variables that we are interested in optimizing.

Crowding Distance — The crowding distance is a measure of the closeness of an individual to its nearest neighbors. The gamultiobj algorithm measures distance among individuals of the same rank. By default, the algorithm measures distance in objective function space. However, you can measure the distance in decision variable space, named design variable space. Individuals of the same rank with a higher distance have a higher chance of selection: higher distance is better. Crowding distance is one factor in the calculation of the spread, which is part of a stopping criterion. **Spread** — The spread is a measure of the movement of the Pareto set. To calculate the spread, the gamultiobj algorithm first evaluates σ, the standard deviation of the crowding distance measure of points that are on the Pareto front with finite distance. Q is the number of these points, and d is the average distance measure among these points. The algorithm then evaluates μ, the sum over the k objective function indices of the norm of the difference between the current minimum-value Pareto point for that index and the minimum point for that index in the previous iteration. The spread is then

$$\text{spread} = (\mu + \sigma)/(\mu + Qd) \tag{5.3}$$

The spread is small when the extreme objective function values do not change much between iterations (that is, μ is small) and when the points on the Pareto front are spread evenly (that is, σ is small). The gamultiobj function uses the spread in a stopping condition: iterations halt when the spread does not change much, and the final spread is less than an average of recent spreads.

5.8.2 gamultiobj Matlab toolbox - Flowchart and Technical Description

The first step is the initialization of the *gamultiobj* algorithm: it needs to create an initial population. The user gives an initial population though the GA Pre-processing routine named *OptyWing_GAPrePro*.
The ***OptyWing_GAPrePro*** function sets:

- the limit values for the optimization variables (panel and stringer thickness);
- the number of elements of the GA population;
- the Initial Population i.e. the design configuration from which the GA starts the evolution towards optimal individuals or Optimal design configuration);
- the fitness function for the analysis by means *OptyWing_Fitness* function.

The subroutine ***OptyWing_Stress_Section_Composta***:

- Executes the strength and buckling analysis identifying the MS af all the panels and stringer of the wing box;
- Calculates the mass of the wing box and the wing box sections;
- Calculates the EI and GJ characteristics of the wing box spanwise.

The De Saint-Venant's Theory or Classic Beam Theory considers an initially straight beam whose length L is much greater than the maximum size of the cross section

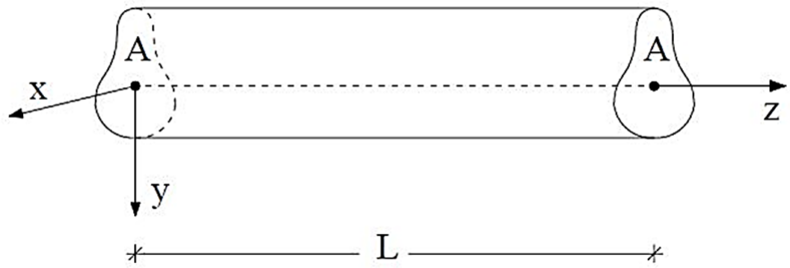

FIGURE 5.16: Generic Beam.

(5.16).
This theory adopts several assumptions:

1. Material homogeneous, isotropic and elastic according to Hooke's law.
2. Smooth and bilateral constraints.
3. Loads applied statically.
4. Lateral surface forces negligible compared to the forces acting on the bases at the ends of the beam.
5. No volume forces.
6. σ_{xx}=σ_{yy}=σ_{xy}=0 i.e. the beam can be considered as a set of longitudinal fibers that exchange tangential mutual forces along the fibers.

By omitting to develop the whole treatment, the De Saint-Venant problem provides the relationships between tensions, deformations, and displacement in a point of a generic section and the stress characteristics in that section. By considering the T-WING cross-section it can be seen as a multi-cell box beam of rectangular shape with skin-stringer panels on top and bottom connected by three vertical beams. A two-cell box is used for the three-spar wing box design to provide the right stiffness to the structure. About the T-WING structural technology, the peculiarity is represented by the rear spar integrated with the upper skin. The skin-stringer panels are subjected to shear flow due to bending moment and torsion. The thin skins take little of the axial compression load and carry shear loads very well and even though they may buckle under the loads they do not fail but continue to carry the buckling loads plus significant additional shear loads. Stringer carries axial loads and shear flow induces a change in axial load in the stringer. For this reason, it is important to perform an analysis of the strength and buckling of these structural elements. For determining beam axial stresses due to bending, the assumptions of the classic Beam Theory are valid. T-WING can be considered as an assembly of panels of multi-cell closed sections subject to bending, shear, torsional and axial loads. Because the thickness

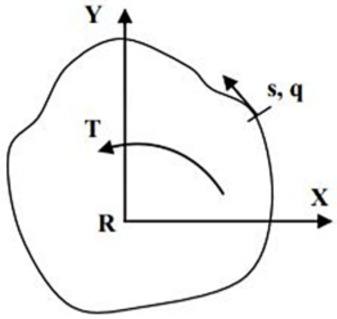

FIGURE 5.17: Shear flow distribution in a closed section beam subject to torsion.

of these panels is small compared to the cross-sectional dimensions, these components could be treated as thin-walled beams. So, a simplifying assumption can be made when calculating stresses and displacements. A detailed analysis of open and closed isotropic thin-walled beams under various types of loadings can be found in [101–112].
In this section thin skill is considered and the methods to analyze the behaviour of closed section beams under torsion are briefly introduced to show the logical flow of the subroutine *OptyWing_Stress_Section_Composta*. Consider a generic shape closed section, the application of a pure torque to a closed section beam results in the development of a constant shear flow in the beam wall.

The relationship between the applied torque T and this constant shear flow is:

$$T = \oint pqds \tag{5.4}$$

since the shear flow is constant and $\oint pqds$=2A

$$T = 2Aq \tag{5.5}$$

Which is known as the Shear Stress Bredt's Formula.
The rate of twist in an isotropic material is defined as

$$\frac{d\theta}{dZ} = \frac{q}{2A} \oint \frac{ds}{Gt} \tag{5.6}$$

Where G is the section shear modulus.
Because the torque and twist rate relationship is $= GJ\frac{d\theta}{dz}$, we can derive the stiffness

$$GJ = \frac{T}{\frac{d\theta}{dZ}} = \frac{4A^2}{\oint \frac{ds}{Gt}} \tag{5.7}$$

Another important subroutine of the optimization process is ***OptyWing_Fitness*** . This function:

- Receives as inputs *xOpt*, *wingGeom*, *wingLoad matDatabase*. Where *xOpt* are all the thickness that define the wing configuration (the variables that must be optimized);
- Transforms the input data for optimization in input data suitable for the stress analysis by means the subroutine ***OptyWing_MCmapping***;
- Runs the subroutine ***OptyWing_Stress_Section_Composta***;
- Calculates the minimum MS among the MS of Tension, Shear and Buckling: this will be the MS assigned to the wing box structure.

Figure 5.19 shows an example of the T-WING wing-box strength and buckling optimization process: a total of 26 variables (characterizing the inner and the outer two cell wing box) were considered as design variables.
Moreover, the figure shows the different panel thickness (t_i) and different spar caps area values (A_i) at a defined wing section. The section properties were supposed constant along the wing while two different sets of stiffness properties were assumed respectively for the inner and outer wing.

In general, as said, to use the *gamultiobj* function, we need to provide at least two input arguments, a fitness function, and the number of variables in the problem. The first two output arguments returned by *gamultiobj* are X, the points on Pareto front, and FVAL, the objective function values at the values X. A third output argument, exitFlag, tells you the reason why *gamultiobj* stopped. A fourth argument, OUTPUT, contains information about the performance of the solver. *gamultiobj* can also return a fifth argument, POPULATION, that contains the population when *gamultiobj* terminated and a sixth argument, SCORE, that contains the function values of all objectives for POPULATION when *gamultiobj* terminated.
More in detail, the main iteration of the *gamultiobj* algorithm proceeds as follows:

1. Evaluate the objective function and boundaries/constraints for the population, and uses those values to create scores for the population.
2. Select parents that have better fitness values for the next generation using the selection function on the current population.
3. Create children from the selected parents by mutation and crossover. In natural evolution, mutation is a random process where one allele of a gene is replaced by another to produce a new genetic structure. In GAs, mutation is randomly applied with low probability, typically in the range 0.001 and 0.01, and modifies elements in the chromosomes. Usually considered as a background operator, the role of mutation is often seen as providing a guarantee that the probability of searching any given string will never be zero and acting

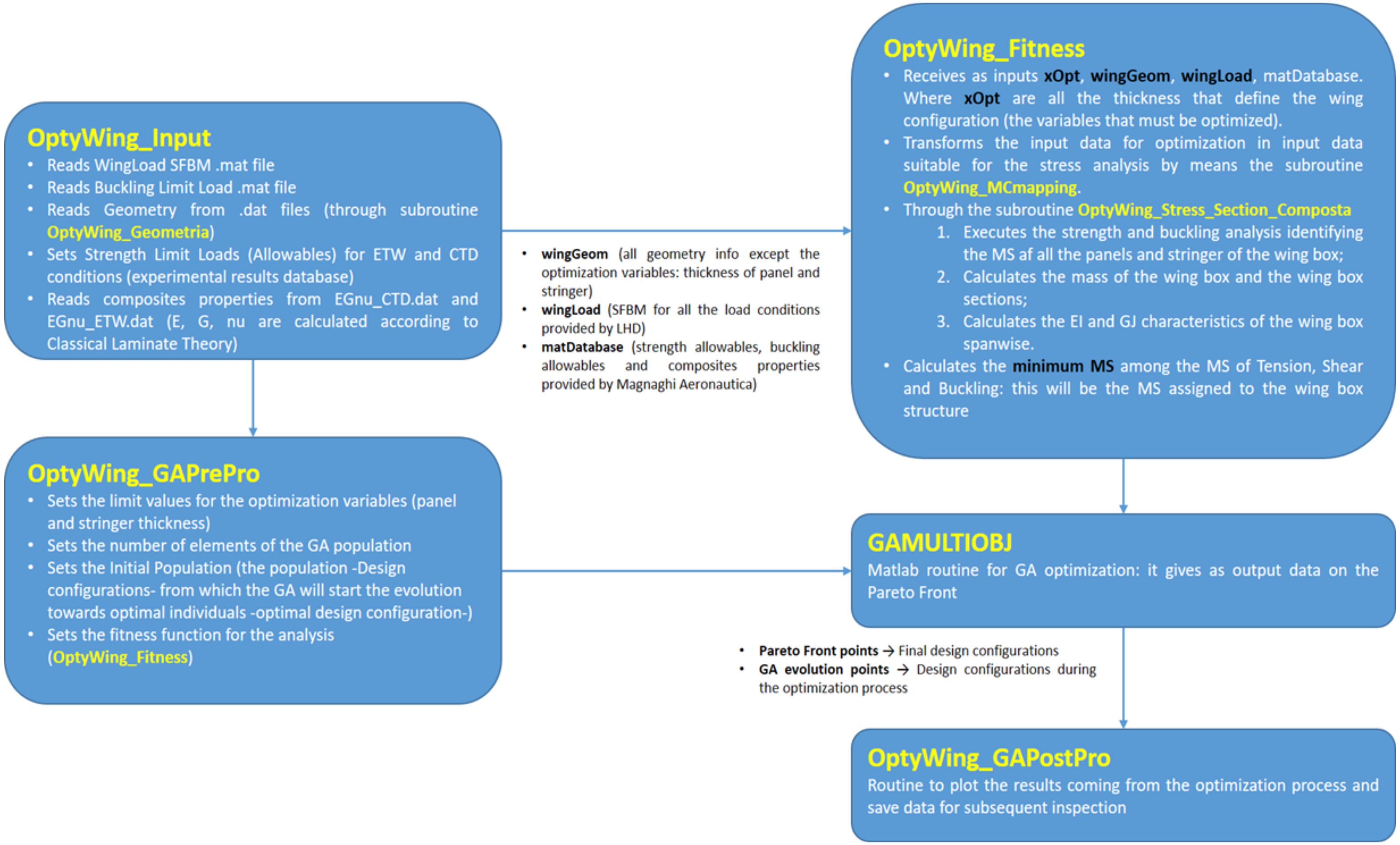

FIGURE 5.18: Block Diagram of Multicella

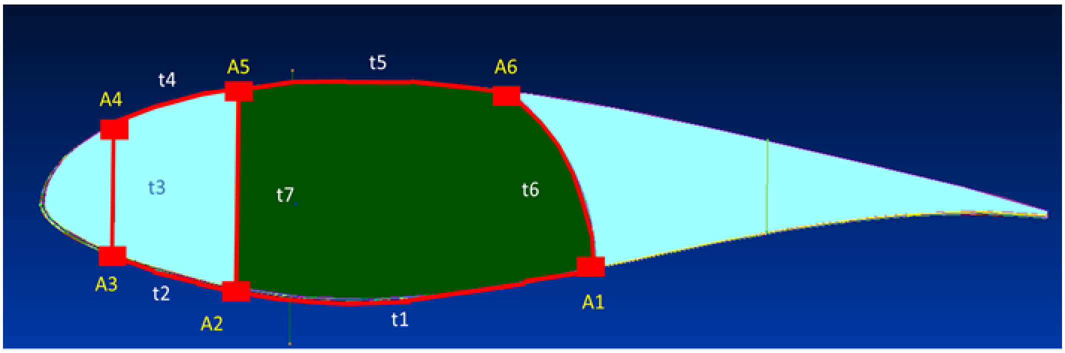

FIGURE 5.19: Wing section design variables.

as a safety net to recover good genetic material that may be lost through the action of selection and crossover Like its counterpart in nature, crossover or recombination, produces new individuals that have some parts of both parent's genetic material.

4. Score the children by calculating their objective function values and feasibility.

5. Combine the current population and the children into one matrix, the extended population.

6. Compute the rank and crowding distance for all individuals in the extended population.

7. Trim the extended population by retaining the appropriate number of individuals of each rank.

8. Provide the GA evolution points i.e. design configurations during the optimization process.

9. Iterate the optimization process until the optimal design configuration is reached; halt the GA and output Pareto Front points i.e. the final design configurations.

Finally, the GA Post-Processing routine, named ***OptyWing_GAPostPro*** plots the results coming from the optimization process and save data for subsequent inspection.
Because the optimization process toolbox finds the minimum of the fitness function, the best fitness value for a population is the selection of noninferior solution points i.e. points in which improvement cannot be attained in all the objectives. Noninferior solutions are also called Pareto optima. As said, a general goal in multiobjective optimization is constructing the Pareto optima. The Figure 5.20 shows an example of Pareto front obtained from the wing optimization process of the parameters half wing structural mass (to minimize) and margin of safety (to maximize).

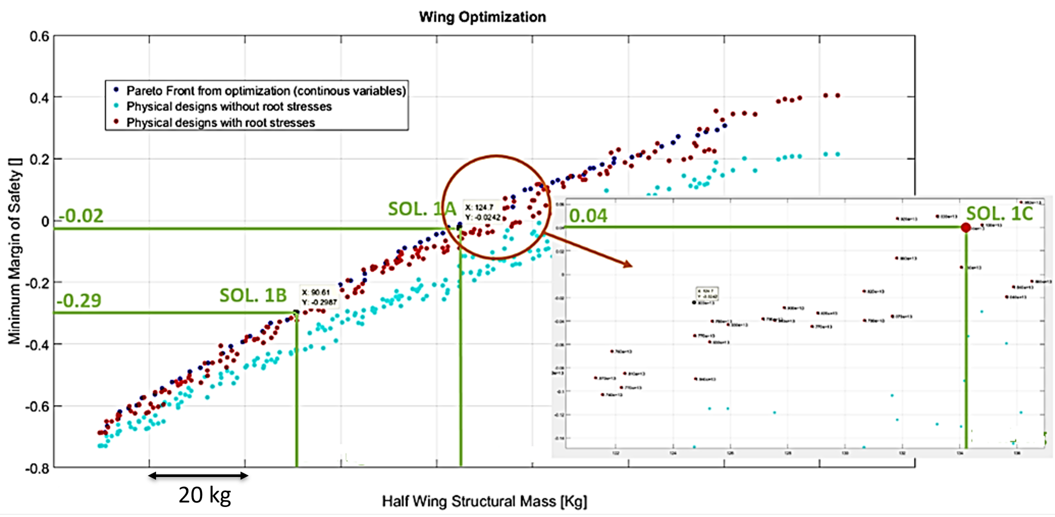

FIGURE 5.20: Optimization Process results and Pareto front (strength optimization)

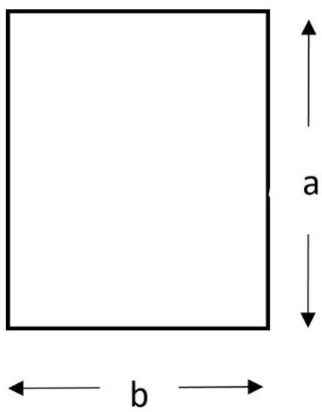

FIGURE 5.21: Scheme of a Generic Panel subject to Buckling Analysis.

5.9 Some preliminary Optimization analysis results. Considerations about Buckling

Some cases have been examined to gain confidence with the Multicella results and to correlate numerical aspects of the optimization with theoretical and engineering aspects.
The Figure 5.5 shows the airfoil of the wing box. The blue markers along them represent the coordinates of the points that describe the airfoil. These points, opportunely grouped, represent the panels along the chord, i.e. in the plane of the airfoil, the thickness of which is to be optimized for the Buckling analysis.
Figure 5.21 schematizes a generic panel and allows the introduction of the Buckling Critical Load formula 5.8 and the expression of the Margin of Safety 5.9, both implemented in the optimization process.

$$F_{cr} = KE\left(\frac{t}{b}\right)^2 = \frac{k\pi^2 Et^2}{12\left(1-\mu^2\right)b^2} \tag{5.8}$$

where:

- K and k = Non-dimensional coefficients or constants that depend upon conditions of edge restraint and shape of plate;
- E = Young's modulus in psi;
- t = Thickness of plate in inch;
- b = Width of plate in inch;
- μ = Poisson's ratio.

$$M.S = \frac{F_{cr}}{F} - 1 \tag{5.9}$$

Starting from an initial structural reference of the wing box in terms of stiffness (Margin of Safety) and structural weight, using the same materials and the same loads, the following examples of Scalability were carried out:

A. Geometric scalability: 30% chord increment.

B. Change of the dimensions of the panels subjected to Buckling load: this is equivalent to inserting a stringer along the airfoil.

The Pareto fronts for the cases examined are shown in figure 5.22. In particular, figure (a) above relates to the reference starting wingbox while figure (b) in the middle and figure (c) below relate to the cases respectively of raising the string and inserting a stringer. For each Pareto front, the two best optimal solutions were considered. The results are shown only in terms of MS while the abscissa axis indicating the weight value is masked for reasons of industrial secrecy. For the first case, by increasing the chord length by 30%, the following are observed:

- an increase in weight of the wing of about 10%;
- an increase in stiffness.

Since a linear increase in total weight does not correspond to the increase in the chord, it can be concluded that the optimization tool decreases the thicknesses of the panels as the stiffness increases.
In the second case, with a string increase of 30% and the insertion of an additional stringer, as shown in Figure 5.23, the following are observed:

- a weight increase of the wing of about 4% compared to the reference wingbox.
- a 6.5% decrease in the weight of the scaled wing and with extra stringer, compared to the only up-scaled wing.

Therefore, the stiffening offered by the additional stringer is such that the optimization tool provides thicknesses to the structure which overall is lightened.

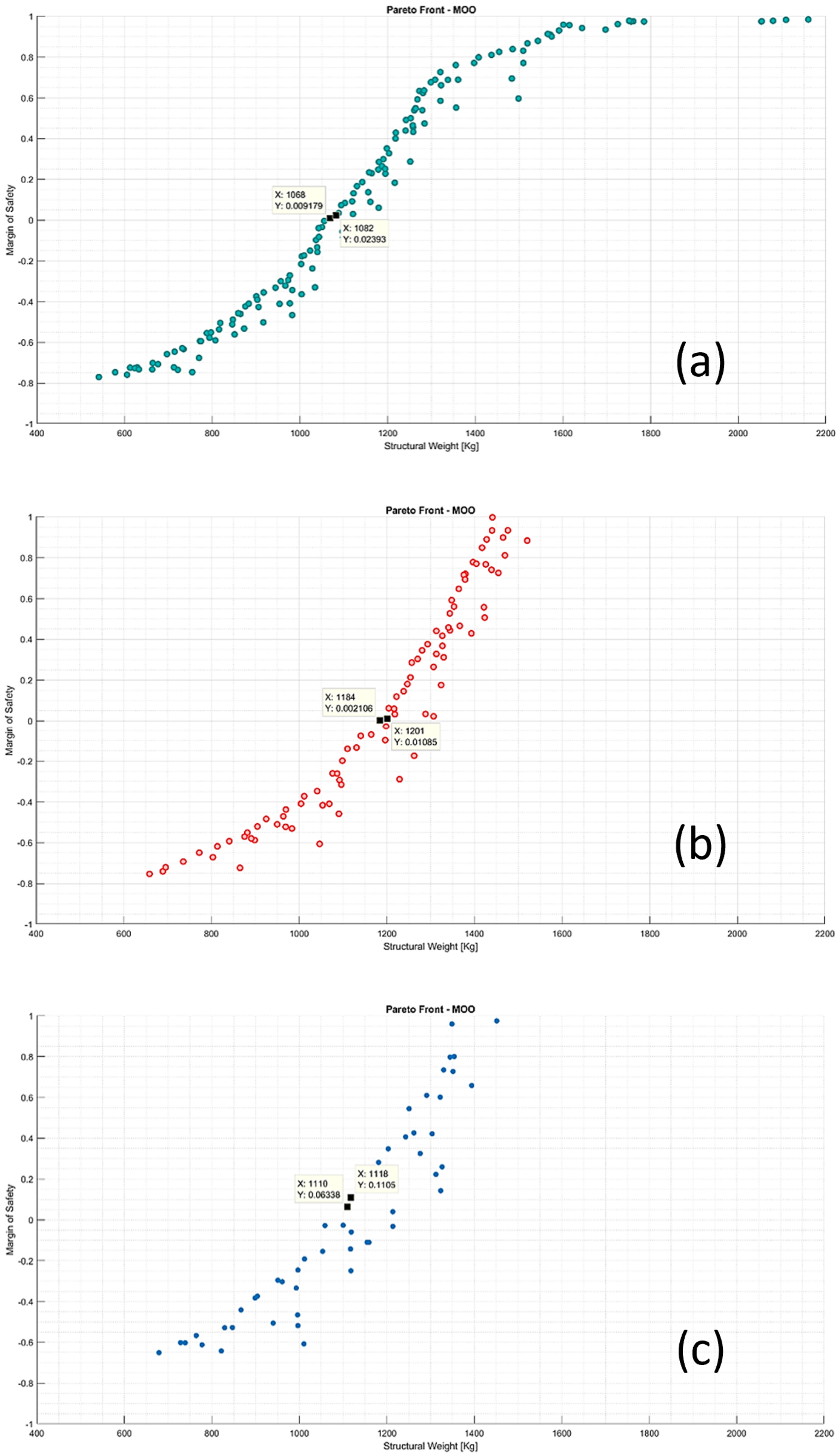

FIGURE 5.22: Pareto front: (a) starting reference wing-box structure; (b) chord up-scaled by 30%; (c) up-scaled chord and insertion of a stringer.

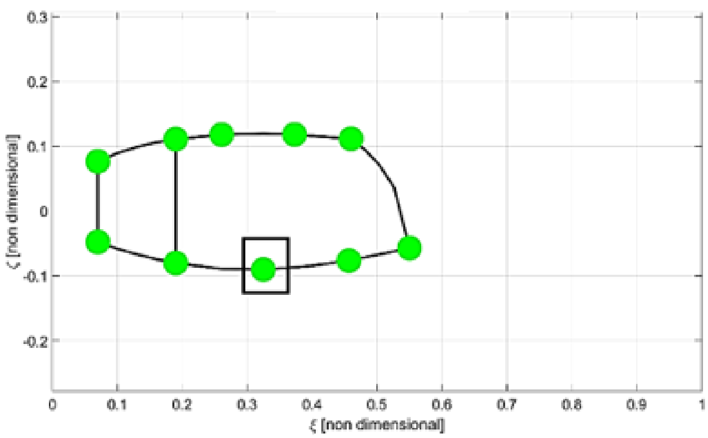

FIGURE 5.23: Airfoil in dimensionless coordinates with an additional stringer.

5.10 Optimization Cases

The optimization was performed into two steps, in order to better identify the most relevant contribution to the up-scaled wing mass.

- Optimization with respect to Whirl Flutter
- Combined case: optimization with respect to Crash and Whirl Flutter

The results reported in this thesis are related to the optimization with respect to both stiffness and crashworthiness requirements, for both configurations, T-WING and Up-scaled wing.

5.11 Crashworthiness investigation Criteria

The crashworthiness requirements are implemented as a request to have a margin of safety of at least 0.1 at the wing root and of at least 0.4 from the root to the tip of the wing. To take into account also the stiffness requirements at the same time a penalty (minus 1) on the MS are added for solutions that do not respect the torsional stiffness requirements. For the T-WING, the investigative section from the crashworthiness point of view is the one corresponding to the Buttock Line 24 (BL24 = 24 inches from the root) while for the up-scaled wing, the session concerned is the Buttock Line 31 (BL31 = about 31 inches from the root).
In other words, the crashworthiness requirements are to have a safety margin:

- at least 10% in the BL $\pm$ 100 mm zone;
- at least 40% on the outboard part of the wing

The results of the optimization are Pareto Fronts showing the wing-box solutions compatible with the optimization constraints. From these solutions an up-scaled optimized composite wing-box at minimum mass will be selected for the 2^{nd} phase of the activity (Fig.5.9).

5.12 Multi-Objective Optimization Up-scaled Wing

The present section is devoted to the results obtained by the optimizer with respect to the up-scaled wing.
As said, Pareto front is a set of point that verify the property that each one of these points is not dominated by another one (does not exist a point that have better properties on all the optimization objectives).
The first level is the Pareto front. The next level is the Pareto front of the set of points that have been obtained removing from all the points those belonging to the preceding Pareto fronts) The results are provided as Pareto fronts, in which: the blue points represent all the points analysed by the optimization algorithm; the red points are the first 40 levels of the Pareto front; the green points are derived from the red points and represent the feasible optimization solutions (discrete thicknesses) closest to the optimization solutions evaluated by the algorithm (continuous thicknesses); the cyan points are the first 5 levels of the green points. For each material the following Pareto fronts are provided, optimization with respect to:

- ΔEI_{xx} [%];
- ΔEI_{zz} [%];
- ΔGJ [%];
- the maximum of (ΔEI_{xx} [%], ΔEI_{zz} [%], ΔGJ [%]);
- the sum of (ΔEI_{xx} [%], ΔEI_{zz} [%], ΔGJ [%]);
- ΔGJ [%] & Crashworthiness;

The whirl flutter requirement is implemented as a constraint on the wing stiffness values (flexural and torsional). The results are expressed as Pareto fronts. The explored solutions were obtained by performing the Multi-Objective-Optimization (MOO) aimed at minimizing the structure weight and at minimizing the absolute differences between the structural stiffness of the solution under consideration and the required stiffness. The y-axis values represent the minimum of the absolute differences between the stiffness of each solution and the required stiffness.
The crash optimization was performed taking into account crashworthiness requirements and verifying that the solutions fulfil also whirl flutter specs. The constraint of the crash optimization problem is that under crash loads, the wing fails around the frangible section, whilst maintaining a minimum Margin of Safety elsewhere in the wing. In this case on the y-axis a safety margin is reported that represents the

TABLE 5.4: Up-scaled wing optimization results.

	UP-SCALED WING STRUCTURAL MASS (lbs)					
	EI_{xx}	EI_{zz}	GJ	max(EI_{xx},EI_{zz},GJ)	sum(EI_{xx},EI_{zz},GJ)	WF+crash
MAT01	2138	1936	3589	2667	2260	NE
MAT02	1495	1443	2362	1921	1502	NE
MAT03	na	na	1566	na	na	2527
MAT04	na	na	1905	na	na	3743
MAT05	1213	1089	2254	1472	1224	2933

minimum difference between the solution safety margin and the one required. It is possible to note that the Pareto fronts of the crash optimization generally present two clouds/branches of data (an upper branch and a lower branch) due to the penalty applied to solutions that do not fulfil whirl flutter req. (the lower branch is composed of the ensemble of points that do not respect the whirl flutter requirements).

In the table 5.4 a summary of the optimized results is reported, in terms of structural mass of the up-scaled wing box. The crash requirements has been introduced after stiffness optimization. This means that the crash data have to be read as "wing optimized with respect to whirl flutter stiffness requirement and to crash". Where the value reported is "*na*", it means that for the stiffness optimization the algorithm cannot decrease the configuration below laminates minimum thickness, i.e. the minimum laminate thicknesses of the database considered satisfy the requirement under consideration. Where it is reported a value equal to "*NE*" for crash, it means that an optimized solution which is complaint to both whirl flutter and crash cannot be found. In the histogram of figure 5.34, the up-scaled wing optimized mass is reported with respect to each constraint in the optimization. Red, blue, grey, yellow and dark blue bars are the optimized solutions with respect to each stiffness (grey is with respect to torsional stiffness, the most demanding one). Green bar is the optimized solution with respect to whirl flutter (torsional stiffness) and crash.

The following considerations can be drawn for the upscaled wing:

- Optimization using the max or sum norm does not allow to obtain a solution with minimum possible weight (suboptimal results obtained) due to the trade-off of the optimizer to reduce contemporarily all the stiffness differences concerning the targets.

- by optimizing the wing concerning whirl flutter, the leading stiffness is the torsional stiffness (grey color in the histogram), this is fully in accordance with respect to NGCTR-TD wing design heritage.

- Crashworthiness requirements have a non-negligible impact on the weight, this is also in accordance with T-WING design heritage, this is due to the big masses at the wing tip which causes high loads developing on the wing, under

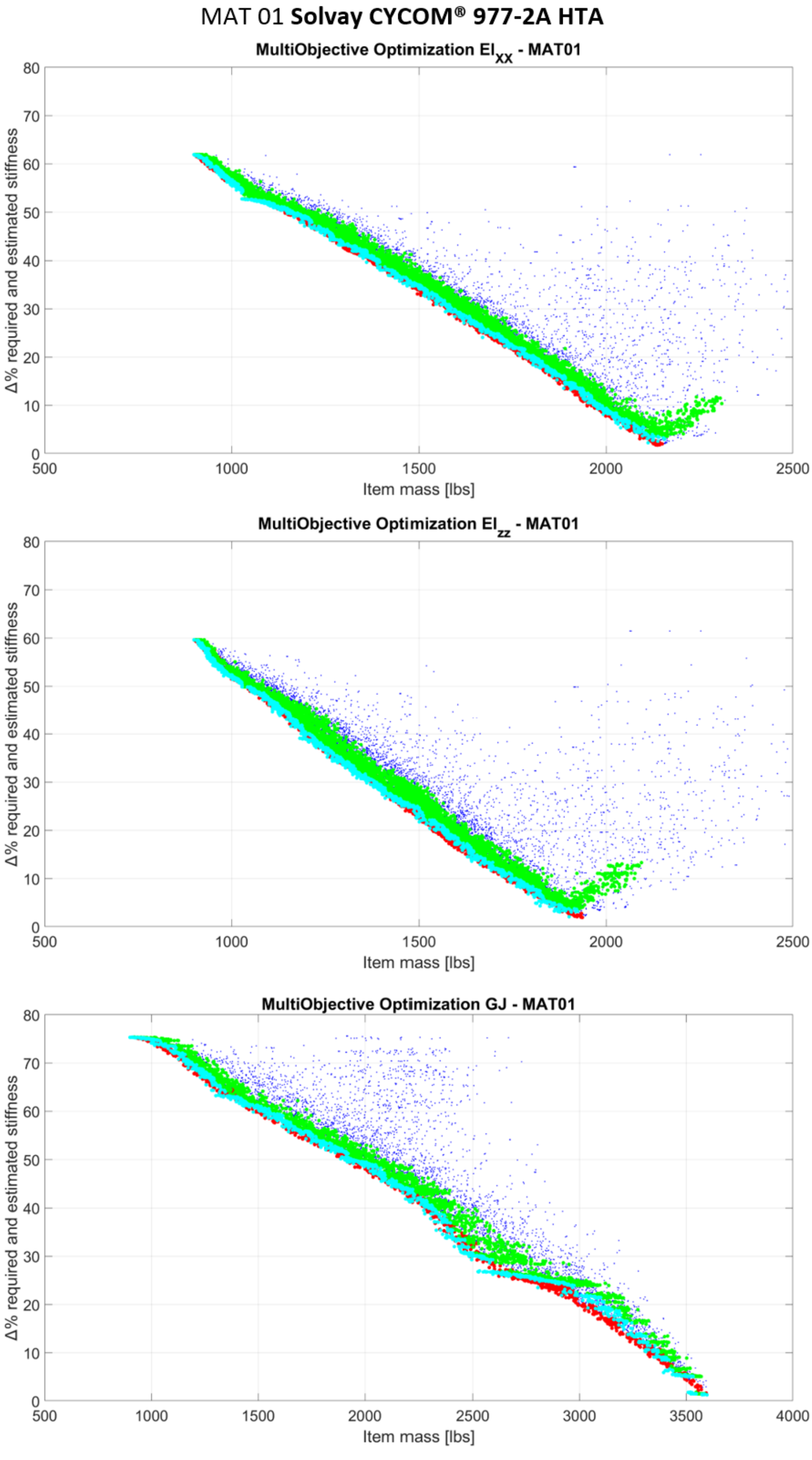

FIGURE 5.24: Up-Scaled wing Optimization - MAT01.

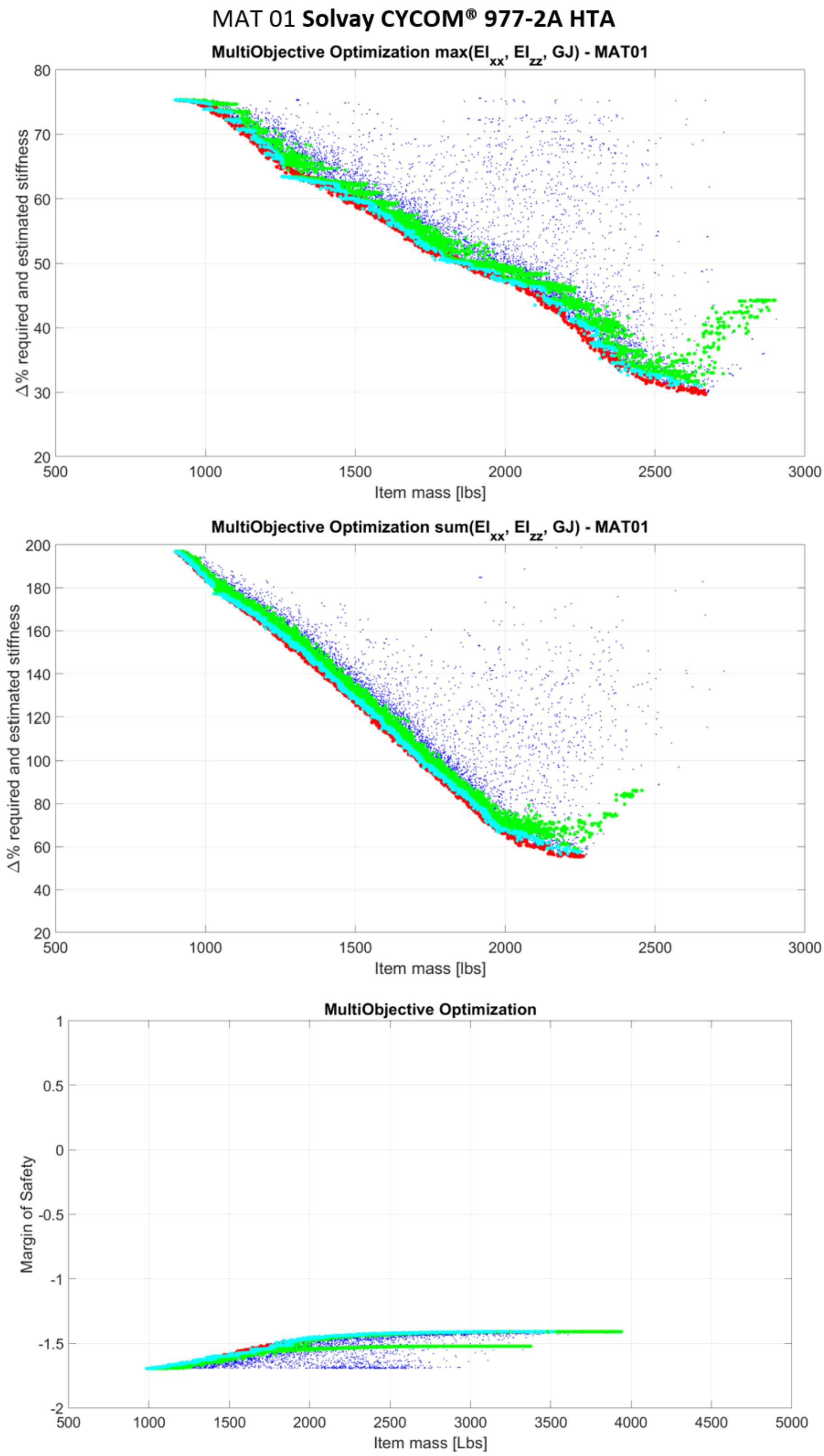

FIGURE 5.25: Up-Scaled wing Optimization - MAT01.

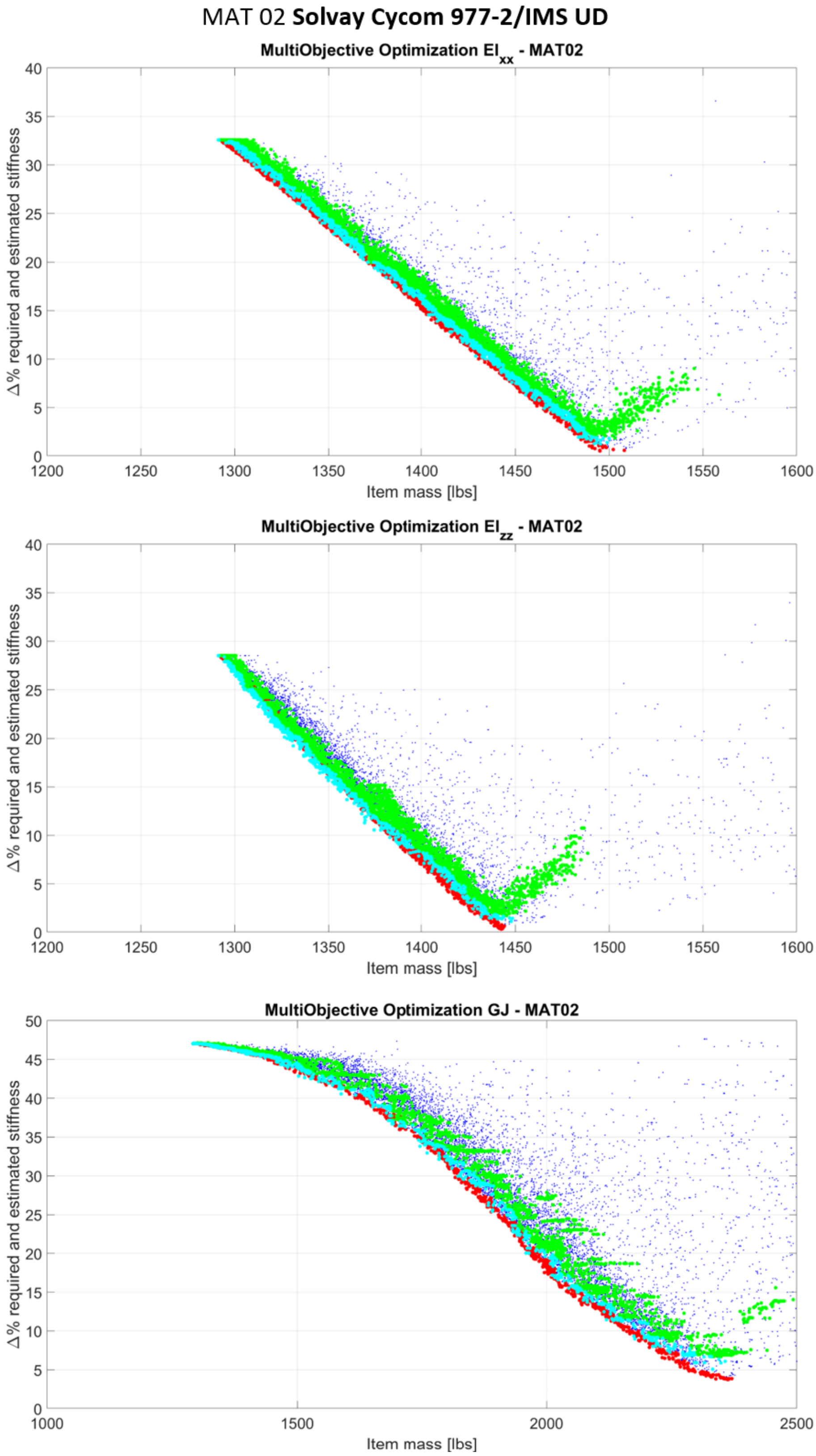

FIGURE 5.26: Up-Scaled wing Optimization - MAT02.

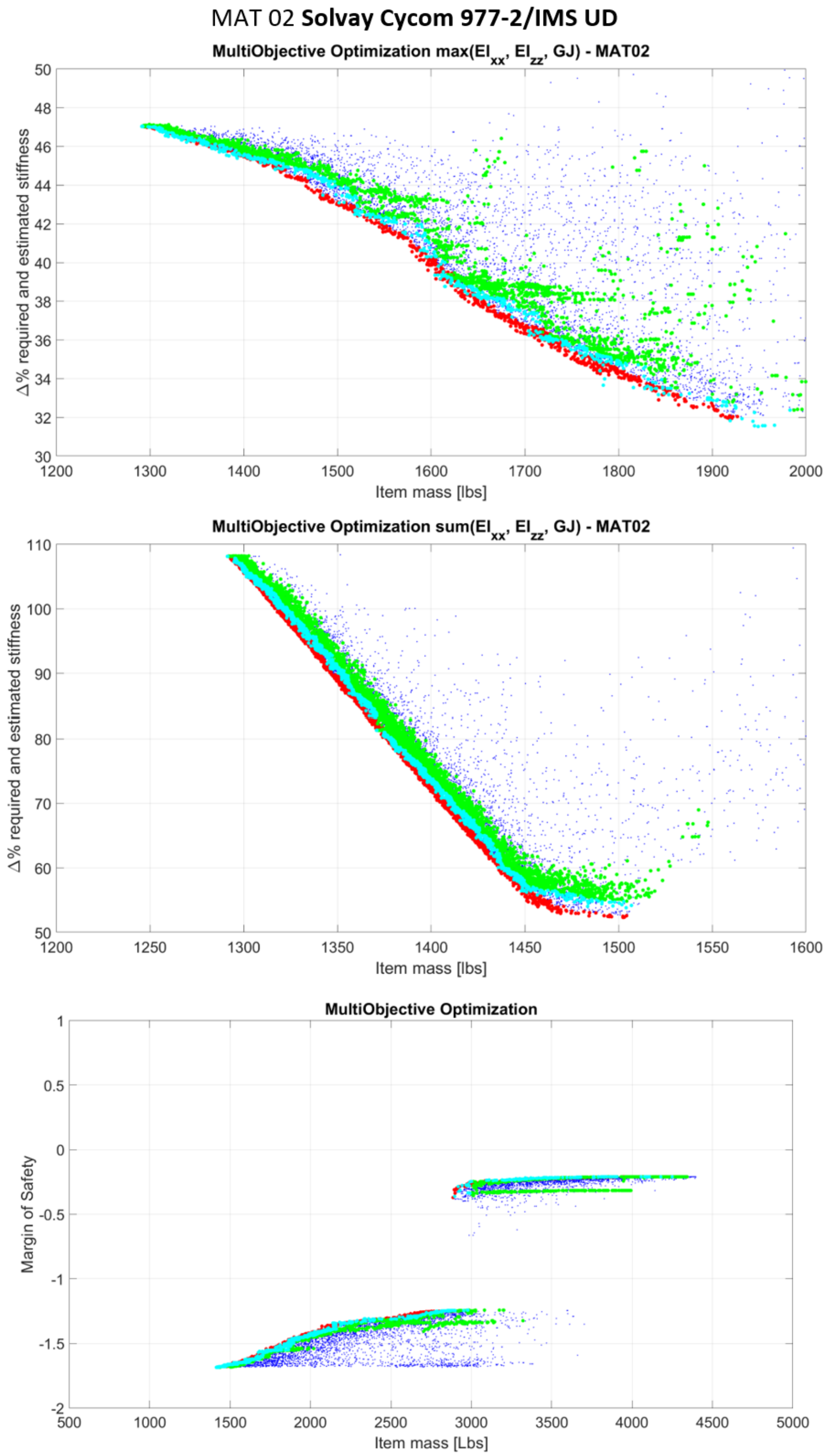

FIGURE 5.27: Up-Scaled wing Optimization - MAT02.

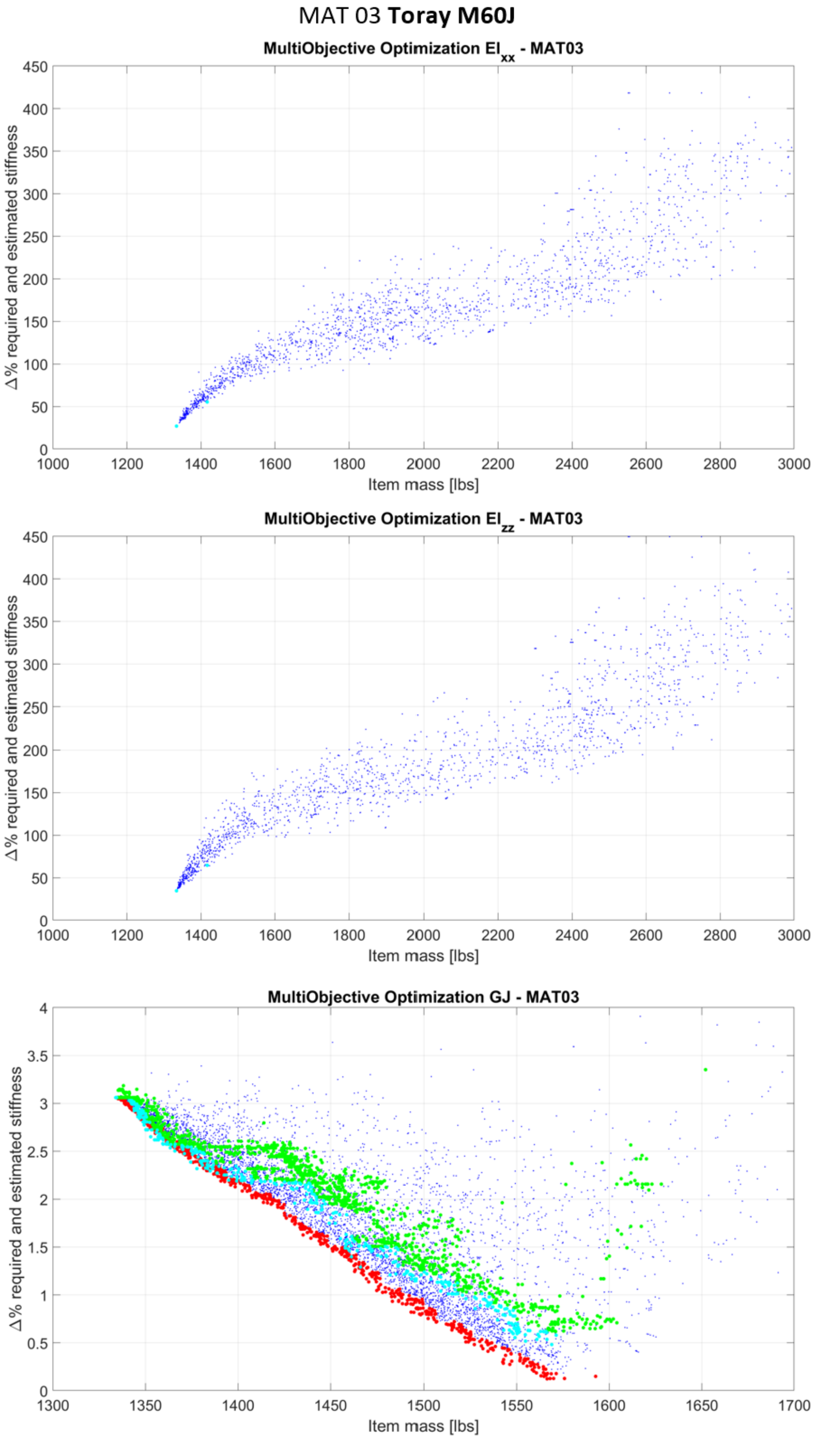

FIGURE 5.28: Up-Scaled wing Optimization - MAT03.

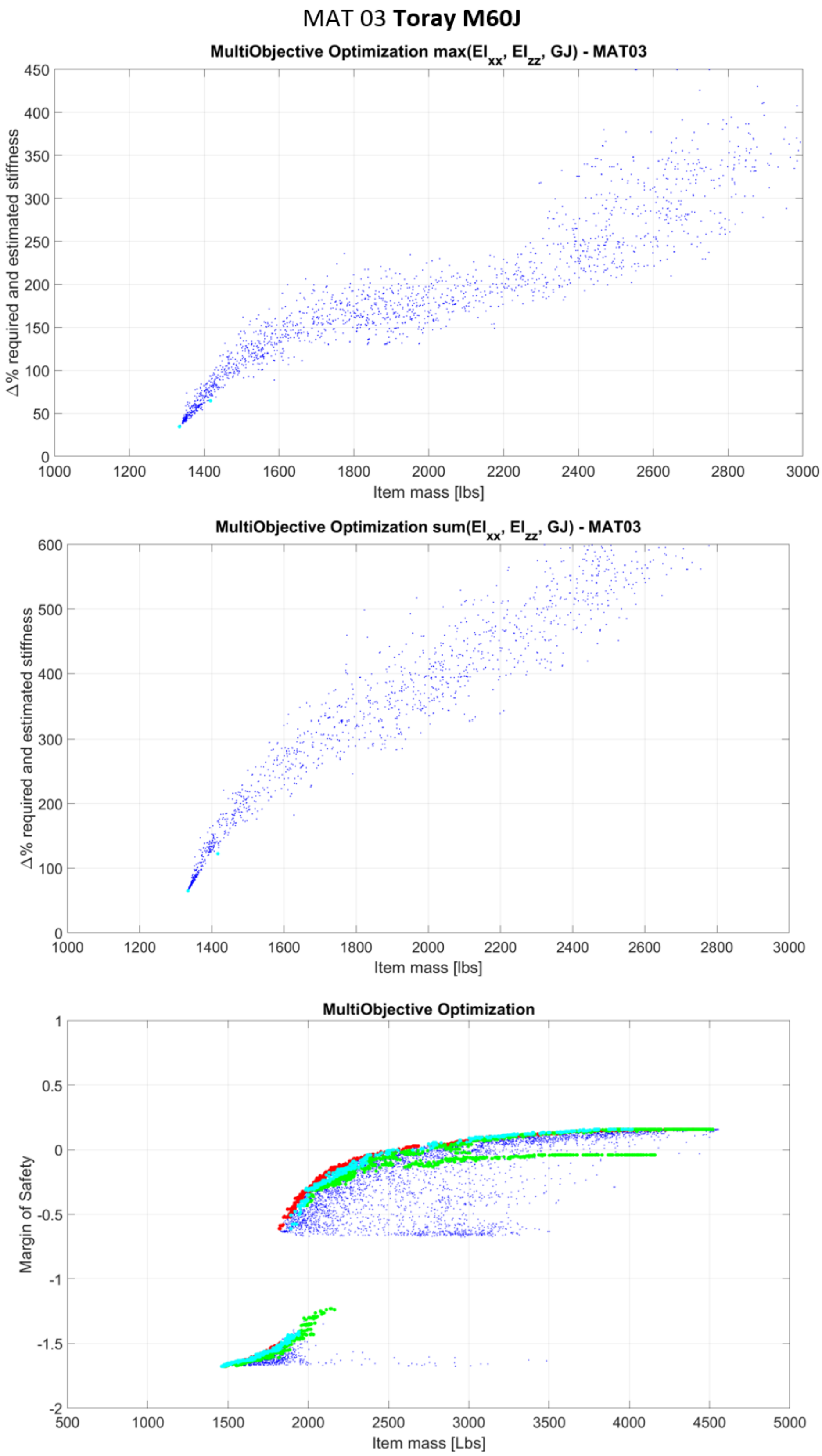

FIGURE 5.29: Up-Scaled wing Optimization - MAT03.

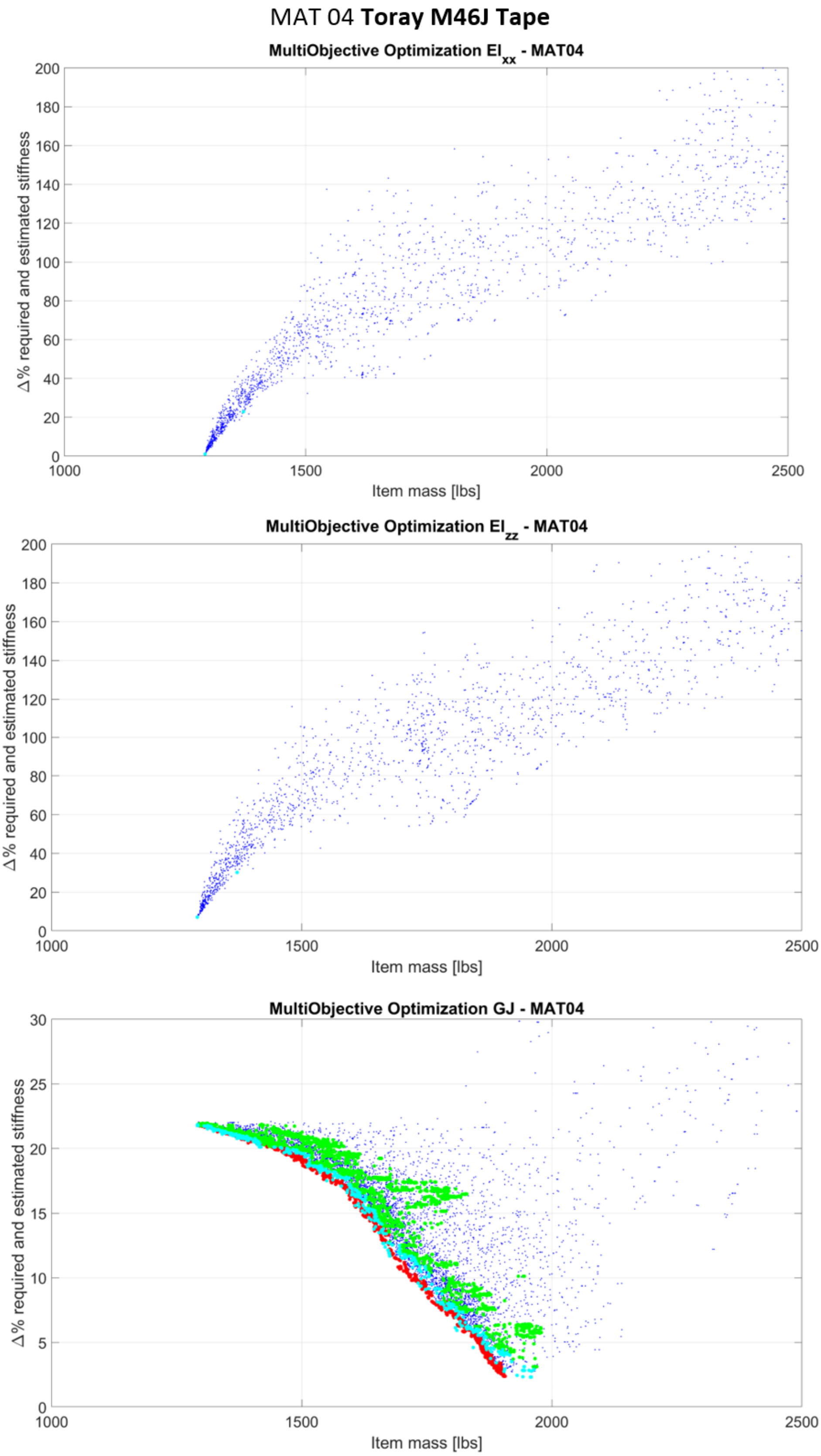

FIGURE 5.30: Up-Scaled wing Optimization - MAT04.

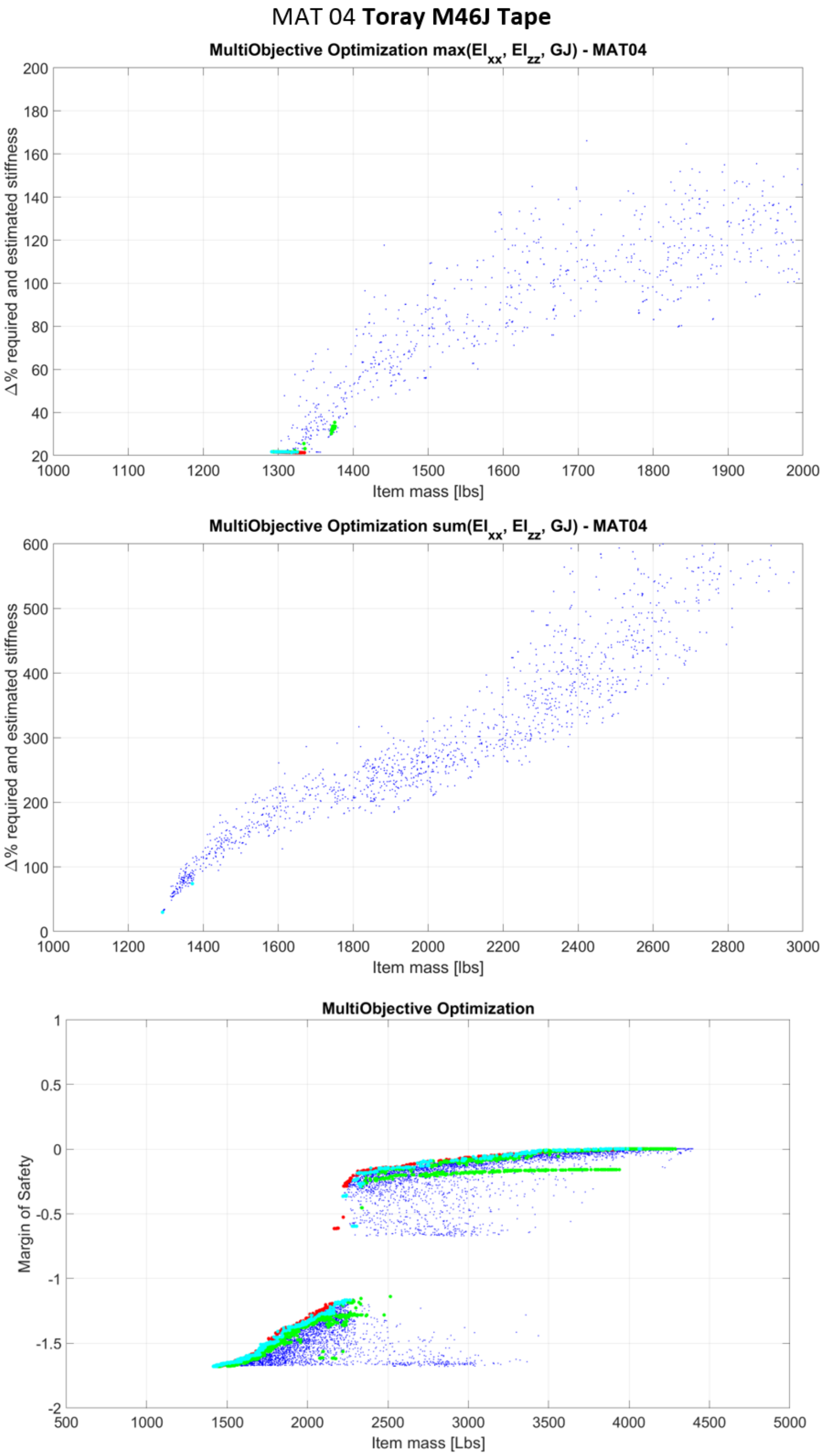

FIGURE 5.31: Up-Scaled wing Optimization - MAT04.

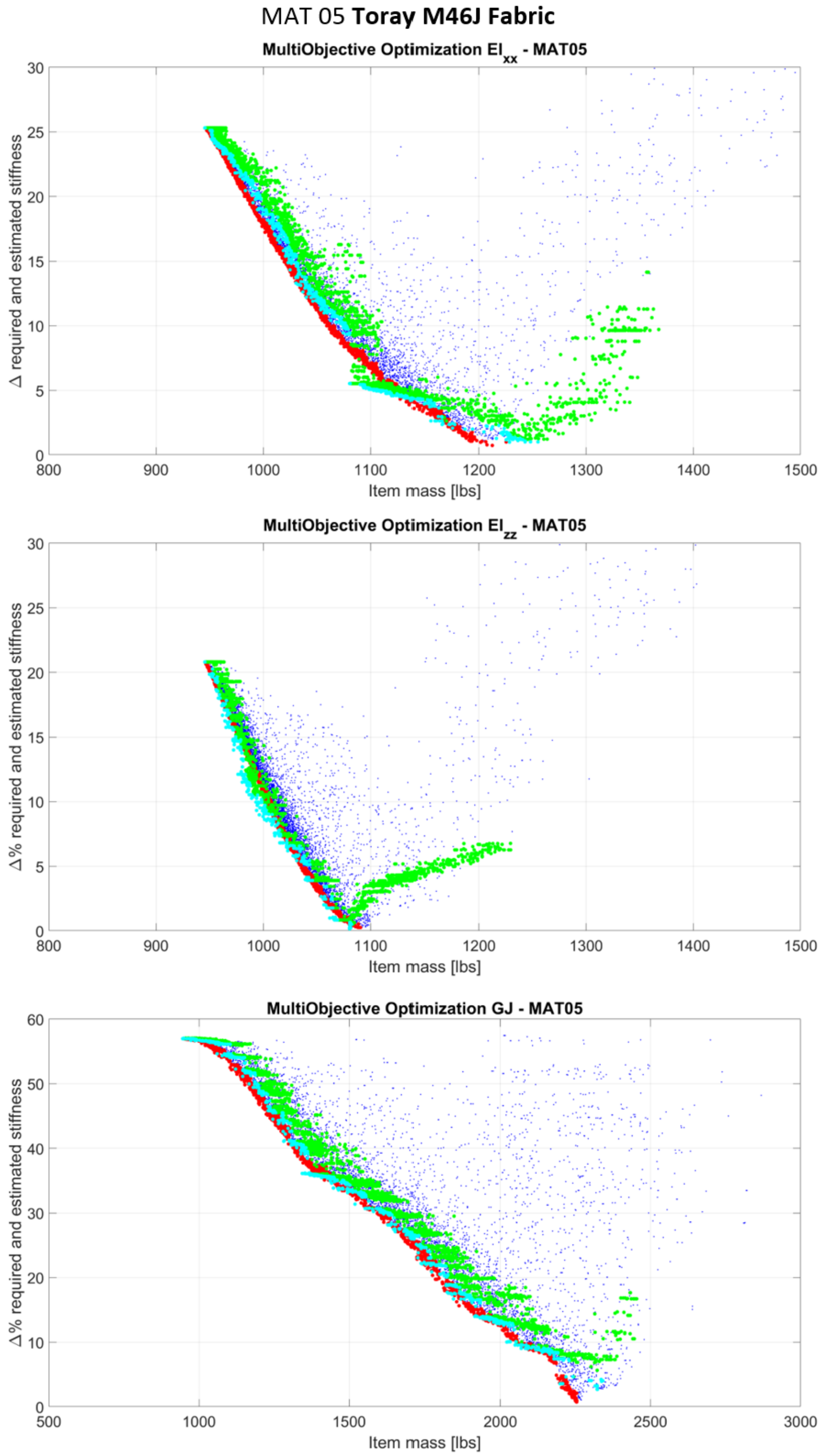

FIGURE 5.32: Up-Scaled wing Optimization - MAT05.

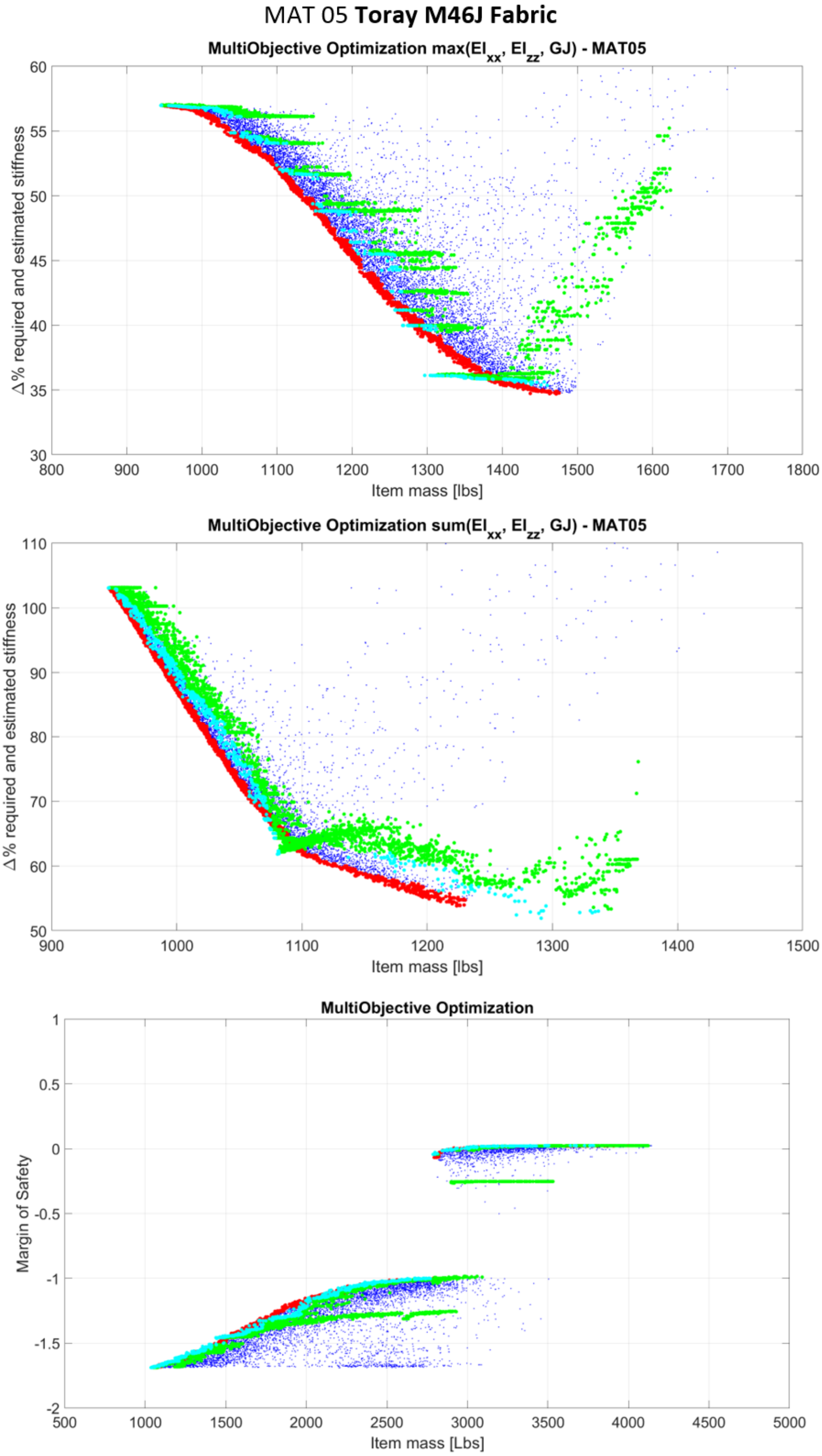

FIGURE 5.33: Up-Scaled wing Optimization - MAT05.

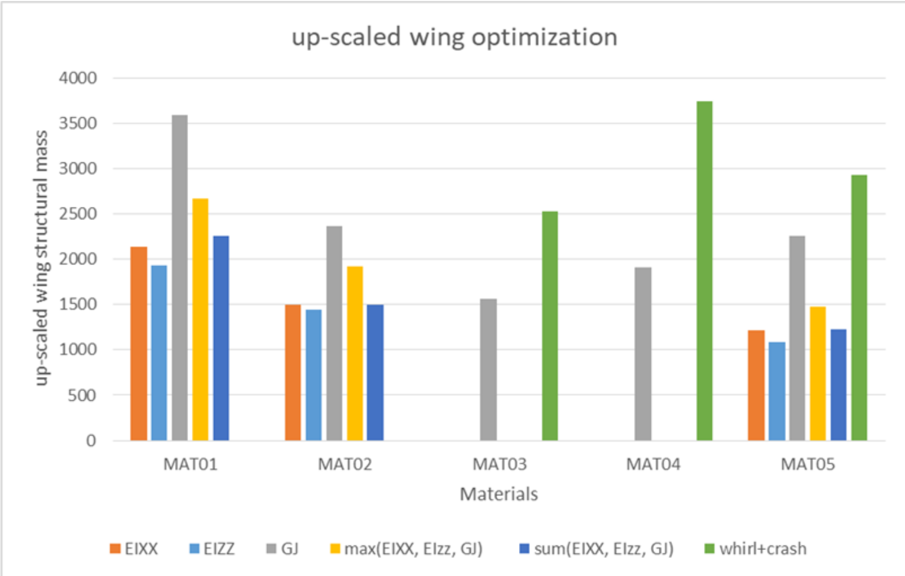

FIGURE 5.34: Up-scaled wing results.

crash vertical load factor. MAT01 and MAT02 are not able to fulfill both whirl flutter and crashworthiness requirements.

- The maximum weight saving which fulfills both whirl flutter and crashworthiness is reached with MAT 03 Toray M60J, the other materials have solutions that are heavier with respect to MAT 03.

In Figure 5.35 it is reported the percentage exceedance of each solution with respect to the best one.

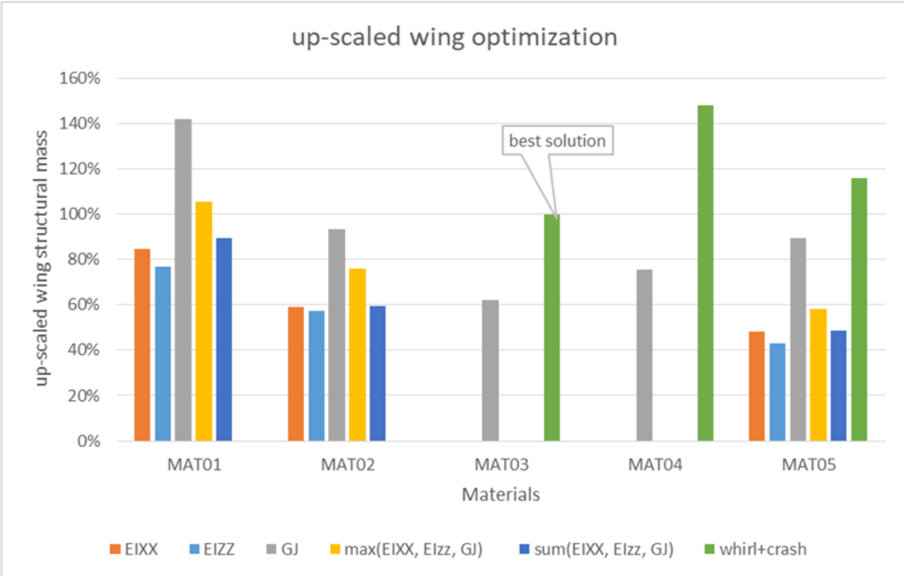

FIGURE 5.35: Up-scaled wing results in %.

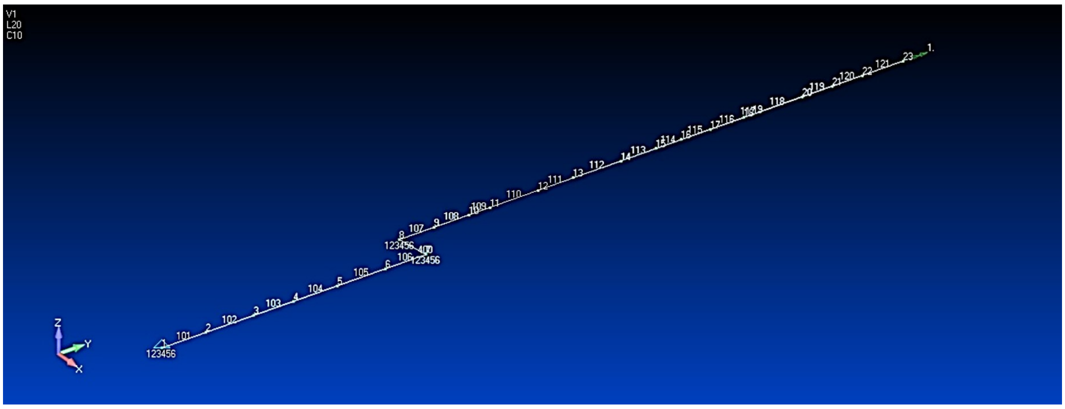

FIGURE 5.36: Simplified stick-beam aeroelastic model of T-WING.

5.13 Multi-Objective Optimization TD Wingbox

A similar optimization exercise has been performed on the TWING geometry, by using the same materials database. The values of the target stiffness were obtained starting from the simplified stick-beam aeroelastic model of TWING (Figure 5.36), compliant with free from Whirl Flutter condition.
The stiffness values found are:

- EI_{xx} = 6.304E9 Lbs x in^2 (out-of-plane flexural stiffness);
- EI_{zz} = 3.179E10 Lbs x in^2 (fore-and-aft flexural stiffness);
- GJ = 5.91E9 Lbs x in^2 (torsional stiffness).

T-WING wingbox, which is compliant with whirl flutter requirement, was the result of an aeroelastic tailoring activity that foresaw the addition of a proper number of MAT 02 UD plies to the MAT01 which constitutes the main part of the wing structure. The weight of this optimized configuration is 1302,7 lbs. Crashworthiness requirement was partially fulfilled since it was evaluated that the weight penalty was too high to be managed at system level.
In this optimization study, it has been explored the possibility, for T-WING wingbox, to fulfil both whirl flutter and crashworthiness requirements by enlarging the materials database. It is a study based on materials different from the qualified materials used in T-WING project, for which a qualification campaign would be required, in case if they were selected for the up-scaled configuration.
The optimization results are reported in terms of Pareto fronts and histograms, and pertain the most demanding requirements namely torsional stiffness and crash. In the following figures, Pareto fronts on the left are relative to optimization with respect to GJ, whereas Pareto fronts on the right to both GJ and crash. Each of the five materials has been analysed.

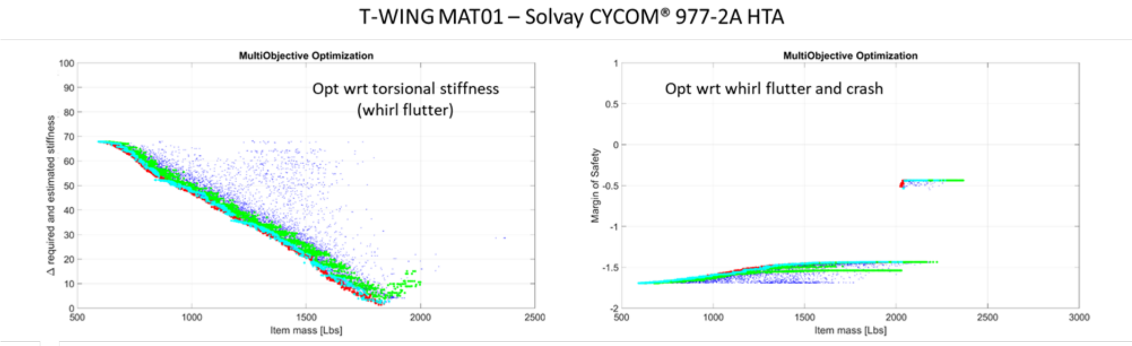

FIGURE 5.37: NGCTR-TD wing optimization – MAT01.

In the table 5.6 a list of the optimized solutions with respect to GJ and crash + GJ are reported. For "*na*" and "*NE*" values the same notes reported in the previous chapter apply. The histograms show the optimized solutions for each material

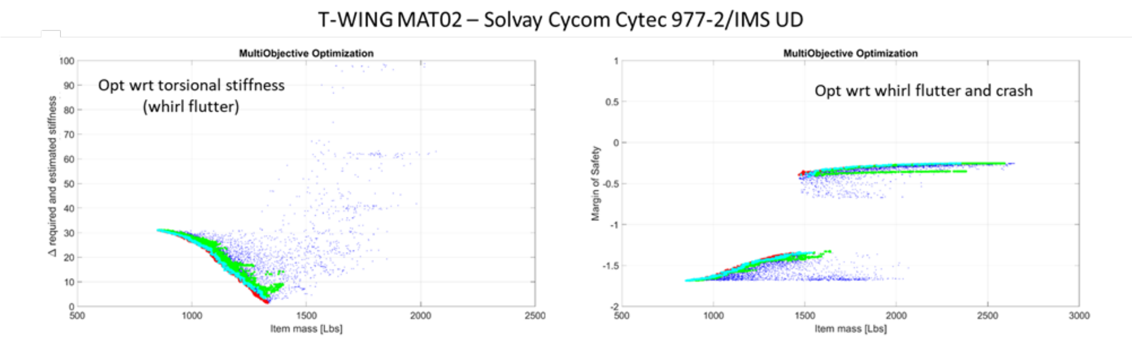

FIGURE 5.38: NGCTR-TD wing optimization – MAT02.

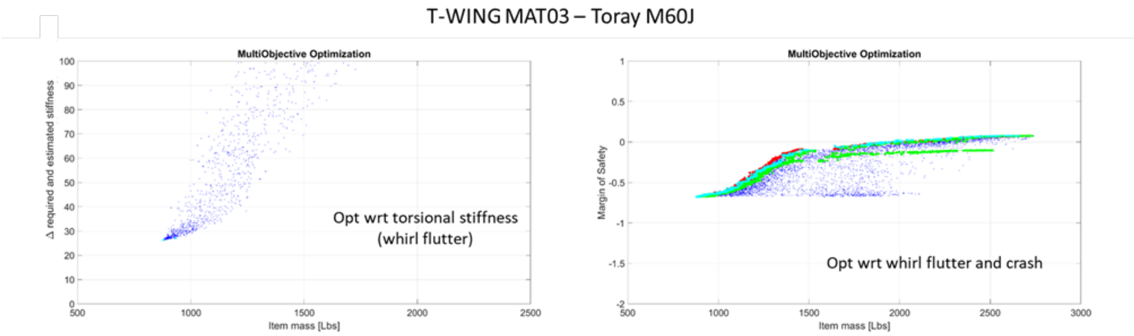

FIGURE 5.39: NGCTR-TD wing optimization – MAT03.

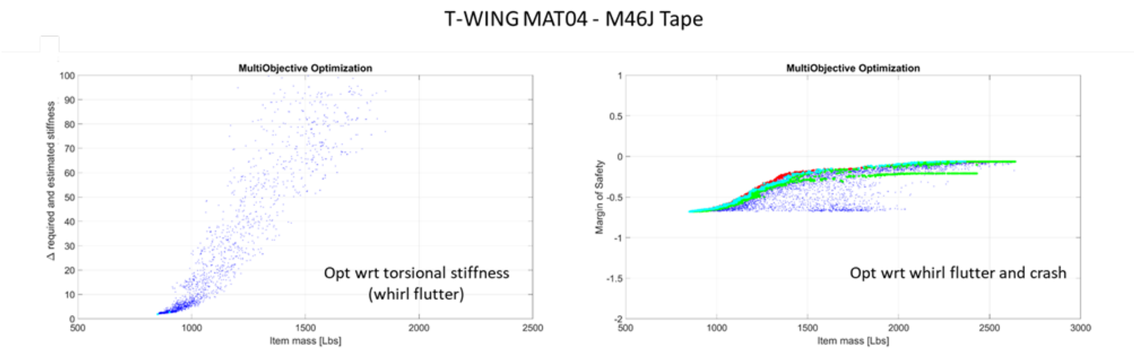

FIGURE 5.40: NGCTR-TD wing optimization – MAT04.

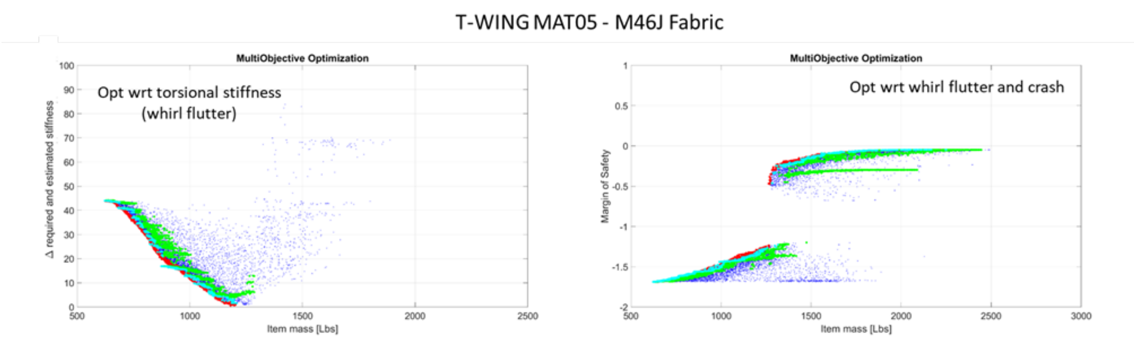

FIGURE 5.41: NGCTR-TD wing optimization – MAT05.

TABLE 5.5: NGCTR-TD wing optimization results.

	T-WING STRUCTURAL MASS (lbs)	
	GJ	WF+crash
MAT01	1839	NE
MAT02	1316	NE
MAT03	na	1889
MAT04	na	NE
MAT05	1199	NE

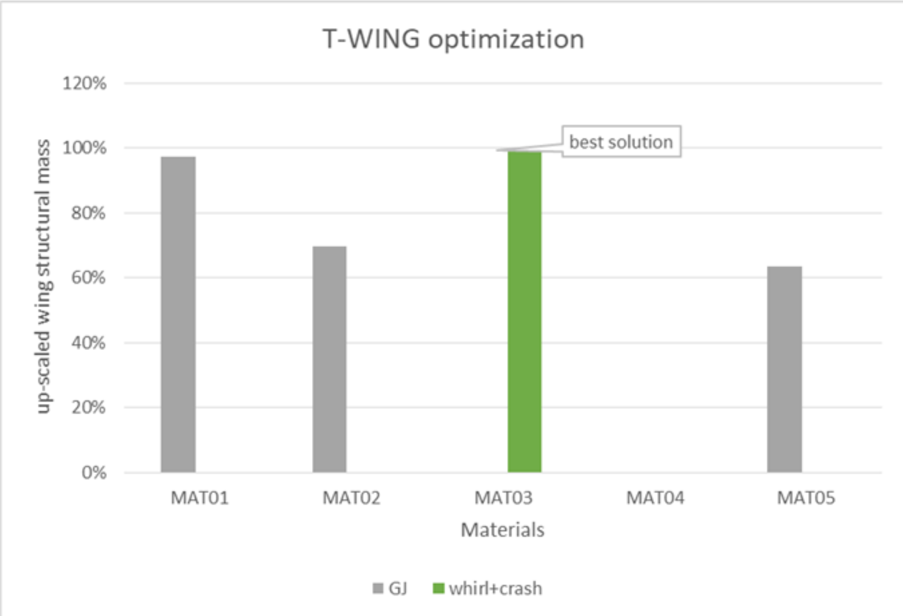

FIGURE 5.42: NGCTR-TD wing optimization results.

analysed. There's an optimized solution which complies with both requirements. It is obtained with the most performing material, i.e. MAT03. The weight of this solution is higher than T-WING CDR weight. This weight exceedance is due to two main reasons: the first one lies in the fact that, in general, Multicella estimation of the structural mass is made by using some contingency factors which take into account all the contributions which are not a direct result of the calculation (e.g. moveable surfaces, provisions, secondary structure, ect.), whereas the T-WING CDR structural mass is the result of tight optimization and CAD evaluation. The second reason is that T-WING only partially complies with crashworthiness requirement. It was already known from calculation, that a non-negligible mass increase was expected to fulfil crashworthiness requirements.

5.14 Comparison of results between up-scaled and TD wing and Conclusions

Comparable results are obtained in terms of materials effectiveness between the two different wing boxes (up-scaled and T-WING).
Materials selection has a great impact on the achievable weight saving, with tape materials performing better than fabric materials. The most performing material results to be the MAT 03 Toray M60J (a high strength modulus CFRP) for both.
The geometrical scale factor that was used to upscale from TD wing to the up-scaled version is equal to 1.289, the best solutions that were found for the two wing are in a ratio equal to 1.338 (2527 lb/ 1889 lb).

TABLE 5.6: NGCTR-TD versus NGCTR.

	NGCTR-TD	NGCTR	RATIO
Wing Geometrical Scale Factor	–	–	1.289
MTOW		30865	
Wing Weight Reqmt (% WRT MTOW)	1100	1742	1.584
Optimized Weight vs WF + CRASH	1889	2527	1.338

From table 5.6 and figure 5.43, it can be concluded that for the NGCTR, the ratio between the structural weight of the wing and the design MTOW of the tiltrotor, is around 8.19%. This means that, at present, this percentage is slightly above the average defined by the study of the state of the art on the various tiltrotors and prototypes. However, this is an excellent result bearing in mind that the results obtained through the Multicella optimizer are not as reliable as a study defined by FEM analysis and certainly require subsequent iterations to refine the result but they represent a valid alternative to carry out a very quick preliminary sizing of the wing box.

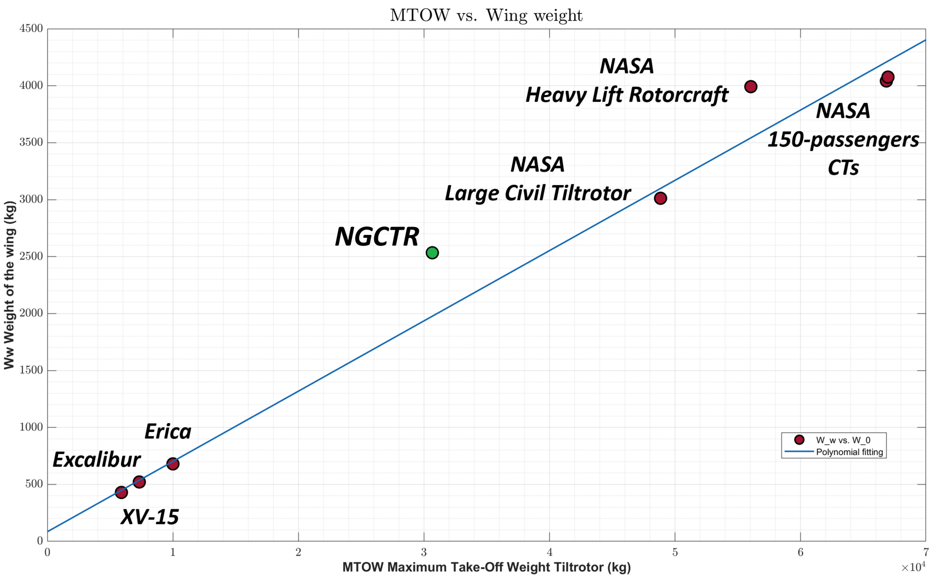

FIGURE 5.43: Weight of the wing vs. MTOW tiltrotor with NGCTR

Chapter 6

Conclusion and future directions

This thesis is part of a consolidated experience acquired by the Vibration and Acoustics aerospace Research Group at the Department of Industrial Engineering of the University of Naples in the field of vibroacoustic of aircraft and rotorcraft in collaboration with Leonardo Helicopters Division and T-WING consortium.
This work shows the three years of activity that have contributed to acquiring a greater knowledge of some aspects related to the use of tiltrotor and the design and construction of its wing.
The experimental, numerical and research point of view carried out within the T-WING research project and some results obtained above all in the vibroacoustic and structural fields were shown. The activities relate to both existing and flying Tiltrotors and the design of components for the next generation ones.
From the acoustic point of view, the experimental campaign for the acquisition of acoustic loads in flight allowed to validate of numerical tools for noise prediction. The numerical-experimental correlation between the data collected, analyzed, and illustrated by the author and the expected calculated results is satisfactory. The procedure followed to carry out these tests is also satisfactory, so much so that we can consider the extension to other types of aircraft in a context in which the problem of both atmospheric and acoustic pollution becomes increasingly discussed.
The advantages and disadvantages of using MIMO-type methods in the execution of the vibration tests were investigated, arriving at the definition of the most functional test set up for the test to be carried out on the test article of the NGCTR-TD wing. Some critical issues and the objectives to be achieved in these future tests have been highlighted.
As far as the aeroelastic topic is concerned, the design, construction, and use of a laboratory device made it possible to better understand the parameters that affect the whirl flutter phenomenon. The latter is not only an instability problem that predominantly weighs on the integrity of the tiltrotor but one of the main preliminary design requirements of a wing box for an upscaled tiltrotor was carried out in the last part of the work.
The Scalability process provided the first important points of reflection on innovative composite materials to be used to obtain the best compromise margin of safety versus structural weight for the aeroelasticity and frangible section requirements.

The proposed process is a much faster than FEM analysis, based on the use of Matlab tools which therefore allows you to make rapid changes to the structure such as changing the number or position of stringers, or the position and size of the ribs and start the calculation runs again, obtaining results with a high degree of reliability.
A further and more in-depth part of the process will include the building of a coarse FEM of the Up-scaled wing and the modal and flutter analyses, stress and buckling studies, crash and ditching evaluations.

Appendix A

Tiltrotors 3 view drawings and dimensions

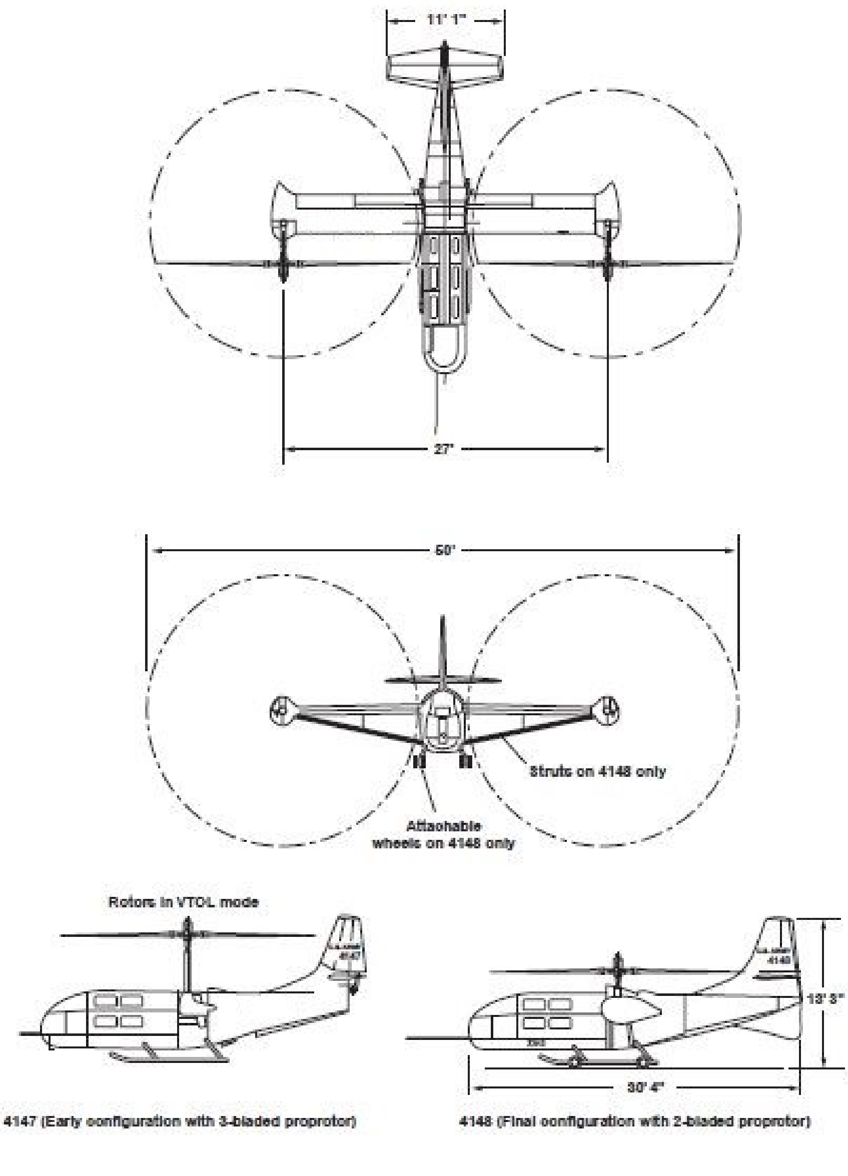

FIGURE A.1: XV-3 3-view drawings

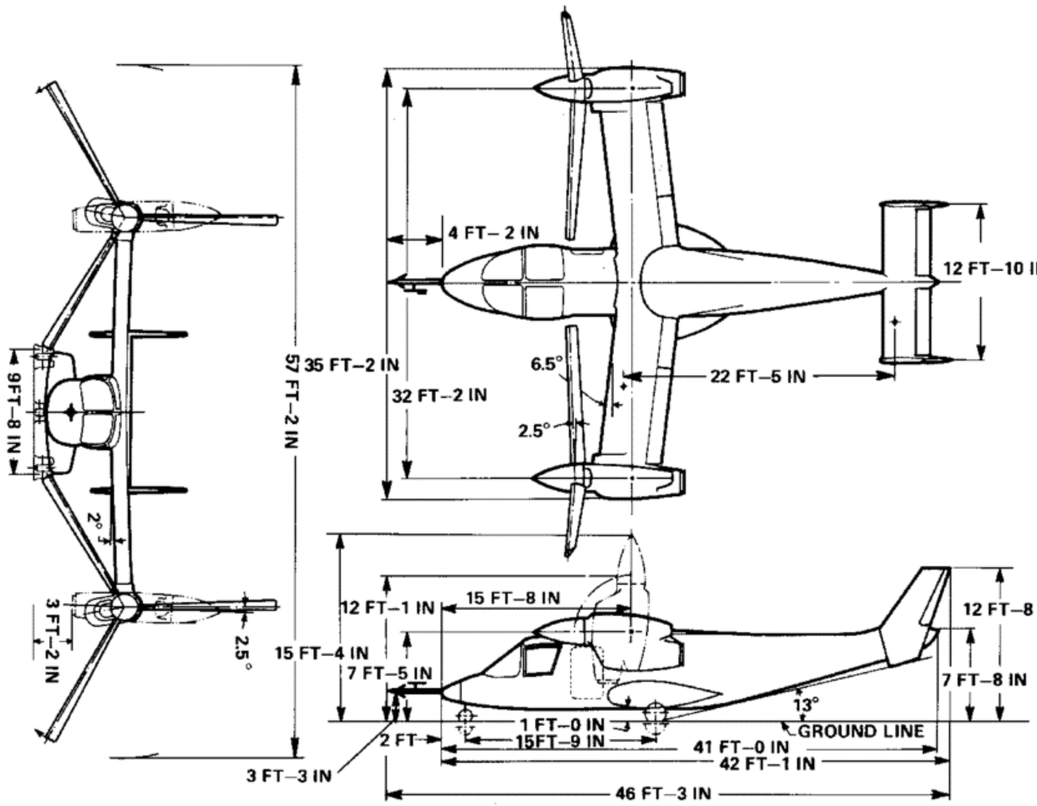

FIGURE A.2: XV-15 3-view drawings

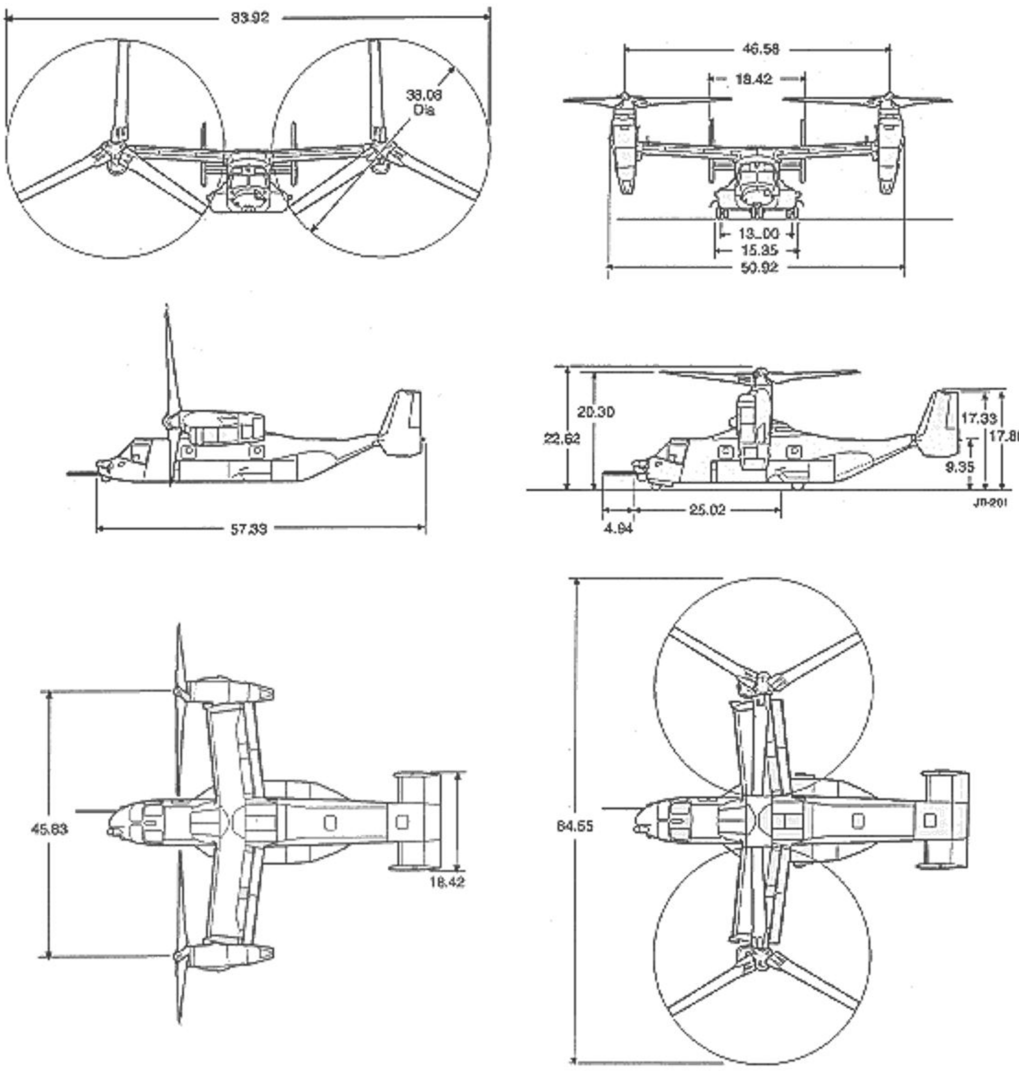

FIGURE A.3: Bell V-22 three-view drawing, Airplane mode and VTOL mode

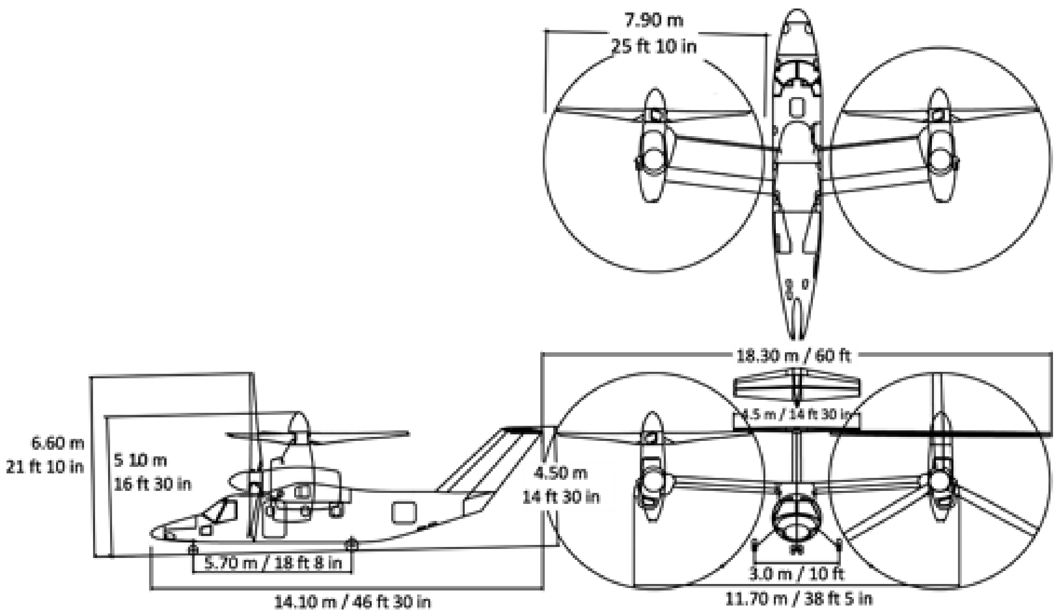

FIGURE A.4: AW609 3-view drawings

Appendix B

DNA - Data Noise Analyzer

B.1 A Matlab® code to analyze experimental acoustic loads

```

%% DNA - Data Noise Analizer
% DNA plots the TestLab Spectral Testing results stored in a
% .mat or a .txt format file

% Instructions for exporting data from TestLab
% Workbook LMS Signature Throughput Processing
% In order to generate the right input file, in TestLab environment ...
    select
% Tools-->Add-ins...
% Worksheet Time Recording During Spectral Testing
%          MEASURE Throughput (Acquisition parameters)
%          NAVIGATOR Section no.** --> RUN
%                      LDSF Throughput Data
%                          Export (.txt, .univ, .mat, .wav,...)
% * * * * * * * * * * * * * * * * * * * * * * * * * * * * * * * * *
%   release 1.0 03/12/19
%   release 2.0 26/03/20  Written by A.D. Marano
%   Department of Industrial Engineering, University of Naples ...
    Federico II
% * * * * * * * * * * * * * * * * * * * * * * * * * * * * * * * * *
%%
clc; clear all; close all;
%% Load Data by means .mat file and Input struct
[filename]=uigetfile('*.mat','Choose a .mat input file');
load(filename)                          % load 'filename.mat'

if filename≠0
    fprintf('Ok, data file was correctly loaded\n')
end

p_Pa=Signal_0.y_values.values;          % Pressure Fluctuations [Pa]
t_i=Signal_0.x_values.start_value;      % Initial time
d_t=Signal_0.x_values.increment;        % Time Increment
n_v=Signal_0.x_values.number_of_values; % Lenght Signal Vector
t=t_i:d_t:d_t*(n_v-1);                  % Measured Time Vector
```

```
t_f=t(end);                             % Final Time

% Alternative input forms
%(depends on how Testlab files are stored: notice the absence of ...
    '_0' in Signal_0.)
% p_Pa=Signal.y_values.values;          % Pressure Fluctuations [Pa]
% t_i=Signal.x_values.start_value;      % Initial time
% d_t=Signal.x_values.increment;        % Time Increment
% n_v=Signal.x_values.number_of_values; % Lenght Signal Vector
% t=t_i:d_t:d_t*(n_v-1);                  % Measured Time Vector
% t_f=t(end);                             % Final Time
%% Other Values
fs = 1/d_t;                             % Sample Frequency
p_ref = 2e-5;                           % Reference pressure in air
p_dB = 20*log10(p_Pa/p_ref);            % Pressure Fluctuation [dB]
%% Alternative assignments signal input
% Load the Signal data by means .wav file
% p_Pa=audioread('test_mic.wav');
%% Load the Signal data by means .txt file
% fid = fopen('time1_150kts.txt','rt');
% C = textscan(fid, '%f%f', 'HeaderLines',47);
% fclose(fid);
% A = cell2mat(C);
% t_i=A(1,1);          % Initial time
% t_f=A(end,1);        % Final time
% t=A(:,1);            % Measurement times
% p_Pa=A(:,2);         % Pressure Fluctuations [Pa]
% d_t=A(2,1)-A(1,1);   % Time Increment
% n_v=length(A);

% To extract the speed value from the loaded filename
a=find(filename=='k'); % k of kts in filename 'ext_xxxkts'
vel=str2num(filename(a-3:a-1));

%%%%%%%%%%%%%%%%%%%%%%%%%%%%%%%%%%%%%%%%%%%%%%%%%%%%%%%%%%%%%%%%%%%%%%%%
% * * * * * * * * * * * TIME DOMAIN ANALYSIS * * * * * * * * * * *
%%%%%%%%%%%%%%%%%%%%%%%%%%%%%%%%%%%%%%%%%%%%%%%%%%%%%%%%%%%%%%%%%%%%%%%%
%% Plot Input Pressure Values
% Plot Pressure Fluctuation [Pa] vs. Time
B1=figure(1);
plot(t,p_Pa(:,3)); % The second index in parentheses refers to the ...
    microphone
title(['Exterior Pressure Time History, ',num2str(vel),' kts']);
grid on; grid minor;
hold on
plot(t,p_Pa(:,12)); % The second index in parentheses refers to the ...
    microphone
legend('mic.3','mic.12');
    %'mic.3','mic.4','mic.5','mic.6',...
    %'mic.7','mic.8','mic.9','mic.10','mic.11','mic.12');
xlabel('Time [s]'); ylabel('Pressure [Pa]');
xlim([0 t(end)]);
```

```

%Plot Pressure [dB]
B2=figure(2);
plot(t,real(p_dB(:,1)));
grid on; grid minor;
hold on
plot(t,real(p_dB(:,2)));
plot(t,real(p_dB(:,3)));
plot(t,real(p_dB(:,4)));
plot(t,real(p_dB(:,5)));
plot(t,real(p_dB(:,6)));
plot(t,real(p_dB(:,7)));
plot(t,real(p_dB(:,8)));
plot(t,real(p_dB(:,9)));
plot(t,real(p_dB(:,10)));
%plot(t,real(p_dB(:,11)));
plot(t,real(p_dB(:,12)));
legend('mic.1','mic.2','mic.3','mic.4','mic.5','mic.6',...
     'mic.7','mic.8','mic.9','mic.10',      'mic.12');
hold on;
xlabel('Time [s]'); ylabel('SPL [dB]');
xlim([0 10]);
title(['Exterior Pressure Time History, ',num2str(vel),' kts']);
hold off

%%%%%%%%%%%%%%%%%%%%%%%%%%%%%%%%%%%%%%%%%%%%%%%%%%%%%%%%%%%%%%%%%%%%%%%%
% * * * * * * * * * * FREQUENCY DOMAIN ANALYSIS * * * * * * * * * *
%%%%%%%%%%%%%%%%%%%%%%%%%%%%%%%%%%%%%%%%%%%%%%%%%%%%%%%%%%%%%%%%%%%%%%%%
%% Fast Fourier Transform
Ts=1;                    % Sampled Time
n_s=fs*Ts;               % Sampled values
Ns=floor(fs*Ts);         % Samping number rounded
n_int=floor(n_v/Ns);     % Number of intervals

p_sum=0;                 % Initialization Sum Vector
for ii=1:n_int;
    FFTx=p_Pa(1+(Ns*(ii-1)):(Ns*ii),:);
    FFTx=fft(FFTx);
    % Delete the second half of the estimates divided by Sampled Values
    FFT=FFTx(1:size(FFTx,1)/2,:)/n_s;
    p_sum=p_sum + abs(FFT);
    FFTmatrix(:,:,ii)=FFT; % FFT matrix
end

freq=linspace(0,(Ns/2),(Ns/2));          % Frequency Vector
p_Pa_av=p_sum./(n_int);                  % Mean SPL [Pa] for Each Canal
p_Pa_av_dB = mag2db((p_Pa_av/p_ref));    % Mean SPL [dB]

% plot SPL.
B3=figure(3);
hold on
for ii=1:7
```

```
    plot(freq,p_Pa_av_dB(:,ii))
end
plot(freq,p_Pa_av_dB(:,8),'r'); % out from cicle for in order to ...
    distinguish the color of the markers
plot(freq,p_Pa_av_dB(:,9),'y');
plot(freq,p_Pa_av_dB(:,10),'g');
plot(freq,p_Pa_av_dB(:,12),'k'); %Mic. 11 is not considered here
title(['Noise Spectrum dB ',num2str(vel),' kts']);
grid on; grid minor;
hold off
legend('mic.1','mic.2','mic.3','mic.4','mic.5','mic.6',...
    'mic.7','mic.8','mic.9','mic.10',...'mic.11',
    'mic.12');
xlabel('Frequency [Hz]'); ylabel('SPL [dB]');
xlim([0 400]); ylim([80 135]);

%% Fast Fourier Transform - One Third Octave Frequency Bands
% Mean SPL 1/3 Octave Band center Frequencies
F_1_3 = [16 20 25 31.5 40 50 63 80 100 125 160 200 250 315 400 ...
    500 630 800 1000 1250 1600 2000 2500 3150 4000 5000 ...
    6300 8000]; % 10000 12500 16000 20000]; % center frequencies ANSI

p_sum=0;            % Initialization Sum Vector
for ii=1:n_int;
    % Delete the second half of the estimates divided by Sampled Values
    [FFt_1_3 ...
        cf]=poctave(p_Pa(1+(Ns*(ii-1)):(Ns*ii),:),fs,'BandsPerOctave',3,...
        'FrequencyLimits',[F_1_3(1)  F_1_3(end)]);
    FFt_1_3=sqrt(FFt_1_3);
    p_sum=p_sum + abs(FFt_1_3);
end

p_Pa_av_1_3=p_sum./(n_int);                   % Mean SPL [Pa] for ...
    Each Canal
p_Pa_av_1_3_dB=mag2db(p_Pa_av_1_3./p_ref);    % Mean SPL [dB]

% Plot SPL 1/3 octave band
B4=figure(4);
nm=6;    % no. microphone
bar(p_Pa_av_1_3_dB(:,nm),'LineWidth',1.5);
set(gca,'XTick',(1:1:length(F_1_3)))% Label frequency axis on octaves.
set(gca,'XTickLabel',F_1_3(1:1:length(F_1_3)));
xlabel('Frequency band [Hz]'); ylabel('SPL [dB]');
title(['One-third-octave spectrum ',num2str(vel),' kts ...
    mic.',num2str(nm)])
ylim([90 130]);

B5=figure(5);
for ii=1:7
    hold on
    plot(p_Pa_av_1_3_dB(:,ii));
end
```

```
plot(p_Pa_av_1_3_dB(:,8),'r'); % out from cicle for in order to ...
    distinguish the color of the markers
plot(p_Pa_av_1_3_dB(:,9),'y');
plot(p_Pa_av_1_3_dB(:,10),'g');
plot(p_Pa_av_1_3_dB(:,11),'b');
plot(p_Pa_av_1_3_dB(:,12),'k');
set(gca,'XTick',(1:1:length(F_1_3)))% Label frequency axis on octaves.
set(gca,'XTickLabel',F_1_3(1:1:length(F_1_3)));
title(['Sound Pressure Level dB ',num2str(vel),' kts']);
grid on;
legend('mic.1','mic.2','mic.3','mic.4','mic.5','mic.6',...
    'mic.7','mic.8','mic.9','mic.10',...'mic.11',
    'mic.12');
xlabel('Frequency [Hz]'); ylabel('SPL [dB]');
ylim([95 130]);
hold off

%% Analysis of the Symmetric, Longitudinal and Transverse noise fields

% Microphones in symmetrical positions
B6=figure(6);
hold on
plot(p_Pa_av_1_3_dB(:,3));
plot(p_Pa_av_1_3_dB(:,12));
set(gca,'XTick',(1:1:length(F_1_3)))% Label frequency axis on octaves.
set(gca,'XTickLabel',F_1_3(1:1:length(F_1_3)));
title(['Sound Pressure Level dB ',num2str(vel),' kts']);
grid on;
legend('mic.3','mic.12');
xlabel('Frequency [Hz]'); ylabel('SPL [dB]');
ylim([95 130]);

B7=figure(7);
plot(freq,p_Pa_av_dB(:,3));
hold on
plot(freq,p_Pa_av_dB(:,12));
title(['Noise Spectrum dB ',num2str(vel),' kts']);
grid on; grid minor;
hold off
legend('mic.3','mic.12');
xlabel('Frequency [Hz]'); ylabel('SPL [dB]');
xlim([0 400]); ylim([80 135]);

% Transversal microphones
B8=figure(8);
hold on
plot(p_Pa_av_1_3_dB(:,1));
plot(p_Pa_av_1_3_dB(:,2));
plot(p_Pa_av_1_3_dB(:,3));
plot(p_Pa_av_1_3_dB(:,4));
plot(p_Pa_av_1_3_dB(:,5));
plot(p_Pa_av_1_3_dB(:,12));
```

```
set(gca,'XTick',(1:1:length(F_1_3)))% Label frequency axis on octaves.
set(gca,'XTickLabel',F_1_3(1:1:length(F_1_3)));
title(['Sound Pressure Level dB ',num2str(vel),' kts']);
grid on;
legend('mic.1','mic.2','mic.3','mic.4','mic.5','mic.12');
xlabel('Frequency [Hz]'); ylabel('SPL [dB]');
ylim([95 130]);

B9=figure(9);
hold on
plot(freq,p_Pa_av_dB(:,1));
plot(freq,p_Pa_av_dB(:,2));
plot(freq,p_Pa_av_dB(:,3));
plot(freq,p_Pa_av_dB(:,4));
plot(freq,p_Pa_av_dB(:,5));
plot(freq,p_Pa_av_dB(:,12));
title(['Noise Spectrum dB ',num2str(vel),' kts']);
grid on; grid minor;
hold off
legend('mic.1','mic.2','mic.3','mic.4','mic.5','mic.12');
xlabel('Frequency [Hz]'); ylabel('SPL [dB]');
xlim([0 400]); ylim([80 135]);

B10=figure(10);
subplot(4,3,1)
plot(freq,p_Pa_av_dB(:,1));
grid on; grid minor;
title('Microphone 1');
% xlabel('Frequency [Hz]');
ylabel('SPL [dB]');
xlim([0 1000]); ylim([80 130]);
subplot(4,3,2)
plot(freq,p_Pa_av_dB(:,2));
grid on; grid minor;
title('Microphone 2');
% xlabel('Frequency [Hz]');
% ylabel('Pressure [dB]');
xlim([0 1000]); ylim([80 130]);
subplot(4,3,3)
plot(freq,p_Pa_av_dB(:,3));
grid on; grid minor;
title('Microphone 3');
% xlabel('Frequency [Hz]');
% ylabel('Pressure [dB]');
xlim([0 1000]); ylim([80 130]);
subplot(4,3,4)
plot(freq,p_Pa_av_dB(:,4));
grid on; grid minor;
title('Microphone 4');
% xlabel('Frequency [Hz]');
ylabel('SPL [dB]');
xlim([0 1000]);
```

```
ylim([80 130]);
subplot(4,3,5)
plot(freq,p_Pa_av_dB(:,5));
grid on; grid minor;
title('Microphone 5');
% xlabel('Frequency [Hz]');
% ylabel('Pressure [dB]');
xlim([0 1000]);
ylim([80 130]);
subplot(4,3,6)
plot(freq,p_Pa_av_dB(:,6));
grid on; grid minor;
title('Microphone 6');
% xlabel('Frequency [Hz]');
% ylabel('Pressure [dB]');
xlim([0 1000]); ylim([80 130]);
subplot(4,3,7)
plot(freq,p_Pa_av_dB(:,7));
grid on; grid minor;
title('Microphone 7');
% xlabel('Frequency [Hz]');
ylabel('SPL [dB]');
xlim([0 1000]); ylim([80 130]);
subplot(4,3,8)
plot(freq,p_Pa_av_dB(:,8));
grid on; grid minor;
title('Microphone 8');
% xlabel('Frequency [Hz]');
% ylabel('Pressure [dB]');
xlim([0 1000]); ylim([80 130]);
subplot(4,3,9)
plot(freq,p_Pa_av_dB(:,9));
grid on; grid minor;
title('Microphone 9');
% xlabel('Frequency [Hz]');
% ylabel('Pressure [dB]');
xlim([0 1000]); ylim([80 130]);
subplot(4,3,10)
plot(freq,p_Pa_av_dB(:,10));
grid on; grid minor;
title('Microphone 10');
xlabel('Frequency [Hz]'); ylabel('SPL [dB]');
xlim([0 1000]);
ylim([80 130]);
subplot(4,3,11)
plot(freq,p_Pa_av_dB(:,11));
grid on; grid minor;
title('Microphone 11');
xlabel('Frequency [Hz]');
% ylabel('Pressure [dB]');
xlim([0 1000]); ylim([80 130]);
subplot(4,3,12)
```

```
plot(freq,p_Pa_av_dB(:,12));
grid on; grid minor;
title('Microphone 12');
xlabel('Frequency [Hz]');
% ylabel('Pressure [dB]');
xlim([0 1000]); ylim([80 130]);
suptitle(['SPL of all microphones at a speed of ',num2str(vel),' kts'])


% Longitudinal microphones
B11=figure(11);
hold on
plot(p_Pa_av_1_3_dB(:,6));
plot(p_Pa_av_1_3_dB(:,3));
plot(p_Pa_av_1_3_dB(:,7));
plot(p_Pa_av_1_3_dB(:,8));
plot(p_Pa_av_1_3_dB(:,9));
plot(p_Pa_av_1_3_dB(:,10));
% plot(p_Pa_av_1_3_dB(:,11));
set(gca,'XTick',(1:1:length(F_1_3)))% Label frequency axis on octaves.
set(gca,'XTickLabel',F_1_3(1:1:length(F_1_3)));
title(['Sound Pressure Level dB ',num2str(vel),' kts']);
grid on;
legend('mic.6','mic.3','mic.7','mic.8','mic.9','mic.10');
xlabel('Frequency [Hz]');
ylabel('SPL [dB]'); ylim([95 130]);


B12=figure(12);
hold on
plot(freq,p_Pa_av_dB(:,6));
plot(freq,p_Pa_av_dB(:,3));
plot(freq,p_Pa_av_dB(:,7));
plot(freq,p_Pa_av_dB(:,8));
plot(freq,p_Pa_av_dB(:,9));
plot(freq,p_Pa_av_dB(:,10));
title(['Noise Spectrum dB ',num2str(vel),' kts']);
grid on; grid minor;
hold off
legend('mic.6','mic.3','mic.7','mic.8','mic.9','mic.10');
xlabel('Frequency [Hz]');
ylabel('SPL [dB]');
xlim([0 400]);
ylim([80 135]);

%% Overall RMS
p_rms_Pa = sqrt(sum(p_Pa_av_1_3.^2)); %  [Pa]
p_rms_dB = mag2db((p_rms_Pa/p_ref)); % [dB]
fprintf('Overall SPL is %4.1f dB\n',p_rms_dB);

B13=figure(13);
hold on
```

```
 for ii=1:7
     scatter(vel,p_rms_dB(ii),'filled');
 end
scatter(vel,p_rms_dB(8),'r','filled');
scatter(vel,p_rms_dB(9),'y','filled');
scatter(vel,p_rms_dB(10),'g','filled');
scatter(vel,p_rms_dB(11),'b','filled');
scatter(vel,p_rms_dB(12),'k','filled');
grid on; grid minor;
title(['Overall SPL dB ',num2str(vel),' kts']);
xlabel('Flight speed [kts]'); ylabel('SPL [dB]');
legend('mic.1','mic.2','mic.3','mic.4','mic.5','mic.6',...
    'mic.7','mic.8','mic.9','mic.10',...'mic.11',
    'mic.12');
ylim([125 136]);
hold off

% The Overall data will be save in a .mat file. When all flight ... conditions
% have been analyzed, it is possible to draw an only overall graph

% save(['OverAll_',filename(a-3:end)],'vel','p_rms_dB');

%%
% Rotor Characteristics
RPM=478;            % Round Per Minute
T_rot_t=60/RPM;     % Period of the Propeller [s]
T_rot_f=RPM/60;     % Period of the Propeller [Hz]
BPF=3*T_rot_f;      % Blade Passage Frequency

% Time Signal Average Propeller
N_samp=floor(t_f/T_rot_t);
flag=find(t≥T_rot_t);
t_lim=flag(1)-1;

B14=figure(14);
nmicr=6; % select microphone
plot(t(1:t_lim),p_Pa(1:t_lim,nmicr));
grid on; grid minor;
hold on;
M=movmean(p_Pa(1:t_lim,nmicr),100);
plot(t(1:t_lim),M,'LineWidth',2);
legend('Instantaneous','Time Average','Location','southeast');
xlabel('Rotation of the Propeller Period [s]'); ylabel('Pressure ... [Pa]');
xlim([t_i T_rot_t]); ylim([-600 600]);
title(['Pressure time histories mic.' num2str(nmicr), 'at ' ... num2str(vel),' kts']);
hold off

B15=figure(15);
n_micr=6; % Select microphone
```

```
for i=1:100
   hold on;
   scatter(t(1:t_lim),p_Pa( 1+(t_lim*(i-1)) : t_lim+(t_lim*(i-1)) ...
       ,n_micr),'k','filled','SizeData',1);
   alpha(0.3);
end
title(['Pressure time histories mic.',num2str(n_micr), ' at ' ...
    num2str(vel),' kts']);
xlabel('Rotation of the Propeller Period [s]'); ylabel('Pressure ...
    [Pa]');
xlim([t_i T_rot_t]); ylim([-300 300]);

%% * * * * * * * * * * * * * * * * * * * * * * * * * * * * * * * * * ...
    * * * *
% Max values of the tones for the different microphones
n_t=7;  % Number of the first tones to be analyzed
w3=p_Pa_av_dB([1:500],[1:6]);
for i=1:n_t
    if i==1
        peak(i,:)=p_Pa_av_dB(25,:); %peak(i,c) i=tone, c=mics
    elseif i==2
        peak(i,:)=p_Pa_av_dB(49,:);
    elseif i==3
        peak(i,:)=p_Pa_av_dB(73,:);
    elseif i==4
        peak(i,:)=p_Pa_av_dB(97,:);
    elseif i==5
        peak(i,:)=p_Pa_av_dB(121,:);
    elseif i==6
        peak(i,:)=p_Pa_av_dB(144,:);
    else
        peak(i,:)=p_Pa_av_dB(168,:);
    end
end

B16=figure(16);
hold on;
xlim([0.5 size(p_Pa_av_dB,2)+3]);
grid on;
grid minor;
for i=1:size(p_Pa_av_dB,2)
    for j=1:n_t
    scatter(i,peak(j,i),'filled')
    end
end
legend('1Âř tone','2Âř tone','3Âř tone','4Âř tone','5Âř tone','6Âř ...
    tone','7Âř tone');
xlabel('Mic nÂř'); ylabel('Peak value [dB]');
title(['Tone at ',num2str(vel),' kts (RPM=478, BPF=23.9 Hz)'])
```

Appendix C

Comparison of aeroelastic problems calculation methods based on numerical and experimental results. Overview of NASTRAN™ and ZAERO Aeroelastic Capabilities

C.1 Introduction

The Flutter is the unstable self-excited oscillation of an airfoil and its associated structure, caused by a combination of aerodynamic, inertia, and elastic effects in such a manner as to extract energy from the airstream. At the critical flutter speed, the amplitude of oscillation following an initial disturbance will be maintained while at a higher speed these amplitudes will increase [113].
The general purpose of any methods of Vibration and Flutter analysis for a conventional airplane is to prove that the airplane is free from flutter, control reversal, and divergence for any condition of operation within the limit V-n envelope, plus a supplementary safety margin. In other terms, the main scope of flight flutter test and numerical analysis is to determine the aeroelastic stability for new or modified vehicles and sub-components of them in the nominal flight envelope established by the project. The approval process concerning aeroelastic matters, flutter, divergence, and control reversal at all speeds in the entire flight envelope, during the design and certification phase of a new aircraft, is a combination of numerical modeling backed up by testing. Flight flutter testing is very expensive, time-consuming, and often undertaken at a time-critical part of an aircraft's development program. For this reason, aeroelastic computational modeling and prediction are of fundamental importance in the design and certification process.
The flutter numerical investigations of aircraft are frequently based on the normal

modes structural analysis and no aerodynamic model was required. The natural modes are initially computed by means FEM using a model of the structure and then, after the inclusion of aerodynamics in the structural model by spline operation, the output Velocities vs Damping and Velocities vs Frequencies curves are used for the Flutter speed estimation and establish the aeroelastic stability conditions.
In addition to the easily interpreted frequency and damping plots versus airspeed for strongly coupled systems, a second advantage is offered by the P-K method regarding computational effort. The k method requires numerous computer runs at a constant density to ensure matching of the Mach number with air-speed and altitude. Currently, most flutter analyses in the aircraft industry are per-formed using k and/or P-K methods. Although the k method remains popular because of its speed, when accuracy is important and the p method is not feasible, industry users seem to favor the P-K method, especially those who run the NASTRAN™ package [114].
The ZAERO flutter module contains different flutter solution techniques. For this article, the K-method and the g-method are used. The g-method is ZONA's newly developed flutter solution method that generalizes the K-method and the P-K method for true damping prediction. It is shown that the P-K method is only valid at the conditions of zero damping, zero frequency, or linearly varying generalized aerodynamic forces with respect to reduced frequency. In fact, if the generalized aerodynamic forces are highly nonlinear, the P-K method may produce unrealistic roots due to its inconsistent formulation.
One of the aims of this work is to get confident with ZAERO, a relatively new software compared to the much more used NASTRAN™. Section C.2 briefly reports the operational flow of ZAERO and some useful information obtained from the manuals. Finally, the results obtained for two case studies are reported. In the first case, the aeroelastic behavior of an innovative design for-ward-swept wing is analyzed. In the second case, based on the availability of data deriving from vibration measurements on an ultralight aircraft, a problem of a more practical than design nature is reported. Both the experimental results obtained through vibration tests on the stabilator of an ultralight aircraft, and numerical aeroelasticity activity are shown [115].

C.2 A brief overview of NASTRAN and ZAERO

To achieve the aeroelastic behavior of the wing, the flexural and torsional stiffness and structural and non-structural mass distribution along the wingspan, will feed the dynamic structural Finite Elements model. For the case studies reviewed in this article, stick-beam models are used.
The firsts Aeroelastic analyses are performed using NASTRAN™ solver. NASTRAN™

computes matrices of aerodynamic influence coefficients from the input data describing the structural model and also provides an automated interpolation procedure to relate the aerodynamics (panels) to the structural degrees of freedom (structural grid point of the model) [116, 117].
Splining techniques for both lines and surfaces can be used to generate the transformation matrix from structural grid point deflections to aerodynamic grid point deflections. The transpose of this matrix transfers the aerodynamic forces and moments at aerodynamic boxes to structural grid points. For this work, the subsonic theory is used and in particular the Doublet-Lattice Method (DLM) [118–121], an extension of the steady Vortex-Lattice method to unsteady flow. It can be used for interfering with lifting surfaces in subsonic flow.
The second step of the aeroelastic analyzes consists of comparing the results obtained by the NASTRAN^{TM} and Zonatech ZAERO software respectively [122]. ZAERO integrates the crucial disciplines required for aeroelastic analysis and it represents a valid alternative to the widespread commercial codes such as NASTRAN^{TM}. For the aeroelastic analysis, ZAERO does not run the structural finite element solutions, but firstly it imports the structural grid point and the externally calculated structural normal modes solutions generated by one of the following FEM codes: NASTRAN^{TM}, ANSYS, ABAQUS, ASTROS, and I-DEAS. Then, the aerodynamic method is implemented. In particular, the six methods (or aerodynamic codes) incorporated in the ZAERO software, cover the entire Mach number range:

- ZONA6 - Subsonic Unsteady Aerodynamics;
- ZSAP - Sonic Acceleration Potential Method;
- ZTAIC - Transonic Unsteady Aerodynamics using a Transonic Equivalent Strip Method;
- ZTRAN - Transonic Unsteady Aerodynamics using an Overset Field-Panel Method;
- ZONA7 - Supersonic Unsteady Aerodynamics;
- ZONA7U - Hypersonic Unsteady Aerodynamics.

About the capability and applicability advantages of the ZAERO code over that of other commercially available aeroelastic analysis software is that ZAERO seems to provide a higher level of geometric fidelity than other aeroelastic packages such as NASTRAN.
The figure C.1 shows the ZAERO file processing that occurs during code execution.

Three files are required to run the code:

- the input file which contains the executive control, case control, and bulk data sections that describe the aerodynamic model, flight conditions, etc.;

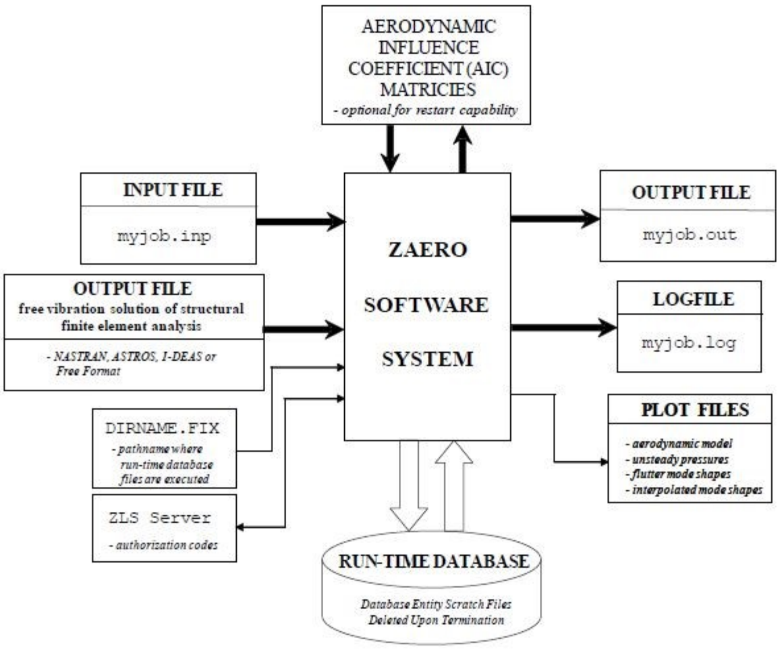

FIGURE C.1: The ZAERO Software System File Processing [122].

- the structural FEM output file containing the structure natural frequencies and mode shapes;
- DIRNAME.FIX which contains the pathname where the ZAERO run-time database files are to be located.

About the outputs, a minimum of two files is generated for every ZAERO run. These are:

- the output file of the job;
- the log file which contains the elapsed and step CPU times for each module call during the execution of ZAERO. Additional output plot files can be generated through bulk data input requests.

C.3 Comparison Between the g-Method and the P-K Method

C.3.1 1^{st} Test Case - Forward swept wing

The first test case presented is the aeroelastic analysis of a forward-swept wing. This type of wing, unlike conventional wings, presents a criticality due to the phenomenon of static aeroelasticity of divergence. In other words, the negative sweep angle causes the divergence speed to be lower than the equivalent straight or sweep back wing [122, 123].
Figure C.4 shows the aeroelastic model: aerodynamic paneling or Double Lattice panel model connected to the structural beam-like model. In a stick model, the wing is represented by beams capable of bending, shear, torsional and axial deformations.

In this example figures C.2 and C.3 represent the wingspan distribution of the stiffness and mass respectively. Each beam is divided into several elements with a flexural stiffness *EI* and torsional stiffness *GJ* estimated from the member section properties by classical structural analysis methods.
A considerable degree of detail is known for the mass distribution on the wing structure, but only part of the mass is structural, and therefore associated with the FE structural model, whereas a significant amount of mass is linked with non-structural elements such as fuel [124].
To represent the mass distribution, the wing is divided into several strips, centered on the nodes of the beam-like model. For each section, the mass is lumped at the reference positions and attached to the beam axis node by a rigid link element that allows the lumped mass to be represented by section mass, a moment of inertia, and mass moments [125, 126].
The aerodynamic panels distribution for the wing is carried out by taking into account the criteria suggested by [127]. The first ten structural elastic modes are used for flutter analysis. Figure C.5 shows the mode shapes and natural frequencies only for the first 4 modes for the sake of brevity.
Figures C.6 show the V-g and V-f diagrams of the P-K-method and the V-g and V-f diagrams of the G method for the wing with 10 modes at Mach number $M = 0$.

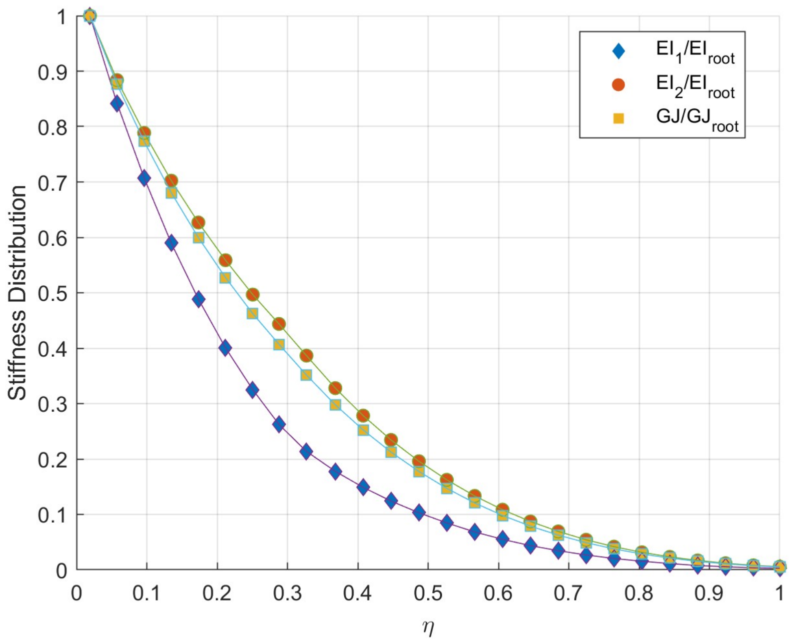

FIGURE C.2: Flexural and Torsional Stiffness distribution along wingspan.

Figure C.6 shows the NASTRANâĎć P-K solutions of the wing previously described at different given velocities from 50 to 500 m/s.
From the damping plot versus airspeed, it is possible to observe that the aerodynamic damping of mode 5, corresponding to the wing torsional mode, is nil at a

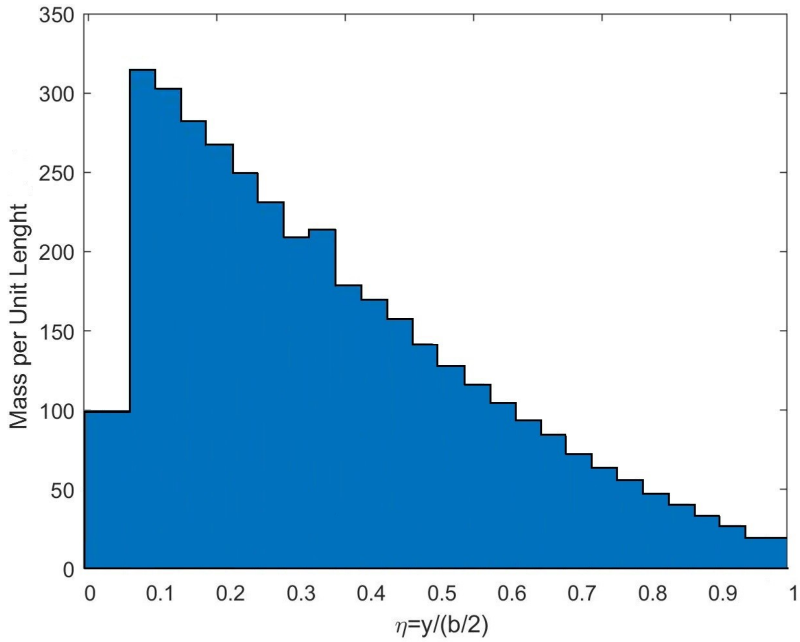

FIGURE C.3: Mass distribution along wingspan.

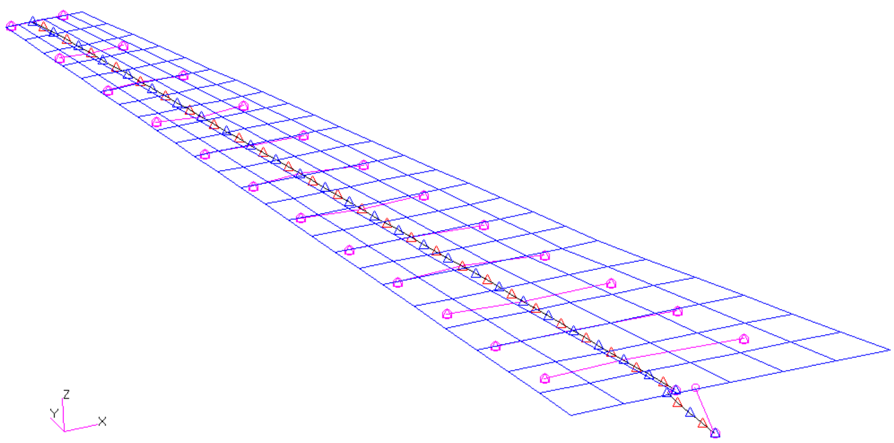

FIGURE C.4: Forward swept wing - aeroelastic stick model.

speed of about 430 m/s.

In the frequency versus airspeed plot, at the same velocity, a coalescence of the frequencies of mode 3 and mode 5 is observed: there is a modal coupling between the aforementioned wing torsional mode and the 2^{nd} wing bending mode. A flutter condition is attributed to this speed.

A significant aeroelastic observation is needed where divergence speed instability appears at 300 m/s i.e. a speed lower than the flutter velocity. This divergence speed instability is evident by its associated zero frequency. Comparing the upper plots with the lower ones in figure C.6, it can be seen that the agreement between the

damping computed by the P-K method and the g-method is expected. Good agreement in terms of the overall V-g and V-f comparisons between these methods is obtained except the g-method predicts one extra aerodynamic lag root (represented by the crosses in Figure C.6).
This aerodynamic lag root appears at divergence speed (about V=300 m/s) with stable damping. This is an interesting phenomenon because it indicates that the divergence speed could be a bifurcation point. This result suggests that the divergence speed is caused by the coupling of a structural mode and an aerodynamic lag root and should be considered as a special case of flutter instability, the so-called *dynamic divergence*. This is supported by the g-method results shown in the lower plots of the figures where the frequency coalescence of the first bending mode and the aerodynamic lag root is seen. On the other hand, the plots of the P-K method do not show this result due to its incapacity of generating the non-zero-frequency aerodynamic lag root.

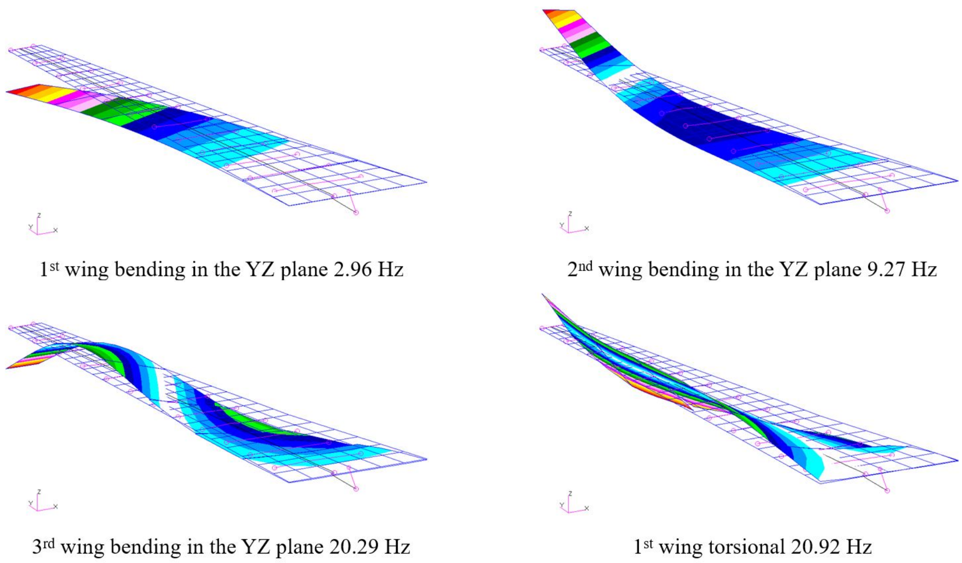

1st wing bending in the YZ plane 2.96 Hz

2nd wing bending in the YZ plane 9.27 Hz

3rd wing bending in the YZ plane 20.29 Hz

1st wing torsional 20.92 Hz

FIGURE C.5: Nastran Dynamic Analysis - Wing Normal Modes.

Table C.1 shows the flutter analysis results obtained by means ZAERO, in terms of the mode associated with flutter, natural frequency, and flutter speed.
For this first comparison, two types of instability are predicted by both the P-K method and the g-method: a flutter speed at about $V = 430$ m/s and a divergence speed at about $V = 300$ m/s. This agreement is expected since at damping $g = 0$ the flutter equation of both methods reduces to the same form. The damping curves of the structural modes computed by both methods are in excellent agreement. The frequency curves of the two structural modes computed by both methods are also in good agreement except for the absence of the aerodynamic lag roots of the P-K method.

For a question of investigation completeness, a second step involved an analysis of the same wing by adding the mass due to the fuel. The V-g and V-f diagrams

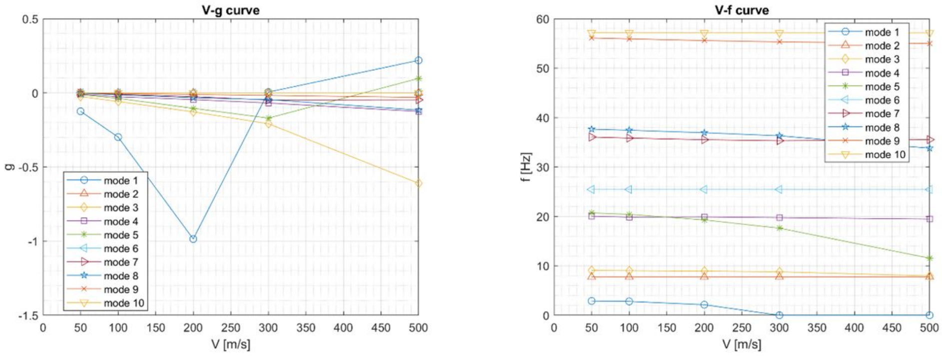

V-g and V-f curves P-K method NASTRAN – wing with empty fuel tank

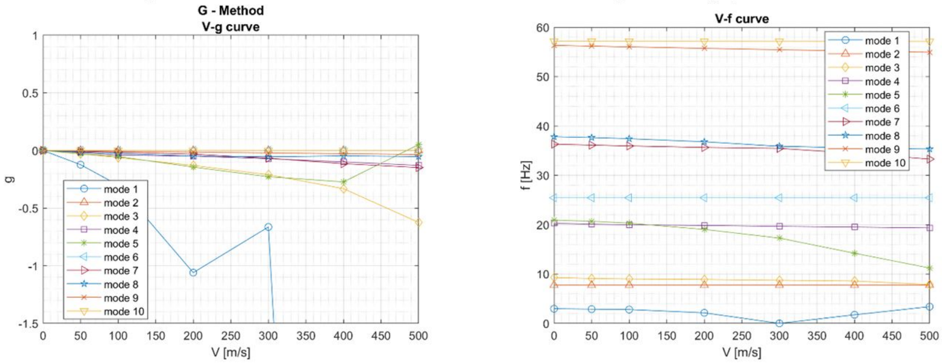

V-g and V-f curves G method ZAERO – wing with empty fuel tank

FIGURE C.6: V-g and V-f curves P-k method (Nastran) and G method (ZAERO) - wing with empty fuel tanks.

TABLE C.1: ZAERO Aeroelastic Analysis results - wing with empty fuel.

K **method**			G **method**		
mode	v_f(m/s)	Freq. (Hz)	mode	v_f(m/s)	Freq. (Hz)
2	428.7	7.74	2	452.2	7.74
5	486.3	11.57	5	484.2	11.69

relating to the case of full fuel tanks and a table with the flutter data are reported. The V-g diagram shows that the damping of mode 3 crosses the zero damping axis, indicating a fluctuation limit of the wing structure, at higher values than in the previous case.
From the V-g and V-f diagrams, calculated for the different load conditions we can draw the following conclusions:

- in all the calculations the divergence condition for the wing is present, the latter being independent of the mass contributions from the model;
- in both cases, with and without fuel, the divergence rate does not change;
- the most critical condition for flutter occurs when the wing is unloaded (the addition of the masses of the fuel involves the removal of the bending frequencies from the torsional ones);

TABLE C.2: ZAERO Aeroelastic Analysis results - wing with full fuel tanks.

	K method			G method	
mode	v_f(m/s)	Freq. (Hz)	mode	v_f(m/s)	Freq. (Hz)
2	326.1	6.53	2	324.5	6.53
3	671.0	5.60	4	665.8	5.77
5	591.9	19.59	5	581.8	19.59

- when the wing tanks are full there is the annulment of the aerodynamic damping of the first torsional frequency at a speed of about 44% higher than in the case of empty tanks. From the V-f diagram, we can ob-serve a coalescence of the aforesaid frequency with the second flexural frequency.

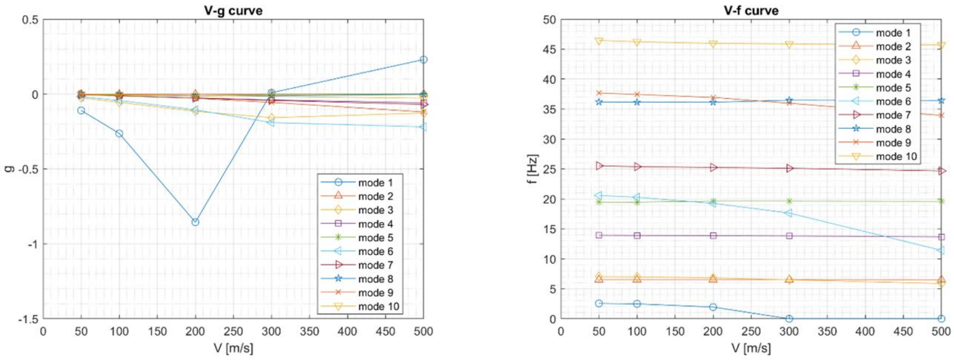

V-g and V-f curves P-K method NASTRAN – wing with full fuel tank

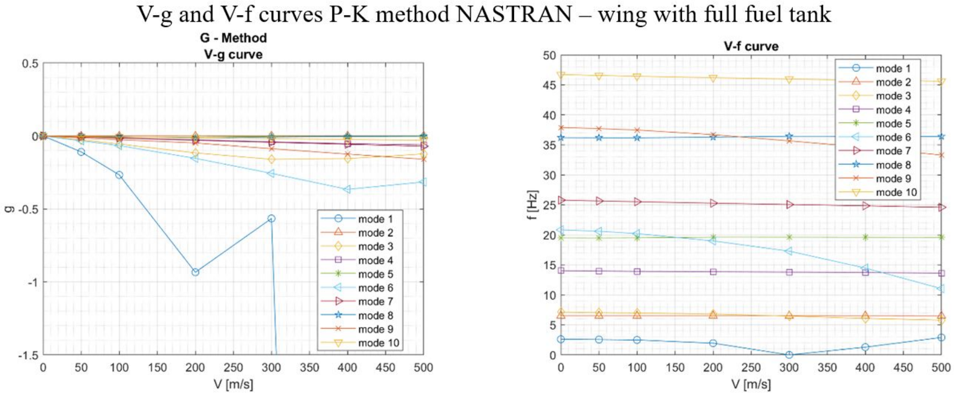

V-g and V-f curves G method ZAERO – wing with full fuel tank

FIGURE C.7: V-g and V-f curves P-k method (Nastran) and G method (ZAERO) - wing with full fuel tank.

Upon completion of the study of the first test case, a dynamic flutter analysis was performed as the stiffness distribution varies along the wingspan. In particular, a wing section of about 1 meter was chosen, a representative for example of an inspection window for maintenance or the extraction of the landing gear. It has been hypothesized that, in the notch area, with the same mass distribution, the flexural and torsional stiffnesses decreased by 30% of the initial value, i.e. wing without the door.

TABLE C.3: Results of the aeroelastic analysis as the stiffness varies along the wingspan.

Reference stiffness distribution	Stiffness var. @ 20-30%	Stiffness var. @ 30-40%
$v_f(m/s)$	$v_f(\Delta\%)$	$v_f(\Delta\%)$
430	−4.7	−2.8

To study how the flutter speed varies as a function of the location of the trap door, for the two stiffness variations the first area was considered respectively between 20 and 30% of the wingspan figure C.8 (a) and the second between 30 and 40% figure C.8 (b). For the first variation of stiffness distribution, a flutter speed of 410 m/s is obtained (Figure C.8 (c)) or a decrease of about 4.7% compared to the starting wing. For the second variation of stiffness distribution, on the other hand, the flutter speed is about 418 m/s (Figure C.8 (d)) and therefore is decreased by 2.8% compared to the reference wing.

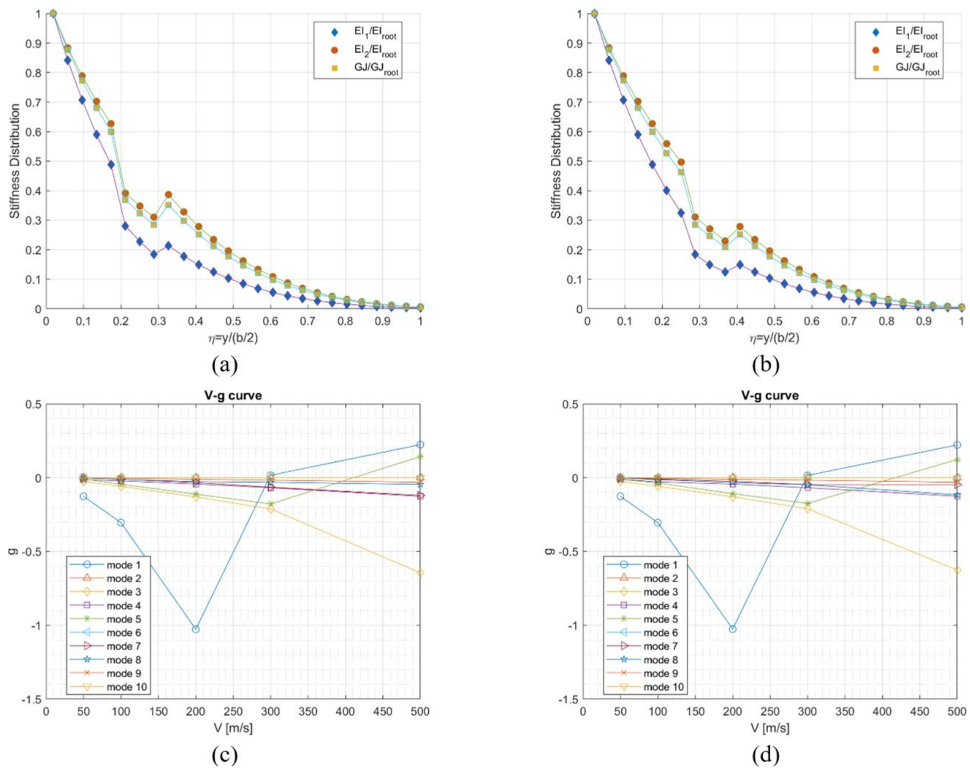

FIGURE C.8: Variation of stiffness distribution along the wingspan and consequent variation of the flutter speed.

C.3.2 2nd Test Case - Forward swept wing

The second test case has been selected due to the availability of the experimental modal analysis results and offered the opportunity to study a realistic case. The aircraft under study is an ultralight twin-seat aircraft whose fuselage has been changed from metallic to a carbon-fiber material (max cruise speed = 59 m/s and max take-off weight = 600 kg). The main dimensions are shown in figure C.9. A complex FEM

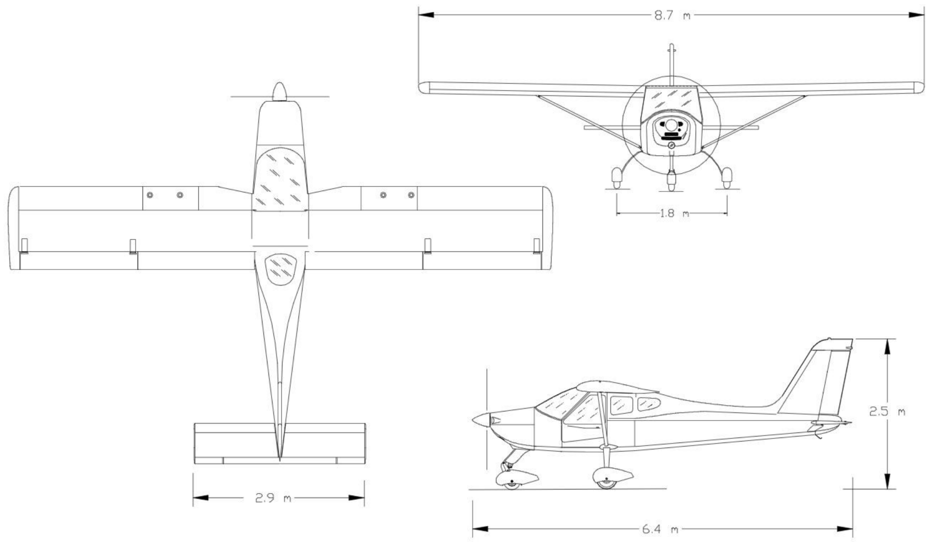

FIGURE C.9: Ultralight aircraft 3-views drawing.

model of the aircraft under examination made it possible to perform preliminary dynamic flutter analyzes. This model and the mode shapes deriving from the dynamic analysis, is shown in the figure C.10.
For the study of the comparison between the two different codes, it was instead decided to adopt a simplified model of the horizontal tailplane, which would allow obtaining adequate results with the advantage of saving time.

In particular, the flutter analysis refers only to the horizontal tailplane. As regards the first, simplified stabilator FEM model, the structure of the fuselage is simplified and idealized through six elastic elements that constitute the degrees of freedom. In more detail, the central node of the stabilator is connected to a fixed node of the fuselage utilizing six elastic elements, which represent the stiffness of the fuselage. Rigid elements have also been introduced in the model to better highlight the modes, facilitating their visualization in the post-processing phase and therefore the distinction between bending and torsional mode shapes. The aeroelastic FEM model is shown in figure C.11, in which it is possible to appreciate the constraint, the concentrated masses, the rigid elements, the aerodynamic panels, the set of nodes used for the interpolation, the spline itself.
For the analysis of flutter of the stabilator, various study cases are taken into account and they differ in the constraint condition (fixed) or in the unconstrained degree of freedom (rotation around the longitudinal axis x, rotation around the transverse axis y, and rotation around the vertical axis z) and for the value assumed for the stiffness of the elastic element.
From the calculations performed by NASTRAN$^{\text{TM}}$, the Flutter condition is not found

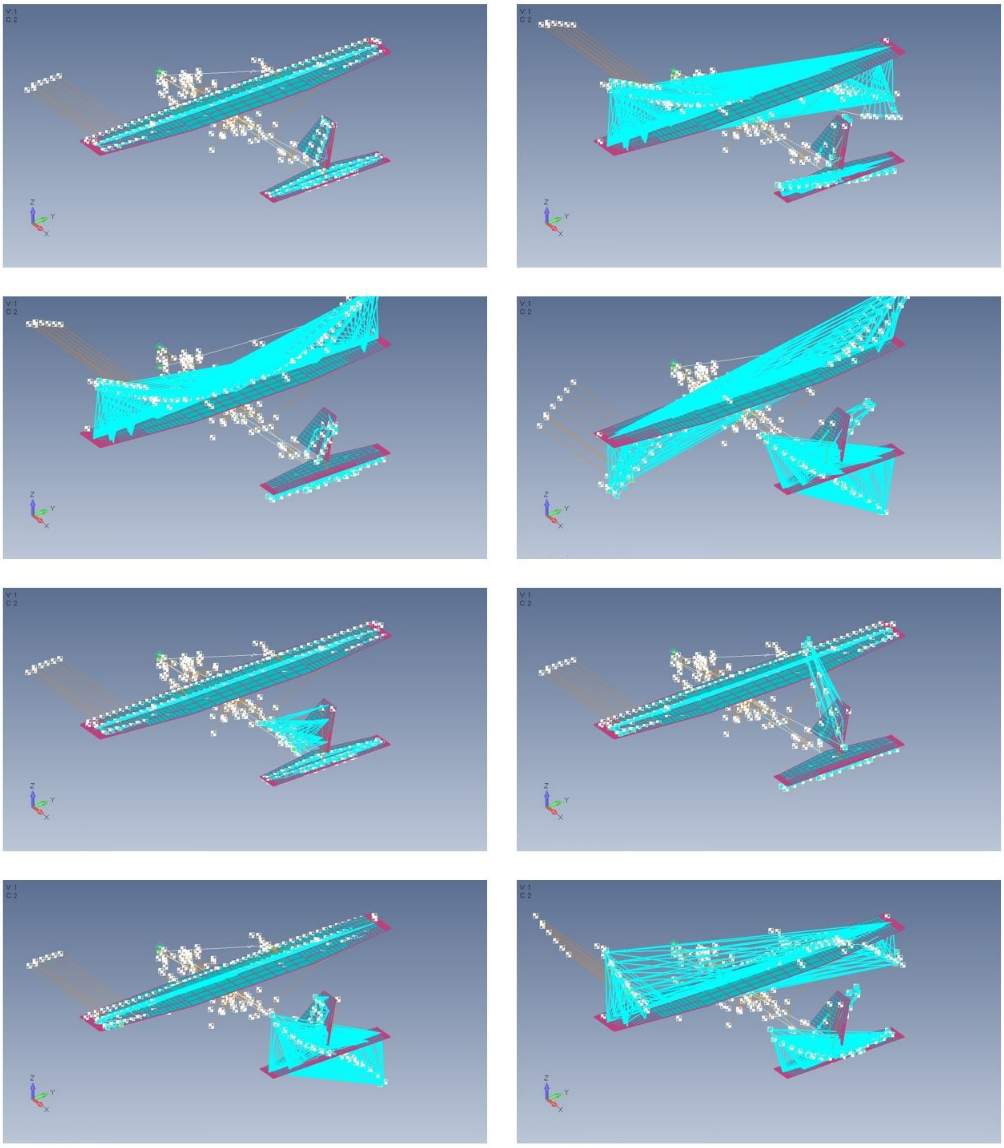

FIGURE C.10: Whole ultralight aircraft FEA model and mode shapes.

in any of the previously mentioned cases. A comparison is then made with the results obtained using the ZAERO code. First, however, it was deemed necessary to carry out a sort of sensitivity analysis to better understand how the aeroelastic responses of the structure are influenced by changes to the variables of the ZAERO code such as the number of aerodynamic panels along chord and along wingspan, nodes used for structural and aerodynamic interpolation, type of spline: linear or surface spline.

The purpose is to identify the parameters that make the analysis more conservative concern-ing the identification of the Flutter condition.

By neglecting to report the results of the numerous sensitivity analysis, from an evaluation of the values and the trend of the V-g and V-f graphs obtained from the analysis, it is possible to conclude that the best way to proceed is to use a surface-type

spline that allows the end nodes of the rigid elements to be included for interpolation. In any case, the numerical flutter modes obtained through this model have too high and unrealistic natural frequencies.
When ensuring the safety of aircraft against aeroelasticity phenomena, one of the important steps of investigation is Ground Vibration Test.
GVT can be performed to obtain the vibration amplitude distributions and the frequencies of the structure. The GVT results can be used for checking FEM results or used directly in the prediction of the flutter problems [128].
The next phase concerns the verification and tuning of the analytical results to the experimental ones. At this point, aerodynamic loads are modeled and measured using a wind tunnel test and combined with the dynamic properties in an analytical flutter prediction.
Finally, test flights are carried out for validation of the reached results and final certification, according to the requirement of the airworthiness standard [129].
The vibrations test has been performed by measuring the frequency response functions (FRF) between several points of the stabilator structure, each concerning a fixed position of the excitation point.
The excitation point is located in the middle of the rear spar of the horizontal tail. A maximum of 12 points for each side of the stabilator was measured. The excitation signal used during these tests has been a Sine Sweep Excitation, obtained through an electro-dynamic exciter Modal Shop Model 2100 E11 while the structural response has been measured with PCB 333B32 ICP piezoelectric accelerometers.
The evaluation of the FRF was carried out by using a standard 8 channels FFT analyzer, the LMS Scadas 05 Mobile. The LMS TestLab software provides the subsequent steps for the analysis and the extraction of the modal parameters by means LMS PolyMAX algorithm.
This modal parameters identification method yields extremely clear stabilization charts. Following the vibration tests, based on the experimental modal analysis results (C.4), the idea of updating the model of the horizontal tailplane was evaluated, thus making it better representative of the test article on which the tests were carried out.

The best modeling consists of discretizing the tailplane in as many points as are those considered in the test setup, in which the accelerometers have been placed (figure C.12). As regards the masses, it has been assumed that the stabilator weighs a total of 0.8 kg. This weight is distributed equally over the 24 nodes in which the stabilator is discretized while for the fuselage section weight of about 2 kg is assumed, equally distributed over the 5 nodes of the fuselage.
The aerodynamic model consists of 10 boxes along the chord and 15 along the wingspan.
The new aeroelastic model is shown in figure C.13 in which the distribution of concentrated masses and the nodes used for the aerodynamic-structural spline are highlighted.
Preliminarily, a modal analysis and a Dynamic Flutter analysis are carried out of the

TABLE C.4: Experimental Modal Analysis and Nastran Dynamic Analysis Results.

No. mode	Nastran Freq. (Hz)	EMA Freq. (Hz)	mode shape description
7	9.67	9.76	Fuselage tail torsion
8	12.27	12.59	Fuselage bending along z, wing sym. bending
9	14.09	14.61	Fuselage torsion, wing anti-sym. bending
10	19.32	18.23	Fuselage bending along y
11	21.10	20.42	Horizontal tail bending along z
12	25.81	24.48	Fuselage torsion
13	30.19	30.42	Horizontal tail bending

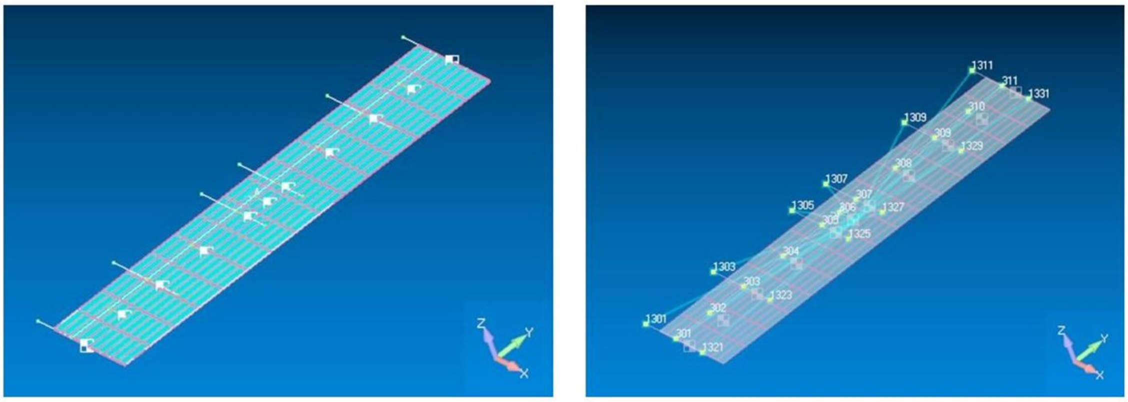

FIGURE C.11: FEM model Horizontal tail.

new model using the P-K method. The results of these analyzes are reported for the first 20 modes. Table 4 indicates the natural frequencies obtained while figure 13 indicates the mode shapes.

As regards the dynamic flutter analysis, as can be seen from figure C.14, employing the P-K method of Nastran, no Flutter instability occurs for zero structural damping up to V_{max} = 200 m/s. The analysis results obtained using the ZAERO software, on the other hand, highlights a flutter instability associated with the 9^{th} mode of a torsional nature, as shown in figures C.15 and C.16. The flutter speed calculated with both the k and g methods is shown in table C.5. In the same table it is also observed how by increasing the value of the structural damping, the flutter speed increases.

TABLE C.5: ZAERO Aeroelastic Analysis results - Horizontal tail

	K method			G method	
mode	v_f(m/s)	Freq. (Hz)	mode	v_f(m/s)	Freq. (Hz)
9	176.47	13.57	(No Damping, G = 0)	211.8	13.54
—	—	—	(Damping, G = 0.5)	259.7	13.54

FIGURE C.12: Test setup Vibration Tests Horizontal tail twin-seat ultralight aircraft.

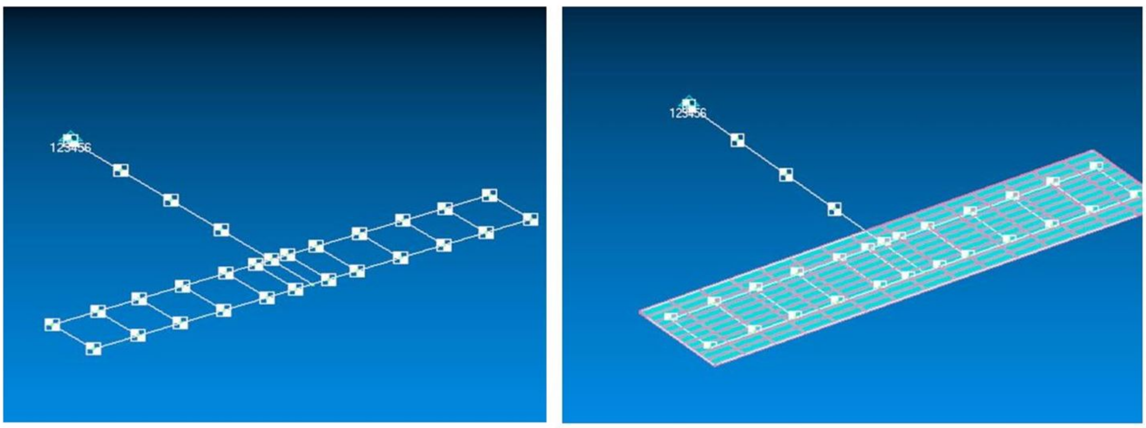

FIGURE C.13: Updated FEM model Horizontal tail.

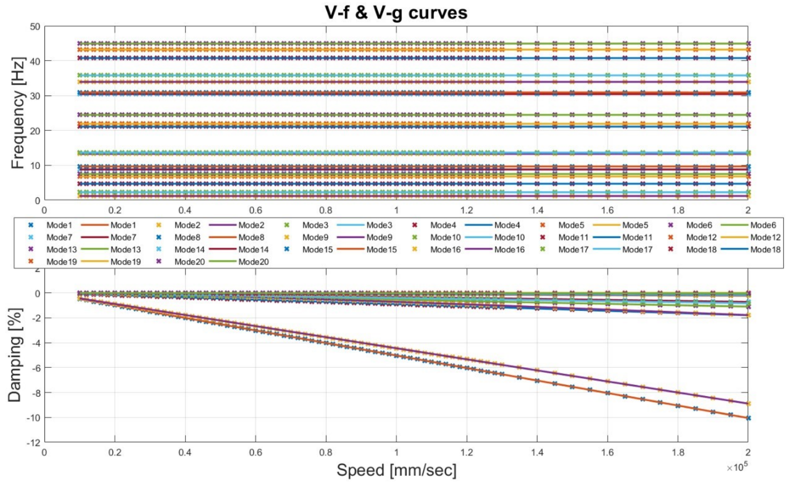

FIGURE C.14: Damping and Frequency vs Velocities plots, Method P-K, NASTRANâĎć.

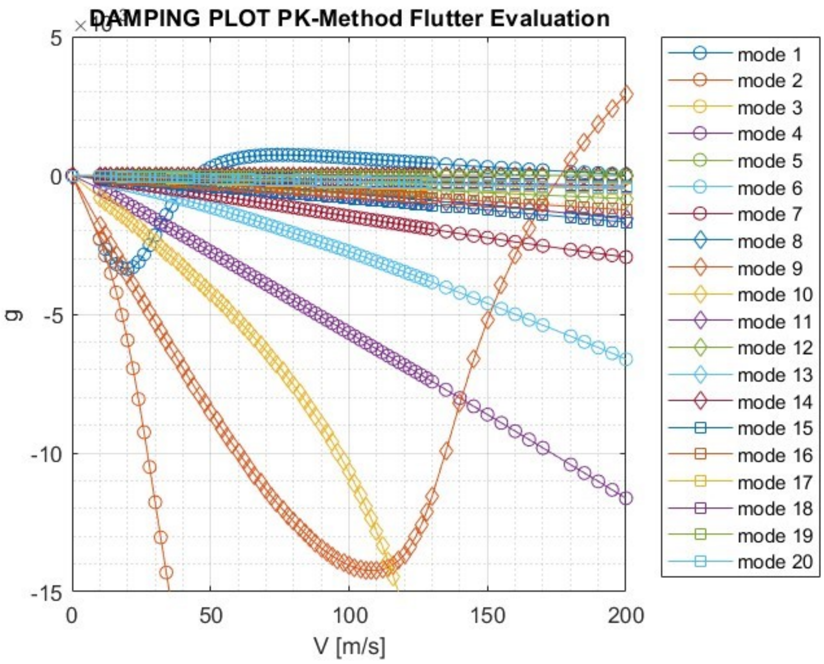

FIGURE C.15: Damping vs Velocities plots, Method P-K, ZAERO.

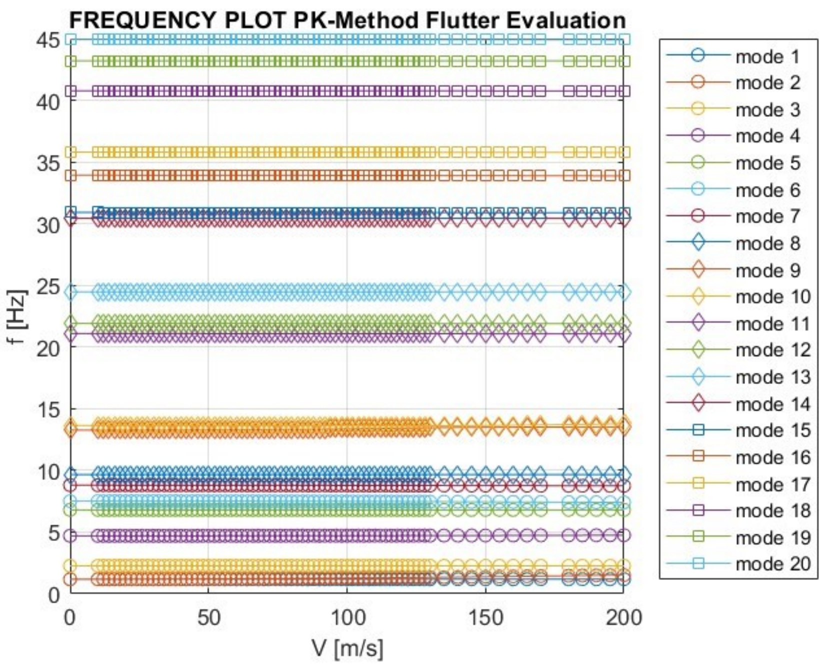

FIGURE C.16: Frequency vs Velocities plots, Method P-K, ZAERO.

Bibliography

[1] Esler D. “Leonardo’s AW609: Bringing tiltrotor technology to civil aviation.” In: *Business & Commercial Aviation* (2020), pp. 46–54.

[2] B. Norton. “Bell Boeing V-22 Osprey, Tiltrotor Tactical Transport”. In: *Review of Scientific Instruments* (2004).

[3] “CLEAN SKY 2 joint undertaking third amended bi-annual work plan and budget 2018–2019, annex to decision CS-GB-2019-04-09 decision third amended and budget 2018–19.” In: (2018). URL: https://ec.europa.eu/research/participants/data/ref/h2020/other/wp/jtis/h2020-wp1819-cleansky_en.pdf.

[4] M. Belardo et al. “On the Preliminary Structural Design Strategy of the Wing of the Next-Generation Civil Tiltrotor Technology Demonstrator”. In: *International Journal of Aeronautical and Space Sciences* (2020). URL: https://link.springer.com/article/10.1007/s42405-020-00330-2.

[5] Yin P., Huang B.G., and Liu Z.C. “Analysis of noise characteristics in helicopter cabin.” In: *Helicopter Technique* (2019), pp. 28–31.

[6] AIAAIASMEISAEIASEE 25th Joint Propulsion Conference., ed. *Noise considerations for tilt-rotor.* Monterey, CA, Nov. 1989.

[7] P. Avitabile et al. “Modal parameter estimation for large, complicated MIMO test”. In: *Sound & Vibration, 40(1)* (2006).

[8] W. Heylen, S. Lammens, and P. Sas. *Modal Analysis Theory and Testing.* K. U. Leuven, Belgium. Faculty of Engineering, Dept. of Mechanical Engineering, Division of Production Engineering, Machine Design and Automation, 1998.

[9] N.M.M. Mala and J.M.M. Silva. *Theoretical and Experimental Modal Analysis.* Ed. by Taunton Research Studies Press. 1997.

[10] P. Avitabile. *Modal Testing: A Practitioner’s Guide*. Ed. by John Wiley & Sons Ltd. 2017.

[11] D.J. Ewins. *Modal testing: Theory, Practice and Application, 2nd Ed.* Ed. by John Wiley & Sons Ltd. 2009.

[12] J. He and Z.F. Fu. *Modal analysis. 1st Edition*. Ed. by Butterworth-Heinemann. 2001.

[13] F. Lembrets et al. “Multiple Input Modal Analysis of Frequency Response Function based on Direct Parameter Identification”. In: *Proceeding of the International Modal Analysis Conference, IMAC 4*. 1986, pp. 589–598.

[14] K.J. Lemler and W.H. Semke. "Application of Modal Testing and Analysis Techniques on a sUAV." In: vol. 6. 2013, pp. 47–57.

[15] K.J. Lemler and W.H. Semke. "Application of Modal Testing and Analysis Techniques on a sUAV." In: vol. 6. Sept. 2013, pp. 47–57.

[16] Penny Jia et al. "Experimental and FEM Modal Analysis of a Deployable-Retractable Wing". In: *Modern Mechanical Engineering* 04 (Jan. 2014), pp. 183–197. DOI: 10.4236/mme.2014.44018.

[17] P. Guillaume et al. "A poly-reference implementation of the least-squares complex frequency-domain estimator". In: *International Modal Analysis Conference*. 2003.

[18] T. G. Carne, D. T. Griffith, and M. Casias. "Support Conditions for experimental modal analysis". In: *25th International Modal Analysis Conference, IMAC 4*. Orlando, USA, 2007.

[19] Bart Peeters et al. "Advanced shaker excitation signals for aerospace testing". In: vol. 1. Apr. 2011, pp. 229–241. ISBN: 978-1-4419-9301-4. DOI: 10.1007/978-1-4419-9302-1_20.

[20] A. Erturk and D. J. Inman. "On the Fundamental Transverse Vibration Frequency of a Free-Free Thin Beam with Identical End Masses". In: *Journal of Vibration and Acoustics, 129(5)* (2007), pp. 656–662.

[21] C.L. Kirk and S.M. Wiedemann. "Natural Frequencies and Mode Shapes of a Free-Free Beam with Large End Masses". In: *Journal of Sound and Vibration* (2002).

[22] J. Haener. "Formulas for the Frequencies Including Higher Frequencies of Uniform Cantilever and Free-Free Beams With Additional Masses at the Ends". In: *ASME J. Appl. Mech., 25* (1958), p. 412.

[23] R. D. Blevins. *Formulas for Natural Frequency and Mode Shape*. Ed. by Van Nostrand Reinhold. New York, 1979.

[24] J. Pilkey. *Formulas for Stress, Strain, and Structural Matrices*. Ed. by Wiley. Hoboken, NJ, 2005.

[25] K. Studebaker and A. Abrego. *Ground Vibration Test of XV-15 Tiltrotor Research Aircraft and Pre-test Prediction*. Moffett Field California: Ames Research Center, 1992.

[26] Bart Peeters et al. "Modern solutions for Ground Vibration Testing of large aircraft". In: *Conference Proceedings of the Society for Experimental Mechanics Series* (Jan. 2008).

[27] Anatolyi V. Bykovsky et al. "Research of elastic suspension systems influence on the accuracy of aircraft modal parameters estimation". In: *Conference Proceedings of 8th European Conference for Aeronautics and Space Sciences* (2019).

[28] Yves Govers et al. “AIRBUS A350XWB Ground Vibration Testing: Efficient techniques for customer oriented on-site modal identification”. In: Sept. 2014.

[29] J. Lau et al. “Ground Vibration Testing Master Class: Modern Testing and Analysis Concepts Applied to an F-16 Aircraft. Advanced Aerospace Applications.” In: vol. 1. 2011, pp. 221–228.

[30] Richard Boynton and Kurt Wiener. “Measuring Mass Properties of Aircraft Control Surfaces”. In: St. Louis, Missouri, 2000.

[31] Richard Boynton. “Measuring weight and all three axes of the center of gravity of a rocket motor without having to re-position motor”. In: Virginia Beach, Virginia, 2002.

[32] Beranek L.L. *Noise and vibration control*. McGraw-Hill Book Co., Inc., c., 1971.

[33] Wilby J. F. *Propeller aircraft interior noise, propeller performance and noise*. Von Karman Inst. for Fluid Dynamics, 1982.

[34] Van Dyke J.D. Jr. et al. “Cabin noise reduction in the DC-9”. In: *AIAA Paper No.67–401,* (1967).

[35] Wilby J.F., McDaniel C.D., and E.G. Wilby. “In-flight acoustic measurements on a light twin-engined turboprop airplane”. In: *NASA CR-178004* (1985).

[36] Magliozzi B. “Acoustic pressures on a prop-fan aircraft fuselage surface”. In: (1980).

[37] Petrone G. et al. “A statistical energy analysis (SEA) model of a fuselage section for the prediction of the internal Sound Pressure Level (SPL) at cruise flight conditions.” In: *Aerospace Science and Technology* (2019).

[38] Marulo F. et al. “Interior noise sources identifications, in-flight measurements and numerical correlations of an advanced business aircraft.” In: *12th AIAA/CEAS Aeroacoustics Conference*. Ed. by 27th AIAA Aeroacoustics Conference. Cambridge, Massachusetts, 2006.

[39] Hayden R.E., Murray B.S., and Theobald M.A. “A study of interior noise levels, noise sources and transmission paths in light aircraft”. In: *NASA CR-I72152* (1983).

[40] Wilby J. F. and Gloyna F. L. “Vibration measurements of an airplane fuselage structure”. In: *I. Turbulent boundary layer excitation. J. Sound Vib. 23(4),* (1972), pp. 443–466.

[41] H. Lyle Karen. *XV-15 structural acoustic data*. NASA technical memorandum 112855. U.S. Army Research Laboratory Technical Report 1423. Langley Research Center, Virginia: 443-466, 1997.

[42] Barton C. K. and Mixson J. S. “Characteristics of Propeller Noise on an Aircraft Fuselage.” In: *J. Aircr. 18(3)* (1981), pp. 200–205.

[43] Wilby J. F. and Wilby E. G. “Analysis of in-flight acoustic data for a twin-engined turboprop airplane.” In: *NASA CR-178389* (1988).

[44] Howlett J. T. and Schoenster J. A. “An experimental study of propeller induced structural vibration and interior noise.” In: *SAE Paper 790625* (1979).

[45] D. G. Karczub M. P. Norton. *Fundamentals of Noise and Vibration Analysis for Engineers, 2nd Edition*. CAMBRIDGE UNIVERSITY PRESS, 2003.

[46] Ungar E. E. et al. *A Guide for Estimation of Aeroacoustic Loads on Flight Vehicle Surfaces.* AFFDL-TR-76-91. U.S. Air Force, 1977.

[47] Allan D. Pierce. *Acoustics: An Introduction to Its Physical Principles and Applications, 3th Edition*. Ed. by Springer. ASA PRESS, 2019.

[48] F. H. Schmitz. *"Rotor Noise." Acoustics of Flight Vehicles: Theory and Practice.* WRDC Technical Report 90-3052. NASA Reference Publication 1958, 1991.

[49] Jiri Cecrdle. *Noise and Vibration Analysis*. Ed. by Wiley. John Wiley & Sons, Ltd, 2011.

[50] Bendat J. S. and Piersol A. G. *Random data: analysis and measurement procedures.* 4th edn. Wiley,Hoboken, 2010.

[51] Aniello Daniele Marano et al. *Tiltrotor Acoustic Data Acquisition and Analysis through 130B40 ICP® Surface Microphones*. Tech. rep. Department of Industrial Engineering - University of Naples Federico II, Oct. 2021. URL: https://www.pcb.com/contentstore/mktgcontent/whitepapers/WPL_86_130B40.pdf.

[52] T.H.G. Megson. *Aircraft Structures for Engineering Students 6th Edition*. Butterworth-Heinemann, 2016.

[53] J. R. Wright and J. E. Cooper. *"Introduction to Aircraft Aeroelasticity and Loads"*. John Wiley & Sons, Ltd, 2007.

[54] Jiri Cecrdle. *Whirl flutter of turboprop aircraft structures*. Ed. by Elsevier. Woodhead Publishing, 2015.

[55] WR Krüger. “Multibody analysis of whirl flutter dynamics on a tiltrotor wind tunnel model”. In: *Proceedings of international forum of aeroelasticity and structural dynamics (IFASD)*. 2009.

[56] R. E. Donham and G. A. Watts. *Whirl flutter first case.* In The Revolution in Structural Dynamics.: MIT Memorial book., 1997. ISBN: 0-9659773-0-7.

[57] Jiri Cecrdle et al. “Development and wind tunnel test of W-WING whirl flutter aeroelastic demonstrator”. In: *57th AIAA/ASCE/AHS/ASC Structures, Structural Dynamics, and Materials Conference*. 2016, p. 1961.

[58] J. Cecrdle, O. Vich, and P. Malinek. “Wind tunnel test of a whirl flutter aeroelastic demonstrator.” In: *Proceedings of the Institution of Mechanical Engineers, Part G: Journal of Aerospace Engineering*. 233. 2019, pp. 969–977.

[59] Reed III and Wilmer H. “Propeller-rotor whirl flutter: A state-of-the-art review”. In: *Journal of Sound and Vibration* 4.3 (1966), pp. 526–544.

[60] Richard L Bielawa. *Rotary wing structural dynamics and aeroelasticity*. American Institute of Aeronautics and Astronautics, 2006.

[61] Wilmer H Reed. "Review of propeller-rotor whirl flutter". In: (1967).

[62] Taeseong Kim, Shin SangJoon, and Kim Taehyoun. "Analysis of tiltrotor whirl flutter in time and frequency domain." In: 23 (2009), pp. 3281–3291. URL: https://doi.org/10.1007/s12206-009-1002-3.

[63] Omri Rand and Richard J Peyran. "Experimental demonstration of the influence of wing couplings on Whirl-Flutter instability". In: *Journal of aircraft* 37.5 (2000), pp. 859–864.

[64] John C Houbolt and WILMER H REED III. "Propeller-nacelle whirl flutter". In: *Journal of the Aerospace Sciences* 29.3 (1962), pp. 333–346. URL: https://doi.org/10.1016/0022-460X(66)90142-8.

[65] David J Piatak et al. "A wind-tunnel parametric investigation of tiltrotor whirl-flutter stability boundaries". In: (2001).

[66] CW Acree, RJ Peyran, and Wayne Johnson. "Rotor Design Options for Improving Tiltrotor Whirl-Flutter Stability Margins". In: *Journal of the American Helicopter Society* 46.2 (2001), pp. 87–95.

[67] CW Acree Jr. "Rotor design options for improving V-22 whirl-mode stability". In: *ANNUAL FORUM PROCEEDINGS-AMERICAN HELICOPTER SOCIETY*. Vol. 58. 2. AMERICAN HELICOPTER SOCIETY, INC. 2002, pp. 2095–2110.

[68] Donald L Kunz. "Analysis of proprotor whirl flutter: review and update". In: *Journal of aircraft* 42.1 (2005), pp. 172–178.

[69] Jae-Sang Park and et al. "Design optimization framework for tiltrotor composite wings considering whirl flutter stability." In: *Composites Part B: Engineering* 41 (2010), pp. 257–267. URL: https://doi.org/10.1016/j.compositesb.2010.03.005.

[70] Hao Kang, Shen Jinwei, and Andrew R. Kreshock. "Validation of Comprehensive Analysis for Tiltrotor Whirl Flutter Predictions." In: *Journal of Aircraft* 54 (2017), pp. 1566–1570. URL: https://doi.org/10.2514/1.C034272.

[71] Jinwei Shen and Hao Kang. "Comparison study of tiltrotor whirl flutter using two rotorcraft comprehensive analyses." In: *Journal of Aircraft* 54 (2017), pp. 845–850. URL: https://doi.org/10.2514/1.C033905.

[72] et al. Yeo Hyeonsoo. "Comparison of CAMRAD II and RCAS Predictions of Tiltrotor Aeroelastic Stability." In: *Journal of the American Helicopter Society* 63 (2018), pp. 1–13. URL: https://doi.org/10.4050/JAHS.63.022001.

[73] Andrew R. Kreshock, Robert P. Thornburgh, and Hyeonsoo Yeo. “Comparison of Comprehensive Analyses Predicting Whirl Flutter Stability of the Wing and Rotor Aeroelastic Test System.” In: *Journal of the American Helicopter Society* 64 (2019), pp. 1–12. URL: https://doi.org/10.4050/JAHS.64.042010.

[74] Frederick Tsai and Anubhav Datta. “Design of A New Tilt Rotor Test Facility at the University of Maryland.” In: *AIAA Scitech* 64 (2019). URL: https://doi.org/10.2514/6.2019-2136.

[75] Hyeonsoo Yeo and Andrew R. Kreshock. “Whirl Flutter Investigation of Hingeless Proprotors.” In: *Journal of Aircraft* 57 (2020), pp. 586–596. URL: https://doi.org/10.2514/1.C035609.

[76] Herbert S Ribner. *Propellers in yaw*. NATIONAL AERONAUTICS and SPACE ADMIN LANGLEY RESEARCH CENTER HAMPTON VA, 1943.

[77] J Thirstrup Petersen, Kenneth Thomsen, and Helge Aagaard Madsen. *Local blade whirl and global rotor whirl interaction*. 1998. URL: https://backend.orbit.dtu.dk/ws/portalfiles/portal/7751088/ris_r_1067.pdf.

[78] Jong-Shyong Wu, Foung-Tang Lin, and Huei-Jou Shaw. “Analytical solution for whirling speeds and mode shapes of a distributed-mass shaft with arbitrary rigid disks”. In: *Journal of applied mechanics* 81.3 (2014).

[79] Samuel R Bland and Robert M Bennett. “Wind-tunnel measurement of propeller whirl-flutter speeds and static-stability derivatives and comparison with theory”. In: (1963).

[80] Reed III Wilmer H and Robert M Bennett. “Propeller whirl considerations for V/STOL aircraft”. In: (1963).

[81] Michael C.Y. Niu. *Airframe Structural Design: Practical Design Information and Data on Aircraft Structures, 2th Edition*. Ed. by Adaso Adastra Engineering Center. Hong Kong Conmilit Press LTD., 1999.

[82] Ryan Decker et al. “Affordable Design and Manufacturing of the V-280 Wing”. In: *AHS International Forum 73 May 9-11, 2017* (2017).

[83] Cecil Acree, R. Peyran, and Wayne Johnson. “Rotor Design Options for Improving XV-15 Whirl-Flutter Stability Margins”. In: *Journal of the American Helicopter Society* 46 (Apr. 2001), pp. 87–95. DOI: 10.4050/JAHS.46.87.

[84] Sandilya Kambampati. “Optimization of Composite Tiltrotor Wings with Extensions and Winglets”. PhD thesis. The Pennsylvania State University, The Graduate School College of Engineering, 2016.

[85] Sandilya Kambampati. “Excalibur. The Cutting Edge in Tiltrotor Technology Flying Further, Higher, Faster”. In Response to 2011 Annual AHS International Student Design Competition - Graduate Category. Alfred Gessow Rotorcraft Center Department of Aerospace Engineering University of Maryland, College Park Maryland, 20742, 2011.

[86] Charles C. Crawford, Michael W. Heiges, and Mark Wasikowski. “Analysis of Tiltwing Aircraft Configuration Potential”. In: *SAE Transactions* 105 (1996), pp. 1267–1280. ISSN: 0096736X, 25771531. DOI: 10.2307/44725615. URL: http://www.jstor.org/stable/44725615.

[87] D. P. Chappell and R. J. Peyran. “Methodology for Estimating Wing Weights for Conceptual Tilt Rotor and Tilt Wing Aircraft”. In: *Society of Allied Weight Engineers 51st Annual Conference*. Hartford, Connecticut, 1992.

[88] G. Costa. “Conceptual Design of a 150-Passenger Civil Tiltrotor”. In: 2012.

[89] William W. Chung et al. *Modeling High-Speed Civil Tiltrotor Transports in the Next Generation Airspace*. 2011.

[90] Alessandro Stabellini. “The European Tilt Rotor-Status of ERICA Design and Test Activities”. In: *Aerodays 2011*. Madrid, 2011.

[91] Wayne Johnson, Gloria Yamauchi, and Michael Watts. “NASA Heavy Lift Rotorcraft Systems Investigation”. In: (Oct. 2005). DOI: 10.4271/2005-01-3149.

[92] D. E. Goldberg. *Genetic Algorithms in Search, Optimization and Machine Learning*. Ed. by Addison Wesley Publishing Company. 1989.

[93] W. E. Schmitendorgf et al. *Using Genetic Algorithms for Controller Design: Simultaneous Stabilization and Eigenvalue Placement in a Region*. Technical Report No. CS92-9. Dept. Computer Science, College of Engineering, University of New Mexico, 1992.

[94] M. F. Bramlette. “Initialization, Mutation and Selection Methods in Genetic Algorithms for Function Optimization.” In: *Proc ICGA 4*. 1991, pp. 100–107.

[95] C. B. Lucasius and G. Kateman. “Towards Solving Subset Selection Problems with the Aid of the Genetic Algorithm.” In: *In Parallel Problem Solving from Nature 2, R. Männer and B. Manderick, (Eds.)* Amsterdam: North-Holland, 1992, pp. 239–247.

[96] A. H. Wright. “Genetic Algorithms for Real Parameter Optimization.” In: *In Foundations of Genetic Algorithms, J. E. Rawlins (Ed.), Morgan Kaufmann*. 1992, pp. 205–218.

[97] Z. Michalewicz. *Genetic Algorithms + Data Structures = Evolution Programs*. Ed. by Springer Verlag. 1992.

[98] T. Bäck, F. Hoffmeister, and H.-P. Schwefel. “A Survey of Evolution Strategies”. In: *Proc ICGA 4*. 1991, pp. 2–10.

[99] J. E. Baker. “Adaptive Selection Methods for Genetic Algorithms”. In: *Proc ICGA 1*. 1985, pp. 101–111.

[100] C. M. Fonseca and P. J. Fleming. “Genetic Algorithms for Multiple Objective Optimization: Formulation, Discussion and Generalization”. In: *Proc ICGA 5*. 1993, pp. 416–423.

[101] V.Z. Vlasov. *Thin-walled Elastic Beams.* Washington, D.C: Office of Technical Services, US Department of Commerce, 1961.

[102] S.U. Benscoter. "A theory of torsion bending for multicell beams". In: *Journal of Applied Mechanics* 21 (1954), pp. 25–34.

[103] A. Gjelsvik. *The Theory of Thin Walled Barss*. Ed. by Wiley. New York, 1981.

[104] H. Shakourzadeh, Y.Q. Guo, and J.-L. Batoz. "A torsion bending element for thin-walled beams with open and closed cross sections." In: *Computers & Structures,* 55(6) (1995), pp. 1045–1054.

[105] N.R. Bauld and L.S. Tzeng. A Vlasov. "Theory for fiber-reinforced beams with thin-walled open cross-sections." In: *International Journal of Solids and Structures* 20(3) (1984), pp. 277–297.

[106] R. Chandra and I. Chopra. "Experimental and theoretical analysis of composite I-beams with elastic couplings." In: *AIAA Journal* 29(12) (1991), pp. 2197–2206.

[107] X.X. Wu and C.T. Sun. "Simplified theory for composite thin-walled beams." In: *AIAA Journal* 30(12) (1992), pp. 2945–2951.

[108] E. Carrera and G. Giunta. "Refined beam theories based on a unified formulation." In: *International Journal of Applied Mechanics* 02(1) (2010), pp. 117–143.

[109] V.V. Volovoi and D.H. Hodges. "Single- and multi-celled composite thin-walled beams." In: *AIAA Journal* 40 (2003), pp. 960–965.

[110] J.M. Davies and P. Leach. "First-order generalised beam theory." In: *Journal of Constructional Steel Research* 31(2-3) (1994), pp. 187–220.

[111] W.B. Yu et al. "A generalized Vlasov theory for composite beams." In: *Thin-Walled Structures* 43(9) (2005), pp. 1493–1511.

[112] P. Leach and J.M. Davies. "An experimental verification of the generalized beam theory applied to interactive buckling problems." In: *Thin-Walled Structures* 25(1) (1996), pp. 61–79.

[113] S. Pines. "An Elementary Explanation of the Flutter Mechanism." In: *Proceedings Nat. Specialists Meeting on Dynamics and Aeroelasticity, Institute of the Aeronautical Sciences*. Ft. Worth, Texas, 1958, pp. 52–58.

[114] Dewey H. Hodges and G. Alvin Pierce. *Introduction to Structural Dynamic and Aeroelasticity.* Cambridge Aerospace Series, 2014.

[115] B. Peeters et al. "Modern solutions for ground vibration testing of large aircraft." In: *26th Conference and Exposition on Structural Dynamics, IMACXXVI*. 2008.

[116] R.L. Bisplinghoff and H. Ashley. *Principle of Aeroelasticity*. Dover Publications, 1962.

[117] Raymond L. Bisplinghoff, Holt Ashley, and Robert L. Halfman. *Aeroelasticity*. Dover Publications, Inc.

[118] E. Albano and W.P. Rodden. "Doublet-lattice method for calculating lift distributions on oscillating surfaces in sub-sonic flows". In: *AIAA Journal* 7.2 (1969), pp. 279–285.

[119] William P. Rodden and Erwin H. Johnson. *MSC/NASTRAN Aeroelastic Analysis User's Guide Ver.68.* MSC Software Corporation. Los Angeles, CA, USA., 1994.

[120] *MSC Nastran Aeroelastic Analysis User's Guide,* MSC Software Corporation. Los Angeles, CA, USA., 2004.

[121] W.P. Rodden. "The development of the doublet-lattice method." In: *International Forum on Aeroelasticity and Structural Dynamics*. Rome, 1997.

[122] *ZAERO User's Manual ver.9.3*. Zona Technology Inc. Scottsdale, Arizona, USA.

[123] T.A. Weisshaar. "Forward Swept Wing Static Aeroelasticity." In: *AFFDL, TR-79-3087*. 1979.

[124] T.A. Weisshaar. "Aeroelastic Stability and Performance Characteristics of Aircraft with Advanced Composite Sweptforward Wing Structures." In: *AFFDL, TR-78-116*. 1978.

[125] Jan R. Wright and Jonathan Edward Cooper. *Introduction to Aircraft Aeroelasticity and Loads, 2nd Edition.* John Wiley Sons Inc., 2015.

[126] J. R. Wright and J. E. Cooper. *Aircraft Aeroelasticity and Loads.* Manchester, United Kingdom: Jon Wiley Sons Ltd, 2007.

[127] W.R. Rodden and E.H. Johnson. *MSC/Nastran Aeroelastic Analysis*. MSC. 1994.

[128] W. T. Thomson. *Theory of Vibration with Applications, Third Edition.* Prentice-Hall, 1988.

[129] W. H. III Reed. "Flight Flutter Testing: Equipment and Techniques." In: *FAS Southwest Region Annual Designer Conference*. Ft. Worth, Texas, 1991.